

Sterically flexible molecules in the gas phase

A spectroscopic study

DISSERTATION

zur Erlangung des akademischen Grades
doctor rerum naturalium
(Dr. rer. nat.)
im Fach Chemie

eingereicht an der
Mathematisch-Naturwissenschaftlichen Fakultät I
Humboldt-Universität zu Berlin

von
Frau Dipl.-Chem. Undine Erlekan
geboren am 23.02.1981 in Staßfurt

Präsident der Humboldt-Universität zu Berlin:
Prof. Dr. Dr. h.c. Christoph Marksches

Dekan der Mathematisch-Naturwissenschaftlichen Fakultät I:
Prof. Dr. Christian Limberg

Gutachter:

1. Prof. Dr. Gerard J. M. Meijer
2. Prof. Dr. Klaus Rademann

Tag der mündlichen Prüfung: 28. Januar 2008

Promotor: Prof. Dr. Gerard J. M. Meijer

Co-Promotor: Gert von Helden, Ph.D.

Die Arbeiten zur vorliegenden Dissertation wurden am Fritz-Haber-Institut der Max-Planck-Gesellschaft in Berlin durchgeführt.

Contents

List of Figures	ix
List of Tables	xvii
1 General Introduction	1
1.1 Motivation	1
1.2 Experimental setups	2
1.2.1 IR and UV spectroscopy	3
1.2.2 Microwave spectroscopy	7
1.3 Spectroscopic techniques	9
1.3.1 UV spectroscopy	9
1.3.2 Infrared spectroscopy	12
1.3.3 Microwave spectroscopy	14
1.4 Permutation-inversion group theory	19
1.4.1 Nuclear spin statistics	20
1.5 The benzene dimer	23
1.5.1 Experimental approaches to the benzene dimer	23
1.5.2 Theoretical attempts	24
1.5.3 UV spectra of the benzene dimer	26
2 Infrared Spectroscopy on the benzene dimer	35
2.1 The \mathbf{B}_{1u} C-H stretching mode of the benzene monomer	35
2.1.1 Introduction	35
2.1.2 Experimental method	37
2.1.3 Results and Discussion	38
2.1.4 Conclusion	42
2.2 Revealing the vibrational properties of the two benzene subunits in the dimer	42
2.2.1 Introduction	42
2.2.2 Infrared spectra	44
2.2.3 Discussion	46
2.2.4 Conclusion	56

3	Microwave spectroscopy of the benzene dimer	59
3.1	Introduction	59
3.1.1	Experimental method	60
3.2	Experimental results	62
3.2.1	(C ₆ H ₆) ₂	62
3.2.2	(C ₆ H ₆)(C ₆ D ₆)	66
3.2.3	Stark effect measurements	70
3.3	MS group theory of the benzene dimer	74
3.3.1	Permutation-inversion groups	74
3.3.2	Tunneling splitting of rotational levels	77
3.4	Discussion	86
3.4.1	Benzene dimer - a symmetric top	86
3.4.2	Tunneling splitting pattern	87
3.4.3	Stark effect and dipole moment	89
3.4.4	Comparison of experimental and theoretical intensity patterns	89
3.5	Conclusion and future prospects	90
4	Control and manipulation of conformational interconversion	93
4.1	Introduction	93
4.2	Conformational interconversion driven by rare gas atoms	95
4.2.1	Experimental method	95
4.2.2	Results and Discussion	96
4.2.3	Catalysis model	99
4.2.4	Application	100
4.2.5	Conclusion	102
4.3	Conformational interconversion controlled by selective vibrational excitation	102
4.3.1	Introduction	102
4.3.2	Experimental method	103
4.3.3	Results and Discussion	104
4.3.4	Conclusion and perspectives	108
5	The amino acid phenylalanine	109
5.1	Introduction	109
5.2	Experimental method	112
5.3	Results and Discussion	112
5.3.1	Missing conformer E	112
5.3.2	On the observed conformer abundances of phenylalanine	114
5.4	Conclusion	120
	Summary and outlook	121
	Bibliography	125

A	Appendix: The character tables	139
B	Appendix: The IR laser system - troubleshooting	143
	Zusammenfassung	147
	Résumé	151
	Publikationsliste	155
	Selbstständigkeitserklärung	157
	Danksagung	159

List of Figures

1.1	Scheme of the molecular beam machine used for the UV and IR experiments described in the following chapters.	3
1.2	(a) Scheme of the laser desorption source used to bring molecules with low vapor pressure into the gas phase. (b) Modifications of the laser desorption setup for the experiments presented in section 4.3.	5
1.3	Scheme of the infrared (IR) laser system. The IR light is generated and amplified in a series of LiNbO ₃ crystals by difference frequency mixing of the output of a pulsed dye laser with the 1064 nm beam of an injection seeded Nd:YAG laser.	6
1.4	Scheme of the experimental setup used to perform microwave experiments. The molecules enter the chamber through a pulsed valve placed in the center of the left spherical mirror. The spherical mirrors serve as resonator for the microwaves, but can also be used as electrodes for Stark effect measurements.	8
1.5	Schematic representation of different types of Resonance Enhanced Multi Photon Ionization (REMPI). The first UV photon excites resonantly an electronically excited state, for example S ₁ , the second UV photon subsequently ionizes the molecule. (a) 1-color REMPI excites the molecule to energies far above the ionization potential IP. (b) 2-color REMPI ionizes the molecule with two photons of independently tunable frequencies. (c) Double resonance experiment in which an IR laser excites vibrational energy levels of the electronic ground state prior to electronic excitation depleting the ground state and thus reducing the UV ionization yield (shown as light lines). Electronic excitation from the vibrationally excited state is very unlikely due to the different vibrational frequencies in S ₀ and S ₁	11

1.6	(a) Without an electromagnetic field the molecular dipoles are oriented statistically. (b) The interaction with a microwave pulse of duration τ_p orients the dipoles. (c) The decay of the so formed macroscopic molecular field is recorded in the time domain and (d) Fourier transformed into the frequency domain.	15
1.7	Schematic representation of the (a) quadratic and (b) linear Stark effect on the rotational levels of a symmetric top species. The selection rules for a transition are $\Delta J = \pm 1$, $\Delta K = 0$ and $\Delta M_J = \pm 1$ or 0, depending on the relative orientation of the microwave and electric field. (adapted from Reference [35]) . .	18
1.8	Symmetry operations expressed in terms of point group theory (\mathbf{D}_{6h}) and permutation-inversion group theory ($\mathbf{D}_{6h}(\text{M})$) where the pairs of C-H bonded nuclei are numbered 1-6 around the benzene ring.	19
1.9	Structures of theoretically often considered benzene dimer geometries. While the (a) "Sandwich" (\mathbf{D}_{6h}) and the (b) T-shaped structure (\mathbf{C}_{2v}) on the left represent saddle points, the (c) parallel displaced (\mathbf{C}_{2h}) and (d) distorted T-shaped (\mathbf{C}_s) structures on the right represent minima on the potential energy surface [70].	23
1.10	UV spectra of $(\text{C}_6\text{H}_6)_2$ (black line), $(\text{C}_6\text{H}_6)(\text{C}_6\text{D}_6)$ (gray line) and $(\text{C}_6\text{D}_6)_2$ (light gray line) obtained by exciting the 0_0^0 transition (bottom) and the 6_0^1 transition (top). The spectra of C_6H_6 and C_6D_6 excited via the 6_0^1 transition are shown as dashed lines. .	27
1.11	Overview of possible orientations of two benzene molecules. Additionally, the symmetries of the individual subunits are given next to the respective moieties, and the symmetry of the whole system is given together with its label (I-IX). The symmetries for structures I and II given in brackets refer to the non-rigid structure (see text).	29
2.1	Overview of the normal modes of C_6H_6 (\mathbf{D}_{6h} point group). The modes of A_{2u} and E_{1u} symmetry are IR active. The vibrations shown in a box are the relevant C-H stretch vibrations in this chapter.	36

2.2	IR overview spectra in the region between 3010 and 3110 cm^{-1} of $(\text{C}_6\text{D}_6)^S(\text{C}_6\text{H}_6)^T$ (top) and $(\text{C}_6\text{H}_6)^S(\text{C}_6\text{D}_6)^T$ (bottom), corresponding to the two subunits of the benzene dimer, the "top" and the "stem", respectively. The positions of the IR active C-H stretch modes of the benzene monomer (D_{6h}) are indicated as solid vertical lines and those of the two known IR inactive fundamental modes ν_7 (E_{2g}) and ν_2 (A_{1g}) as dashed vertical lines. In the inset the region between 3054 and 3059 cm^{-1} is shown for $(\text{C}_6\text{H}_6)^S(\text{C}_6\text{D}_6)^T$, measured with a 10 times higher laser fluence. The red most absorption signal in the spectrum of $(\text{C}_6\text{H}_6)^S(\text{C}_6\text{D}_6)^T$ is attributed to result from the so far unknown ν_{13} (B_{1u}) fundamental mode of C_6H_6	39
2.3	IR spectra of the Fermi triad in the range between 3010 and 3110 cm^{-1} for the benzene monomer (bottom) and the two monomeric subunits, the "stem" (middle) and the "top" (top), of the benzene dimer. The ν_{20} (E_{1u}) fundamental mode (left) is in Fermi resonance with the E_{1u} components of the $\nu_1 + \nu_6 + \nu_{19}$ (middle) and $\nu_8 + \nu_{19}$ (right) combination bands which have both $B_{1u} + B_{2u} + E_{1u}$ symmetry.	44
2.4	IR spectra of the indirectly measured fundamental modes ν_{13} , ν_7 and ν_2 (of B_{1u} , E_{2g} and A_{1g} symmetry, respectively) of the benzene monomer. These modes are IR inactive in the D_{6h} environment of the benzene monomer, however, activated in the lowered symmetry of the "stem" (C_s or C_{2v}) and thus observable in the spectrum of $(\text{C}_6\text{H}_6)^S(\text{C}_6\text{D}_6)^T$	45
2.5	Inertial axis system of the benzene dimer in a C_s T-shaped geometry.	48
2.6	Rotational band contours of a-, b- and c-type transitions in the "stem" of the benzene dimer assuming a rotational temperature of 5 K. The contours calculated from experimental (black lines) and theoretical " C_s over bond" (gray lines) rotational constants are very similar. For the a-type transition the P-, Q- and R-branches are indicated.	50
2.7	The simulated rotational band contours (gray) assuming a rotational temperature of 5 K are shown in comparison with the experimental absorption bands (black) of (a) the ν_{20} fundamental mode in the "top", (b) the ν_{20} fundamental mode in the "stem" and (c) the ν_7 fundamental mode in the "stem".	51
2.8	Rotational band contours (gray lines) for a-, b- and c-type transitions at 1 K rotational temperature in $(\text{C}_6\text{H}_6)^S(\text{C}_6\text{D}_6)^T$ and $(\text{C}_6\text{D}_6)^S(\text{C}_6\text{H}_6)^T$, representing those of the two subunits, the "stem" and the "top". The envelopes are fitted by Gauss functions (black lines).	51

2.9	Full width at half maximum (FWHM) of the Gauss functions fitting the rotational band contours of the a-, b- and c-type transitions of the "stem" and the "top" in the benzene dimer as a function of the rotational temperature. Additionally shown are fits of the FWHM assuming exclusively contributions from a- and b-type transitions and from b- and c-type transitions for the "stem" and the "top", respectively.	52
2.10	The contours of the observed fundamental modes and combination bands are reproduced by a superposition of Gaussians. Assuming a rotational temperature of 1 K, the full width at half maximum (FWHM) is 0.67 cm^{-1} for all spectral features resulting from the "stem" and 0.77 cm^{-1} for those of the "top". These values correspond to the average FWHM of the a-b-type (of $(\text{C}_6\text{H}_6)^S(\text{C}_6\text{D}_6)^T$) and b-c-type (of $(\text{C}_6\text{D}_6)^S(\text{C}_6\text{H}_6)^T$) transitions, respectively. The simulated envelope at 1 K is shown as a black line together with the Gaussians it is composed of as dark gray lines. The rotational envelope assuming a rotational temperature of 1.5 K is reproduced as well and indicated as black dashed line. The appropriate components are not shown. The experimental spectrum is shown as a light gray solid line. . . .	53
3.1	Typical symmetric top transition of $(\text{C}_6\text{H}_6)_2$ measured with neon as carrier gas. As an example the $J', K' \leftarrow J, K$: $6, 0 \leftarrow 5, 0$ transition is shown.	62
3.2	Rotational transitions that do not contribute to the symmetric top spectrum of $(\text{C}_6\text{H}_6)_2$. Possibly these transitions result from larger C_6H_6 clusters.	63
3.3	The Gaussian microwave intensity distribution creates a distorted relative intensity pattern. The real relative intensities can be obtained by separate measurements, indicated by the dashed lined Gaussian functions, for each component.	67
3.4	The rotational transition $J', K' \leftarrow J, K = 7, 2 \leftarrow 6, 2$ of $(\text{C}_6\text{H}_6)^S(\text{C}_6\text{D}_6)^T$ measured with neon as a carrier gas is shown in the right panel. For comparison, the same transition is shown on the left for $(\text{C}_6\text{H}_6)_2$	68
3.5	Expected Stark patterns of the torsional components of the transitions $5, 0 \leftarrow 4, 0$ and $7, 0 \leftarrow 6, 0$ at a given electric field strength. ν is the transition frequency shift, B the rotational constant, μ the dipole moment and E the electric field strength. $\frac{\Delta\nu 2h^2 B}{\mu^2 E^2}$ corresponds to α_i and the intensity to f_i (see text). The unperturbed transition is located at 0.	71

- 3.6 The $5,0 \leftarrow 4,0$ transition (left) and two of the four components of the $7,0 \leftarrow 6,0$ transition (right) measured in the presence of an external electric field with various field strengths. Each component is split by the Doppler effect. For comparison the spectra without electric field are shown. The given voltages (applied to the rear parabolic mirror (see Figure 1.4)) correlate with the electric field strength according to U/d with $d_{5,0 \leftarrow 4,0} = 0.59644$ m and $d_{7,0 \leftarrow 6,0} = 0.58746$ m, respectively. 72
- 3.7 The minimum structure is presumed to be the " C_s over bond" structure [71]. The bonded carbon-hydrogen nuclei are numbered 1-6 for the "top" and 1'-6' for the "stem". In the " C_s over bond" structure the "stem" plane bisects the "top" between 216 and 345 with 4' pointing at the bond connecting 5 and 6. Different tunneling pathways in the benzene dimer are depicted as nuclear permutations. The tunneling motions are labeled in terms of symmetry operations and of permutations. 75
- 3.8 Pictorial representation of the tunneling splitting of the $C_s(M)$ rotational states of A' and A'' symmetry, allowing for "top" C_6 torsion ($C_{6v}(M)$) and "stem" bending in $(C_6H_6)_2(G_{24})$ (left) and of the tunneling splitting of the $C_{2v}(M)$ rotational states of A_1 , A_2 , B_1 and B_2 symmetry, allowing for "top" C_6 torsion in $(C_6H_6)_2(G_{24})$ (right). The relative nuclear spin statistical weights are given in parentheses. 79
- 3.9 Pictorial representation of the tunneling splitting of the $C_s(M)$ rotational states of A' and A'' symmetry, allowing for "top" and "stem" C_6 torsion in $(C_6H_6)_2 (C_{6v}(M)_{top} \otimes C_6(M)_{stem} = G_{72})$. The relative nuclear spin statistical weights are given in parentheses. 80
- 3.10 Pictorial representation of the tunneling splitting of the $C_s(M)$ rotational states of A' and A'' symmetry allowing for the "top" C_6 torsion and the "stem" bending (G_{24}) and additional "stem" C_6 torsion in $(C_6H_6)_2 (G_{144})$. The relative nuclear spin statistical weights are given in parentheses. 81
- 3.11 Schematic representation of allowed transitions between torsional energy levels in the benzene dimer for the MS groups $C_s(M)$, $C_{2v}(M)$, $C_{6v}(M)$ and G_{24} . Torsional levels originating from one rotational level are shown together in one frame. 82

4.1	Two-color (1+1')-REMPI spectra of the benzene dimer around the origin of the $S_1 \leftarrow S_0$ transition. The measurements are performed in a molecular beam using helium (left) and neon (right) as a carrier gas. The upper spectra are recorded on the mass of the deuterated homodimer, the middle spectra on the mass of the mixed dimer and the lower spectra on the mass of the protonated homodimer. When neon is used as a carrier gas, the mixed dimer with the protonated monomer unit in the "stem" position is exclusively observed.	97
4.2	Scheme of the potential energy surface of the isotopically mixed benzene dimer (C_6H_6)(C_6D_6). The two distorted T-shaped dimer isomers are separated by two transition states and a local minimum, corresponding to a parallel displaced configuration [70]. .	98
4.3	Schematic representation of the formation and dissociation of the neon-benzene dimer complex, converting the high energy isomer into the low energy isomer.	99
4.4	Electronic excitation spectrum in the region of the origin transition of the amino acid phenylalanine in the gas phase. While in argon the conformers A, B, C, D and X are identified, in neon an additional conformer, conformer E, is observed and the intensity of the signal representing conformer A is significantly reduced. Weak, additional peaks are observed in the spectrum to the low energy side of conformer D, when using argon as a carrier gas. These peaks probably originate from the excitation of complexes with argon atoms, which dissociate upon ionization, leaving an imprint of the spectrum of the phenylalanine-argon complex on the spectrum of plain phenylalanine.	101
4.5	Schematic representation of the involved energy levels in the IR pump - UV probe experiment. (1) IR radiation excites the NH_2 antisymmetric stretch vibration of a chosen conformer. (2) Collisional cooling relaxes the excited molecules to the original or to a different conformational minimum. (3) The population changes are probed by a UV laser later in the collision free region of the expansion.	103
4.6	REMPI spectra of L-phenylalanine in the region of the vibrational origin of the $S_1 \leftarrow S_0$ transition recorded with (black line) and without (gray line) excitation of the NH_2 antisymmetric stretch vibration of conformer A. Spectrum (a) is measured using argon as a carrier gas and spectrum (b) with neon. The difference spectra (dashed lines below the respective absolute spectra) show directly the change of the conformational distribution induced by vibrational excitation.	105

4.7	Absorption bands of the NH_2 antisymmetric stretch vibration in the six low energy conformers A, B, C, D, X, E. The spectra are vertically arranged according to their increasing $S_1 \leftarrow S_0$ excitation energy. The absorption spectrum A' (dashed line) results from a hot band of conformer A.	106
5.1	Structures of five low energy conformers of phenylalanine calculated at the MP2/6-311+(2df,2p) level of theory [173]. The labeling scheme is the same as the one introduced in Reference [152].	111
5.2	IR spectra of the phenylalanine conformers A, E and X in the range between 3150 and 3450 cm^{-1} . The calculated structures [173] support the assignment of conformer E to the structural subgroup represented by conformer A.	113
5.3	Structures and their relative energies are presented from different regions of the conformation space. The structures I, III and IV, having an internal $\text{CO}_2\text{H} \rightarrow \text{NH}_2$ hydrogen bond, are separated by the highest transition state at 3740 cm^{-1} from structure V, having a $\text{NH}_2 \rightarrow \text{CO}_2\text{H}$ hydrogen bond. A transition state at 1377 cm^{-1} leads from this structure to structure II, and therefore to the structures depicted in Figure 5.4. Some of the low energy structures can be assigned to the experimentally observed conformers A, B, C, D, E and X. The assignments are given in brackets.	115
5.4	Relative energies and structures for five of the nine lowest energy conformers, as well as of the transition states separating them. Some of the low energy structures can be assigned to the experimentally observed conformers A, B, C, D, E and X. The assignments are given in brackets. The sequence corresponds from left to right to a clockwise rotation of the amino acid group about the $\text{C}_\alpha\text{-CH}_2\text{C}_6\text{H}_5$ bond, accompanied by a reorientation of the amino group.	116
5.5	Vibrational state densities of the nine lowest energy conformers of phenylalanine. The relative origins are shifted according to their relative zero point energies.	117
5.6	Comparison of the simulated intensity distributions (gray Gauss functions) with the experimental abundances (black contours) of conformers A, B, C, D, X and E, probed by 1-color REMPI and using neon as a carrier gas.	118
A.1	The benzene monomer with the bonded carbon-hydrogen nuclei being numbered 1-6.	139

A.2	The benzene dimer with the bonded carbon-hydrogen nuclei being numbered 1-6 for the "top" and 1'-6' for the "stem". The "stem" plane bisects the "top" between 612 and 543 with 4' pointing at the bond connecting 5 and 6.	139
B.1	Scheme of the laser system that has been used for the IR experiments described in this thesis. The circles indicate the technically weak points of the system.	143

List of Tables

1.1	Character table of the representations Γ of the 64 nuclear spin functions Φ_{nspin} and of the internal wavefunction Φ_{int} of C_6H_6 . .	21
1.2	The representations Γ^{nspin} of the spin functions Φ_{nspin} are given as sums of the irreducible representations $\Gamma^{(l)}$	21
1.3	Overview of the $S_1 \leftarrow S_0$ electronic excitation energies for the benzene dimer isotopologues $(C_6H_6)_2$, $(C_6H_6)(C_6D_6)$ and $(C_6D_6)_2$ excited via the 0_0^0 and 6_0^1 transition. For the heterodimer the site of electronic excitation is labeled with *. (Later, in chapter 2, it is shown that this site corresponds to the "stem" and the unlabeled site to the "top" in a (distorted) T-shaped structure.) Additionally, the splitting values and the positions relative to the appropriate benzene monomer transitions are given.	28
1.4	Symmetry properties of the benzene dimer subunits in various possible configurations. The 0_0^0 transitions is symmetry allowed if $\Gamma(\Psi_e'') \otimes \Gamma(\mu_e) \otimes \Gamma(\Psi_e')$ contains the totally symmetric representation.	29
2.1	Experimental and calculated (harmonic and anharmonic) wavenumbers $[cm^{-1}]$ for the benzene monomer and dimer. . . .	40
2.2	Symmetry properties of the four fundamental modes and two combination bands of benzene C_6H_6 in the region between 3010 and 3110 cm^{-1} in dependence of the symmetry environment. The correlation table is adapted from Reference [32]. The symmetry representations of IR active vibrational modes are underlined. . .	41
2.3	Rotational constants $[MHz]$ of both isomers of $(C_6H_6)(C_6D_6)$, assuming the theoretical near-prolate structures " C_s over bond" and " C_{2v} T-shaped" from Reference [71]. The rotational constants are calculated at the Austin Model 1 (AM 1) level of theory. For comparison, the experimentally determined values for $(C_6H_6)^S(C_6D_6)^T$ and the theoretical values of C_6H_6 are given. . .	49

2.4	Overview of the transition energies of the components of the experimentally observed fundamental modes and combination bands in the region between 3010 and 3110 cm^{-1} for the "stem" and the "top" of the benzene dimer. Additionally, the values of the central positions of the IR active modes for the benzene monomer are given. Due to the inferior signal to noise ratio in the monomer spectra possible splittings are not mentioned. All values are given in cm^{-1}	54
3.1	Frequencies of the rotational transitions observed for a symmetric top benzene dimer $(\text{C}_6\text{H}_6)_2$ and the residuals to the fitted symmetric top frequencies.	65
3.2	Rotational constant B and centrifugal distortion parameters for each component of the $(\text{C}_6\text{H}_6)_2$ quartet structure, fitted using all observed transitions with $K = 0$ and 1 (see Table 3.1) according to equation 3.4. The four lines are numbered with increasing frequency as observed in the microwave spectrum. In the last line, the root mean square deviation of the fitted values from the experimental value for all considered transitions with $K = 0$ and 1 is given. The terms $-2D_{JK}(J+1)K^2$ and $+2H_{KJ}(J+1)K^4$ in equation 3.4 are equivalent if only transitions with $K = 0$ and 1 are considered. Therefore, the sum of both terms is fitted and parameterized with Σ	66
3.3	Frequencies of the observed rotational transitions of $(\text{C}_6\text{H}_6)^S(\text{C}_6\text{D}_6)^T$, that can be assigned to $J+1, K \leftarrow J, K$ transitions, as well as the residuals of the central frequencies to the fitted symmetric top line center.	69
3.4	Experimentally determined Stark shifts of the individual torsional transitions in dependence of the voltage applied to the rear parabolic mirror (see Figure 1.4). The electric field strength U/d can be determined with $d = 0.59644$ m for the $5, 0 \leftarrow 4, 0$ transition and with $d = 0.58746$ m for the $7, 0 \leftarrow 6, 0$ transition.	73
3.5	Correlation table for the energy levels of the MS group \mathbf{G}_{288} to those of the MS group \mathbf{G}_{144} . The spin statistical weights of the energy levels given result when considering the "top" and "stem" C_6 torsion, the "stem" bending and the "top" turnover tunneling in $(\text{C}_6\text{H}_6)_2$	83

3.6	Spin statistical weights for the torsional energy levels of the benzene dimer isotopologues $(\text{C}_6\text{H}_6)_2$, $(^{13}\text{C}_6\text{H}_6)_2$, $(^{13}\text{C}_6\text{H}_6)^S(\text{C}_6\text{H}_6)^T$ and $(\text{C}_6\text{H}_6)^S(^{13}\text{C}_6\text{H}_6)^T$ in several MS groups. The spin statistical weights are given as absolute values for $\mathbf{C}_s(\text{M})$ and as relative values for all other MS groups. The labels $^{(e)}$ and $^{(o)}$ designate spin statistical weights of levels with even and odd K_a values, respectively. The labels $^{(s)}$ and $^{(a)}$ designate spin statistical weights of levels originating from s or a levels in \mathbf{G}_{24} , respectively.	84
3.7	Splittings between the torsional energy levels ($K_i = 0, 1, 2$ and 3) as a function of the C_6 torsional barrier height.	85
3.8	Rotational constants [MHz] of the near-prolate theoretical structures from Reference [71] calculated at the Austin Model 1 (AM 1) level of theory.	86
A.1	The group $\mathbf{D}_{6h}(\text{M})$	140
A.2	The group $\mathbf{C}_s(\text{M})$	140
A.3	The group $\mathbf{C}_{2v}(\text{M})$	141
A.4	The group $\mathbf{C}_{6v}(\text{M})$	141
A.5	The group \mathbf{G}_{24}	142

Chapter 1

General Introduction

1.1 Motivation

The macroscopically observable properties and functionalities of biological matter are determined by intra- and intermolecular interactions of its building blocks on the microscopic level. Often, the sum of many weak interactions are of fundamental importance for the structure and dynamics of the macroscopic system. Such weak interactions are, for example, hydrogen bonding or van der Waals interactions. The secondary structure of proteins and the base pair stacking in DNA are prominent examples where hydrogen bonding and van der Waals interactions determine the properties of the system on a macroscopic level [1].

In general, hydrogen bonding interactions are important in polar systems, while van der Waals interactions that are present in non-polar species are for example assumed to enable a gecko to hang from a ceiling [2]. To understand macroscopic observations, it is of interest to investigate such interactions on a fundamental level.

This can be done on isolated systems in gas phase experiments where perturbations by interactions with the environment can be excluded. The benzene dimer is a prototype system to investigate dispersive interactions as the two benzene units are bound by van der Waals and electrostatic interactions. Experimentally, this complex can be formed in a supersonically expanding molecular beam. Such beams are frequently used in experiments that require vibrationally, rotationally and/or translationally cold molecules: either to investigate them directly via spectroscopic techniques (as presented in this thesis) or after manipulation by external electric or magnetic fields [3]. In addition, reactive collisions can be investigated using molecular beams [4]. As molecular beams have become widely used tools in molecular physics and physical chemistry, it is important to understand the dynamics of cooling the various degrees of freedom of molecules

in these beams. It is frequently observed that in such a molecular beam, the internal degrees of freedom of the respective species are not in thermal equilibrium. This can lead, for example in the case of flexible molecules such as amino acids, to the observation that, additionally to the minimum energy conformer, many other conformers are simultaneously present. This conformational distribution is investigated and discussed for the amino acid phenylalanine in this thesis.

One focus in this thesis is the benzene dimer. It is investigated in a supersonically expanding molecular beam by means of spectroscopy in the energy range of electronic transitions, vibrations and rotations. The results are discussed in terms of dispersive interactions, hydrogen bonding as well as symmetry. In addition, the benzene dimer is used for conformational dynamics studies in a molecular beam at ultra-low temperatures.

1.2 Experimental setups

All experiments presented in this thesis are performed in the gas phase using molecular beams. Molecular beams have become an essential technique to investigate gas phase molecules at low temperatures [3]. In molecular beam experiments, the molecules cool adiabatically by inelastic collisions with the carrier gas. Depending on the mass of the molecule, the carrier gas is chosen such that optimum energy transfer and cooling of the internal degrees of freedom of the molecule is assured. Frequently used carrier gases are light and heavy rare gases but also molecular N₂ or polyatomics like CO₂ and SF₆. Depending on the expansion conditions the molecules can be cooled rotationally and vibrationally down to some degrees K and the velocity of the supersonically expanding molecular beam varies between 500 and 1000 ms⁻¹. The translational temperature is reflected in the velocity distribution of the molecular beam and can be as low as a few degrees K. Cooling in the expansion can lead to complexation of the molecules with carrier gas atoms as well as to the formation of molecular clusters.

The particle density ρ in a molecular beam is very low as it behaves at larger distances from the valve according to

$$\rho \propto \frac{\cos^m \Theta}{r^2} \quad (1.1)$$

with Θ being the angular deviation from the molecular beam axis and r the distance from the nozzle. The coefficient m takes the value 1 for ideally effusive beams and 3 for ideally supersonic beams [5, 6]. The main advantage of spectroscopy in the gas phase using molecular beam techniques is that the molecules can be investigated individually without interference by neighboring molecules.

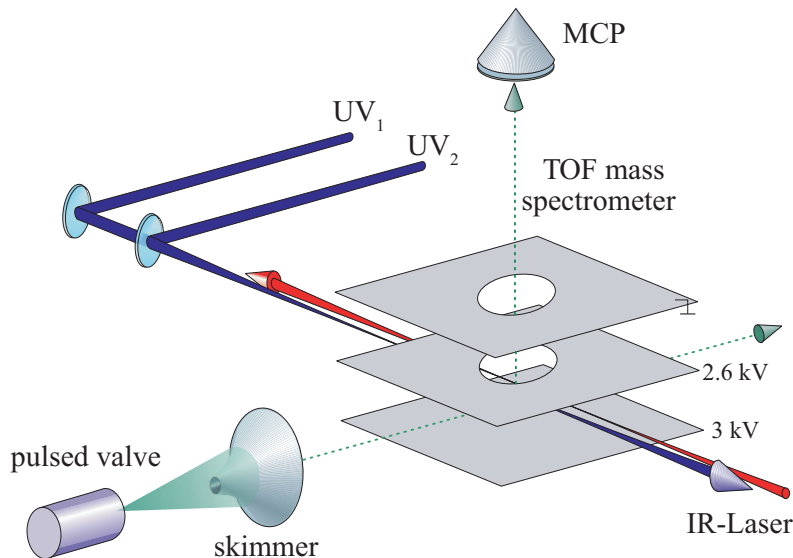


Figure 1.1: Scheme of the molecular beam machine used for the UV and IR experiments described in the following chapters.

1.2.1 IR and UV spectroscopy

The infrared (IR) and UV experiments are performed with the molecular beam set up that is schematically shown in Figure 1.1. A carrier gas, usually a rare gas, is expanded through a pulsed valve (Jordan TOF products, Inc. [7]) with a backing pressure of a few bar into vacuum. Typically, the gas pulse has a width of a few $10\ \mu\text{s}$ and the repetition rate is 10 Hz. The molecule of interest can, depending on its vapor pressure, either be premixed directly with the carrier gas, or it is vaporized by laser desorption or by sublimation right after the nozzle of the valve. In all cases a co-expansion of the carrier gas and the molecular species is obtained. The vaporization sources will be described in more detail later in this section.

After collisional cooling the molecules (and clusters) pass through a conically shaped skimmer with a diameter of 2 mm placed 50 mm downstream, separating the source chamber and the detection chamber. The two chambers are differentially pumped (Pfeiffer turbo molecular pumps, 520 l/s and 210 l/s) and the pressures are 10^{-5} and 10^{-7} mbar, respectively. The detection chamber houses a Wiley-McLaren type linear Time-Of-Flight (TOF) mass spectrometer [8] at a distance of 255 mm from the nozzle of the valve. At this distance collisions do not occur anymore in the molecular beam and the molecules interact with (UV and IR) laser beams that are aligned perpendicularly to the molecular beam axis. The interaction of the molecules with the UV photons can lead to electronic

excitation and ionization of the molecules. The interaction zone is located in the electric field between two extraction plates and the ions are accelerated perpendicularly to the molecular beam and the laser beam axes towards a one meter remote Multi Channel Plate (MCP) detector where they arrive separated in time according to their m/q ratio ($t^2 \sim m$). The ion signal is recorded as a function of time, amplified and stored on a LeCroy oscilloscope, which is read out by a PC. The mass spectra thus obtained have a mass resolution $m/\Delta m$ of ~ 200 .

Vaporization sources

For molecules with a sufficiently high vapor pressure the preparation is fairly simple since the sample can be mixed directly with the carrier gas. Since benzene is volatile, the gaseous molecules resulting from the vapor pressure (110 mbar, 20°C) can be premixed and co-expanded with the carrier gas. In our experiments the benzene concentration is about 0.03%, and rotational temperatures ≤ 3 K can be reached in the supersonic expansion, when using helium as a carrier gas.

However, the number of molecules with a high vapor pressure is limited. In order to investigate solids or liquids with low vapor pressures, heating is necessary to vaporize the molecules. If the sample is heated before passing through the valve or inside the valve body, the maximum temperature is limited by recondensation in the valve and the technical properties of the valve. The valve used in the experiments for this thesis can be heated to only 70°C [7]. When higher temperatures are needed a sublimation oven [9, 10] can be placed directly after the nozzle of the valve. This allows one to heat the sample to higher temperatures but care has to be taken not to reach the point of decomposition. An additional complication is that the expansion is disturbed by the presence of the oven.

Laser desorption Decomposition during vaporization of the sample molecules can be avoided using the method of laser desorption [11] which is schematically shown in Figure 1.2 (a). The setup we have constructed for the experiments presented in this thesis is similar to the one described in Reference [11] and will be presented in the following.

The solid sample is mixed with graphite powder and the mixture is deposited on the flat surface of a graphite target ($1 \times 50 \text{ mm}^2$). The target is brought through a lock chamber into the source chamber, where it is mounted on a holder very close to the front plate of the valve. The holder can be regulated in height and is horizontally moved by a motor driven translation stage. The slightly focused beam ($f = 300 \text{ mm}$) of the desorption laser, a pulsed Nd:YAG laser (Thales laser DIVA II, 1064 nm, 100 μJ /pulse, 10 Hz), hits the sample from above, 0.5 mm in front of the nozzle. The desorbed molecules are entrained in the pulse of carrier gas that is released through a 1 mm diameter nozzle of a

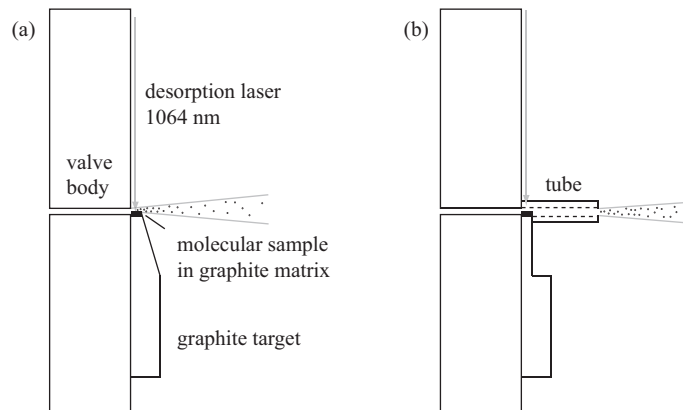


Figure 1.2: (a) Scheme of the laser desorption source used to bring molecules with low vapor pressure into the gas phase. (b) Modifications of the laser desorption setup for the experiments presented in section 4.3.

pulsed valve (Jordan) from a backing pressure of 3 bar into vacuum. In order to avoid a perturbation of the expansion, the side of the graphite target showing away from the valve is beveled off. The desorbed molecules initially have a vertical velocity vector component and have to be forced into the direction of the carrier gas pulse. Therefore, the collisions with the carrier gas have to provide adequate momentum transfer. This can be controlled by choosing the atomic/molecular mass of the expansion gas with respect to the mass and the cross section of the desorbed molecule. The time delay between the opening of the valve and the trigger for the desorption laser is optimized to yield the best cooling conditions and the largest overall signal. Other critical parameters are the height of the sample with respect to the nozzle of the valve and the alignment of the desorption laser beam relative to the molecular beam axis. When the sample has reached its end position it is removed through the load lock and replaced by a fresh one.

For the experiments on the amino acid phenylalanine (see section 4.3 and chapter 5) laser desorption has been used successfully with argon and neon as a carrier gas. Cooling and overall detection efficiency are inferior using helium as a carrier gas. The optimum height of the sample is found to be when the lower third of the orifice of the valve is covered by the target. For the experiments presented in section 4.3 the setup has been slightly changed as shown in Figure 1.2 (b), aiming to improve the cooling conditions for laser desorbed phenylalanine molecules. The additional tube is installed directly on the front plate of the valve and the shape of the graphite target is adapted in order to form a sealed unit with the tube. Several shapes of the tube (cylindrical and conical geometries with varying diameter, length and angle) are used.

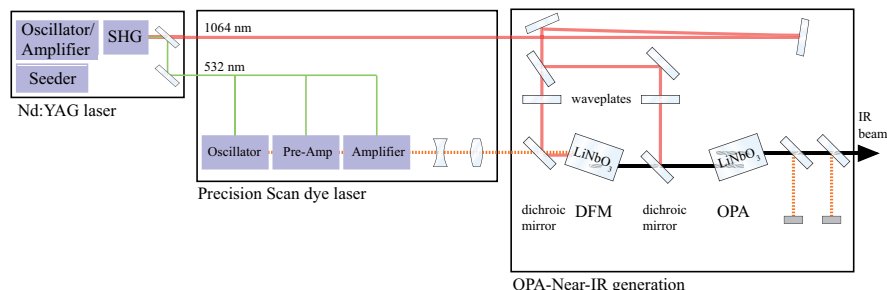


Figure 1.3: Scheme of the infrared (IR) laser system. The IR light is generated and amplified in a series of LiNbO_3 crystals by difference frequency mixing of the output of a pulsed dye laser with the 1064 nm beam of an injection seeded Nd:YAG laser.

A major problem of the laser desorption technique is the shot to shot fluctuation in the amount of vaporized sample molecules. These fluctuations result from fluctuations in the desorption laser power and from the (in)homogeneity of the sample density. The signal stability also depends on the exact horizontal adjustment of the graphite target.

Laser systems

The UV spectra (see Figures 1.10 and 4.4) are obtained by one- or two-color Resonance Enhanced Multi Photon Ionization, REMPI (see section 1.3.1). The laser systems used are frequency doubled Nd:YAG pumped pulsed dye lasers (Spectra Physics PDL and Radiant Dyes Narrow Scan). For the UV experiments on the benzene dimer two laser systems are used: one for the excitation of the molecules from the electronic ground state to the first electronically excited state and a second laser for subsequent ionization from the excited state. The excitation laser is operated with Coumarin 307 dye (Radiant Dyes) and the ionization laser with Rhodamin 6G dye (Exciton). While Coumarin 307 is pumped by the third harmonic output of the Nd:YAG laser (355 nm), Rhodamin 6G is pumped by the second harmonic output (532 nm). For the experiments on phenylalanine excitation and ionization are performed with one laser (Coumarin 153 dye (Radiant Dyes)). UV light is obtained by second harmonic generation (SHG) of the dye laser output in a non-linear crystal, such as BBO ($\beta\text{-BaB}_2\text{O}_4$), suitable for the spectral range 34500 - 47600 cm^{-1} , or KDP (KH_2PO_4), suitable for the spectral range 25000 - 38500 cm^{-1} .

The infrared laser system (see Figure 1.3) used for the experiments, described in chapters 2 and 5 and section 4.3, is similar to one used by Gerhards and coworkers [12]. It consists of three building blocks, an injection seeded Nd:YAG pump laser (Spectra Physics Quanta Ray, linewidth 0.005 cm^{-1}), a dye laser

system (Precision Scan SL Sirah) and a unit for IR generation by difference frequency mixing (DFM). The Nd:YAG laser (10 Hz repetition rate) generates radiation of 1064 nm that is frequency doubled in a non-linear KD*P (KD_2PO_4) crystal with an efficiency of about 35 %. The second harmonic radiation (532 nm, ~ 400 mJ/pulse) is separated from the residual fundamental frequency beam and pumps a dye (Styryl 9) laser generating light around 800 nm (35 mJ/pulse). Special care is taken to guarantee a sharp spectral distribution of the dye laser output (0.05 cm^{-1} spectral linewidth), using a grazing incidence grating and a Littrow grating for the wavelength selection. A portion of the residual Nd:YAG light of 1064 nm is mixed with the dye laser beam in a LiNbO_3 crystal generating a signal and an idler wave. The idler wave corresponds to the difference frequency of the two incoming laser beams (around 3100 cm^{-1} , ~ 1 mJ/pulse). For the experiments, amplification of the IR light is necessary. Therefore, the IR light (idler wave) is mixed with the remaining residual 1064 nm beam of the Nd:YAG laser in a second LiNbO_3 crystal, the OPA (optical parametric amplifier), generating the difference frequency and an amplified (up to 10 mJ/pulse) IR laser beam around 3100 cm^{-1} . The different generated frequencies are separated by a series of dichroic mirrors. The spectral width of the IR laser beam is determined by the bandwidths of the Nd:YAG (0.005 cm^{-1}) and dye (0.05 cm^{-1}) laser beams and by the difference frequency mixing process. The resulting IR laser beam has a spectral linewidth that is increased by a factor of only 1.1 compared to that of the dye laser beam. By phase matching of the LiNbO_3 crystals, laser light in the spectral range from 2650 to 5500 cm^{-1} can be generated. Choosing the appropriate dye (DCM, Pyridine 1, Pyridine 2, Styryl 8, Styryl 11, Styryl 9) this spectral range can be continuously covered by this table top laser system. Several problems encountered when working with the IR laser system and the appropriate solutions are presented in Appendix B.

1.2.2 Microwave spectroscopy

High resolution rotational spectroscopy is performed in a Fourier-Transform-microwave (FT-MW) spectrometer. The molecules are premixed with a carrier gas (helium, neon or argon) and co-expanded through the nozzle of a pulsed valve (20 Hz, General Valve series 9) from a backing pressure of a few bar into a confocal Fabry-Pérot resonator (10^{-6} mbar) with two spherical, 63 cm diameter aluminum mirrors. In the molecular beam the rotational and vibrational temperatures are $\sim 1.5\text{ K}$ and $\sim 50\text{ K}$, respectively [13]. The pulse duration is on the order of several 100 μs and can be regulated, as well as the time delays of the microwave irradiation (duration $\sim 0.5\text{ }\mu\text{s}$) and of the detection (duration $\sim 20\text{ }\mu\text{s}$) relative to the opening of the valve. The valve is placed in the center of the left spherical mirror (see Figure 1.4), which also houses a pair of antennas emitting microwaves in the frequency range from 2 to 26.5 GHz ($0.07\text{-}0.88\text{ cm}^{-1}$). By linearly changing the distance between both reflectors, the

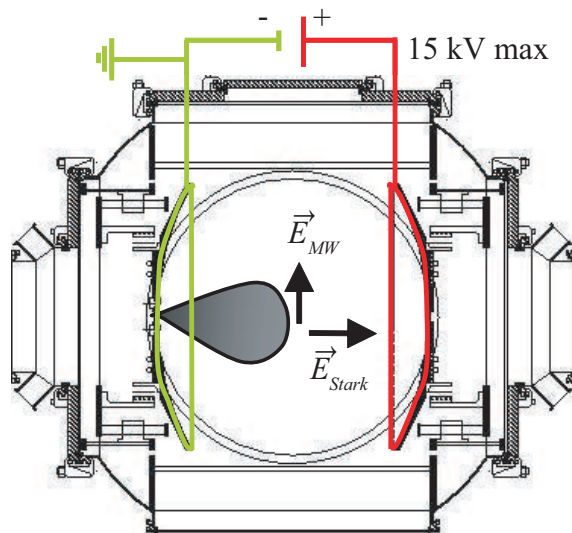


Figure 1.4: Scheme of the experimental setup used to perform microwave experiments. The molecules enter the chamber through a pulsed valve placed in the center of the left spherical mirror. The spherical mirrors serve as resonator for the microwaves, but can also be used as electrodes for Stark effect measurements.

frequency of the standing wave is selected. This setup, the so-called Coaxially Oriented Beam Resonator Arrangement (COBRA) [14, 15], achieves a resolution up to 5 kHz [13] and has an enlarged sensitivity compared to earlier setups [16–18] with the molecular beam and the resonator axis perpendicularly arranged. Therefore, even though microwave spectroscopy can only observe polar species, molecules and clusters with small dipole moments, such as the benzene dimer, are accessible as well.

The setup shown in Figure 1.4 can (after small modifications) be used to perform Stark effect measurements. For that, a well defined and homogeneous electric field is required. In earlier setups, in which high voltage (HV) has been applied between two parallel plates which were perpendicularly arranged with respect to the resonator axis, this requirement has not been met, which limits the accuracy [19]. In the current experimental setup the spherical mirrors are thermally and electrically insulated and therefore suitable to serve as Stark electrodes. A high voltage potential of up to 15 kV is applied to the rear reflector, while the reflector equipped with the supersonic valve and the microwave antennas is kept at ground potential (see Figure 1.4). In order to warrant a homogeneous electric field, additional ring electrodes of the same radius as the spherical mirrors are coaxially mounted between both reflectors (this modification is not shown in

Figure 1.4). The spherical mirrors and the ring electrodes are connected via equal resistors and spaced such that a constant potential gradient along the resonator axis is generated. This so-called Coaxially Aligned Electrodes for Stark effect Applied in Resonators (CAESAR) setup provides a homogeneous electric field over a large volume [20]. Inhomogeneities occur only far away from the molecular beam/resonator axis and do not contribute significantly to the molecular signal, as the particle density decreases with increasing distance from the molecular beam axis according to expression 1.1. Inhomogeneities in the vicinity of the spherical reflectors are not important as the particle density is low near the rear electrode and as the molecular signal is detected only after the supersonic expansion, i.e. at a certain distance from the valve and thus from the front electrode. The CAESAR setup does not affect the high sensitivity of the COBRA design allowing for Stark effect measurements on molecules with substantial as well as with small dipole moments.

1.3 Spectroscopic techniques

In spectroscopy the interaction between molecules/atoms and electromagnetic radiation is investigated. These interactions can be elastic and inelastic scattering of light, as well as the absorption and emission of light. The spectroscopic techniques used in this thesis are based on the emission and/or absorption of photons: UV spectroscopy, infrared spectroscopy and microwave spectroscopy allow for the investigation of electronic transitions, molecular vibrations and molecular as well as internal rotations, respectively, as well as of the symmetry properties of the corresponding energy levels. This thesis describes spectroscopic experiments performed on dilute samples in the gas phase.

1.3.1 UV spectroscopy

Transitions between electronic states can be induced by visible or UV radiation, preferably laser light that has a well defined frequency.* The selection rules for allowed transitions can be deduced from symmetry considerations. Transitions between two electronic states described by the wavefunctions Ψ'_e and Ψ''_e are observable if the transition dipole moment \mathbf{R}_e is non-zero

$$\mathbf{R}_e = \int \Psi'^*_e \mu_e \Psi''_e d\tau_e \quad (1.2)$$

with μ_e being the operator of the electric dipole moment and τ_e the electron coordinates. This condition is met if the (ir)reducible presentation Γ of \mathbf{R}_e

$$\Gamma(\mathbf{R}_e) = \Gamma(\Psi'^*_e) \otimes \Gamma(\mu_e) \otimes \Gamma(\Psi''_e) \supset A \quad (1.3)$$

*The theory of molecular electronic transitions is in detail presented for example in Reference [21].

contains the totally symmetric irreducible representation A of the point group of the molecule.

The electronic ground state of benzene (point group \mathbf{D}_{6h}), for example, is A_{1g} and the dipole moment operator spans $A_{2u}(z) + E_{1u}(x, y)$. Therefore, allowed transitions can be expected to be $A_{2u} \leftarrow A_{1g}$ and $E_{1u} \leftarrow A_{1g}$. Other, formally forbidden, transitions can gain intensity if simultaneously to the electronic excitation a vibration is excited. In this case equation 1.2 is enlarged by the vibrational wavefunctions and the transition dipole moment is

$$\mathbf{R}_{ev} = \iint \Psi_e'^* \Psi_v'^* \mu_e \Psi_e'' \Psi_v'' d\tau_e d\tau_N \quad (1.4)$$

with τ_N being the coordinates of the nuclei. The selection rule formulated in equation 1.3 applies similarly, including additionally the irreducible representations of the vibrational wavefunctions. Such a vibronic transition is for example observed in benzene for the $S_1 \leftarrow S_0$ electronic transition ($B_{2u} \leftarrow A_{1g}$) when being coupled to the vibrational mode ν_6 that excites a vibrational state of E_{2g} symmetry [22, 23]. In this case the representation of the transition dipole moment is $A_{1g} + A_{2g} + E_{2g}$ and the integral 1.4 is non-zero.

Electronic spectra of gas phase molecules can be obtained by several techniques. Their applicability depends on the electronic properties of the molecule. One commonly used technique is Laser Induced Fluorescence (LIF) [24]. In LIF a photon excites a rovibronic level of an electronically excited state. In the absence of collisions, the molecule spontaneously de-excites to a specific (depending on the Franck-Condon factors) rovibrational level of the electronic ground state while emitting a photon. This emission is detected as a function of the excitation energy providing information about the electronic and rovibronic molecular properties. LIF can be used when the electronically excited state involved has a substantial fluorescence quantum yield. The molecular systems, investigated in the experiments that are presented in this thesis, have a very low fluorescence quantum yield [25, 26]. Therefore, the LIF technique is not used in this work.

In another technique a second photon is used to ionize the resonantly excited molecule. The ion yield is mass-selectively detected as a function of the energy of the first photon, the excitation photon. (Alternatively, the simultaneously produced electrons can be detected; the mass-selectivity, however, is then lost.) This so-called Resonance Enhanced Multi Photon Ionization (REMPI) technique [27–30] is schematically shown in Figure 1.5 (a). The applicability of REMPI depends on the lifetime of the excited state. If the molecule tends to a fast intersystem crossing to a different electronically excited state from which the molecule cannot be ionized efficiently, the REMPI technique cannot be applied.

If the excitation and ionization photon have the same energy (1-color REMPI) the molecule is often excited far above the ionization threshold. Larger clusters of the molecular species can be non-resonantly excited at the same time and the excess energy can be transferred to vibrational modes inducing dissociation

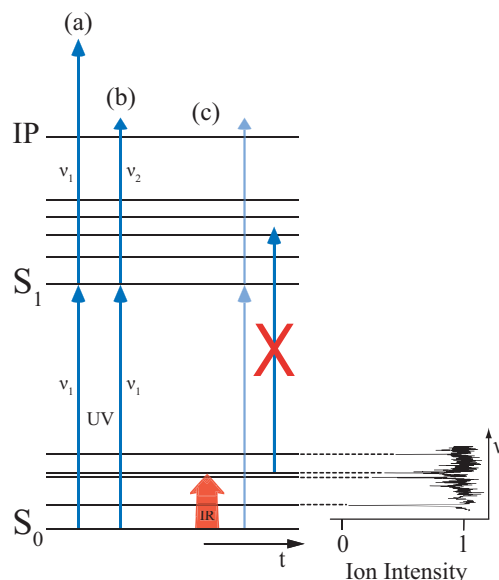


Figure 1.5: Schematic representation of different types of Resonance Enhanced Multi Photon Ionization (REMPI). The first UV photon excites resonantly an electronically excited state, for example S_1 , the second UV photon subsequently ionizes the molecule. (a) 1-color REMPI excites the molecule to energies far above the ionization potential IP. (b) 2-color REMPI ionizes the molecule with two photons of independently tunable frequencies. (c) Double resonance experiment in which an IR laser excites vibrational energy levels of the electronic ground state prior to electronic excitation depleting the ground state and thus reducing the UV ionization yield (shown as light lines). Electronic excitation from the vibrationally excited state is very unlikely due to the different vibrational frequencies in S_0 and S_1 .

of the clusters. The fragments can be detected in the mass channel of the species of interest and can thus contaminate its spectrum. This interference can be reduced using two photons of different energy: 2-color REMPI or R2PI (resonance enhanced two-photon ionization). The energy of the second photon can be adjusted such that the molecule (and possibly present larger clusters) is excited just above the ionization threshold (see Figure 1.5 (b)) avoiding that larger clusters dissociate. Additionally, experiments are possible in which the energy of the ionization photon is tuned while that of the excitation photon is fixed allowing one to study the onset of ionization and the vibrational properties of the ion.

1.3.2 Infrared spectroscopy

Molecular vibrations occur in the energy range of the IR radiation.* The energy of a vibrational state of the harmonic oscillator is

$$E_v = h\nu \left(v + \frac{1}{2} \right) \quad (1.5)$$

with ν being the frequency of the fundamental mode and v the vibrational quantum number. The dipole moment μ has the form

$$\mu = \mu_0 + \sum_i \left(\frac{\partial \mu}{\partial Q_i} \right)_0 Q_i + \frac{1}{2} \sum_{i,j} \left(\frac{\partial^2 \mu}{\partial Q_i \partial Q_j} \right)_0 Q_i Q_j + \dots \quad (1.6)$$

where μ_0 is the dipole moment of the rigid molecule and Q the normal coordinates of the respective normal mode. In the harmonic approximation the quadratic and higher terms are ignored and the transition dipole moment \mathbf{R}_v for a transition $v' \leftarrow v$ with $\Delta v = \pm 1$ is

$$\mathbf{R}_v = \langle v'_i | \mu | v_i \rangle = \langle 1_i | \mu | 0_i \rangle = \mu_0 \langle 1_i | 0_i \rangle + \left(\frac{\partial \mu}{\partial Q_i} \right)_0 \langle 1_i | Q_i | 0_i \rangle. \quad (1.7)$$

A vibrational transition is IR active if \mathbf{R}_v is non-zero. As the first term in equation 1.7 is zero, a vibrational transition can only be observed if the dipole moment varies with the displacement of the nuclei. The latter can be regarded as a selection rule for vibrational transitions.

Frequently, vibrations are anharmonic. In the case of electronic anharmonicities, the quadratic and higher terms, including cross terms between different normal modes $Q_i Q_j$, in equation 1.6 are not necessarily zero and the transition dipole moment is

$$\begin{aligned} \langle v'_i v'_j | \mu | v_i v_j \rangle &= \langle 1_i 1_j | \mu | 0_i 0_j \rangle = \mu_0 \langle 1_i 1_j | 0_i 0_j \rangle + \left(\frac{\partial \mu}{\partial Q_i} \right)_0 \langle 1_i | Q_i | 0_i \rangle \langle 1_j | 0_j \rangle \\ &+ \left(\frac{\partial \mu}{\partial Q_j} \right)_0 \langle 1_j | Q_j | 0_j \rangle \langle 1_i | 0_i \rangle + \frac{1}{2} \left(\frac{\partial^2 \mu}{\partial Q_i \partial Q_j} \right)_0 \langle 1_i 1_j | Q_i Q_j | 0_i 0_j \rangle + \dots \end{aligned} \quad (1.8)$$

Electronic anharmonicities can thus result in combination bands ($Q_i \neq Q_j$) in which more than one mode is excited simultaneously, as well as in overtones ($Q_i = Q_j$) with $\Delta v = \pm 2, \pm 3, \dots$. However, electronic anharmonicities are usually weak and the intensities of the allowed overtones and combination bands are thus comparatively low.

Anharmonicities can also be of mechanical nature that change the potential well such that it is compared to the harmonic potential well steeper for displacements $r < r_e$ and shallower for displacements $r > r_e$, with r_e being the

*As the theory of molecular vibrations is presented in detail in several textbooks [31, 32], only a short introduction shall be given in this section.

interatomic distance in the equilibrium geometry. The potential energy of the vibrational level is then

$$E_v = E_0 + \sum_i \left(\frac{\partial E}{\partial q_i} \right)_0 q_i + \frac{1}{2} \sum_{i,j} \left(\frac{\partial^2 E}{\partial q_i \partial q_j} \right)_0 q_i q_j + \frac{1}{3!} \sum_{i,j,k} \left(\frac{\partial^3 E}{\partial q_i \partial q_j \partial q_k} \right)_0 q_i q_j q_k + \dots \quad (1.9)$$

with q being the mass weighted coordinates $\sqrt{m}x$ and m the mass being displaced by x . The effect of mechanical anharmonicity is that modes couple with each other, and overtones and combination bands become IR active. Due to electronic and mechanical anharmonicities also combination bands of overtones and fundamental modes can be excited:

$$\langle 2_i 1_j | E | 0_i 0_j \rangle = \frac{1}{3!} \left(\frac{\partial^3 E}{\partial Q_i^2 \partial Q_j} \right)_0 \langle 2_i | Q_i^2 | 0_i \rangle \langle 1_j | Q_j | 0_j \rangle + \dots \quad (1.10)$$

As the lower terms that are not shown in equation 1.10 are zero (see equation 1.8) the modes will mix only if the derivative $\left(\frac{\partial^3 E}{\partial Q_i^2 \partial Q_j} \right)_0$ is non-zero. The interaction between a fundamental mode and a combination band is called a Fermi resonance. Fermi resonances play a role, for example, in the benzene dimer (see chapter 2).

Similar to equation 1.3 the IR activity of a vibrational transition can be determined by considering the symmetry properties of the dipole moment and of all vibrational (and electronic) wavefunctions involved in the transition:

$$\Gamma(\mathbf{R}_{ev}) = \Gamma(\Psi_e^*) \otimes \Gamma(\Psi_v'^*) \otimes \Gamma(\mu) \otimes \Gamma(\Psi_e'') \otimes \Gamma(\Psi_v'') \supset A \quad (1.11)$$

with $\Gamma(\Psi_e'^*) \otimes \Gamma(\Psi_e'') = A$ if the vibrational transition is within one electronic state.

The IR spectra in this thesis are measured with a double resonance technique which is schematically shown in Figure 1.5 (c). A one- or two-color ionization scheme is used to resonantly excite and then to ionize molecules which are in the vibrational and electronic ground state. This process is optimized to yield an intense and stable ion signal. A few ns before the electronic excitation the molecules interact with tunable IR laser light that, in case of a resonance, excites a vibrational transition in the electronic ground state. This leads to a depletion of the vibrational ground state population leaving a reduced number of molecules for the subsequent resonant electronic excitation and ionization. Resonant electronic excitation from the vibrationally excited state is unlikely as the vibrational force constants are different in the two electronic states, giving rise to different transition frequencies. Therefore, the ion signal is reduced in the case of vibrational excitation prior to ionization. The ion yield is measured as a function of the IR wavelength giving the IR spectrum. This technique is

called resonant ion-dip IR spectroscopy (RIDIRS) [33]. Simultaneously, the ion signal (IS) without preceding IR excitation is measured in order to determine the absorption cross section

$$\sigma(\nu) = -\frac{1}{E_\nu} \ln \frac{IDS_\nu}{IS_\nu} \quad (1.12)$$

with E_ν being the IR laser fluence at frequency ν , IDS_ν the ion-dip signal and IS_ν the pure ion signal.

A similar technique, fluorescence-dip IR spectroscopy (FDIRS) can be used if the electronic states of the molecule have a sufficiently large fluorescence quantum yield. In that case a fluorescence transition is resonantly excited monitoring the population of a specific state in the electronic ground state. If the population of this state is depleted as a consequence of vibrational excitation prior to electronic excitation, the fluorescence quantum yield is reduced. The fluorescence quantum yield measured as a function of the IR wavelength gives the IR spectrum of the electronic ground state [34].

1.3.3 Microwave spectroscopy

The rotational properties of a molecule can be investigated via microwave spectroscopy revealing the precise structure and internal dynamics of the respective system.*

A molecule interacts only with a microwave electromagnetic field if it has a permanent electric/magnetic dipole moment. A non-linear and non-spherical (spherical in the sense that all three moments of inertia are equal) molecule can have two equal principal moments of inertia $I_A = I_B < I_C$ or $I_A < I_B = I_C$ (oblate or prolate symmetric top molecule) or three different principal moments of inertia $I_A < I_B < I_C$ (asymmetric top molecule). In a symmetric top, the dipole moment is oriented along the symmetry axis. In an asymmetric top molecule the dipole moment can lie in any arbitrary direction.

In the field free molecular beam the dipole moments of the molecules are statistically oriented, producing no macroscopic dipole moment (see Figure 1.6 (a)). Upon irradiation by a resonant microwave pulse of the duration τ_p ($0.5 \mu s$) the individual dipole moments of all molecules are oriented due to the interaction with the external electromagnetic field (see Figure 1.6 (b)). The superposition of the molecular dipole moments results in an oscillating macroscopic dipole moment. The oscillation frequency corresponds to the difference of rotational frequency of the two coherent states. Since the microwave radiation is temporally limited (τ_p) and due to the decreasing particle density during the expansion, the amplitude of the molecular field, induced by the orientation of the individual dipole moments, decays. This transient emission (free induction decay (FID))

*For a more detailed introduction into the theory of molecular rotations, than the one given here, the reader is referred to the standard textbooks [31, 35, 36].

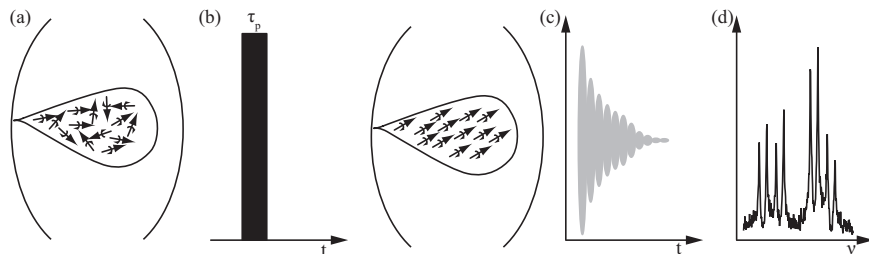


Figure 1.6: (a) Without an electromagnetic field the molecular dipoles are oriented statistically. (b) The interaction with a microwave pulse of duration τ_p orients the dipoles. (c) The decay of the so formed macroscopic molecular field is recorded in the time domain and (d) Fourier transformed into the frequency domain.

is measured in the time domain and Fourier transformed into the frequency domain (see Figure 1.6 (c) and (d)).

The spectroscopic signal is thus a transition between two rotational states which are each uniquely defined by the angular momentum quantum number J and by the quantum number of the angular momentum component along the molecular axis K with the values from $-J$ to $+J$. The term energy of a rotational level in a symmetric top molecule as a first approximation is defined by

$$E = BJ(J+1) + (X-B)K^2 \quad (1.13)$$

with the rotational constants B and $X = A$ or $X = C$, for a prolate and an oblate symmetric top molecule, respectively. From equation 1.13 it can be seen that the rotational states with $K \neq 0$ are doubly degenerate in a symmetric top. In an asymmetric top the degeneracy of the $\pm K$ levels is lifted ($K_a K_c$). If the molecule is subject to an external electric field, the quantum number of the projection of the total angular momentum onto a space fixed axis (M_J) is additionally required to define the rotational state. As J is $2J+1$ fold degenerate M_J can adopt $2J+1$ different values.

The selection rules for observable (purely rotational) transitions are $\Delta J = \pm 1$, $\Delta K = 0$ for a symmetric top species and $\Delta J = 0, \pm 1$ for an asymmetric top molecule. In a near-prolate asymmetric top molecule K_c has to change parity and K_a has to maintain parity, so that transitions $K'_c K'_a \leftrightarrow K_c K_a = ++ \leftrightarrow -+$ and $-- \leftrightarrow +-$ are allowed (Dennison notation [37]). $+$ and $-$ characterize the behavior of the rotational energy levels with respect to rotation through π about the principal axes c and a , respectively. In the notation of King, Hainer and Cross [38] the designations ee , oe , eo and oo have been introduced for $K_a K_c$, where e and o indicate the even- and oddness of K_a and K_c . In a near-prolate asymmetric top molecule the observable transitions $K'_a K'_c \leftrightarrow K_a K_c$ are then $ee \leftrightarrow eo$ and $oo \leftrightarrow oe$. For the symmetric top, as well as for the asymmetric

top M_J changes with $\Delta M_J = 0$ or ± 1 , depending on whether the external field is parallel or perpendicular to the electromagnetic field, respectively. The experimental setup described in section 1.2.2 corresponds to the latter geometry.

Stark effect measurements

When a system with a permanent electric or magnetic dipole moment is subject to a static homogeneous electric or magnetic field the $2J + 1$ fold degeneracy of the directional quantum number M_J with the values $\pm J, \pm(J - 1), \dots, \pm 1, 0$ is lifted and the resulting splittings (and shifts) can be observed in the rotational spectrum. The spectral changes that are a consequence of the interaction of the molecule with an external electric or magnetic field are called the Stark or Zeeman effect, respectively.

The interaction of a static electric field \vec{E} with a polar molecule having the dipole moment $\vec{\mu}$ is given classically by $-\vec{\mu} \cdot \vec{E}$. The static electric field \vec{E} is defined along the Z axis in a fixed coordinate system and the permanent molecular dipole moment $\vec{\mu}$ in the coordinates of the molecular frame. The Hamiltonian for the interaction is given by

$$\hat{H}_E = -E_Z \sum_{g=x,y,z} \mu_g \Phi_{Zg} \quad (1.14)$$

with Φ_{Zg} being the projection cosine between the axes x, y and z of the molecular frame and the Z axis of the electric field frame. For a symmetric top, where the dipole moment is oriented along the principal symmetry z axis of the molecule and where $\vec{\mu}_x = \vec{\mu}_y = 0$, the expression reduces to

$$\hat{H}_E = -E_Z \mu \Phi_{Zz}. \quad (1.15)$$

The effect on the energy levels can be calculated quantum mechanically by perturbation theory. The energy shift that a rotational level of a symmetric top molecule experiences in an external electric field can be described by

$$E_E^1 = -\langle \Psi^* | \mu E \Phi_{Zz} | \Psi \rangle = -\frac{\mu E}{h} \frac{M_J K}{J(J+1)}. \quad (1.16)$$

The change in energy of a rotational state is thus proportional to the first power of $\mu \cdot E$ (linear Stark effect). The second order or quadratic Stark effect for a symmetric top given by

$$E_E^2 = \frac{\mu^2 E^2}{2Bh^2} \left\{ \frac{(J^2 - K^2)(J^2 - M_J^2)}{J^3(2J-1)(2J+1)} - \frac{[(J+1)^2 - K^2][(J+1)^2 - M_J^2]}{(J+1)^3(2J+1)(2J+3)} \right\} \quad (1.17)$$

is usually much smaller than the linear Stark effect and can be neglected. However, if $K = 0$ equation 1.16 becomes zero and the frequency shift results

solely from the quadratic Stark effect. The quadratic Stark effect for states with $K = 0$ is obtained from equation 1.17 then as

$$E_{E,J \neq 0,K=0}^2 = \frac{\mu^2 E^2}{2Bh^2} \frac{J(J+1) - 3M_J^2}{J(J+1)(2J-1)(2J+3)}. \quad (1.18)$$

In the special case that $J = 0$ the rotational level cannot be split and M_J is 0. The quadratic Stark effect is obtained when setting $J = K = M_J = 0$ in equation 1.17:

$$E_{E,J=0}^2 = -\frac{\mu^2 E^2}{6Bh^2}. \quad (1.19)$$

From equations 1.16 and 1.17 it can be seen that whereas a linear Stark effect lifts completely the $2J+1$ fold degeneracy of M_J , a quadratic Stark effect leaves all states $M_J \neq 0$ doubly degenerate due to the quadratic term M_J^2 . The change in the transition frequencies depends on the difference between the Stark effects of the upper and lower level of a transition. With the selection rules for symmetric top species $\Delta J = \pm 1$, $\Delta K = 0$ and the knowledge about the relative orientation of the microwave and static electric field vectors the shifts of the transition frequencies can be determined with equations 1.16 and 1.17. For transitions with $\Delta J = +1$, $\Delta K = 0$ and $\Delta M_J = \pm 1$ the transition frequency shifts by

$$\Delta\nu = \frac{\mu EK}{h} \frac{(2M_J \mp J)}{J(J+1)(J+2)} \quad (1.20)$$

for a linear Stark effect and by

$$\Delta\nu = \frac{\mu^2 E^2}{2Bh^2} \left\{ \frac{(J+1)(J+2) - 3(M_J \pm 1)^2}{(J+1)(J+2)(2J+1)(2J+5)} - \frac{J(J+1) - 3M_J^2}{J(J+1)(2J-1)(2J+3)} \right\} \quad (1.21)$$

for a pure quadratic Stark effect ($K=0$), where M_J and J are the quantum numbers of the initial state.

Degenerate states, as for example the doubly degenerate states in symmetric tops with $K \neq 0$, have a linear Stark effect, whereas all states of linear molecules and the symmetric top states with $K = 0$ have a quadratic Stark effect (see Figure 1.7). Asymmetric top states have a quadratic Stark effect as the degeneracy of the $\pm K$ levels is lifted.

Provided that the electric field is fairly homogeneous and well defined the Stark effect can, in combination with high resolution spectroscopic techniques, such as rotational spectroscopy, be exploited to determine precisely the molecular dipole moment μ . Furthermore, Stark effect experiments can be used to classify the quantum numbers J and K of rotational transitions for example in the very beginning of an experiment when assignments are still unknown.

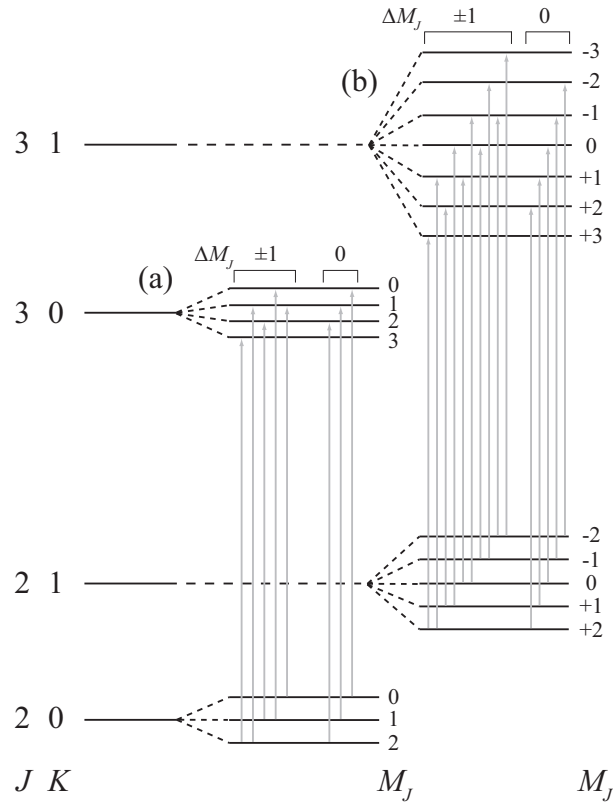


Figure 1.7: Schematic representation of the (a) quadratic and (b) linear Stark effect on the rotational levels of a symmetric top species. The selection rules for a transition are $\Delta J = \pm 1$, $\Delta K = 0$ and $\Delta M_J = \pm 1$ or 0 , depending on the relative orientation of the microwave and electric field. (adapted from Reference [35])

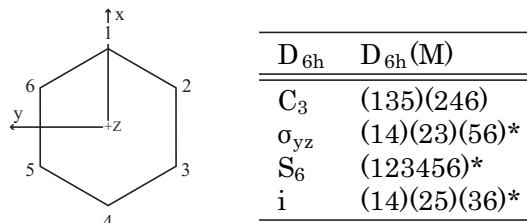


Figure 1.8: Symmetry operations expressed in terms of point group theory (D_{6h}) and permutation-inversion group theory ($D_{6h}(M)$) where the pairs of C-H bonded nuclei are numbered 1-6 around the benzene ring.

1.4 Permutation-inversion group theory

Permutation-inversion (PI) group theory is a concept employing molecular symmetry that allows one to describe rigid and non-rigid molecular systems [39–41]. This concept differs from the point group symmetry concept by Schönflies which is limited to rigid species. Non-rigid systems easily change their conformation by large amplitude motions (LAM) and thus their symmetry properties. The benzene dimer, for example, is such a non-rigid system. The effects of LAM can be observed as tunneling splittings in high resolution spectra (see chapter 3). Permutation-inversion group theory can be used to adequately describe large amplitude motions changing the molecular symmetry. PI group theory allows one to determine spectroscopic selection rules and to calculate nuclear spin statistical weights as well as the number and degeneracies of sublevels split apart as a consequence of tunneling. It can thus be used to predict and to analyze rotational spectra.

The complete permutation-inversion group of a molecule consists of the identity operation E , all permutations P of identical nuclei, the inversion E^* and the product of E^* with all permutations P of identical nuclei, P^* . However, for many molecules not all elements have to be taken into account. Restricting the group to feasible operations gives the Molecular Symmetry (MS) group. The feasibility of an operation/tunneling is limited by the experimental time scale, i.e. by the resolution of the experiment. The MS group is thus a subgroup of the complete permutation-inversion group and can be adapted to the respective problem. For rigid non-linear molecules the MS group is isomorphic to its point group.

Point group operations affect the vibrational and electronic coordinates of a molecule; they are called rotation C_n , reflection σ , inversion i and improper rotation S_n . These operations are described by permutation, inversion and permutation-inversion in the PI theory, which affect additionally the rotation and spin coordinates. The correlation between the operations is shown in Figure 1.8 for benzene, as an example.

1.4.1 Nuclear spin statistics

The nuclear spin statistical weights specify the population of a rotational energy level with a specific symmetry and depend on the MS group. Consequently, these weights determine the intensity pattern of rotational transitions. The experimentally determined relative transition intensities can be compared to spin statistical weights obtained when assuming different MS groups. This allows one to determine the MS group of the non-rigid molecule (i.e. its equilibrium structure) and thus its tunneling motions that produce observable splittings in the spectrum. In the following the determination of the nuclear spin statistical weights shall be introduced.

The internal wavefunction Φ_{int} , including a coordinate and a spin part, changes in sign by a nuclear permutation involving an odd permutation of identical nuclei with half integer spin (fermions)

$$P_{odd}\Phi_{int} = -\Phi_{int} \quad (1.22)$$

and is invariant to a nuclear permutation involving an even permutation of fermions

$$P_{even}\Phi_{int} = +\Phi_{int}. \quad (1.23)$$

This is the Pauli exclusion principle. A permutation, involving even or odd permutations, of identical nuclei with integer spin (bosons) does not change the sign of Φ_{int} . Φ_{int} can be written in zeroth order as the product of the nuclear spin and the rovibronic wavefunction

$$\Phi_{int} = \Phi_{nspin}\Phi_{rot}\Phi_{vib}\Phi_{el} = \Phi_{nspin}\Phi_{rve}. \quad (1.24)$$

Φ_{nspin} is invariant to the operation E^* and therefore the effect of the permutation-inversion operation P^* is the same as of the permutation P .

In the following, the spin statistical weights of the rotational levels of C_6H_6 , as an example, shall be determined according to the method shown in Reference [42]. The MS group of C_6H_6 is $D_{6h}(M)$ and the character table is given in Appendix A.

For a nucleus n with the nuclear spin I_n , $2I_n+1$ spin functions exist. They are written in the form $|I_n, m_{I_n}\rangle$ with $m_{I_n} = -I_n, -I_n + 1, \dots, +I_n$. In C_6H_6 only the six protons with $I_n=1/2$ contribute to the nuclear spin statistical weights. The spin up and spin down functions $|\frac{1}{2}, \frac{1}{2}\rangle$ and $|\frac{1}{2}, -\frac{1}{2}\rangle$, respectively, shall be called α and β . The total nuclear spin function of C_6H_6 is the sum over all combinations of α and β for the six protons. The characters $\chi_{nspin}[P]$ of the 64 nuclear spin functions under each permutation are shown in Table 1.1. From this the representation Γ^{nspin} of each nuclear spin function Φ_{nspin} can be determined according to

$$\Gamma^{nspin} = \sum_l a_l \Gamma^{(l)} \quad (1.25)$$

Φ_{nspin}	E	(123456)	(135)(246)	(14)(25)(36)	(26)(35)	(14)(23)(56)	E^*	(123456)*	(135)(246)*	(14)(25)(36)*	(26)(35)*	(14)(23)(56)*
	1	2	2	1	3	3	1	2	2	1	3	3
$\alpha\alpha\alpha\alpha\alpha\alpha$	1	1	1	1	1	1	1	1	1	1	1	1
$\beta\beta\beta\beta\beta\beta$	1	1	1	1	1	1	1	1	1	1	1	1
$\alpha\beta\beta\beta\beta\beta$	6	0	0	0	2	0	6	0	0	0	2	0
$\beta\alpha\alpha\alpha\alpha\alpha$	6	0	0	0	2	0	6	0	0	0	2	0
$\alpha\alpha\beta\beta\beta\beta$	15	0	0	3	3	3	15	0	0	3	3	3
$\beta\beta\alpha\alpha\alpha\alpha$	15	0	0	3	3	3	15	0	0	3	3	3
$\alpha\alpha\alpha\beta\beta\beta$	20	0	2	0	4	0	20	0	2	0	4	0
Φ_{int}	1	-1	1	-1	1	-1	± 1	∓ 1	± 1	∓ 1	± 1	∓ 1

Table 1.1: Character table of the representations Γ of the 64 nuclear spin functions Φ_{nspin} and of the internal wavefunction Φ_{int} of C_6H_6 .

multiplicity	Φ_{nspin}	Γ^{nspin}
1	$\alpha\alpha\alpha\alpha\alpha\alpha$	A_{1g}
1	$\beta\beta\beta\beta\beta\beta$	A_{1g}
6	$\alpha\beta\beta\beta\beta\beta$	$A_{1g} + B_{1u} + E_{1u} + E_{2g}$
6	$\beta\alpha\alpha\alpha\alpha\alpha$	$A_{1g} + B_{1u} + E_{1u} + E_{2g}$
15	$\alpha\alpha\beta\beta\beta\beta$	$3A_{1g} + B_{1u} + B_{2u} + 2E_{1u} + 3E_{2g}$
15	$\beta\beta\alpha\alpha\alpha\alpha$	$3A_{1g} + B_{1u} + B_{2u} + 2E_{1u} + 3E_{2g}$
20	$\alpha\alpha\alpha\beta\beta\beta$	$3A_{1g} + A_{2g} + 3B_{1u} + B_{2u} + 3E_{1u} + 3E_{2g}$

Table 1.2: The representations Γ^{nspin} of the spin functions Φ_{nspin} are given as sums of the irreducible representations $\Gamma^{(l)}$.

with a_l being the number of times the irreducible representation $\Gamma^{(l)}$ appears. The coefficients a_l can be determined from

$$a_l = \frac{1}{h} \sum_P g[P] \chi_l[P] \chi_{nspin}[P] \quad (1.26)$$

with h being the order of the PI group, $g[P]$ the coefficient of the permutation P , $\chi_l[P]$ the characters of the irreducible representation $\Gamma^{(l)}$ under permutation P and $\chi_{nspin}[P]$ the characters of the nuclear spin function representation Γ^{nspin} under permutation P . The sum over all nuclear spin function representations Γ^{nspin} gives the total nuclear spin function representation. From Table 1.1 and equations 1.25 and 1.26 the total nuclear spin function representation of C_6H_6 can be determined as the sum of the irreducible representations $13A_{1g} + A_{2g} + 7B_{1u} + 3B_{2u} + 9E_{1u} + 11E_{2g}$ (see Table 1.2).

According to equations 1.22 and 1.23 the internal wavefunction Φ_{int} of C_6H_6 changes sign by a specific permutation as shown in Table 1.1. For C_6H_6 the representation Γ^{int} corresponds thus to the irreducible representations $\Gamma^{(l)} = B_{1g}$ and B_{1u} . A rovibronic state is only combined with a nuclear spin state to form a basis function of Φ_{int} , if the product of the two symmetries is an allowed symmetry for Φ_{int} (see equation 1.24). It follows that

$$\Gamma^{int} = \Gamma^{nspin} \otimes \Gamma^{rve} \quad (1.27)$$

with $\Gamma^{int} = B_{1g}$ or B_{1u} , so that

$$B_{1g} = \Gamma^{nspin} \otimes \Gamma^{rve} \quad \text{or} \quad B_{1u} = \Gamma^{nspin} \otimes \Gamma^{rve}. \quad (1.28)$$

As $\Gamma^{nspin} = 13A_{1g} + A_{2g} + 7B_{1u} + 3B_{2u} + 9E_{1u} + 11E_{2g}$, the nuclear spin statistical weights 13, 1, 7, 3, 9 and 11 are correlated to the rovibronic energy levels of the symmetries $B_{1g/u}$, $B_{2g/u}$, $A_{1u/g}$, $A_{2u/g}$, $E_{2u/g}$ and $E_{1g/u}$, respectively.

The effort necessary to determine the states of allowed rovibronic transitions and their nuclear spin statistical weights in molecules can be reduced by determining directly the characters χ of the representation Γ^{rve} for any nuclear permutation operation P [43, 44] by

$$\chi_{rve}^{sw}[P] = 2 \prod \left[(2I_a + 1)(-1)^{(2I_a)(n_a - 1)} \right]. \quad (1.29)$$

The product contains one factor for each set of n_a nuclei having spin I_a and being permuted by P (including sets of one nucleus for which $n_a=1$). χ_{rve}^{sw} is zero for all permutation-inversion operations in the MS group [42]. The representation Γ^{rve} can be expressed as a sum of irreducible representations $\Gamma^{(l)}$ of the MS group with the respective coefficients a_l

$$a_l = \frac{1}{h} \sum_P g[P] \chi_l[P] \chi_{rve}^{sw}[P] \quad (1.30)$$

giving the symmetries of the allowed states and their nuclear spin statistical weights.

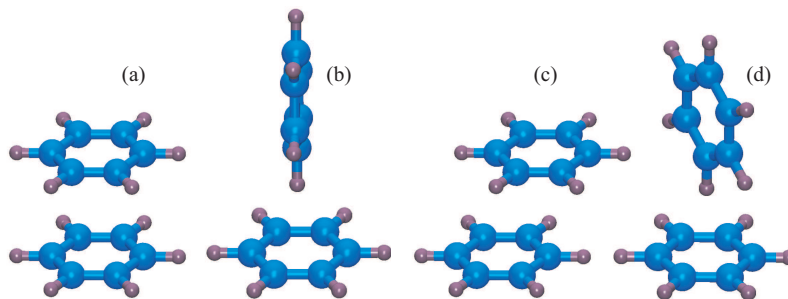


Figure 1.9: Structures of theoretically often considered benzene dimer geometries. While the (a) "Sandwich" (D_{6h}) and the (b) T-shaped structure (C_{2v}) on the left represent saddle points, the (c) parallel displaced (C_{2h}) and (d) distorted T-shaped (C_s) structures on the right represent minima on the potential energy surface [70].

1.5 The benzene dimer

Dispersive intra- and intermolecular forces between aromatic species are of tremendous importance, for example, for the stabilization of the secondary and higher order structures of biological systems, such as proteins and DNA strands. Furthermore, such forces play a major role for intercalation of different drugs into DNA and for the stabilization of clusters and aggregates. Benzene is one of the smallest aromatic systems and has high symmetry, i.e. it has properties that should facilitate experimental spectra, and adequate simulations should be possible. Therefore, the benzene dimer can serve as a prototypical system to investigate dispersive interactions between aromatic systems. For more than 30 years it has attracted the attention of both, experimentalists [45–57] and theoreticians [58–71]. However, although being investigated intensively and although the properties of the monomer are well known, it is still today far from being fully understood. The most controversial subject concerning the benzene dimer is the geometry of the complex and the zero-point-vibrational-energy of the global ground state structure. Structures, that are very often considered, are schematically shown in Figure 1.9.

1.5.1 Experimental approaches to the benzene dimer

Experiments in the liquid phase show that benzene pairs are arranged almost at right angle (roughly T-shaped) [72], which is very similar to the structure of crystalline benzene [73, 74]. The first experiment on the benzene dimer in

the gas phase, performed in 1975 by Klemperer and coworkers, used electric deflection methods and concluded that the benzene dimer is polar, i.e. that it has a permanent dipole moment [45, 75]. This hinted to an asymmetric nuclear arrangement not being in agreement with a "Sandwich" or parallel displaced structure (see Figure 1.9 (a) and (c)). Since then, many experimental techniques have been used to investigate the structure and dynamics of the ground state benzene dimer, also exploiting the effects of complete and partial isotopic labeling (mainly H-D exchange). In 1993, Gutowsky *et al.* have investigated the rotational properties of the benzene dimer in a microwave experiment [57]. This technique is only applicable for structures with a permanent dipole moment and non-polar structures cannot be studied (see section 1.3.3). A controversial result has been found: although all polar benzene dimer structures are in their rigid form asymmetric top molecules, the rotational transitions measured can be nicely fitted to a symmetric top Hamiltonian. The explanation of how an asymmetric top molecule can have a symmetric top rotational spectrum was, however, rather speculative at that time. The latest results, addressing this problem with microwave (MW) spectroscopy in combination with Molecular Symmetry (MS) group theory, give new and interesting results and are presented in chapter 3.

The vibrational properties of the benzene dimer have been investigated by infrared [10, 53, 76] and Raman spectroscopy [55, 77, 78]. It seems difficult to assign a structure to the benzene dimer exclusively on the basis of IR spectra in the C-H stretching range, since the C-H stretching frequencies compared to those of the benzene monomer are only slightly shifted [53]. However, a structural assignment has been made based on theoretical spectra of different benzene dimer geometries and on an experimental IR spectrum in the range between 400 and 1700 cm^{-1} . Experiment and theory seem to fit best assuming a distorted T-shaped structure [10]. Raman experiments by Felker *et al.* [55, 77, 78] on the benzene dimer and several isotopologues are discussed in terms of symmetry leading to the conclusion that the two benzene subunits are symmetrically inequivalent.

Double resonance techniques involving electronic excitation via REMPI, as described before, are often used to obtain information about vibrational properties (see chapter 2). Also UV spectra without double resonance can give valuable information about electronic states and dynamics in the molecule or complex (see section 4.2). A more detailed introduction of the electronic spectra of the benzene dimer is given in section 1.5.3.

1.5.2 Theoretical attempts

With ongoing progress in computational chemistry the issue of geometry and binding energy of the global ground state structure of the benzene dimer has been addressed on different levels of theory, mostly based on (second order) Møller-Plesset perturbation theory (MP), Coupled Cluster theory (CC) or density

functional theory based symmetry adapted perturbation theory (SAPT(DFT)). However, a definite determination seems difficult, as the binding between the two benzene subunits is caused by dispersive (van der Waals) as well as electrostatic (hydrogen bonding) interactions [63, 64, 68, 71, 79]. Depending on the contribution of each type of interaction, the orientation of the two benzene molecules with respect to each other can vary (see structures in Figure 1.9). While electrostatic interactions favor a perpendicular arrangement, dispersive interactions rather lead to a parallel orientation of the two benzene subunits [60].

Some of the numerous theoretical investigations identify the parallel displaced structure as the global minimum structure [59, 60, 79–85], others rather find a C_{2v} T-shaped [58, 62, 68, 86–88] structure to be more stable. However, in some studies the C_{2v} T-shaped and the parallel displaced structures are found to be isoenergetic [61, 63, 65]. In a few studies a bent T-shaped structure with an angle $\alpha < 90^\circ$ between the two benzene planes [58, 80, 86], a V-shaped structure [60, 82] or a C_{2v} distorted chain structure [81, 89] are considered additionally to the "Sandwich", parallel displaced and C_{2v} T-shaped structures, but are not found to represent the global minimum on the potential energy surface. Recently, a C_s distorted T-shaped structure as shown in Figure 1.9 has also been considered [10, 70, 71, 83, 90] and is found to be the lowest energy structure [10, 70, 71].

Due to the challenging complexity, the benzene dimer has become a reference system to check the accuracy of new theoretical approaches aiming to reproduce dispersive interactions and to allow for a precise structure determination. The goal is to include adequately these interactions when investigating molecules, even bigger than the benzene dimer, at lower costs than with the CCSD(T) method, which is considered as the benchmark method for such problems at this time [79, 85, 88].

The possibility of a benzene dimer structure in which the two benzene rings are oriented (almost) perpendicularly to each other and the existence of O-H $\cdots\pi$ hydrogen bonds in benzene-water complexes [91–93] have initiated speculations about the existence of a C-H $\cdots\pi$ hydrogen bond between the C-H group of one benzene ring pointing into the π -electron cloud of the other benzene ring (see structures b and d in Figure 1.9). Theoretical studies on C-H bond lengths and C-H stretching frequencies in the benzene dimer have been performed, giving unexpected results. In contrast to normal hydrogen bonds (proton donor - proton acceptor), in which an elongation of the bond and a decrease of the stretching frequency of the proton donor are observed, the bondlength of the C-H oscillator pointing into the π -electron cloud of the other benzene ring is calculated to be 0.3 % shorter than that of the other C-H groups and its stretching wavenumber is shifted to the blue by $\sim 50\text{ cm}^{-1}$ [94].

The measurable effects of a normal hydrogen X-H \cdots Y bond are the consequence of electrostatic interactions [95] (and a small fraction of covalent interactions [96]) which lead to electron density transfer from lone π -electron

pairs of the proton acceptor Y to an antibonding σ^* -orbital of the proton donor X-H. The so-called improper blue shifting hydrogen bond is assumed to originate in dispersion and electrostatic quadrupole-quadrupole interactions. Different (sometimes contradicting) interpretations are proposed: The "repulsion wall" hypothesis, for example, assumes that the attraction ($\sim r^{-6}$, $\sim r^{-5}$) which comes along with a reduction of the intermolecular distance exceeds the Pauli repulsion [94]. Another attempt assumes an electron density transfer from the proton acceptor Y not to the antibonding σ^* -orbital of the X-H bond but to remote orbitals of the proton donor which results in its structural reorganization, including the contraction of the X-H bond [97–100]. Still another explanation focuses on the response of the dipole moment of the X-H proton donor to the electric field of the polar proton acceptor (dipole-dipole interaction) [101–104].

The theoretically established phenomenon of improper blue shifting hydrogen bonds can explain several experimental observations made in the past [98, 105–108]. This shows how the complexity of the benzene dimer allows one to develop new models that can be of general importance and applicable to a variety of molecular systems and clusters.

1.5.3 UV spectra of the benzene dimer

REMPI techniques (see section 1.3.1) are preferentially used with two different photon energies in order to investigate mass selectively the electronic states and transitions of molecules and molecular clusters in a beam without the influence from fragments of larger clusters. Although benzene tends to form clusters of different sizes in a molecular beam, the contributions from fragments of larger clusters to the electronic spectrum of the benzene dimer can be largely suppressed this way. Electronic excitation spectra of the benzene dimer have been recorded not only in our [109] but in many other laboratories before [46, 48–51, 56]. The electronic spectra of different isotopologues of the benzene dimer are measured as described in section 1.2.1 and 1.3.1 and are shown in Figure 1.10. The carrier gas is helium. The intermediate state is reached by exciting the 0_0^0 and the 6_0^1 transitions, respectively. The characteristics of these spectra are described and discussed in the following; the exact values of the transition energies and splittings are listed in Table 1.3.

The 0_0^0 transition is the transition from the vibrational ground state of the A_{1g} electronic ground state to the vibrational ground state of the B_{2u} electronically excited state. The 200 cm^{-1} displacement between the transitions of $(\text{C}_6\text{H}_6)_2$ and $(\text{C}_6\text{D}_6)_2$, (the so-called homodimers), is due to the isotope shifts of the involved energy levels. Both transitions are split in two components and the splitting is slightly bigger for $(\text{C}_6\text{D}_6)_2$. For both transitions the red component is more intense than the blue one. For the mixed or heterodimer $(\text{C}_6\text{H}_6)(\text{C}_6\text{D}_6)$ two single lines, each about 2.5 cm^{-1} to the blue of the two homodimer transitions, are observed.

Exciting the 6_0^1 transition leads to the ν_6 vibrational level in the first

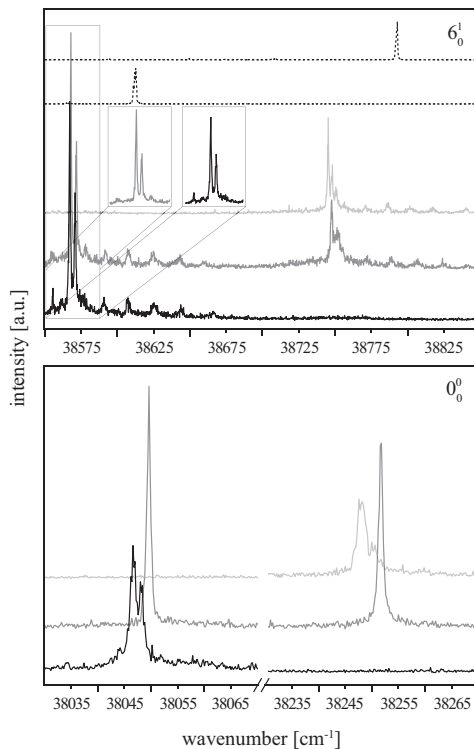


Figure 1.10: UV spectra of $(\text{C}_6\text{H}_6)_2$ (black line), $(\text{C}_6\text{H}_6)(\text{C}_6\text{D}_6)$ (gray line) and $(\text{C}_6\text{D}_6)_2$ (light gray line) obtained by exciting the 0_0^0 transition (bottom) and the 6_0^1 transition (top). The spectra of C_6H_6 and C_6D_6 excited via the 6_0^1 transition are shown as dashed lines.

electronically excited state, which is of E_{2g} symmetry. In the monomers C_6H_6 and C_6D_6 this transition is doubly degenerate and a single line is observed in the electronic spectra in both cases. The 6_0^1 transitions in the dimers are, similarly to the 0_0^0 transitions, shifted about 40 cm^{-1} to the red relative to the appropriate monomer transitions. Contrary to the 0_0^0 transition, the 6_0^1 transition is split in at least two components for all dimer isotopologues. Additionally, a van der Waals progression at the blue end of each sharp spectral feature occurs. The transitions of the two homodimers are separated by about 180 cm^{-1} .

Symmetry considerations

In the benzene monomer, whose transition dipole moment operator spans $A_{2u} + E_{1u}$, the 0_0^0 transition ($B_{2u} \leftarrow A_{1g}$) is forbidden by symmetry [22] as

$$A_{1g} \otimes A_{2u} \otimes B_{2u} \quad \text{and} \quad A_{1g} \otimes E_{1u} \otimes B_{2u} \quad (1.31)$$

	species	bandposition ^a [cm ⁻¹]	splitting [cm ⁻¹]	$\Delta\nu$
0_0^0	(C ₆ H ₆) ₂	38042.27	1.62	-43.83 ^b
	(C ₆ H ₆)*(C ₆ D ₆)	38044.56	-	-41.54 ^b
	(C ₆ D ₆)*(C ₆ H ₆)	38246.26	-	-42.84 ^c
	(C ₆ D ₆) ₂	38243.73	2.42	-45.37 ^c
6_0^1	(C ₆ H ₆) ₂	38564.01	3.92	-43.47 ^d
	(C ₆ H ₆)*(C ₆ D ₆)	38564.58	3.93	-42.91 ^d
	(C ₆ D ₆)*(C ₆ H ₆)	38744.74	n.d. ^e	-42.83 ^f
	(C ₆ D ₆) ₂	38742.69	2.83; 2.79	-44.88 ^f

^aband position is the center of the observed peak

^brelative to the transition of C₆H₆ at 38086.1 cm⁻¹ [110]

^crelative to the transition of C₆D₆ at 38289.1 cm⁻¹ [110]

^drelative to the transition of C₆H₆ at 38607.48 cm⁻¹

^enot determined

^frelative to the transition of C₆D₆ at 38787.57 cm⁻¹

Table 1.3: Overview of the S₁←S₀ electronic excitation energies for the benzene dimer isotopologues (C₆H₆)₂, (C₆H₆)(C₆D₆) and (C₆D₆)₂ excited via the 0_0^0 and 6_0^1 transition. For the heterodimer the site of electronic excitation is labeled with *. (Later, in chapter 2, it is shown that this site corresponds to the "stem" and the unlabeled site to the "top" in a (distorted) T-shaped structure.) Additionally, the splitting values and the positions relative to the appropriate benzene monomer transitions are given.

do not contain the totally symmetric representation A_{1g} (see section 1.3.1). In the dimer this transition can be allowed, under the conditions that will be discussed in the following.

In the electronic spectrum of (C₆H₆)(C₆D₆) two distinct features, separated by about 200 cm⁻¹, are observed when exciting the 0_0^0 transition (see Figure 1.10 (bottom)). Their transition energies are very close to those of the two homodimers, (C₆H₆)₂ and (C₆D₆)₂, giving rise to the assumption that the isotopic composition of the second benzene ring in the dimer has no significant influence on the electronic excitation energy, i.e. that the electronic excitation is localized in one moiety. Due to the weak interaction and due to the similarities to the homodimer spectra the two spectral signatures in the spectrum of (C₆H₆)(C₆D₆) can be ascribed to the excitation of the protonated and the deuterated subunits, respectively.

In Figure 1.11 possible relative orientations of two benzene molecules in a dimer are schematically shown, together with the symmetry properties of the respective subunits as well as of the whole complex. The 0_0^0 transition is allowed by symmetry only for those subunits shown there that have C_{2v} or C_s

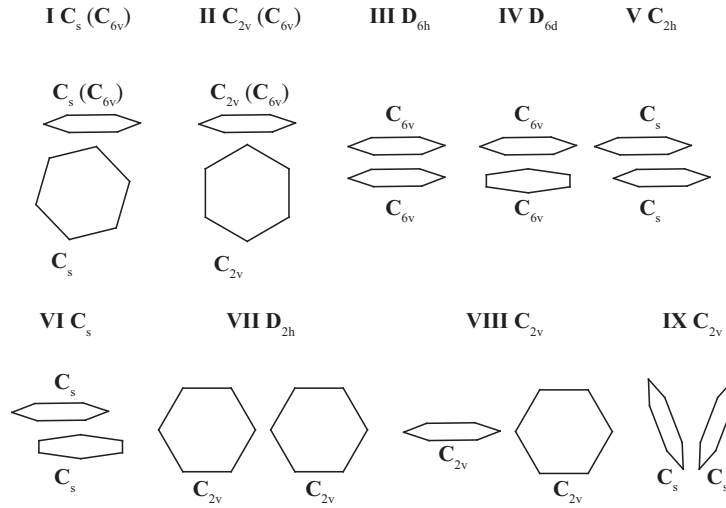


Figure 1.11: Overview of possible orientations of two benzene molecules. Additionally, the symmetries of the individual subunits are given next to the respective moieties, and the symmetry of the whole system is given together with its label (I-IX). The symmetries for structures I and II given in brackets refer to the non-rigid structure (see text).

	D_{6h}	C_{6v}	C_{2v}	C_s
$\Gamma(\Psi_e'')$	A_{1g}	A_1	A_1	A'
$\Gamma(\mu_e)$	$A_{2u} + E_{1u}$	$A_1 + E_1$	$A_1 + B_1 + B_2$	$2A' + A''$
$\Gamma(\Psi_e')$	B_{2u}	B_2	B_1/A_1	A'/A''

Table 1.4: Symmetry properties of the benzene dimer subunits in various possible configurations. The 0_0^0 transitions is symmetry allowed if $\Gamma(\Psi_e'') \otimes \Gamma(\mu_e) \otimes \Gamma(\Psi_e')$ contains the totally symmetric representation.

symmetry (see Table 1.4). Therefore, structures I, II and V-IX from Figure 1.11, having each two subunits of the adequate symmetry, are candidates that could give rise (from the symmetry point of view) to two separate transitions in the 0_0^0 transition spectrum of $(\text{C}_6\text{H}_6)(\text{C}_6\text{D}_6)$.

However, in a T-shaped structure (I and II in Figure 1.11), consisting of a "top" (upper benzene molecule) and of a "stem" (lower benzene molecule), the internal rotation of the "top" about its C_6 axis has a very low barrier [70], so that the dynamically averaged symmetry of the "top" becomes C_{6v} for structures I and II, while the symmetry of the "stem" remains unchanged. That is, structures I and II have two symmetrically inequivalent subunits when the "top" moiety is freely rotating. The 0_0^0 transition is forbidden in a C_{6v} symmetry (see Table 1.4), so that in the case of a freely rotating "top" moiety only the "stem" of structures I and II can contribute to the 0_0^0 electronic excitation spectrum. This would imply that the two spectral features in the spectrum of $(\text{C}_6\text{H}_6)(\text{C}_6\text{D}_6)$ result from two substitution isomers: $(\text{C}_6\text{H}_6)^S(\text{C}_6\text{D}_6)^T$ and $(\text{C}_6\text{D}_6)^S(\text{C}_6\text{H}_6)^T$, with "S" and "T" designating the "stem" and the "top" position, respectively. In this case, and only in this case, the C-H stretch spectra of both subunits are expected to be different (see chapter 2).

The 6_0^1 transition is allowed by symmetry in the benzene monomer and in both subunits of all structures shown in Figure 1.11. The relative arrangement in structures I and II is such that the lower benzene ring directly points into the π -electron cloud of the upper benzene ring. When exciting electronically the upper benzene moiety, the intermolecular potential energy surface is expected to change considerably, which might lead to the van der Waals progression observed to the blue side of the sharp spectral features in both homodimer spectra. This is not expected when electronically exciting the lower benzene moiety. The van der Waals progression is not plausible when assuming any other structure than structures I and II from Figure 1.11.

Discussion

The electronic spectra of the benzene dimer have been subject of numerous previous studies [46, 48–51, 56]. From the observed 0_0^0 and 6_0^1 excitation spectra many interesting questions arise, which cannot all be unambiguously answered yet. The following discussion will focus mainly on the open questions. For further information, the reader is referred to the given References.

(1) Why are the homodimer transitions relative to the appropriate monomer transitions consistently larger redshifted than the heterodimer transitions?

The observed transition energy shifts, relative to the appropriate monomer transition energies, result from shifts of the involved energy levels. The energy of a vibronic level of the benzene dimer can be described by

$$E = E_{el} + E_{vdW} + E_{vib} \quad (1.32)$$

with E_{el} being the pure electronic energy in the benzene monomer, E_{vdW} the stabilization by van der Waals interactions and E_{vib} the vibrational energy. E_{el} is for a given geometry for all isotopologues of the benzene dimer identical. The vibrational energy (in the harmonic approximation) is given by

$$E_{vib} = \frac{h}{2\pi} \sqrt{\frac{k}{\mu}} \left(v + \frac{1}{2} \right) \quad (1.33)$$

with k being the force constant, μ the reduced mass and v the vibrational quantum number. The force constant of the electronically excited state k' can be different from that of the initial state k . As the electron density in the binding molecular orbitals is reduced in the electronically excited state, k' is expected to be lower than k . According to equation 1.33, the heavier the isotopologue is, the lower are the vibrational energy levels. The contribution from the vibrational energy to the total transition energy is

$$\Delta E_{vib} = \frac{h}{4\pi} \frac{\sqrt{k'} - \sqrt{k}}{\sqrt{\mu}} \quad (1.34)$$

if $\Delta v = 0$ for the electronic transition. The difference $\sqrt{k'} - \sqrt{k}$ is negative and therefore ΔE_{vib} is smaller the smaller the reduced mass is. The 0_0^0 transition frequencies of the individual isotopologues are thus expected to be in the order $(\text{C}_6\text{H}_6)_2 < (\text{C}_6\text{H}_6)^*(\text{C}_6\text{D}_6) < (\text{C}_6\text{D}_6)^*(\text{C}_6\text{H}_6) < (\text{C}_6\text{D}_6)_2$, when assuming that the electronic excitation is localized in one site. However, $(\text{C}_6\text{D}_6)_2$ is observed with a lower transition energy than $(\text{C}_6\text{D}_6)^*(\text{C}_6\text{H}_6)$.

Additionally to the vibrational energy, the stabilizing van der Waals interaction has to be taken into account. The van der Waals interaction in the benzene dimer is mainly London dispersion $E_L \propto -r^{-6}$. In the electronically excited state the changed electron density distribution can cause bond lengthening and therefore the stabilization by London forces in the electronically excited state is expected to be smaller than in the electronic ground state. The contributions of the vibrational energy difference and the van der Waals energy difference to the total transition energy thus have opposed effects. The van der Waals stabilization energy in the electronic ground state can be assumed to be very similar for all isotopologues of the benzene dimer. However, in the homodimers the changes in electron density in the first electronically excited state may be less disturbing than in the heterodimers, due to a better delocalization. This can lead to a smaller bond lengthening than in the heterodimers and thus to a larger van der Waals stabilization of the electronically excited states of the homodimers. The additional stabilization effect can be reflected in the observed 0_0^0 transition energy order of the different isotopologues that differs from the expected one, when considering exclusively the isotope effects on the vibrational energy levels.

If $\Delta v = 1$, as for example in the case of the 6_0^1 transition, equation 1.34 becomes

$$\Delta E_{vib} = \frac{h}{2\pi} \frac{3\sqrt{k'} - \sqrt{k}}{2\sqrt{\mu}}. \quad (1.35)$$

As k' is not an order of magnitude smaller than k , $\sqrt{9k'} - \sqrt{k}$ is positive, and thus ΔE_{vib} is expected to increase for the individual isotopologues according to $(\text{C}_6\text{H}_6)^*(\text{C}_6\text{D}_6) < (\text{C}_6\text{H}_6)_2 < (\text{C}_6\text{D}_6)_2 < (\text{C}_6\text{D}_6)^*(\text{C}_6\text{H}_6)$. The same discussion of the van der Waals interaction as for the 0_0^0 transition can be conducted here as well, leading to an expected transition energy order that coincides with the experimentally observed one.

(2) What is the origin of the splitting of the 0_0^0 transition of the homodimers? Generally, splittings of transitions can occur when originally degenerate modes lose their degeneracy, for example as a consequence of symmetry reduction, when site splitting, i.e. simultaneous excitation of different sites occurs or when exciton exchange between an excited state and an energetically close lying state occurs.

The 0_0^0 transition is an electronic transition between two non-degenerate energy levels. The loss of the degenerate symmetry can therefore not be responsible for the splitting.

The electronic transitions of the homodimers are redshifted from the appropriate monomer transitions by more than 40 cm^{-1} and split by $1\text{-}2 \text{ cm}^{-1}$. In a possible (distorted) T-shaped dimer geometry the individual benzene molecules are in a very different arrangement. Therefore, the perturbation that one benzene molecule experiences by the presence of the second benzene molecule should strongly depend on the site in the dimer and thus the two subunits should not experience almost the same shift ($40 \pm 1\text{-}2 \text{ cm}^{-1}$) upon dimerization. This is an argument against site splitting. Furthermore, if site splitting plays a role it should be observed also in the case of the heterodimers. Therefore, it seems unlikely that the $1\text{-}2 \text{ cm}^{-1}$ splitting can be referred to site splitting.

Exciton exchange is feasible between two energetically close lying levels. As the perturbation of the two benzene moieties in a T-shaped geometry is expected to be very different, exciton coupling becomes in principle impossible and the exciton splitting, which is described in the literature as possible origin of the splitting [49–51], can be ruled out as an adequate explanation of the small splitting.

However, for a benzene dimer structure in which the two sites are symmetrically equivalent (see Figure 1.11), a very similar shift and thus a small site splitting and also exciton coupling are conceivable. An argument against exciton coupling and site splitting not only in a (distorted) T-shaped, but also in all other structures from Figure 1.11, is the structure of the absorption signals for the two homodimer 6_0^1 transitions (see Figure 1.10). The 6_0^1 transition excites a doubly degenerate state which is most probably split due to the reduced symmetry in the dimer. Additional exciton coupling/site splitting would lead to

a quadruple peak for the two homodimers, which is, however, not observed. The question about the origin of the small splittings of the 0_0^0 homodimer transitions remains thus open.

(3) Why do the 0_0^0 transitions of the heterodimers, in contrast, appear each as a single line?

In some studies [50, 51] it is concluded that the exciton coupling is responsible for the splitting in the homodimers, however, negligible in the heterodimers due to the isotope shift of the energy levels. Actually, this interpretation cannot explain the observations as in the case of the 6_0^1 transition the spectral features for the homodimers resemble very much those of the appropriate heterodimers (see Figure 1.10). However, the isotope shift should have the same effect for the 6_0^1 transition. Also this is still an open question.

(4) Which benzene dimer structure can be identified based on these spectra?

This question has been addressed by several electronic excitation experiments and two different opinions prevail. Some experimental results lead to the conclusion that the benzene dimer consists of two symmetrically inequivalent subunits, as in a non-rigid (distorted) T-shaped structure: (1) the 6_0^1 transitions are found to be split [48] and (2) in the region of the 6_0^1 transition a split peak and a van der Waals progression are found which, according to hole burning experiments on the heterodimer, seem to originate from two different benzene subunits [56]. This structural assignment is supported by a Raman experiment, that unambiguously demonstrates that the two subunits are arranged in the benzene dimer such that they have inequivalent symmetry properties [55]. In that work a structure similar to structure II from Figure 1.11 is proposed.

Other experimental results lead to the conclusion that the benzene dimer consists of two symmetrically equivalent moieties as the 0_0^0 transitions of the heterodimer appear as single lines [49, 51]. Also a parallel displaced structure [49] and a V-shaped structure with an angle $\alpha = 80^\circ$ between the two planes [51] have been proposed. A "Sandwich" structure can be excluded as origin of the observed transitions since the 0_0^0 transition would be forbidden by symmetry in both subunits, as already in the monomer. Interestingly, in one experiment (exciting the 6_0^1 transition), which definitely attributes the main spectral features to a T-shaped structure, evidence of two additional structures is found which become more prominent the better the cooling in the molecular beam is [56]. They are not observed when exciting the 0_0^0 transition of the benzene dimer, which indicates that this transition is symmetry forbidden for both structures. This is for example the case for the staggered and eclipsed "Sandwich" structures whose subunits are all of C_{6v} symmetry.

Chapter 2

Infrared Spectroscopy on the benzene dimer

2.1 The B_{1u} C-H stretching mode of the benzene monomer

2.1.1 Introduction

After the discovery of benzene in 1825 by Michael Faraday the first, often purely chemical, experiments on benzene have been performed. Later, this molecule has also attracted attention of physicists and physical chemists. Since benzene, one of the smallest aromatic systems, has high symmetry (D_{6h}) it has become a model system to understand the symmetry properties of molecular vibrations in polyatomic molecules [111]. Until today, the benzene molecule and its clusters have been continuously in the focus of experimental and theoretical investigations.

The fundamental frequencies of most of the 30 normal modes (see Figure 2.1), 10 of them being doubly degenerate, are well known [112]. However, for two of the modes, for which the frequency can only be determined indirectly, the currently accepted values are 50 years old [113]. These are the ν_3 fundamental mode of A_{2g} symmetry and the ν_{13} fundamental mode of B_{1u} symmetry, and their last-published values are 1350 cm^{-1} and 3057 cm^{-1} , respectively (Wilson numbering is used throughout in this chapter). Both modes are neither Raman nor IR active. The ν_3 fundamental mode can be observed as a weak transition in liquid benzene, as well as via combination bands [113]. The frequency of the ν_{13} fundamental mode, in contrast, has been deduced indirectly by applying product rules on modes of C_6H_6 and of D_{3h} symmetrical $C_6H_3D_3$ [113]. The application

Section 2.1 adapted from:

U. Erlekam, M. Frankowski, G. Meijer, G. von Helden, J. Chem. Phys. **124**, 171101 (2006)

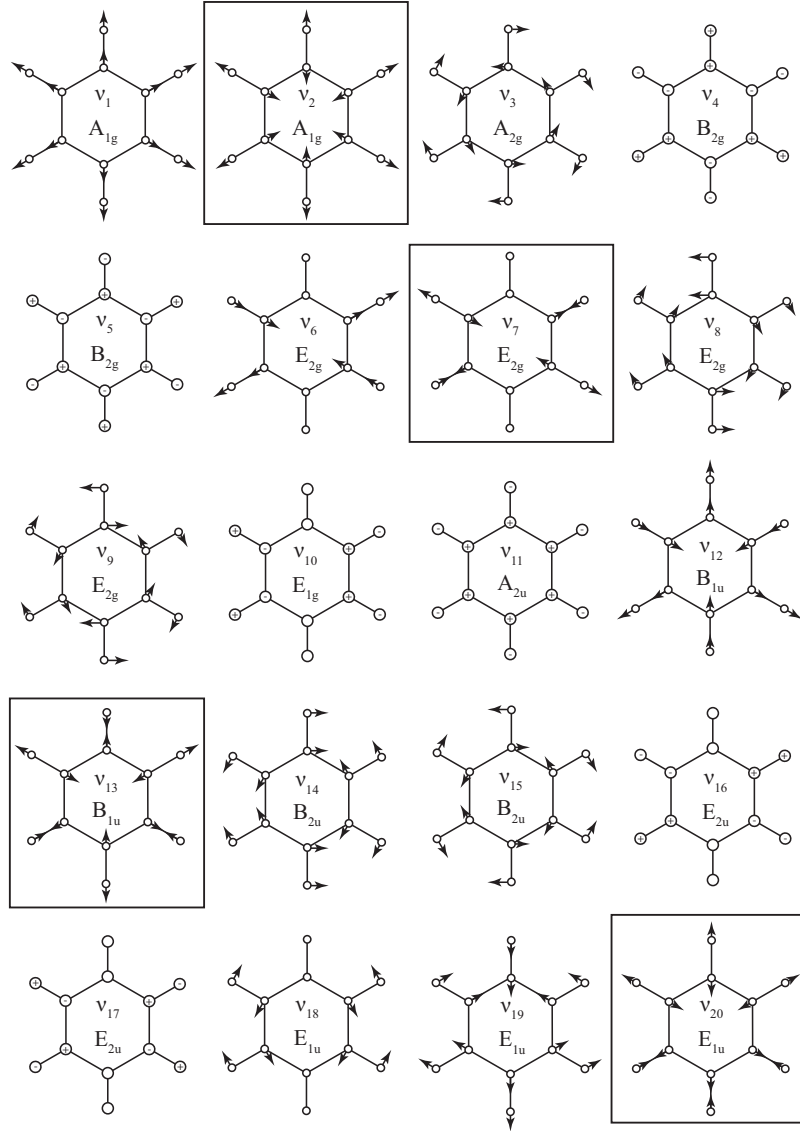


Figure 2.1: Overview of the normal modes of C_6H_6 (D_{6h} point group). The modes of A_{2u} and E_{1u} symmetry are IR active. The vibrations shown in a box are the relevant C-H stretch vibrations in this chapter.

of such product rules is only valid for harmonic vibrations and will fail when modes are coupled, for example via Fermi resonances (see section 1.3.2). It is now known that such Fermi resonances play a role for the ν_{13} mode (B_{1u}), as it strongly interacts with the B_{1u} component of the $\nu_8 + \nu_{19}$ combination band ($B_{1u} + B_{2u} + E_{1u}$) [114]. Therefore, the indirectly determined value of 3057 cm^{-1} for the ν_{13} fundamental mode is highly questionable. The vibrational properties of benzene are theoretically investigated very intensively using empirical force fields [32, 111, 115] as well as *ab initio* harmonic analysis at various levels [116]. Since recently, also the influence of anharmonicities is considered, predicting vibrational wavenumber values of the ν_{13} (B_{1u}) fundamental mode that range from 2988 cm^{-1} [117, 118] to 3083 cm^{-1} [119]. A value of 3028 cm^{-1} is predicted by *ab initio* theory as well as by recent investigations using empirical force fields [120, 121], while another study predicts a value of 3045 cm^{-1} [122]. Although much theoretical effort has already been put into predictions of the frequency of the ν_{13} fundamental mode, this issue has not been satisfactorily solved yet.

Therefore another attempt, based not only on theoretical data, but also on experimental results seems to be necessary. In order to access experimentally the ν_{13} fundamental mode the symmetry properties of the system have to be changed such that the ν_{13} transition becomes IR allowed. This can be realized, for example, by complexation or dimerization. Here it is shown that IR spectroscopy on the benzene dimer can be used to probe the ν_{13} fundamental mode of the benzene monomer. Complementary, the subject has been addressed by *ab initio* calculations on the benzene monomer that include anharmonic and Fermi corrections*.

2.1.2 Experimental method

The IR spectra are obtained by performing ion dip spectroscopy (see section 1.3.2) on the benzene dimer complexes in a pulsed molecular beam in the spectral range between 3010 and 3110 cm^{-1} , probing C-H stretch vibrations. The complexes are generated by expanding a mixture of benzene (0.03%) in helium at a stagnation pressure of 2 bar into vacuum. The experiments are performed on a 1:1 mixture of C_6H_6 and C_6D_6 . Details of the experimental setup are described in section 1.2.1. The benzene dimers are detected in a two color REMPI process (section 1.3.1), using the 0_0^0 transition to the first electronically excited state S_1 . The 0_0^0 excitation energy is, depending on the isotopic composition, between 38000 and 38300 cm^{-1} . For subsequent ionization, laser light around 35460 cm^{-1} is used. Due to the mass selective detection in a Time Of Flight Mass Spectrometer the three different isotopologues of the benzene dimer can be distinguished: $(C_6H_6)_2$, $(C_6H_6)(C_6D_6)$ and $(C_6D_6)_2$. Their electronic excitation spectra (via the 0_0^0 transition) are shown in Figure 1.10 (bottom).

*The calculations are run by G. von Helden.

2.1.3 Results and Discussion

In Figure 2.2 the IR ion dip spectra, when exciting the 0_0^0 transition of $(\text{C}_6\text{H}_6)(\text{C}_6\text{D}_6)$ at 38044.0 cm^{-1} (bottom spectrum) and at 38246.4 cm^{-1} (top spectrum), are shown. These two IR spectra are found to be different, especially concerning the number of spectral signatures. Three important consequences arise from this observation: (1) In the two isomers of $(\text{C}_6\text{H}_6)(\text{C}_6\text{D}_6)$ C_6H_6 is located in two different sites and the C-H stretch spectra result from two symmetrically inequivalent subunits. (2) The two benzene rings do not interchange on the timescale between IR excitation and UV excitation/ionization which is, in the present experiment, about 70 ns. (3) From the discussion on the symmetry properties conducted in section 1.5.3 and from the IR spectra shown in Figure 2.2 it can be concluded that the two spectral features at 38044.0 cm^{-1} and at 38246.4 cm^{-1} in the 0_0^0 transition spectrum of $(\text{C}_6\text{H}_6)(\text{C}_6\text{D}_6)$ (see Figure 1.10 (bottom)) are not the signatures of two different sites, but of the same site in two different substitution isomers. That is, the benzene dimer has a (distorted) T-shaped structure with a "stem" and a freely rotating "top" moiety (structures I or II in Figure 1.11).

If the two benzene molecules were equivalent and/or able to interchange on a 70 ns timescale, identical IR spectra would result when exciting the 0_0^0 transition of $(\text{C}_6\text{H}_6)(\text{C}_6\text{D}_6)$ at 38044.0 cm^{-1} and at 38246.4 cm^{-1} . If the "top" moiety was not freely rotating, the symmetries of both subunits and the two IR spectra would be equivalent. Therefore, the lower spectrum in Figure 2.2 results from a (distorted) T-shaped structure with C_6H_6 in the "stem" position and C_6D_6 in the "top" position ($(\text{C}_6\text{H}_6)^S(\text{C}_6\text{D}_6)^T$) and the upper spectrum in Figure 2.2 results from the substitution isomer $(\text{C}_6\text{D}_6)^S(\text{C}_6\text{H}_6)^T$, where the "stem" is deuterated and the "top" is protonated. Thus the C-H stretch spectra result from the "stem" and the "top" moiety, respectively.

The three well known IR transitions of the benzene monomer that occur in this range [53, 114, 123] are indicated as solid lines in Figure 2.2. These are the ν_{20} fundamental mode (E_{1u} symmetry) at 3047.9 cm^{-1} , the $\nu_1 + \nu_6 + \nu_{19}$ combination band at 3078.6 cm^{-1} and the $\nu_8 + \nu_{19}$ combination band at 3101 cm^{-1} . Shown as dashed lines are the positions of two other, not IR active fundamental C-H stretch modes of the benzene monomer: the ν_7 mode (E_{2g} symmetry) at 3056.7 cm^{-1} [124, 125] and the ν_2 mode (A_{1g} symmetry) at 3073.9 cm^{-1} [124, 125]. An overview over all experimentally determined values is given in Table 2.1.

In both $(\text{C}_6\text{H}_6)(\text{C}_6\text{D}_6)$ benzene dimer spectra, the three resonances that are IR active in the bare benzene are observed. In all cases, they are, compared to the positions for the benzene monomer, redshifted by a few cm^{-1} . In the spectrum of $(\text{C}_6\text{H}_6)^S(\text{C}_6\text{D}_6)^T$ additional resonances are observed, one at 3012.4 cm^{-1} , one at 3070.9 cm^{-1} and a weak split peak (shown enlarged in the inset) at 3056.2 and 3057.3 cm^{-1} .

In the following, the nature of these transitions shall be discussed. Previous

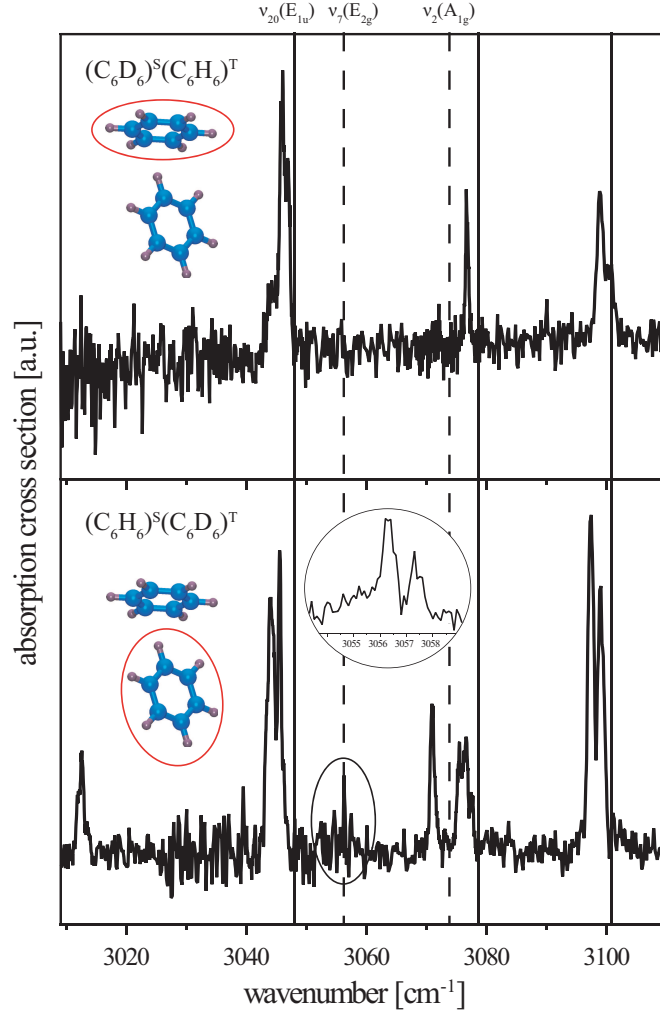


Figure 2.2: IR overview spectra in the region between 3010 and 3110 cm^{-1} of $(\text{C}_6\text{D}_6)^{\text{S}}(\text{C}_6\text{H}_6)^{\text{T}}$ (top) and $(\text{C}_6\text{H}_6)^{\text{S}}(\text{C}_6\text{D}_6)^{\text{T}}$ (bottom), corresponding to the two subunits of the benzene dimer, the "top" and the "stem", respectively. The positions of the IR active C-H stretch modes of the benzene monomer (\mathbf{D}_{6h}) are indicated as solid vertical lines and those of the two known IR inactive fundamental modes ν_7 (E_{2g}) and ν_2 (A_{1g}) as dashed vertical lines. In the inset the region between 3054 and 3059 cm^{-1} is shown for $(\text{C}_6\text{H}_6)^{\text{S}}(\text{C}_6\text{D}_6)^{\text{T}}$, measured with a 10 times higher laser fluence. The red most absorption signal in the spectrum of $(\text{C}_6\text{H}_6)^{\text{S}}(\text{C}_6\text{D}_6)^{\text{T}}$ is attributed to result from the so far unknown ν_{13} (B_{1u}) fundamental mode of C_6H_6 .

2 Infrared Spectroscopy on the benzene dimer

ν	experiment			theory	
	$(\text{C}_6\text{H}_6)^S(\text{C}_6\text{D}_6)^T$	$(\text{C}_6\text{D}_6)^S(\text{C}_6\text{H}_6)^T$	C_6H_6	C_6H_6^a	C_6H_6^b
13 (B_{1u})	3012.4	-	3015 ^c	3159.2	2993.2 ^d
20 (E_{1u})	3044.8	3046.4	3047.9 ^e	3184.4	3030.1 ^d
7 (E_{2g})	3056.8	-	3056.7 ^{c,f}	3169.3	3034.8
2 (A_{1g})	3070.9	-	3073.9 ^{c,f}	3194.9	3053.2

^aharmonic

^banharmonic

^cnot IR active

^din Fermi resonance with $\nu_8 + \nu_{19}$

^esee Reference [114]

^fsee Reference [124, 125]

Table 2.1: Experimental and calculated (harmonic and anharmonic) wavenumbers [cm^{-1}] for the benzene monomer and dimer.

spectra of $(\text{C}_6\text{H}_6)_2$ show similar features. There, in one experiment two [53] and in another experiment all three [126] additional transitions have been observed as well. As tentative assignment for the two stronger additional transitions, combinations with intermolecular vibrations were suggested [53]. Here a different interpretation is proposed.

Our observation of two different IR spectra for the two benzene moieties is in agreement with a T-shaped geometry [55, 57] in which the "top" benzene molecule is freely rotating. Such a T-shaped geometry can be in its rigid form of C_{2v} geometry as shown in Figure 1.9 (b) or it can have C_s symmetry as shown in Figure 1.9 (d). In the dynamic case both benzene dimer structures (of C_{2v} and C_s symmetry) become symmetrically equivalent (C_{6v}); the symmetry of the "top" molecule is then C_{6v} and that of the "stem" remains unchanged C_{2v} and C_s , respectively. Recent *ab initio* calculations predict the benzene dimer of C_s symmetry to be the global minimum structure and the dimer of C_{2v} symmetry to represent a saddle point on the potential energy surface [70, 71].

The four fundamental modes of benzene in the range between 3010 and 3110 cm^{-1} have B_{1u} , E_{1u} , E_{2g} and A_{1g} symmetry in a D_{6h} environment. In D_{6h} , however, only the E_{1u} mode is IR allowed. It can be shown that in the reduced symmetry of the freely rotating "top" (C_{6v}) the ν_2 mode has A_1 symmetry and is IR allowed as well. When the symmetry is reduced to C_s or C_{2v} (monomer \rightarrow "stem"), all four fundamental modes are IR allowed, and additionally, the degeneracy of the E_{1u} and E_{2g} modes is lifted (see Table 2.2). Therefore it is possible, that the additional lines experimentally observed in the spectrum of the "stem" result from those modes that become IR active upon symmetry reduction. These symmetry considerations support the assignment of the upper

2.1 The B_{1u} C-H stretching mode of the benzene monomer

	monomer	"top"	"stem"	
	D_{6h}	C_{6v}	C_{2v}	C_s
ν_{13}	B_{1u}	B_1	$\underline{A_1}$	$\underline{A'}$
ν_{20}	$\underline{E_{1u}}$	$\underline{E_1}$	$\underline{A_1 + B_1}$	$\underline{2A'}$
ν_7	E_{2g}	E_2	$\underline{A_1 + B_1}$	$\underline{2A'}$
ν_2	A_{1g}	$\underline{A_1}$	$\underline{A_1}$	$\underline{A'}$
$\nu_1 + \nu_6 + \nu_{19}$	$B_{1u} + B_{2u} + \underline{E_{1u}}$	$B_1 + B_2 + \underline{E_1}$	$\underline{2A_1 + 2B_1}$	$\underline{4A'}$
$\nu_8 + \nu_{19}$	$B_{1u} + B_{2u} + \underline{E_{1u}}$	$B_1 + B_2 + \underline{E_1}$	$\underline{2A_1 + 2B_1}$	$\underline{4A'}$

Table 2.2: Symmetry properties of the four fundamental modes and two combination bands of benzene C_6H_6 in the region between 3010 and 3110 cm^{-1} in dependence of the symmetry environment. The correlation table is adapted from Reference [32]. The symmetry representations of IR active vibrational modes are underlined.

spectrum in Figure 2.2 to the "top" position in the benzene dimer and the lower spectrum to the "stem" position.

However, pure symmetry considerations do not reveal whether those newly activated IR transitions are strong enough to be observable and, if they are observable, whether they are significantly shifted from the positions of their unperturbed counterparts. Qualitatively, the strength of the symmetry reducing perturbation (i.e. the intermolecular interaction) will affect both, the strength and the frequency shift of the newly allowed transitions. For the benzene dimer the intermolecular interaction is very weak, compared to the intramolecular interactions. This is expected from theory [70, 71], and can also be seen from the shifts and splittings of the transitions in Figure 2.2. For the modes in the dimer that are IR active already in the monomer, the observed splittings are not larger than 2.5 cm^{-1} and the absolute value of the redshifts (compared to the monomer) does not exceed 4 cm^{-1} . The mode at 3070.9 cm^{-1} in the spectrum of $(C_6H_6)^S(C_6D_6)^T$ is shifted by only -3 cm^{-1} from the position of the ν_2 A_{1g} mode in C_6H_6 . The modes at 3056.2 and 3057.3 cm^{-1} can be compared to the ν_7 E_{2g} mode of C_6H_6 at 3056.7 cm^{-1} . In the "stem" of the dimer the degeneracy is lifted (see Table 2.2) which might result in a splitting as the one observed. Consistent with the (negligible) shift and splitting, the band appears to be very weak in the "stem" of the dimer. The third additional transition, observed at 3012.4 cm^{-1} , is thus assigned to the only other fundamental C-H stretch mode in benzene that is left in this energy range, the ν_{13} mode of B_{1u} symmetry.

To further test these assignments calculations of the vibrations of benzene that include the effects of anharmonicities have been performed with GAUSSIAN03 [127] using the B3LYP DFT functional and the cc- p VTZ (correlation consistent polarized valence triple zeta) basis set. The resulting frequencies

for the C-H stretch modes are shown in Table 2.1. Relevant for the direct comparison to the experiment are the anharmonic modes, which also include the effect of Fermi resonances. Comparing those with the (experimentally) known bands (ν_{20} , ν_7 , ν_2) of benzene shows that the calculated wavenumber values are between 0.6% and 0.7% too low for the individual modes. Correcting the calculated value for the ν_2 B_{1u} mode at 2993.2 cm^{-1} for the same amount, results in a predicted value of 3013.0 cm^{-1} for the B_{1u} mode. This is in excellent agreement with the transition in the "stem" position of the dimer observed at 3012.4 cm^{-1} . Comparing now the experimentally observed transitions for the "stem" in the benzene dimer to those for the monomer shows that in the dimer, transitions are up to 3 cm^{-1} shifted to the red. This shift, which is due to van der Waals interactions between the two benzene molecules, is of course not known for the B_{1u} mode, but it would be surprising if this shift was vastly different in this case. Therefore, an empirical shift of $2\text{--}3\text{ cm}^{-1}$ is included for this band and it can be concluded that the ν_{13} fundamental mode of the benzene monomer is located at $3015^{+2}_{-5}\text{ cm}^{-1}$.

2.1.4 Conclusion

Based on the experimentally observed C-H stretch vibrations of $(\text{C}_6\text{H}_6)(\text{C}_6\text{D}_6)$ it has been shown that the two subunits in the benzene dimer are symmetrically inequivalent, and therefore they have distinct IR signatures. One of the two benzene molecules is in a site of low symmetry, which leads to the IR activation of all C-H stretch modes that are forbidden by symmetry in the benzene monomer in the region between 3010 and 3110 cm^{-1} . Thus all four fundamental monomer modes in this region are observed. When comparing to modes that are known for the monomer, the same modes in the dimer are shifted up to 3 cm^{-1} to the red. For the B_{1u} C-H stretch mode (ν_{13}) of the benzene monomer a first experimental value could be determined indirectly by measuring the corresponding mode in the symmetry reduced environment of $(\text{C}_6\text{H}_6)(\text{C}_6\text{D}_6)$. The experimental value of the ν_{13} mode at $3015^{+2}_{-5}\text{ cm}^{-1}$ is also supported by anharmonic DFT calculations.

2.2 Revealing the vibrational properties of the two benzene subunits in the dimer

2.2.1 Introduction

In the previous section it has been shown that the benzene dimer consists of two symmetrically inequivalent subunits as, for example, in a (distorted) T-shaped geometry [55, 57, 76] consisting of a "stem" and a freely rotating "top" moiety. In theoretical studies the distorted T-shaped structure has been found to be lower in energy than the C_{2v} T-shaped structure [10, 70, 71]. The mixed

benzene dimer $(\text{C}_6\text{H}_6)(\text{C}_6\text{D}_6)$ has two isomers that result from the exchange of the C_6H_6 and C_6D_6 moiety: $(\text{C}_6\text{H}_6)^S(\text{C}_6\text{D}_6)^T$ and $(\text{C}_6\text{D}_6)^S(\text{C}_6\text{H}_6)^T$, with S and T indicating the "stem" and the "top" position, respectively. The IR spectra in the C-H stretch range are different for the two isomers and represent the spectra of the two benzene dimer subunits (see Figure 2.2). The spectral signatures of $(\text{C}_6\text{H}_6)^S(\text{C}_6\text{D}_6)^T$ and $(\text{C}_6\text{D}_6)^S(\text{C}_6\text{H}_6)^T$ in the range from 3010 to 3110 cm^{-1} have been shown in section 2.1 to originate from the fundamental modes ν_{13} , ν_{20} , ν_7 and ν_2 and from the combination bands $\nu_1 + \nu_6 + \nu_{19}$ and $\nu_8 + \nu_{19}$ of benzene. The transitions that are observed in the "top" as well as in the "stem" spectrum differ in shape and slightly in their transition frequencies.

A detailed analysis of the shape of the absorption lines and especially of the differences between the signatures observed for the "stem" and for the "top" can allow one to deduce structural properties of the dimer complex. For example, rotational band contour analysis of the vibrational signatures in both spectra can reveal the relative orientations of the two benzene moieties to the three principal axes of inertia (a, b, c) and thus provide information about the benzene dimer structure.

In a (distorted) T-shaped structure the two isomers of $(\text{C}_6\text{H}_6)(\text{C}_6\text{D}_6)$ have two different sets of rotational constants A, B and C, and in these isomers the orientation of C_6H_6 to the three principal axes of inertia is substantially different, leading to different rotational band contours of the C-H stretch signatures. In a parallel displaced or "Sandwich" geometry (see Figure 1.9 (a) and (c)) both benzene subunits would have the same orientation with respect to the three principal axes of inertia, leading to the same rotational envelopes for the same vibrational signature. Additionally, the analysis of the molecular symmetry properties can contribute to elucidate the origin of the observed shapes of the spectral signatures.

In this section the C-H stretch vibrations of the benzene dimer "stem" and of the benzene dimer "top" will be analyzed with focus on the spectral differences between the two benzene moieties. The relevant point groups are \mathbf{D}_{6h} , \mathbf{C}_{6v} , \mathbf{C}_{2v} and \mathbf{C}_s (see Table 2.2). For the sake of clarity, the symmetry labels of the \mathbf{D}_{6h} point group and also the numbering of the vibrations of the benzene monomer introduced by Wilson are used throughout this section.

Experimental method

The experimental setup and experimental details are described in section 1.2.1 and 2.1.2. In the experiment presented here the IR spectra (3010-3110 cm^{-1}) of the fundamental modes and combination bands of $(\text{C}_6\text{H}_6)^S(\text{C}_6\text{D}_6)^T$ and $(\text{C}_6\text{D}_6)^S(\text{C}_6\text{H}_6)^T$ are measured in the gas phase at the spectral resolution of the IR laser (scanning step size 0.05 cm^{-1}) allowing for a detailed interpretation.

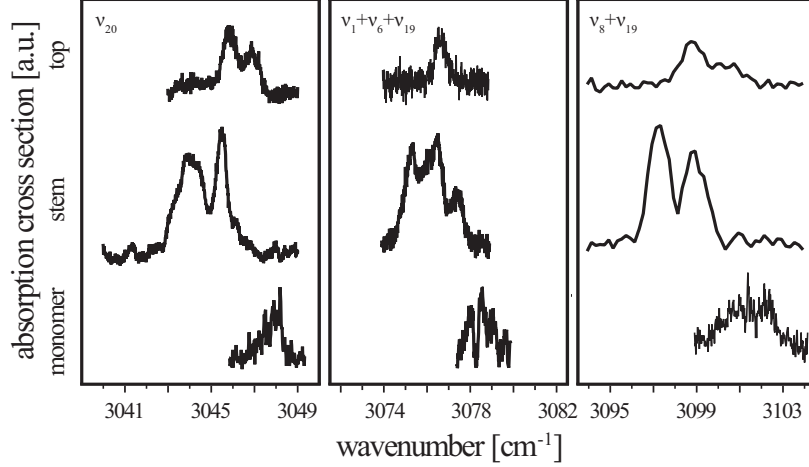


Figure 2.3: IR spectra of the Fermi triad in the range between 3010 and 3110 cm^{-1} for the benzene monomer (bottom) and the two monomeric subunits, the "stem" (middle) and the "top" (top), of the benzene dimer. The ν_{20} (E_{1u}) fundamental mode (left) is in Fermi resonance with the E_{1u} components of the $\nu_1 + \nu_6 + \nu_{19}$ (middle) and $\nu_8 + \nu_{19}$ (right) combination bands which have both $B_{1u} + B_{2u} + E_{1u}$ symmetry.

2.2.2 Infrared spectra

The fundamental mode ν_{20} and the combination bands $\nu_1 + \nu_6 + \nu_{19}$ and $\nu_8 + \nu_{19}$ interact in a Fermi triad. This Fermi triad is shown in detail in Figure 2.3 for the benzene monomer and the "top" and the "stem" of the dimer. The ν_{20} fundamental mode (see Figure 2.3 left) appears at 3047.9 cm^{-1} in the benzene monomer. In both subunits of the dimer this transition is split and a redshift relative to the monomer is observed. The centers of the spectral signatures of the "top" and the "stem" are redshifted relative to the monomer by 1.5 cm^{-1} and 3.6 cm^{-1} , respectively. While the two components of the ν_{20} signature are of comparable width in the "top" spectrum, in the "stem" spectrum the red component is by far broader than the blue one, accompanied by a 50% larger splitting compared to the one of the "top".

The combination band $\nu_1 + \nu_6 + \nu_{19}$ (see Figure 2.3 middle) of the monomer is observed at the central position of 3078.6 cm^{-1} and seems to be split in two components. However, the signal to noise ratio is not sufficient to definitely identify the two components. The spectral position of this vibrational transition is for both, the "top" and the "stem", about 2 cm^{-1} redshifted from the respective monomer transition. For the "stem", a structure with three clearly distinguishable peaks, of which the central one appears to have a shoulder on

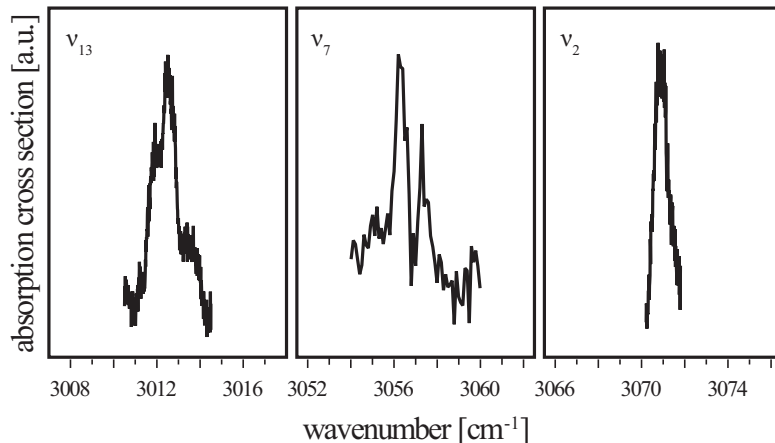


Figure 2.4: IR spectra of the indirectly measured fundamental modes ν_{13} , ν_7 and ν_2 (of B_{1u} , E_{2g} and A_{1g} symmetry, respectively) of the benzene monomer. These modes are IR inactive in the D_{6h} environment of the benzene monomer, however, activated in the lowered symmetry of the "stem" (C_s or C_{2v}) and thus observable in the spectrum of $(C_6H_6)^S(C_6D_6)^T$.

the red side, is observed. The three main peaks are regularly separated by about 1 cm^{-1} . For the "top" benzene ring a single line close to the central position of the "stem" spectral feature (3076.7 cm^{-1}) is found.

Shown in the right panel of Figure 2.3 is the $\nu_8 + \nu_{19}$ combination band, which appears at 3101.4 cm^{-1} for the monomer (bottom). While for the structure of the monomer a splitting can again not unambiguously be determined, a pronounced splitting of 1.7 cm^{-1} is observed for both the "top" and the "stem" benzene rings. The signatures of the "stem" and the "top" are redshifted from that of the monomer, whereas for the "stem" the redshift is twice as big as for the "top".

Besides the Fermi triad, three additional transitions are observed for the "stem" benzene ring in the region between 3010 and 3110 cm^{-1} , as shown in Figure 2.4. By comparison with the known (IR inactive) benzene monomer transitions in this energy range, they can be identified as to result from the fundamental modes $\nu_{13}(B_{1u})$ (left) [76], $\nu_7(E_{2g})$ (middle) [124, 125] and $\nu_2(A_{1g})$ (right) [124] in the benzene monomer. The complicated structure with the main component at 3012.6 cm^{-1} (ν_{13}) appears at first glance to consist of three components. The transition at 3056.9 cm^{-1} (ν_7) is split in two components of different intensity while the feature at 3070.9 cm^{-1} (ν_2) consists of a single line.

2.2.3 Discussion

The gas phase C-H stretch spectra of the benzene monomer and of the "top" and the "stem" benzene of the dimer differ substantially in the number of observed vibrational modes. The spectral signatures of a respective mode differ in frequency and especially in shape for the three species.

The number of vibrational modes observed in a certain energy range depends on the symmetry of the molecule and of the vibrational states involved. Group theoretical considerations can be used to simplify the determination of IR active transitions. The symmetry selection rules are discussed in section 1.3.2. Symmetry considerations provide information about the IR (in)activity of a vibration, however, do not say anything about the strength of the transition dipole moment of the IR active mode.

The frequency of a vibrational mode depends on the energy levels involved in the transition. Frequency shifts can be observed if vibrational modes are involved in anharmonic interactions, in the case of intermolecular perturbations and also if the isotopic composition is changed.

The natural linewidth (Lorentz shape) can be influenced by the Doppler effect and the temperature. Multiply split structures can originate from the (partially) resolved rotational structure as well as from multiply degenerate modes that loose their degeneracy as a consequence of anharmonicities or due to molecular symmetry reduction.

Vibrational modes

The origin of the observed transitions in the C-H stretch spectra of $(\text{C}_6\text{H}_6)^S(\text{C}_6\text{D}_6)^T$ and $(\text{C}_6\text{D}_6)^S(\text{C}_6\text{H}_6)^T$ has been discussed in section 2.1. The presence/absence of individual fundamental modes and combination bands can be explained by the individual symmetry properties, namely by the C_{6v} symmetry of the "top" and the C_{2v} or C_s symmetry in the "stem" (see structures (b) and (d) in Figure 1.9).

Frequencies

It is observed that all C-H stretch modes of the benzene dimer are slightly shifted to the red, compared to the monomer (note, however, that the value of the ν_{13} mode for the monomer is only known with an error bar of a few cm^{-1} , which is on the order of magnitude of the observed wavenumber shifts (see section 2.1.3)). Furthermore, it is observed that the redshifts of the "stem" modes are more pronounced than those of the "top" modes.

Frequency shifts of vibrational modes can be induced by hydrogen bonding. Usually this kind of interaction induces, depending on the interaction strength, a more or less pronounced bond lengthening and redshift of the stretching mode of the proton donor. In a (distorted) T-shaped structure, the benzene in the "stem" position points into the π -electron cloud of the "top" benzene. The

"stem" benzene can thus be regarded as the proton donor and the "top" benzene as the proton acceptor in a hydrogen bond. Such a (comparatively weak) hydrogen bonding interaction might be responsible for the additional redshift of the vibrational modes of the "stem" moiety. However, theory also predicts blue shifting hydrogen bonds [94, 97] which are assumed to originate from dispersion and electrostatic quadrupole-quadrupole interactions. Experimentally, this phenomenon has been observed for example for fluorobenzene complexes [98, 108]. So far there is no experimental evidence for blue-shifting hydrogen bonds in the benzene dimer, and also in the here presented experiment such an effect cannot be identified. Theoretically, a red-shifting hydrogen bond has been predicted for a C_s T-shaped benzene dimer geometry, and a blue-shifting hydrogen bond for a C_{2v} T-shaped benzene dimer structure [128].

Another possible reason for frequency shifts can be anharmonic interactions between modes. Such interactions can occur between modes within one benzene ring as well as between modes of one benzene ring and either intermolecular modes or modes of the other benzene ring. Intramolecular anharmonic interactions are numerous and frequently strong. However, anharmonic interactions with intermolecular modes and modes of the other benzene ring can be expected to be comparatively weak, since a large frequency mismatch between the intra- and intermolecular modes exists and also, since the interaction (binding) between the two rings is weak. Therefore, shifts resulting from anharmonic couplings should be mainly observable for intramolecular modes, and as interactions with intermolecular modes and modes of the second benzene ring are of minor relevance, the effects of anharmonic couplings should not be much different for the monomer and for the dimer subunits.

Structure of the vibrational transitions

There are several factors that can induce splittings of vibrational energy levels, resulting in structured spectral lines. Splittings can be due to rotational structure or due to lifting of degeneracies. Degenerate modes can split up as a consequence of anharmonic couplings to other (dark) states or due to symmetry reduction. The relevance of these possible contributions is discussed in this paragraph.

Rotational structure The spectral signatures of the C-H stretch vibrations of the "top" and the "stem" benzene moieties are investigated in terms of rotational band contours. As the C-H stretch spectra of the "top" and the "stem" correspond to those of $(C_6D_6)^S(C_6H_6)^T$ and $(C_6H_6)^S(C_6D_6)^T$, respectively, the rotational band contour analysis is based on the rotational and vibrational parameters of the two $(C_6H_6)(C_6D_6)$ isomers.

The shape of the rotational contours of a molecular system depends on the orientation of the transition dipole moment relative to the three principal axes of inertia a, b and c. The observed band contours can thus be a characteristic

structural probe. The inertial axis system of the benzene dimer in a C_s T-shaped geometry is shown in Figure 2.5. The "stem" is located in the plane spanned by the principal axes a and b, and the "top" is located in the b-c plane. For the benzene monomer the components of the transition dipole moments for the individual C-H stretch vibrations are located in the molecular

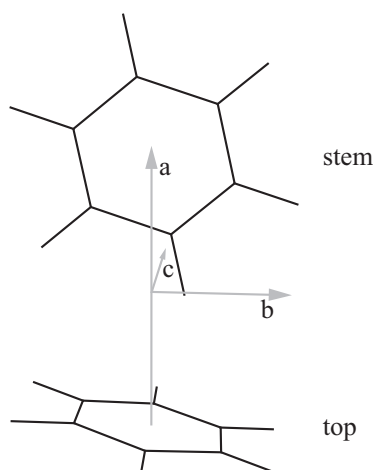


Figure 2.5: Inertial axis system of the benzene dimer in a C_s T-shaped geometry.

plane. Therefore, the vibrational signatures of the "stem" can have contributions of the rotational band contours resulting from a- and b-type transitions, whereas the contribution of a c-type transition is zero. For the "top" the rotational contours are expected to be mainly due to b- and c-type transitions. For a C_{2v} T-shaped geometry as shown in Figure 1.9 (b) the situation is similar, with the difference that the "top" rotational contours can result exclusively from b- and c-type transitions.

Experimental and theoretical rotational constants of $(C_6H_6)^S(C_6D_6)^T$ (see Table 2.3) are used to simulate the rotational envelope of the "stem" transitions along the three principal axes of inertia a, b and c at different temperatures, assuming the same set of rotational constants in the vibrational ground state and the vibrationally excited state. Under the

experimental conditions the rotational temperature can be assumed to be 1-3 K. The band contours for a-, b- and c-type transitions at 5 K as a (safe) upper limit are shown in Figure 2.6. The differences between the experimental and theoretical " C_s over bond" rotational constants are on the order of $1.5 \cdot 10^{-3} \text{ cm}^{-1}$ giving rise to negligible differences in the width of the resulting rotational contours at 5 K or at lower temperatures. The differences between the rotational constants of the " C_s over bond" and the " C_{2v} T-shaped" structures are even smaller. These negligible discrepancies allow one to base the forthcoming analysis of the "top" and the "stem" rotational envelopes exclusively on the calculated rotational constants of $(C_6D_6)^S(C_6H_6)^T$ and $(C_6H_6)^S(C_6D_6)^T$, respectively, assuming the theoretical minimum energy geometry " C_s over bond" [71]. Due to centrifugal distortion the rotational constants of a vibrationally excited state are usually slightly smaller than those of the vibrational ground state ($\Delta \approx 10^{-3} \text{ cm}^{-1}$). From Figure 2.6 it can be seen that differences of rotational constants on that order do not influence the shape of the rotational envelopes. Hence, the approximation, using the same sets of rotational constants for the vibrationally

2.2 Revealing the vibrational properties of the two benzene subunits in the dimer

	A	B	C
C_s over bond			
(C ₆ H ₆) ^S (C ₆ D ₆) ^T	1686.3824	455.0835	422.5678
(C ₆ D ₆) ^S (C ₆ H ₆) ^T	1794.0801	455.2696	416.0929
C_{2v} T-shaped			
(C ₆ H ₆) ^S (C ₆ D ₆) ^T	1669.5224	451.2724	418.2362
(C ₆ D ₆) ^S (C ₆ H ₆) ^T	1778.5094	451.2322	411.8948
(C ₆ H ₆) ^S (C ₆ D ₆) ^T _{exp} ^a	1640.32	409.02	376.51
C ₆ H ₆	5713.3828	5713.3828	2856.6914

^aOnly the value of B is experimentally determined (see section 3.2.2).

The values of A and C are indirectly determined from the rotational constant of the theoretical structure **C_s over bond** and the difference $\Delta B = B_{\text{C}_s \text{ over bond}} - B_{\text{exp}}$.

Table 2.3: Rotational constants [MHz] of both isomers of (C₆H₆)(C₆D₆), assuming the theoretical near-prolate structures "**C_s over bond**" and "**C_{2v} T-shaped**" from Reference [71]. The rotational constants are calculated at the Austin Model 1 (AM 1) level of theory. For comparison, the experimentally determined values for (C₆H₆)^S(C₆D₆)^T and the theoretical values of C₆H₆ are given.

excited state and the vibrational ground state, is valid for the purpose of this study.

The transition dipole moments and the structure of the isotopically pure benzene dimer (C₆H₆)₂ (see Figure 2.5) are calculated at the MP2/6-311++G(2d,p) level of theory and are used to simulate the rotational band contours of the "stem" and the "top" benzene rings. Since the C-H stretch vibrations are localized in one benzene molecule and anharmonic couplings to intermolecular modes are negligible the isotopic composition of the second benzene ring should not influence the orientation and intensity of the transition dipole moments in the first benzene ring, and therefore this approximation, using the transition dipole moments of (C₆H₆)₂ instead of those of the (C₆H₆)(C₆D₆) isomers, is reasonable.

The rotational temperature in the molecular beam is estimated to be below 5 K, and therefore the rotational envelopes for the different vibrational modes are simulated for discrete temperatures ≤ 5 K. The results assuming a rotational temperature of 5 K are shown for a selection of modes in Figure 2.7. The rotational envelope of the ν_{20} fundamental mode in the "top" (see Figure 2.7 (a)) has 5 % a-type, 45 % b-type and 50 % c-type character, and in the "stem" (see Figure 2.7 (b)) 35 % a-type character and 65 % b-type character. The rotational band contour of the ν_7 fundamental mode which is only IR active in the "stem" has 60 % a-type and 40 % b-type character (see Figure 2.7 (c)).

It can be seen that the simulated rotational band contours can reproduce to some extent the width of the "top" ν_{20} spectral signature and the structure

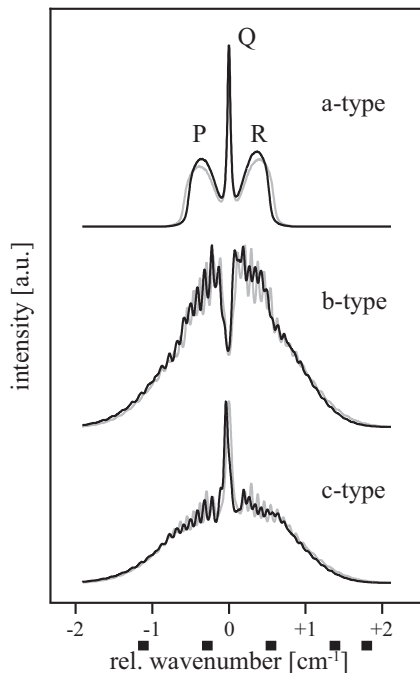


Figure 2.6: Rotational band contours of a-, b- and c-type transitions in the "stem" of the benzene dimer assuming a rotational temperature of 5 K. The contours calculated from experimental (back lines) and theoretical " C_s over bond" (gray lines) rotational constants are very similar. For the a-type transition the P-, Q- and R-branches are indicated.

of the "stem" ν_{20} spectral signature, however, that none of both is reproduced for the "stem" ν_7 absorption signal. If rotational structure was responsible for the shapes of the vibrational absorption signals it would be expected to contribute to the width and to the structure of the spectral signature for all transitions to the same extent. A consistency concerning width and shape is, however, not observed and it can be concluded that the rotational band contour at a rotational temperature of 5 K cannot be used to describe the structural features of the observed vibrational signatures.

At first glance it might appear likely that the ν_2 fundamental mode corresponds to the Q-branch of an a-type transition with the P- and R-branches being too weak to be observed. The fit of an a-type rotational envelope assuming several rotational temperatures (1-50 K) shows that the width of the Q-branch does not change significantly with the temperature, only the intensity of the P- and R-branches is changed. At any temperature the Q-branch is much narrower than the spectral signature of the ν_2 fundamental mode and can thus not be its origin.

In the following simulations, the rotational temperature is gradually reduced and the rotational envelopes are approximated by Gauss functions (see Figure 2.8). The width of the Gauss function must be large enough to adequately reproduce the most narrow spectral feature, which is the ν_2 fundamental mode in the benzene dimer "stem". As the "stem" is located in the a-b plane of the benzene dimer inertial axes system (see Figure 2.5), the shape of the vibrational modes of the "stem" can be reproduced by Gauss functions having a full width at half maximum which corresponds to

2.2 Revealing the vibrational properties of the two benzene subunits in the dimer

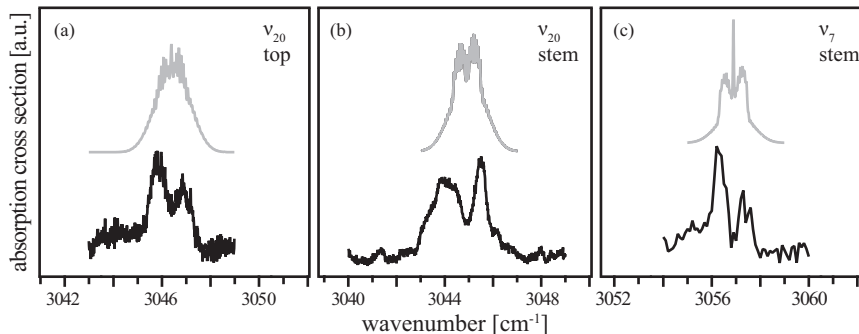


Figure 2.7: The simulated rotational band contours (gray) assuming a rotational temperature of 5 K are shown in comparison with the experimental absorption bands (black) of (a) the ν_{20} fundamental mode in the "top", (b) the ν_{20} fundamental mode in the "stem" and (c) the ν_7 fundamental mode in the "stem".

the average FWHM value of the Gaussian rotational contours for a pure a-type and a pure b-type transition. Similarly, the structure of the vibrational signatures of the "top" can be decomposed in Gaussians with an average FWHM value of a pure b-type and a pure c-type transition, and the a-type component can be neglected.

Reducing the rotational temperature to 3 K does not change the general shape of the rotational band contour and only compresses its width to about 83 % of the 5 K value (see Figure 2.9). When reducing the rotational temperature even more, to 1 K (as the lower limit for the rotational temperature), the full width at half maximum (FWHM) of the rotational band contour is substantially reduced to 50 % of the 5 K value. At 1 K the P-, Q- and R-branches

(see Figure 2.8) are strongly compressed, so that they are expected to remain unresolved in the IR spectrum. The average 1 K FWHM values are 0.67 cm^{-1}

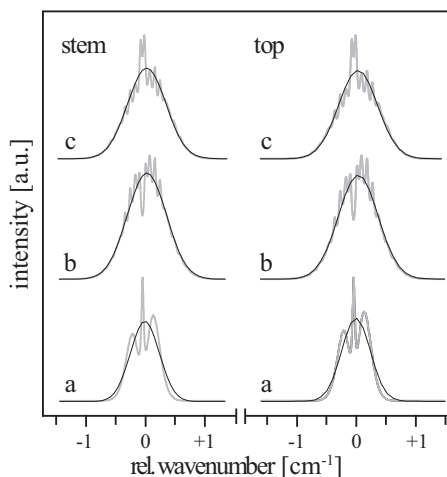


Figure 2.8: Rotational band contours (gray lines) for a-, b- and c-type transitions at 1 K rotational temperature in $(\text{C}_6\text{H}_6)^S(\text{C}_6\text{D}_6)^T$ and $(\text{C}_6\text{D}_6)^S(\text{C}_6\text{H}_6)^T$, representing those of the two subunits, the "stem" and the "top". The envelopes are fitted by Gauss functions (black lines).

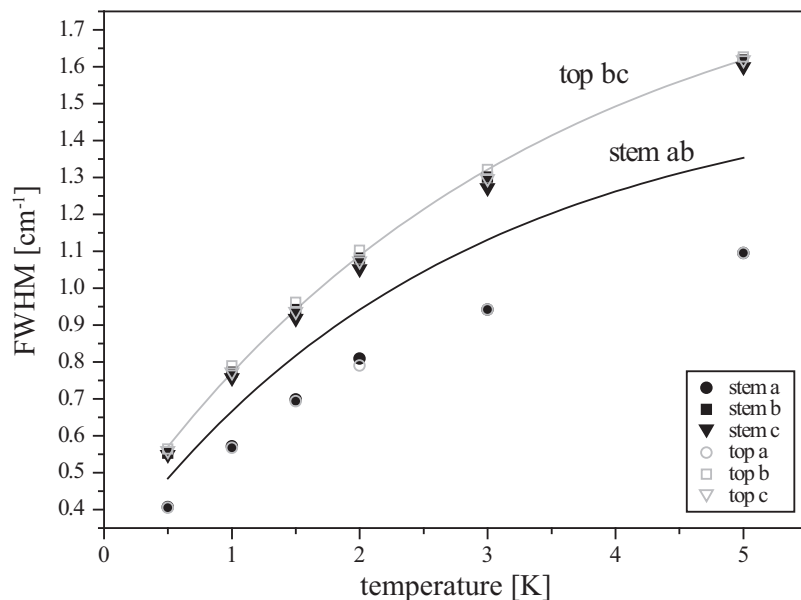


Figure 2.9: Full width at half maximum (FWHM) of the Gauss functions fitting the rotational band contours of the a-, b- and c-type transitions of the "stem" and the "top" in the benzene dimer as a function of the rotational temperature. Additionally shown are fits of the FWHM assuming exclusively contributions from a- and b-type transitions and from b- and c-type transitions for the "stem" and the "top", respectively.

and 0.77 cm^{-1} for the "stem" and the "top", respectively (see Figure 2.9). The Gauss contours with a FWHM corresponding to a rotational temperature of 1 K can be used to fit the components of the contours of the observed vibrational modes. Assuming this temperature, also the most narrow vibrational signature (ν_2 of the "stem") can be adequately reproduced.

The envelopes resulting from the ensemble of Gaussians at 1 K are shown in Figure 2.10 as solid black lines. It can be seen that the simulated contour fits the experimental shape (solid light gray line) very well. The central positions of the individual Gaussians are summarized in Table 2.4. For comparison, the envelopes resulting from Gaussians, that represent the rotational envelope at 1.5 K, are shown as dashed black lines in Figure 2.10. For this fit the same number of Gaussians is used as for the 1 K fit. It can be seen that for several vibrational modes the fit is slightly inferior to that assuming a rotational temperature of 1 K. In general, the results for 1 K and 1.5 K are similar.

In conclusion, the splittings of the vibrational signatures seem too large to be explainable by rotational contours. Instead, the rotational envelopes, obtained

2.2 Revealing the vibrational properties of the two benzene subunits in the dimer

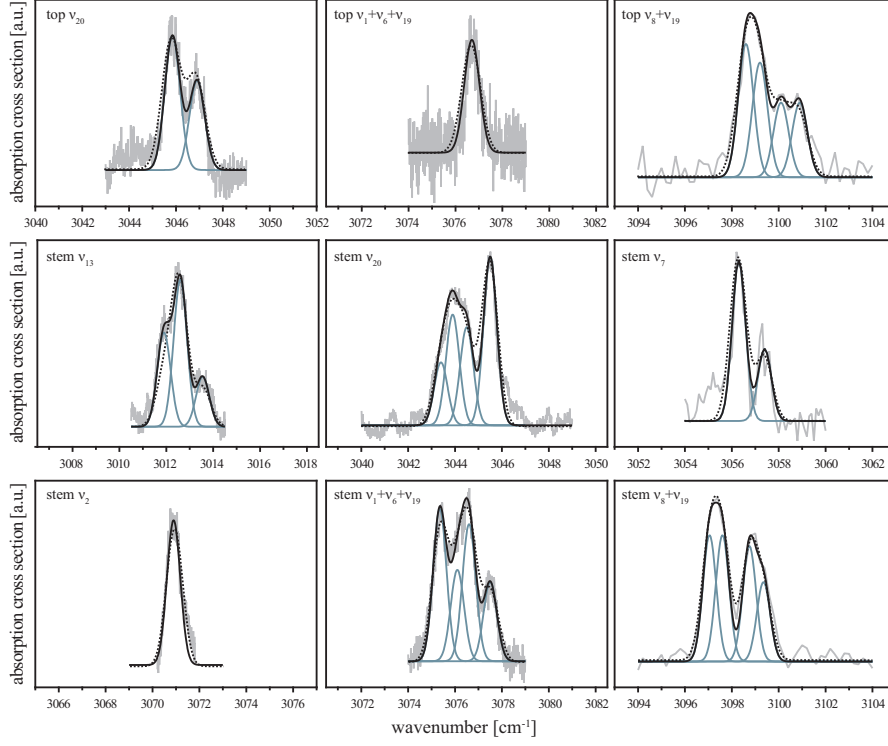


Figure 2.10: The contours of the observed fundamental modes and combination bands are reproduced by a superposition of Gaussians. Assuming a rotational temperature of 1 K, the full width at half maximum (FWHM) is 0.67 cm^{-1} for all spectral features resulting from the "stem" and 0.77 cm^{-1} for those of the "top". These values correspond to the average FWHM of the a-b-type (of $(\text{C}_6\text{H}_6)^S(\text{C}_6\text{D}_6)^T$) and b-c-type (of $(\text{C}_6\text{D}_6)^S(\text{C}_6\text{H}_6)^T$) transitions, respectively. The simulated envelope at 1 K is shown as a black line together with the Gaussians it is composed of as dark gray lines. The rotational envelope assuming a rotational temperature of 1.5 K is reproduced as well and indicated as black dashed line. The appropriate components are not shown. The experimental spectrum is shown as a light gray solid line.

vibration ^a	ν_{stem}	$\Delta\nu_{stem}^b$	ν_{top}	$\Delta\nu_{top}^b$	$\nu_{monomer}$
ν_{13}	3011.9 3012.6 3013.6		n.a. ^c		n.a. ^c
ν_{20}	3043.4 3043.9 3044.5 3045.5	-3.6	3045.9 3046.9	-1.5	3047.9
ν_7	3056.3 3057.4		n.a. ^c		n.a. ^c
ν_2	3070.9		n.o. ^d		n.a. ^c
$\nu_1 + \nu_6 + \nu_{19}^e$	3075.4 3076.1 3076.6 3077.5	-2.2	3076.7	-1.9	3078.6
$\nu_8 + \nu_{19}^f$	3097.1 3097.6 3098.8 3099.4	-3.2	3098.6 3099.2 3100.1 3100.9	-1.7	3101.4

^aWilson numbering

^bshift of the central peak position relative to the appropriate monomer value

^cnot infrared active

^dnot observed

^e $A_{1g} \times E_{2g} \times E_{1u} = B_{1u} + B_{2u} + E_{1u}$

^f $E_{2g} \times E_{1u} = B_{1u} + B_{2u} + E_{1u}$

Table 2.4: Overview of the transition energies of the components of the experimentally observed fundamental modes and combination bands in the region between 3010 and 3110 cm^{-1} for the "stem" and the "top" of the benzene dimer. Additionally, the values of the central positions of the IR active modes for the benzene monomer are given. Due to the inferior signal to noise ratio in the monomer spectra possible splittings are not mentioned. All values are given in cm^{-1} .

when assuming a rotational temperature between 1 and 2 K, can reproduce the individual components of the absorption lines fairly well. Thus, the observed structure is very likely due to vibrational properties that are discussed in terms of symmetry in the following.

Anharmonic interactions and symmetry Many anharmonic interactions between fundamental modes and other states/combination bands are allowed by symmetry in the benzene molecule in the region between 3010 and 3110 cm^{-1} . Besides the four fundamental modes and the two combination bands already presented, there are four combination bands with a B_{1u} component and six combination bands with a E_{1u} component [114]. Some of the six E_{1u} containing combination bands have a B_{2u} component too, and four of them contain also a B_{1u} component. Perturbing states of E_{2g} or A_{1g} symmetry are not known for this frequency range [114].

The ν_{13} (B_{1u}) mode (see Figure 2.4 left) interacts with two of the four B_{1u} containing perturbing states moderately strong, with the other two quite strong [114]. Additionally, the B_{1u} mode can interact with the B_{1u} component of the combination bands $\nu_1 + \nu_6 + \nu_{19}$ and $\nu_8 + \nu_{19}$. These interactions might contribute to a frequency shift of the fundamental mode ν_{13} . However, even when interacting with those perturbing states, the resulting spectral signature should not be split. In the experiment, this mode does not appear as a pure single line but as a broad feature consisting of at least three transitions. Thus, the mode itself cannot be the sole origin for the different components found. However, in this spectral region the density of states is several states/ cm^{-1} . Coupling of some of those in principle dark states to the ν_{13} fundamental mode could induce infrared activity and could cause a complex structure instead of a single line in the IR absorption spectrum.

In both subunits of the benzene dimer the doubly degenerate ν_{20} fundamental mode (E_{1u}) is split in two components, separated by 1-2 cm^{-1} , (see Figure 2.3 left). It can also be seen that the E_{1u} mode in the free benzene ring, however, appears to be a single line, or to have a relatively small splitting of a few tenths of a cm^{-1} . The E_{1u} symmetry reduces to E_1 in the "top" and to $2A'$ or $A_1 + B_1$ in the "stem", depending on whether the T-shaped structure is distorted or not (see Table 2.2). Following those arguments, the "stem" splitting can be due to symmetry reduction in the benzene dimer environment while the splitting observed for the "top" must be of different nature. The splitting in the "top" seems rather due to anharmonic coupling of the ν_{20} mode to E_{1u} components of other modes, such as the six perturbing states already mentioned and/or the combination bands $\nu_1 + \nu_6 + \nu_{19}$ and $\nu_8 + \nu_{19}$. This coupling can lead to a loss of degeneracy. In the experimental spectrum, the splittings of the components of the ν_{20} mode are very different for the "top" and "stem" molecule, supporting that the origins of the splittings are presumably of different nature. For the "stem" the width of the red component is much larger than that of the blue

component and also larger than both components of the "top" signature. This might be ascribed to coupling of the "stem" mode to in principle dark states, inducing IR activity.

The ν_7 (E_{2g}) mode (see Figure 2.4 middle), observable only for the "stem", is doubly degenerate in the monomer. However, in the reduced symmetry of the "stem" this degeneracy is lifted resulting in two components of A' or A_1 and B_1 symmetry, which can all have IR activity (see Table 2.2). In agreement with these symmetry considerations two weak lines are observed for this mode in the experimental spectrum. The ν_2 (A_{1g}) mode (see Figure 2.4 right), again only observable for the "stem", is non-degenerate and does not interact anharmonically via Fermi resonances with dark states. In agreement with that, no splitting of this mode is observed in the experimental spectrum.

The combination band $\nu_1 + \nu_6 + \nu_{19}$ (see Figure 2.3 middle) shows significant spectral differences for the "top" and the "stem" position in the benzene dimer. While in the "top" spectrum one single peak occurs, a splitting in four components is observed for the C-H-oscillators in the "stem". The different symmetry properties of the two benzene dimer subunits might be responsible for the drastic differences in the "stem" and the "top" spectra of this mode. In a D_{6h} environment (benzene monomer) this combination band has $B_{1u} + B_{2u} + E_{1u}$ symmetry, which reduces to $B_1 + B_2 + E_1$ in the C_{6v} environment of the "top" and to four non-degenerate levels of A' symmetry in the C_s environment (or of $2A_1 + 2B_1$ symmetry in the C_{2v} environment) of the "stem" (see Table 2.2). While in the "top" only the E_1 component is IR active, four non-degenerate levels are IR active for the "stem" vibration. Provided that there is no intramolecular anharmonic interaction of this combination band in the "top" with other modes, the E_1 component will remain degenerate and appear as a single line in the spectrum.

In principle, the same holds for the $\nu_8 + \nu_{19}$ combination band (see Figure 2.3 right) too, since it has the same symmetry properties. But the observed vibrational signature is completely different from that of $\nu_1 + \nu_6 + \nu_{19}$. The combination band $\nu_8 + \nu_{19}$ is split in two components for the "stem" and the "top". Such a large splitting (about 1.7 cm^{-1}) cannot be observed for the benzene monomer. For this mode, anharmonic interactions of different strengths within the "top" moiety to one or several states of E_{1u} symmetry mentioned above could (partially) lift the degeneracy. The four components of the "stem" moiety might be only partially resolved (see Figure 2.10).

2.2.4 Conclusion

The vibrational properties of the two subunits of the benzene dimer are measured separately in the C-H stretching region, and the differences concerning number, frequency and structure of the observed modes are discussed. Absence and presence of vibrational modes are due to the symmetry properties, and the frequency shifts can be explained by hydrogen bonding. It is shown that the

2.2 Revealing the vibrational properties of the two benzene subunits in the dimer

observed vibrational structure cannot be ascribed to rotational band contours, but rather to anharmonic coupling within and to the symmetry properties of the individual subunits. The spectra are consistent with a model in which the two benzene rings are arranged in a T-shaped geometry, having one ring in a "stem" position and one in a freely (about its C_6 axis) rotating "top" position. That is, two structures are supported by these experimental results: structures, that are in their rigid forms of C_s or C_{2v} symmetry and in their dynamic forms both of C_{6v} symmetry.

Chapter 3

Microwave spectroscopy of the benzene dimer

3.1 Introduction

The rotational transitions for most molecules and clusters occur in the frequency range of microwaves, and high resolution microwave (MW) spectroscopy is ideally suited to investigate their equilibrium/minimum energy structures. However, also other aspects such as internal dynamics, charge distribution (dipole moment) and polarizability can be addressed.

The benzene dimer is a very floppy system with a relatively flat potential energy surface, and so far the quantitative structural information available from experiments has been insufficient to solve the conflict of the two qualitatively different equilibrium structures predicted by theory.

Microwave spectroscopy applied to the benzene dimer provides valuable information about its dynamics and structure. This information can be deduced from splitting patterns of rotational energy levels and from the relative intensities of their components. Additional information can be obtained via experiments on isotopically labeled systems. Substitution of one benzene ring by a completely deuterated isotopologue, for example, changes the nuclear spin statistics and the rotational constants. Thus the transition frequencies, the splittings of the rotational transitions as well as the (relative) intensities can be different. The tunneling pattern, i.e. the number of torsional energy levels, of a selected transition is expected to be maintained upon full deuteration. However, the width of the splitting can be considerably changed, so that the splitting structure appears at first glance to be completely different. Experiments on several isotopologues therefore allow one to refine an interpretation step by step and also to prove its consistency. However, due to the need of a permanent

electric dipole moment possible non-polar benzene dimer structures cannot be investigated (see Figure 1.11).

Tunneling pathways that are associated with a specific molecular symmetry can be investigated by Molecular Symmetry (MS) group theory. Such studies provide the relative energies and nuclear spin statistical weights of the components of a tunneling rotational energy level. The energies in rotational spectra correspond to transitions between rotational states and not to the absolute energy levels treated by theory. However, splittings within one rotational state and the spin statistical weights of the components can be compared to the experimental observations, allowing for the exploration of feasible tunneling processes and their barriers.

In 1993, the first rotational spectrum of the completely protonated benzene dimer (C_6H_6)₂ has been measured in the range from 2.5 to 6 MHz. It has been found to be strongly congested which was tentatively interpreted as to result from several dynamic states as well as from low frequency tunneling [57]. Among many transitions, 22 with a quartet structure have been observed and assigned to $J + 1, K \leftarrow J, K$ transitions. The observed quartets show a systematic 1 : 2 : 1 splitting which has tentatively been ascribed to two different tunneling pathways, such as two opposed interconversion pathways. The authors have assumed a C_{2v} T-shaped benzene dimer structure with different moments along the three principal axes of inertia. However the transitions in the spectrum have been fitted to a symmetric top Hamiltonian. This disagreement has been explained by the almost unhindered internal rotation of both benzene rings about the molecular A axis (see Figure 2.5). As a second explanation the authors have proposed that the benzene dimer is in a vibrationally excited state, as addition of a fraction of argon to the carrier gas appears to reduce the signal of the symmetric top species, probably indicating a more efficient relaxation from the vibrationally excited state.

Nonetheless, several important questions are still not fully answered. (1) What is the origin of the observed quartet structure? (2) Is the symmetric top behavior due to an excited state, and if so, which state is it? If not, how can a ground state symmetric top spectrum be explained? (3) What is the origin of the additional lines that have not been assigned?

In the following chapter microwave experiments on (C_6H_6)₂ and its partially deuterated analogues, addressing these questions, are presented and discussed together with MS group theoretical considerations.

3.1.1 Experimental method

The rotational spectra are measured in the COBRA setup, described in section 1.2.2.

The benzene dimer has a comparatively small electric dipole moment and the spectral features are expected to be weak. Therefore an elevated concentration of benzene dimer complexes in the microwave cavity is required and the gas

mixture used for the IR and UV experiments (0.03 % benzene in a carrier gas) is not suitable. Instead, the carrier gas (helium, neon or argon) is passed through a reservoir containing liquid benzene, which is cooled down to -15°C . Pure C_6H_6 or a 1:1 mixture of C_6H_6 and C_6D_6 are used to investigate isotopically pure or mixed benzene dimer complexes. Depending on the isotopic composition, the backing pressure of the rare gas is adjusted to obtain optimal experimental conditions.

From several experiments [55, 57, 76] (see also chapter 2) a benzene dimer structure with two symmetrically inequivalent subunits is deduced that do not interchange on the experimental time scale. Therefore, for an isotopically mixed benzene dimer two isomers exist. This is described in detail in section 1.5.3 and 2.1. Briefly, in $(\text{C}_6\text{H}_6)(\text{C}_6\text{D}_6)$ the two subunits, the "stem" and the "top", differ in isotopic composition and the two substitution isomers are: $(\text{C}_6\text{H}_6)^S(\text{C}_6\text{D}_6)^T$ and $(\text{C}_6\text{D}_6)^S(\text{C}_6\text{H}_6)^T$, where S symbolizes the "stem" and T denotes the "top". Since the experimental setup has no mass selective detection, the rotational transitions of four different dimer isotopologues ($(\text{C}_6\text{H}_6)_2$, $(\text{C}_6\text{D}_6)_2$, $(\text{C}_6\text{H}_6)^S(\text{C}_6\text{D}_6)^T$ and $(\text{C}_6\text{D}_6)^S(\text{C}_6\text{H}_6)^T$) can in principle be observed at the same time, complicating significantly the analysis of the rotational spectrum. To simplify the the interpretation of the spectra the experiment is conducted as follows. In $(\text{C}_6\text{D}_6)_2$, the quadrupole coupling of the 12 deuterons with a nuclear spin $I = 1$ contributes significantly to the spectral shape of the rotational transitions. Therefore, the $(\text{C}_6\text{D}_6)_2$ transitions are expected, compared to those of $(\text{C}_6\text{H}_6)_2$, to be broadened and hard to observe in the rotational spectrum. In section 4.2 it is shown that the relative abundance of the two isomers of $(\text{C}_6\text{H}_6)(\text{C}_6\text{D}_6)$ in a molecular beam can be controlled by the choice of the carrier gas [109]. When using neon as a carrier gas $(\text{C}_6\text{H}_6)(\text{C}_6\text{D}_6)$ is exclusively present as the $(\text{C}_6\text{H}_6)^S(\text{C}_6\text{D}_6)^T$ isomer in the molecular beam, whereas in helium $(\text{C}_6\text{H}_6)^S(\text{C}_6\text{D}_6)^T$ and $(\text{C}_6\text{D}_6)^S(\text{C}_6\text{H}_6)^T$ co-exist. Thus, using neon as a carrier gas only $(\text{C}_6\text{H}_6)^S(\text{C}_6\text{D}_6)^T$ and $(\text{C}_6\text{H}_6)_2$ will contribute to the spectral features. $(\text{C}_6\text{H}_6)_2$ can be investigated independently prior to the experiment on the isotopic mixture. Consequently, additional transitions, compared to the $(\text{C}_6\text{H}_6)_2$ spectrum, originate solely from $(\text{C}_6\text{H}_6)^S(\text{C}_6\text{D}_6)^T$. Once the spectral signatures of $(\text{C}_6\text{H}_6)_2$ and $(\text{C}_6\text{H}_6)^S(\text{C}_6\text{D}_6)^T$ are known helium can be used as an expansion gas allowing one to investigate $(\text{C}_6\text{D}_6)^S(\text{C}_6\text{H}_6)^T$ as well. Note however, that the experiment is not mass selective and is performed with a molecular beam, that has, compared to the UV and IR-UV double resonance experiments presented in the previous chapters, a much higher concentration of benzene. The presence of benzene trimers and higher clusters can therefore not be excluded.

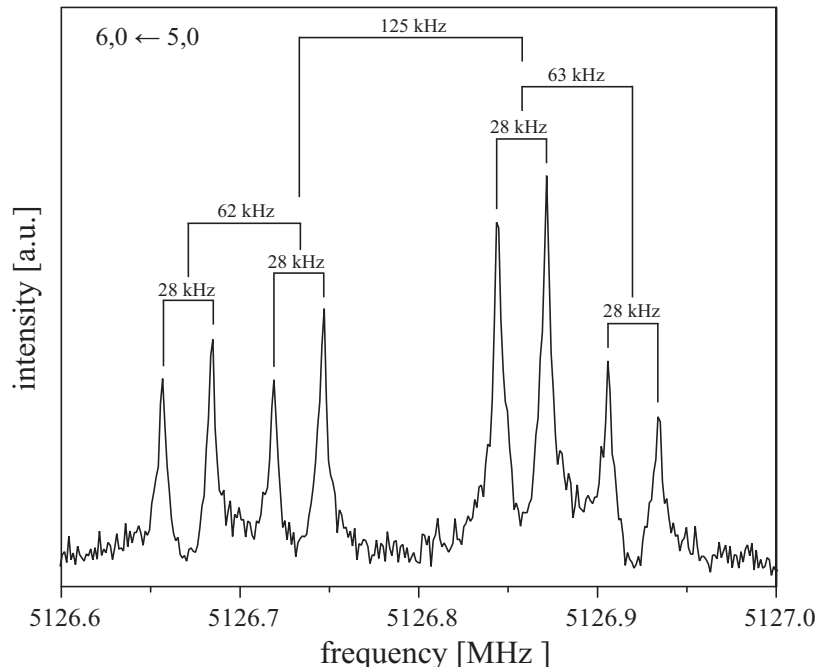


Figure 3.1: Typical symmetric top transition of $(\text{C}_6\text{H}_6)_2$ measured with neon as carrier gas. As an example the $J', K' \leftarrow J, K$: $6, 0 \leftarrow 5, 0$ transition is shown.

3.2 Experimental results

3.2.1 $(\text{C}_6\text{H}_6)_2$

The rotational spectrum of gas phase $(\text{C}_6\text{H}_6)_2$ is entirely measured in the range between 3000 and 6000 MHz and partially measured up to 9000 MHz. For the molecular beam neon is used as a carrier gas. Due to the coaxial propagation of the molecular beam and the microwave field a Doppler splitting is observed for all transitions. This splitting depends on the velocity v of the molecular beam (its terminal velocity after the supersonic expansion is almost exclusively determined by the nature of the carrier gas) and on the frequency ν of the emitted microwave radiation. The Doppler splitting can be approximated by

$$\nu^\pm \cong \nu \left(1 \pm \frac{v}{c} \right). \quad (3.1)$$

The transition frequencies mentioned in this chapter correspond always to the arithmetic mean of the respective components of a Doppler doublet.

In the probed energy range many transitions of comparatively low intensity are found. The low intensity results from the small dipole moment of the benzene

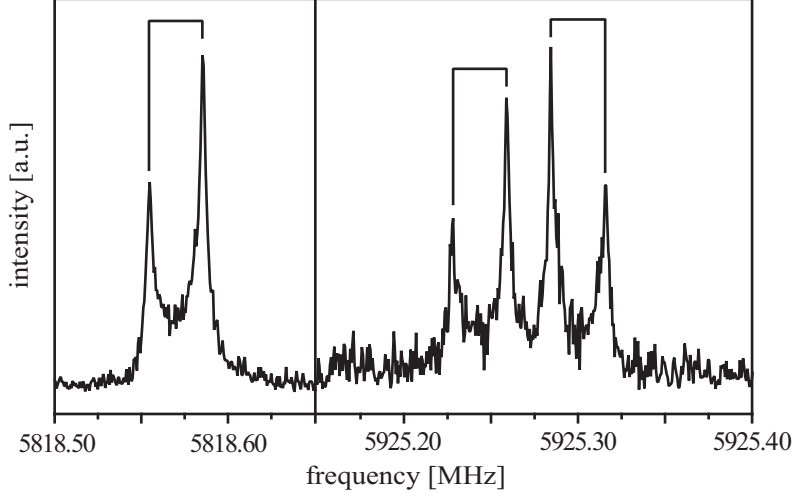


Figure 3.2: Rotational transitions that do not contribute to the symmetric top spectrum of $(\text{C}_6\text{H}_6)_2$. Possibly these transitions result from larger C_6H_6 clusters.

dimer and from a possibly low concentration of $(\text{C}_6\text{H}_6)_2$ in the molecular beam. Additionally, the low rotational constants allow for the simultaneous population of many rotational levels even at low rotational temperatures. Some of the observed transitions are striking due to their similar spectral signature: a quartet splitting with a regular 1 : 2 : 1 spacing between the four components (see Figure 3.1). Additionally, singlet and doublet structures are observed in the rotational spectrum (see Figure 3.2).

Symmetric top spectrum

The moments of inertia along the three principal axes of the (distorted) T-shaped structure are expected to behave according to $I_a < I_b \leq I_c$ (see Figure 2.5). Most of the observed quartets can be attributed to rotational transitions of the type $J+1, K \leftarrow J, K$ and fitted as symmetric top transitions. The rotational energy levels of a prolate symmetric top are given by

$$E(J, K) = BJ(J+1) + (A-B)K^2 - D_J J^2(J+1)^2 - D_{JK} J(J+1)K^2 - D_K K^4 \quad (3.2)$$

with the rotational quantum number J , the projection quantum number K , the rotational constants B and A and the quartic centrifugal distortion constants D_J , D_{JK} and D_K . This expression can be refined by adding sextic centrifugal distortion terms

$$+ H_J J^3(J+1)^3 + H_{JK} J^2(J+1)^2 K^2 + H_{KJ} J(J+1) K^4 + H_K K^6. \quad (3.3)$$

For a $J + 1, K \leftarrow J, K$ transition the transition frequency is then

$$\nu(J, K) = 2B(J + 1) - 4D_J(J + 1)^3 - 2D_{JK}(J + 1)K^2 + 2H_J(J + 1)^3 \\ (3J^2 + 6J + 4) + 4H_{JK}(J + 1)^3K^2 + 2H_{KJ}(J + 1)K^4. \quad (3.4)$$

The quartet components are treated independently according to equation 3.4 to determine the effective rotational parameters as equation 3.4 is strictly valid only for components of A symmetry. The fit of the rotational parameters, including the sextic centrifugal distortion terms, is based on the transitions with $K = 0$ and 1 (see Table 3.1), as in a prolate symmetric top the energy levels increase with increasing K (see equation 3.2), and energy levels with higher K values might come close to the tunneling barrier. In this case perturbations play an increasingly important role and eventually become too difficult to be modeled with a semi-rigid rotor Hamiltonian approach (see equation 3.4 plus higher terms). The rotational parameters are shown in Table 3.2. It can be seen that the fitted transition frequencies of line 1, i.e. of the quartet component with the lowest transition energy, deviate from the experimental value by 1-2 kHz which corresponds to the experimental error bar. For all other components the deviation is much larger, strongly indicating that the low transition energy component is most likely the one of A symmetry. The residuals for the experimental frequencies (also for transitions with $K > 1$) are shown in Table 3.1. It can be seen that for transitions with $K > 1$ the deviation between experimental and fitted values amounts to several 100 kHz, justifying that the fit has been limited to transitions with $K = 0$ and 1.

Intensity pattern

The relative intensities of the components of a rotational transition can give valuable information about the nuclear spin statistical weights. These in turn depend on the tunneling processes and the respective symmetries of a given molecular system. However, since the molecules are polarized by a microwave pulse of a certain linewidth the measured intensities represent the convolution of the Gauss shaped microwave intensity distribution and the real intensity pattern, and they are as such difficult to interpret (see Figure 3.3). Therefore, to measure their relative intensities, all components of a particular transition are measured separately by polarizing the molecular beam with a microwave pulse of the respective frequencies.

The measurements are performed twice with two different microwave intensities to ensure that none of the four components is overpolarized giving wrong relative intensities. Due to technical properties there are small gaps in the frequency range of the spectrometer and some transitions (e.g. $6, 0 \leftarrow 5, 0$ and $6, 1 \leftarrow 5, 1$) cannot be polarized at their central frequency. Therefore the quartet intensity pattern of those transitions are not accessible. Based on the measurements of the transitions $J', K' \leftarrow J, K = 5, 0 \leftarrow 4, 0$, $5, 1 \leftarrow 4, 1$, $7, 0 \leftarrow 6, 0$ and $7, 1 \leftarrow 6, 1$ the relative intensities are obtained:

transition $J', K' \leftarrow J, K$	components [MHz]				residual [kHz]			
	I	II	III	IV	I	II	III	IV
4, 1 \leftarrow 3, 1	3413.60359	3413.64757	3413.73369	3413.77779	0.92968	1.81240	2.15512	-0.50488
5, 0 \leftarrow 4, 0	4273.77542	4273.82724	4273.93072	4273.98150	1.19000	0.56000	-0.73000	-2.51000
5, 1 \leftarrow 4, 1	4265.92613	4265.98056	4266.08941	4266.14408	-0.52000	1.24000	0.58000	-4.09000
5, 2 \leftarrow 4, 2	4242.25713	4242.31927	4242.44349	4242.50611	115.48000	124.53000	126.50000	116.88000
5, 3 \leftarrow 4, 3	4206.11847	4206.18977	4206.33144	4206.40165	-3000.86000	-2975.97000	-2961.45000	-2973.66000
6, 0 \leftarrow 5, 0	5126.67015	5126.73187	5126.85702	5126.92008	2.02872	1.97960	-0.29952	-4.55952
6, 1 \leftarrow 5, 1	5117.52176	5117.58705	5117.71741	5117.78223	-1.50128	0.87960	0.59048	-6.86952
6, 2 \leftarrow 5, 2	5090.09191	5090.16522	5090.31196	5090.38532	-27.41128	-15.05040	-10.11952	-30.43952
7, 0 \leftarrow 6, 0	5978.53872	5978.61238	5978.75914	5978.83346	4.00232	2.75760	-0.18712	-5.90712
7, 1 \leftarrow 6, 1	5968.23788	5968.31392	5968.46615	5968.54257	-1.11768	2.25760	2.24288	-10.89712
7, 2 \leftarrow 6, 2	5937.53987	5937.62386	5937.79242	5937.87591	-220.98768	-204.56240	-195.70712	-231.87712
8, 1 \leftarrow 7, 1	6817.91935	6818.00629	6818.17890	6818.26587	0.56808	5.20440	7.37072	-12.07928
9, 1 \leftarrow 8, 1	7666.40834	7666.50547	7666.70092	7666.79855	2.10088	9.32840	11.83592	-15.95408
9, 2 \leftarrow 8, 2	7630.85305	7630.95793	7631.16467	7631.26881	-669.04912	-642.57160	-618.95408	-708.33408
10, 1 \leftarrow 9, 1	8513.54329	8513.65212	8513.87008	8513.97795	1.09000	10.28000	14.34000	-23.53000
10, 2 \leftarrow 9, 2	8476.47523	8476.58922	8476.81380	8476.92729	-856.85000	-822.82000	-789.38000	-916.87000

Table 3.1: Frequencies of the rotational transitions observed for a symmetric top benzene dimer $(C_6H_6)_2$ and the residuals to the fitted symmetric top frequencies.

parameter	line 1	line 2	line 3	line 4
B [MHz]	427.7277	427.7328	427.7430	427.7479
	± 0.0002	± 0.0003	± 0.0003	± 0.0003
D_J [kHz]	6.970	6.970	6.970	6.970
	± 0.003	± 0.004	± 0.005	± 0.004
Σ^a [MHz]	0.8361	0.8356	0.8350	0.8344
	± 0.0003	± 0.0003	± 0.0004	± 0.0003
H_J [Hz]	-0.81	-0.80	-0.79	-0.79
	± 0.02	± 0.02	± 0.02	± 0.02
H_{JK} [kHz]	1.020	1.020	1.020	1.010
	± 0.003	± 0.003	± 0.004	± 0.004
rms [kHz]	1.79	4.92	6.41	10.95

^a Σ corresponds to $D_{JK} - H_{KJ}$

Table 3.2: Rotational constant B and centrifugal distortion parameters for each component of the $(\text{C}_6\text{H}_6)_2$ quartet structure, fitted using all observed transitions with $K = 0$ and 1 (see Table 3.1) according to equation 3.4. The four lines are numbered with increasing frequency as observed in the microwave spectrum. In the last line, the root mean square deviation of the fitted values from the experimental value for all considered transitions with $K = 0$ and 1 is given. The terms $-2D_{JK}(J+1)K^2$ and $+2H_{KJ}(J+1)K^4$ in equation 3.4 are equivalent if only transitions with $K = 0$ and 1 are considered. Therefore, the sum of both terms is fitted and parameterized with Σ .

$$3.02^{+0.17}_{-0.17} : 1.96^{+0.20}_{-0.20} : 1.95^{+0.07}_{-0.13} : 1.00.$$

It should be particularly noted that transitions with even and odd K values have the same relative intensity pattern.

3.2.2 $(\text{C}_6\text{H}_6)(\text{C}_6\text{D}_6)$

Additionally to $(\text{C}_6\text{H}_6)_2$ the two isotopically mixed isomers $(\text{C}_6\text{H}_6)^S(\text{C}_6\text{D}_6)^T$ and $(\text{C}_6\text{D}_6)^S(\text{C}_6\text{H}_6)^T$ are interesting to investigate, as the separation between the individual tunneling components of a rotational transition changes upon isotopic labeling and can thus also provide valuable information about the tunneling mechanism. Provided that in the benzene dimer the observed quartet splitting can be referred to a single tunneling process localized in one benzene ring, the spacing between the four components should depend on whether that benzene ring is deuterated or not. As the splitting is exponentially inversely proportional to the mass of the tunneling moiety the width of the splitting is expected to decrease with $(\text{C}_6\text{H}_6)_2 > (\text{C}_6\text{H}_6)^S(\text{C}_6\text{D}_6)^T > (\text{C}_6\text{D}_6)^S(\text{C}_6\text{H}_6)^T$ if the corresponding tunneling is located in the "stem", and with $(\text{C}_6\text{H}_6)_2 > (\text{C}_6\text{D}_6)^S(\text{C}_6\text{H}_6)^T > (\text{C}_6\text{H}_6)^S(\text{C}_6\text{D}_6)^T$ if the "top" is involved.

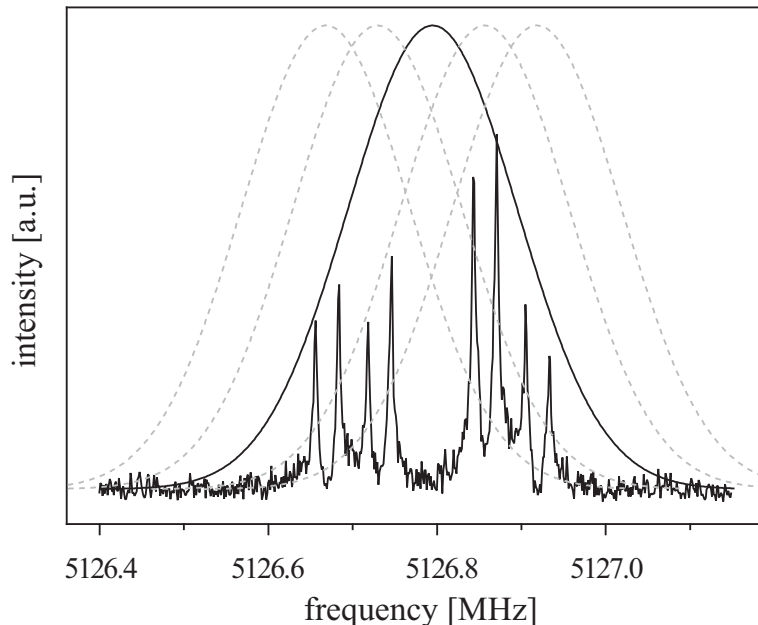
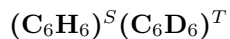


Figure 3.3: The Gaussian microwave intensity distribution creates a distorted relative intensity pattern. The real relative intensities can be obtained by separate measurements, indicated by the dashed lined Gaussian functions, for each component.



In Figure 3.4 the $7, 2 \leftarrow 6, 2$ rotational transition of $(\text{C}_6\text{H}_6)^S(\text{C}_6\text{D}_6)^T$, measured with neon as a carrier gas, is shown. Compared to the same transition in $(\text{C}_6\text{H}_6)_2$ (see Figure 3.4 left) the intensity is reduced and the peaks are significantly broadened. This drastic difference results from the quadrupole coupling of the six deuterons in the "top" benzene ring of $(\text{C}_6\text{H}_6)^S(\text{C}_6\text{D}_6)^T$.

Similarly to $(\text{C}_6\text{H}_6)_2$, mainly quartet patterns are observed in the spectrum of $(\text{C}_6\text{H}_6)^S(\text{C}_6\text{D}_6)^T$, besides some unresolved spectral structures. The four components are split in a ratio 1 : 2 : 1 as well. However, compared to $(\text{C}_6\text{H}_6)_2$, the deviation is in some cases relatively high ($\pm 10\%$) which can be ascribed to the increased density of spectral lines and to the only partly resolved hyperfine structure. This leads to a lower precision in determining the peak frequencies of the individual components. The transitions with a resolved quartet structure are listed in Table 3.3.

Most of the transitions found can be assigned to $J+1, K \leftarrow J, K$ transitions and can be fitted to a symmetric top Hamiltonian. Due to the broadened quartet components and increased uncertainty, the central quartet frequencies

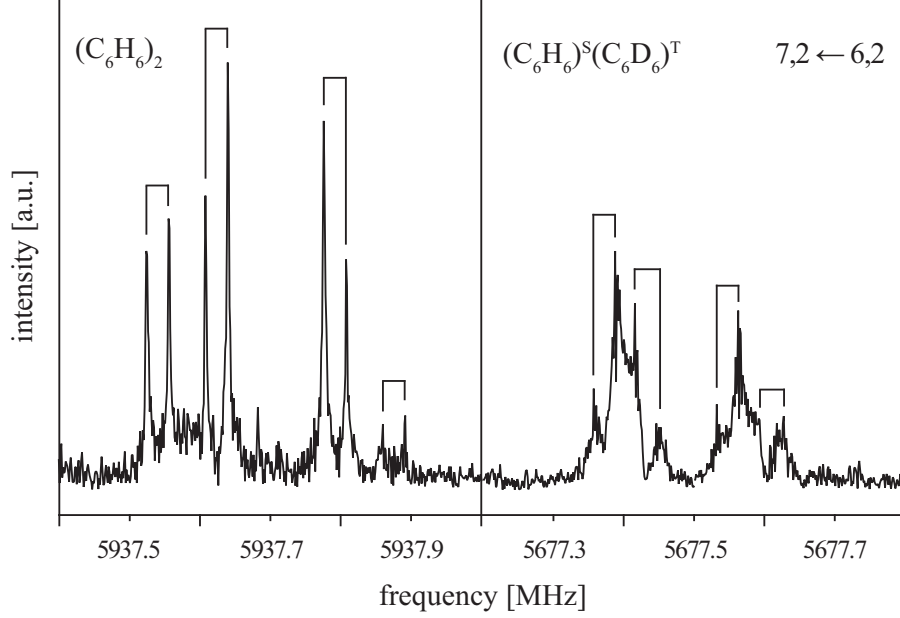


Figure 3.4: The rotational transition $J', K' \leftarrow J, K = 7, 2 \leftarrow 6, 2$ of $(\text{C}_6\text{H}_6)^S(\text{C}_6\text{D}_6)^T$ measured with neon as a carrier gas is shown in the right panel. For comparison, the same transition is shown on the left for $(\text{C}_6\text{H}_6)_2$.

are taken to fit the rotational parameters, using equation 3.4. However, as a higher precision is, considering the experimentally given precision, not justified, the fit parameters are limited to the rotational constant B and the quartic centrifugal distortion terms. The sextic centrifugal distortion constants are those fitted for the central frequencies of the $(\text{C}_6\text{H}_6)_2$ transitions: $H_J = -0.80 \pm 0.02$ Hz and $H_{JK} = 1.020 \pm 0.004$ kHz. The fit is again based on transitions with $K = 0$ and 1 (see section 3.2.1). The best fit values of the parameters are $B = 409.0090 \pm 0.0001$ MHz, $D_J = 5.850 \pm 0.001$ kHz and $D_{JK} - H_{KJ} = 0.8264 \pm 0.0001$ MHz, giving a rms deviation for the central frequencies of the transitions with $K = 0$ and 1 of 2.78 kHz. In Table 3.3 the residuals of the resulting central transition frequencies and the experimental values are shown, also for transitions with $K > 1$. Again it can be seen, that the fitted frequencies of the transitions with $K = 2$ deviate considerably from the experimental values.

The fitted parameters allow one to identify additional transitions that originate from the same symmetric rotor. However, they are not listed in Table 3.3 as they are only partially resolved.

Comparing the rotational transitions assigned to $J + 1, K \leftarrow J, K$ of $(\text{C}_6\text{H}_6)^S(\text{C}_6\text{D}_6)^T$ to the respective ones of $(\text{C}_6\text{H}_6)_2$ shows that the absolute

transition $J', K' \leftarrow J, K$	line center ^a [MHz]	components [MHz]			residual ^b [kHz]
		I	II	III	IV
5, 0 \leftarrow 4, 0	4087.14801	4087.08970	4087.11924	4087.17769	4087.20539
5, 1 \leftarrow 4, 1	4079.39557	4079.32812	4079.36043	4079.43088	4079.46283
6, 2 \leftarrow 5, 2	4866.85210	4866.75013	4866.80221	4866.90334	4866.95272
7, 0 \leftarrow 6, 0	5718.01822	5717.91933	5717.97013	5718.06623	5718.11717
7, 1 \leftarrow 6, 1	5707.84679	5707.74375	5707.79535	5707.89845	5707.94959
7, 2 \leftarrow 6, 2	5677.48926	5677.37197	5677.43036	5677.54695	5677.60775
8, 1 \leftarrow 7, 1	6520.86695	6520.74877	6520.80818	6520.92494	6520.98590
9, 1 \leftarrow 8, 1	7332.91367	7332.77393	7332.85256	7332.97448	7333.05370

^athe frequencies of the four components are averaged to give the line center

^bresidue between the experimental line center and the fitted frequencies

Table 3.3: Frequencies of the observed rotational transitions of $(C_6H_6)^S(C_6D_6)^T$, that can be assigned to $J + 1, K \leftarrow J, K$ transitions, as well as the residuals of the central frequencies to the fitted symmetric top line center.

widths of the $(\text{C}_6\text{H}_6)^S(\text{C}_6\text{D}_6)^T$ quartet splittings are about 60-70 % of the widths of the $(\text{C}_6\text{H}_6)_2$ splittings.

The intensity pattern of the quartet splitting of the $(\text{C}_6\text{H}_6)^S(\text{C}_6\text{D}_6)^T$ transitions is not determined due to the weak and broad signals and the associated low signal to noise ratio.

$(\text{C}_6\text{D}_6)^S(\text{C}_6\text{H}_6)^T$

Using helium as a carrier gas should in principle allow one to investigate the second mixed benzene dimer $(\text{C}_6\text{D}_6)^S(\text{C}_6\text{H}_6)^T$. However, it is difficult to positively identify $(\text{C}_6\text{D}_6)^S(\text{C}_6\text{H}_6)^T$ in the microwave spectrum. Impurities in the carrier gas, such as water, can collisionally isomerize $(\text{C}_6\text{D}_6)^S(\text{C}_6\text{H}_6)^T$ to $(\text{C}_6\text{H}_6)^S(\text{C}_6\text{D}_6)^T$. To lower the isomerization rate, the formation of transient benzene complexes with high binding energies has to be avoided (see section 4.2). Therefore the carrier gas can for example be additionally dehydrated to optimize the experimental conditions for $(\text{C}_6\text{D}_6)^S(\text{C}_6\text{H}_6)^T$.

A few transitions are found which might originate from this conformer, but an unambiguous assignment appears presently not possible. An additional complication is that the rotational constants of $(\text{C}_6\text{H}_6)^S(\text{C}_6\text{D}_6)^T$ and $(\text{C}_6\text{D}_6)^S(\text{C}_6\text{H}_6)^T$ in a (distorted) T-shaped geometry are expected to be very similar leading most probably to even overlapping rotational transitions. At present a comparative study of the 1 : 2 : 1 splittings of $(\text{C}_6\text{H}_6)_2$, $(\text{C}_6\text{H}_6)^S(\text{C}_6\text{D}_6)^T$ and $(\text{C}_6\text{D}_6)^S(\text{C}_6\text{H}_6)^T$ is therefore not possible.

3.2.3 Stark effect measurements

When molecules with a permanent electric dipole moment μ are subject to an external electric field their rotational energy levels experience Stark shifts and/or splittings. The extent of the shift and the splitting is experimentally measurable and correlates with the molecular electric dipole moment. Stark effect measurements can thus be used to determine electric dipole moments. In this work, microwave spectra are therefore also recorded in the presence of an electric field whose strength is precisely determined using the calibration function from Reference [129].

Stark effect measurements are performed on selected transitions $(J', K' \leftarrow J, K = 5, 0 \leftarrow 4, 0; 5, 1 \leftarrow 4, 1; 7, 0 \leftarrow 6, 0; 7, 1 \leftarrow 6, 1; 9, 1 \leftarrow 8, 1)$ of $(\text{C}_6\text{H}_6)_2$. For energy levels with $K = 1$ the linear Stark effect is predominant, and levels with $K = 0$ have a pure quadratic Stark effect (see equations 1.16 and 1.17).

Transitions affected by a linear Stark effect shift significantly in frequency, even in the presence of a weak electric field (< 1 V/cm), and in the case of $(\text{C}_6\text{H}_6)_2$, the resulting spectrum becomes very complicated. An additional complication is that weak electric fields cannot be adjusted with sufficient precision due to the absolute resolution of the HV power supply serving as voltage source in the experimental setup. This makes it very difficult to

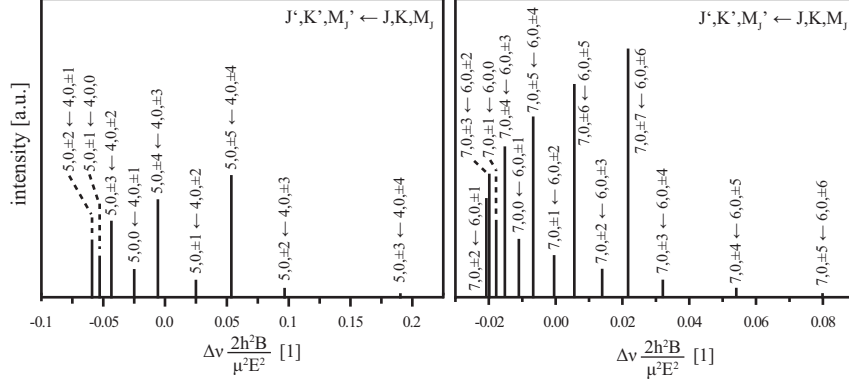


Figure 3.5: Expected Stark patterns of the torsional components of the transitions $5,0 \leftarrow 4,0$ and $7,0 \leftarrow 6,0$ at a given electric field strength. ν is the transition frequency shift, B the rotational constant, μ the dipole moment and E the electric field strength. $\frac{\Delta\nu 2h^2 B}{\mu^2 E^2}$ corresponds to α_i and the intensity to f_i (see text). The unperturbed transition is located at 0.

assign the linearly Stark shifted lines at all field strengths. Measuring the quadratic Stark effect has an advantage over measuring the linear Stark effect: A state $J, K \neq 0$ with a linear Stark effect is split in $2J + 1$ levels with $M_J = -J, (-J + 1) \dots (J - 1), J$, whereas a state $J, K = 0$ with a quadratic Stark effect splits only in $J + 1$ levels with $M_J = \pm J, \pm(J - 1), \dots, \pm 1, 0$ (see Figure 1.7 and equations 1.16 and 1.17). Thus, the spectrum is expected to be considerably simpler for $J + 1, K = 0 \leftarrow J, K = 0$ transitions. Therefore, in this study transitions with $K = 1$ are not considered to estimate the electric dipole moment of $(C_6H_6)_2$, but exclusively those with $K = 0$.

In Figure 3.5 the theoretically expected Stark patterns of the transitions $5,0 \leftarrow 4,0$ and $7,0 \leftarrow 6,0$ are shown. The components of the split transitions are shown relative to the unperturbed transition for a given electric field strength. The absolute splittings of the M_J components depend on the strength of the electric field, on the rotational constant B and on the molecular dipole moment. The relative positions are calculated with equation 1.21 and the relative intensities for transitions with $\Delta J = +1$ and $\Delta M_J = +1$ according to

$$f_i = (J' + M' - 1)(J' + M') \quad (3.5)$$

and with $\Delta J = +1$ and $\Delta M_J = -1$ according to

$$f_i = (J' - M')(J' - M' + 1) \quad (3.6)$$

with J' and M' being always the larger (more positive) values for a chosen transition $J', K, M_J' \leftarrow J, K, M_J$.

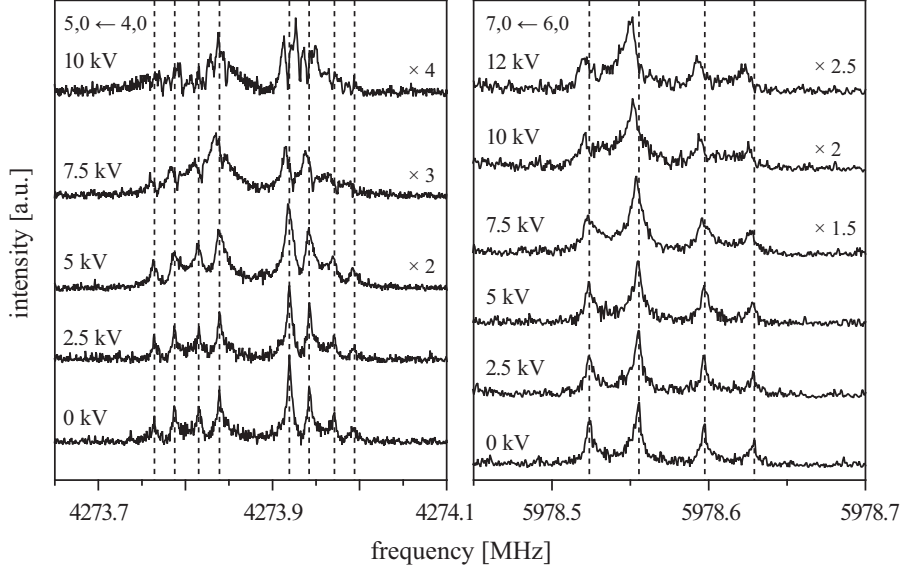


Figure 3.6: The $5,0 \leftarrow 4,0$ transition (left) and two of the four components of the $7,0 \leftarrow 6,0$ transition (right) measured in the presence of an external electric field with various field strengths. Each component is split by the Doppler effect. For comparison the spectra without electric field are shown. The given voltages (applied to the rear parabolic mirror (see Figure 1.4)) correlate with the electric field strength according to U/d with $d_{5,0 \leftarrow 4,0} = 0.59644$ m and $d_{7,0 \leftarrow 6,0} = 0.58746$ m, respectively.

In Figure 3.6 measurements of the rotational transitions $5,0 \leftarrow 4,0$ and $7,0 \leftarrow 6,0$ are shown for different electric field strengths. It can be seen that at low electric fields the torsional components are almost not shifted, and the splitting is too small to be observable. At higher electric fields a slight shift is observed, and possible splitting components cannot be determined precisely as the signal to noise ratio is reduced. Therefore, an assignment of the M_J components is not possible for the transitions $5,0 \leftarrow 4,0$ and $7,0 \leftarrow 6,0$.

Instead a value α is determined that corresponds to the average frequency shift (from the position of the unperturbed transition) of all possible transitions between two defined rotational levels $J', 0, M'_J \leftarrow J, 0, M_J$, where all possible transitions are weighted by their relative intensities f_i

$$\alpha = \frac{1}{i} \sum_i f_i \alpha_i \quad (3.7)$$

	U[kV]	line 1	line 2	line 3	line 4
5, 0 \leftarrow 4, 0					
	0	4273.77535	4273.82670	4273.93047	4273.98205
	2.5	4273.77504	4273.82676	4273.93046	4273.98294
	5	4273.77504	4273.82518	4273.92954	4273.98058
	7.5	4273.77013	n.d.	4273.92692	n.d.
	10	4273.81751	4273.82624	4273.92402	4273.93753
7, 0 \leftarrow 6, 0					
	0	5978.53911	5978.61301	n.d.	n.d.
	2.5	5978.53911	5978.61175	n.d.	n.d.
	5	5978.53884	5978.61213	n.d.	n.d.
	7.5	5978.53806	5978.61080	n.d.	n.d.
	10	5978.53607	5978.60916	n.d.	n.d.
	12	5978.53518	5978.60743	n.d.	n.d.

n.d. not determined

Table 3.4: Experimentally determined Stark shifts of the individual torsional transitions in dependence of the voltage applied to the rear parabolic mirror (see Figure 1.4). The electric field strength U/d can be determined with $d = 0.59644$ m for the 5, 0 \leftarrow 4, 0 transition and with $d = 0.58746$ m for the 7, 0 \leftarrow 6, 0 transition.

with α_i being the transition energy shift of the individual components M_{Ji}

$$\alpha_i = \left\{ \frac{(J+1)(J+2) - 3(M_{Ji} \pm 1)^2}{(J+1)(J+2)(2J+1)(2J+5)} - \frac{J(J+1) - 3M_{Ji}^2}{J(J+1)(2J-1)(2J+3)} \right\}. \quad (3.8)$$

For more information about equation 3.8 the reader is referred to section 1.3.3. The values f_i correspond to the intensities shown in Figure 3.5 and can be calculated according to equations 3.5 and 3.6. For the M_J components of the transition 5, 0 \leftarrow 4, 0, α is -0.0148 and for those of the 7, 0 \leftarrow 6, 0 transition -0.0103. With these values the dipole moment μ can be determined according to

$$\Delta\nu = \frac{\mu^2 E^2}{2Bh^2} \alpha. \quad (3.9)$$

In Table 3.2 the rotational constants B for the individual torsional levels are shown. As the frequency shifts at small electric field strengths are smaller than the differences between the B values of the individual torsional levels, and as at higher field strengths the resolution is considerably lower, a universal value of $B = 427.7$ MHz is used. Based on the components listed in Table 3.4 the dipole moment of the benzene dimer $(C_6H_6)_2$ is determined as 0.580 ± 0.051 D. When assuming a dipole moment of 0.580 ± 0.051 D, the electric

field strength has to be at least 100 V/cm and 140 V/cm in order to observe Stark splittings (~ 4 kHz) with our experimental resolution for the transitions $5,0 \leftarrow 4,0$ and $7,0 \leftarrow 6,0$, respectively. This expected threshold corresponds to the experimental observations. However, in the presence of an electric field of these strengths the resolution is already substantially reduced and the Stark splittings are hard to distinguish.

3.3 MS group theory of the benzene dimer

3.3.1 Permutation-inversion groups

The Molecular Symmetry (MS) group approach becomes necessary when tunneling splittings are observed in the rotational spectrum, as it is the case for the rotational spectra of $(\text{C}_6\text{H}_6)_2$ and $(\text{C}_6\text{H}_6)^S(\text{C}_6\text{D}_6)^T$. The MS group approach contributes to the full analysis of the spectrum as it provides splitting patterns and nuclear spin statistical weights of the rotational energy levels.

In the here presented MS group theoretical analysis the benzene dimer structure shown in Figure 3.7 and the following tunneling pathways are considered: "top" C_6 torsion, "stem" bending, "stem" C_6 torsion, "top" turnover and "top"-"stem" interchange (see Figure 3.7). In Reference [70] the *ab initio* barriers for several of these tunneling motions in $(\text{C}_6\text{H}_6)_2$ are given. The barrier for the internal rotation of the "top" about its C_6 axis is predicted to be smaller than 10 cm^{-1} . The barrier for "stem" bending tunneling through the C_{2v} T-shaped structure is estimated to be 40 cm^{-1} above the C_s distorted T-shaped geometry, and the barrier for the C_6 torsion of the "stem" is about 150 cm^{-1} . "Top" turnover and "top"-"stem" interchange are expected to have still higher tunneling barriers. According to the barrier heights of the individual tunneling motions their feasibility is rated: "top" C_6 torsion > "stem" bending > "stem" C_6 torsion > "top" turnover \geq "top"-"stem" interchange.

The splitting pattern and nuclear spin statistical weights determined by permutation-inversion group theory result from the rigid molecule energy levels being split by these tunneling motions. The complete nuclear permutation-inversion (CNPI) group of the benzene dimer assuming complete intermolecular non-rigidity consists of 576 operations. \mathbf{G}_{576} is given in Reference [130]. \mathbf{G}_{576} is constructed from subgroups which are considered in the following. The character tables of the smaller subgroups are given in Appendix A.

The *ab initio* equilibrium structure of the benzene dimer has C_s symmetry [70, 71]. In the case that no tunneling occurs and the MS group is $\text{C}_s(\text{M})$, only the identity operation E and the permutation-inversion $(14)(23)(56)^*$ are feasible for the benzene dimer, with the bonded carbon-hydrogen nuclei being numbered as in Figure 3.7. Allowing for the "top" C_6 torsion tunneling the MS

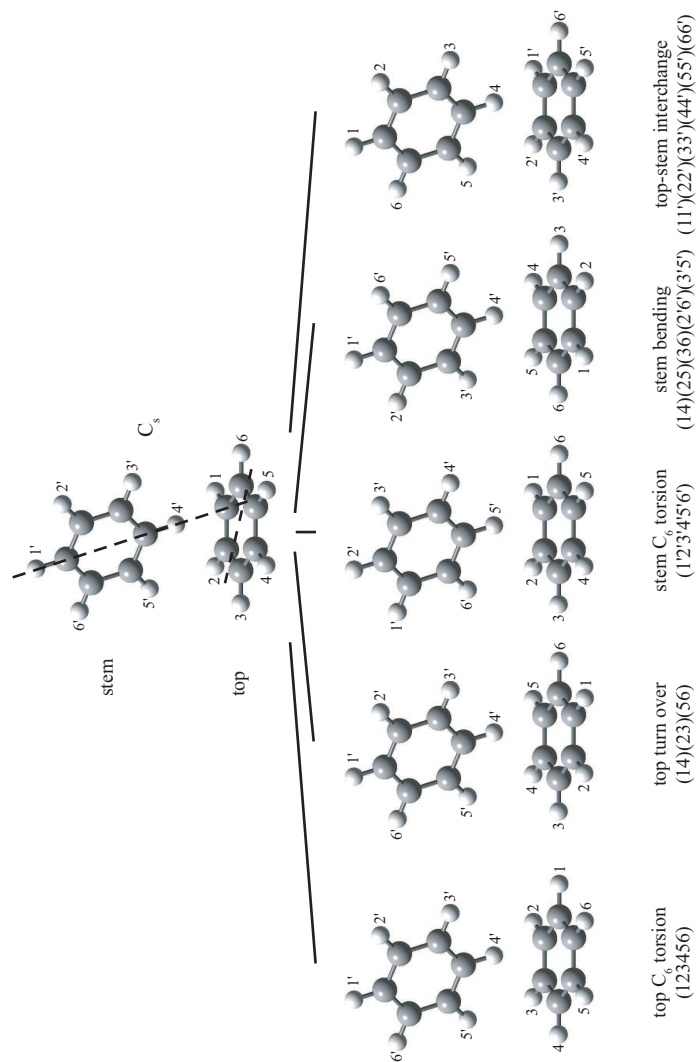


Figure 3.7: The minimum structure is presumed to be the " C_s over bond" structure [71]. The bonded carbon-hydrogen nuclei are numbered 1-6 for the "top" and 1'-6' for the "stem". In the " C_s over bond" structure the "stem" plane bisects the "top" between 216 and 345 with 4' pointing at the bond connecting 5 and 6. Different tunneling pathways in the benzene dimer are depicted as nuclear permutations. The tunneling motions are labeled in terms of symmetry operations and of permutations.

group changes to $\mathbf{C}_{6v}(\text{M})$:

$$\mathbf{C}_{6v}(\text{M}) = \mathbf{C}_s(\text{M}) \otimes \left\{ \begin{array}{l} E, (123456), (135)(246), (14)(25)(36) \\ (165432), (153)(264) \end{array} \right\}. \quad (3.10)$$

In terms of symmetry, the $\mathbf{C}_{6v}(\text{M})$ benzene dimer is equivalent to the benzene-argon [131] or benzene-krypton dimer [132]. Allowing for "stem" bending tunneling the corresponding MS group is $\mathbf{C}_{2v}(\text{M})$:

$$\mathbf{C}_{2v}(\text{M}) = \mathbf{C}_s(\text{M}) \otimes \{E, (14)(25)(36)(2'6')(3'5')\}. \quad (3.11)$$

If both tunneling motions, the "top" C_6 torsion and the "stem" bending, are allowed, the enlarged MS group has 24 elements and is called \mathbf{G}_{24} . \mathbf{G}_{24} can be generated either by starting from the $\mathbf{C}_{6v}(\text{M})$ MS group and allowing for additional "stem" bending:

$$\mathbf{G}_{24} = \mathbf{C}_{6v}(\text{M}) \otimes \{E, (2'6')(3'5')\}. \quad (3.12)$$

or from the $\mathbf{C}_{2v}(\text{M})$ MS group allowing for additional "top" C_6 torsion:

$$\mathbf{G}_{24} = \mathbf{C}_{2v}(\text{M}) \otimes \left\{ \begin{array}{l} E, (123456), (135)(246), (14)(25)(36) \\ (165432), (153)(264) \end{array} \right\}. \quad (3.13)$$

\mathbf{G}_{24} is also the MS group for the benzene-water dimer [133].

The barrier of the "stem" C_6 torsion is calculated to be significantly higher than the barriers of the two tunneling motions already mentioned, but if it is considered to be feasible together with the "top" C_6 torsion the $\mathbf{C}_{6v}(\text{M})$ MS group becomes \mathbf{G}_{72} :

$$\mathbf{G}_{72} = \mathbf{C}_{6v}(\text{M}) \otimes \left\{ \begin{array}{l} E, (1'2'3'4'5'6'), (1'3'5')(2'4'6'), (1'4')(2'5')(3'6') \\ (1'6'5'4'3'2'), (1'5'3')(2'6'4') \end{array} \right\}. \quad (3.14)$$

As the ensemble of the operations $E, (1'2'3'4'5'6'), (1'6'5'4'3'2'), (1'3'5')(2'4'6'), (1'5'3')(2'6'4')$ and $(1'4')(2'5')(3'6')$ constitutes the $\mathbf{C}_6(\text{M})$ MS group, equation 3.14 can also be written as the direct product group

$$\mathbf{G}_{72} = \mathbf{C}_{6v}(\text{M}) \otimes \mathbf{C}_6(\text{M}), \quad (3.15)$$

where $\mathbf{C}_{6v}(\text{M})$ represents the "top" and $\mathbf{C}_6(\text{M})$ the "stem". This description allows one to label the irreducible representations of \mathbf{G}_{72} as direct products $\Gamma_{\mathbf{C}_{6v}(\text{M})} \times \Gamma_{\mathbf{C}_6(\text{M})}$. If all three tunneling motions already mentioned are considered to be feasible the MS group contains 144 operations:

$$\mathbf{G}_{144} = \mathbf{G}_{72} \otimes \{E, (2'6')(3'5')\} = \mathbf{C}_{6v}(\text{M}) \otimes \mathbf{D}_6(\text{M}) \quad (3.16)$$

as $\mathbf{D}_6(\text{M})$ contains the set of operations $\{E, (2'6')(3'5')\} \otimes \{E, (1'2'3'4'5'6'), (1'6'5'4'3'2'), (1'3'5')(2'4'6'), (1'5'3')(2'6'4'), (1'4')(2'5')(3'6')\}$. In this case $\mathbf{C}_{6v}(\text{M})$ represents the "top" and $\mathbf{D}_6(\text{M})$ the "stem".

If additionally the "top" turnover tunneling (14)(23)(56) is feasible the MS group becomes \mathbf{G}_{288} which is the direct product

$$\mathbf{G}_{288} = \mathbf{G}_{144} \otimes \{E, (14)(23)(56)\} = \mathbf{D}_{6h}(\mathbf{M}) \otimes \mathbf{D}_6(\mathbf{M}) \quad (3.17)$$

with $\mathbf{D}_{6h}(\mathbf{M}) = \mathbf{C}_{6v}(\mathbf{M}) \otimes \{E, (14)(23)(56)\}$ representing the "top" and $\mathbf{D}_6(\mathbf{M})$ representing the "stem". \mathbf{G}_{288} can also be expressed by

$$\mathbf{G}_{288} = \mathbf{D}_6(\mathbf{M}) \otimes \mathbf{D}_6(\mathbf{M}) \otimes \{E, E^*\}, \quad (3.18)$$

where E^* is the inversion.

The CNPI group of the benzene dimer \mathbf{G}_{576} [130] is obtained when the "top"- "stem" interchange is considered as feasible as well:

$$\mathbf{G}_{576} = \{\{\mathbf{D}_6(\mathbf{M}) \otimes \mathbf{D}_6(\mathbf{M})\} \odot \{E, (1'1)(2'2)(3'3)(4'4)(5'5)(6'6)\}\} \otimes \{E, E^*\}, \quad (3.19)$$

where \odot symbolizes the semi-direct product.

3.3.2 Tunneling splitting of rotational levels

The rotational spectrum of a rigid \mathbf{C}_s T-shaped benzene dimer would be that of a near-prolate asymmetric top (see Table 3.8). In that case, K is no longer a "good" quantum number, instead the energy levels are specified using K_a and K_c for the limiting prolate and oblate case, respectively. In $\mathbf{C}_s(\mathbf{M})$, the rotational energy levels with even and odd K_c have the symmetry labels A' and A'' , respectively. Allowed transitions would be $A' \leftrightarrow A''$, i.e. $K_a K_c = ee \leftrightarrow eo$ and $oo \leftrightarrow oe$ (see section 1.3.3). The nuclear spin statistical weights for states of A' and A'' symmetry are 2^{12} for $(\text{C}_6\text{H}_6)_2$.

A rigid \mathbf{C}_{2v} T-shaped benzene dimer would also be an asymmetric top with rotational levels of A_1 , A_2 , B_1 and B_2 symmetry, and $K_a K_c = ee, eo, oo$ and oe , respectively. The allowed transitions are $A_1 \leftrightarrow A_2$ and $B_1 \leftrightarrow B_2$ with an alternating statistical weight 1984 and 2112 (31 : 33), respectively.

To determine how the rotational levels A' and A'' are split by tunneling the reverse correlation method is used [42, 134] including the spin statistical weights which are determined as introduced in section 1.4.1. The spin statistical weights are calculated for the benzene homodimer $(\text{C}_6\text{H}_6)_2$.

The correlation between the different MS groups, representing different (groups of) allowed tunneling motions is shown in Figures 3.8, 3.9 and 3.10 and in Table 3.5. The values of all statistical weights given there are relative values, except for the $\mathbf{C}_s(\mathbf{M})$ symmetry levels A' and A'' . The relative spin statistical weights of the sublevels χ_{rvei}^{rel} and the absolute spin statistical weights in the rigid $\mathbf{C}_s(\mathbf{M})$ symmetry χ_{rigid}^{sw} allow for the backwards determination of

the absolute spin statistical weights χ_{rvei}^{sw} of the split energy levels:

$$\chi_{rvei}^{sw} = x \chi_{rigid}^{sw} \prod_{P=1}^n \frac{\chi_{rvei}^{rel}}{m} \quad (3.20)$$

$$\sum_{i=1}^m \chi_{rvei}^{rel}$$

with x being a constant factor so that $\sum_i \chi_{rvei}^{sw} = \chi_{rigid}^{sw}$, n the number of tunneling motions P that are involved and m the number of energy levels resulting from the tunneling P .

When assuming that only the "top" C_6 torsion is feasible, $\mathbf{C}_{6v}(\text{M})$ has to be correlated to $\mathbf{C}_s(\text{M})$ to obtain the energy level splitting patterns which is shown in Figure 3.8 on the left. It can be seen that both, the A' and the A'' , rotational levels of the rigid $\mathbf{C}_s(\text{M})$ benzene dimer are split in four levels with the absolute spin statistical weights 896 : 1152 : 1408 : 640, irrespective of whether K_a is even or odd. In Figure 3.8 the nuclear spin statistical weights are given as relative values 7 : 9 : 11 : 5. If additionally the "stem" bending tunneling is feasible ($\mathbf{C}_{6v}(\text{M}) \leftarrow \mathbf{G}_{24}$ correlation) each component of the quartet is split in two levels with alternating relative spin statistics of 3 : 5 or 5 : 3, depending on whether K_a is odd or even, respectively. In this case the barrier for the "stem" bending is assumed to be higher than that for the "top" C_6 torsion, and experimentally transitions between quartets with a doublet substructure would be observed (see Figure 3.8 left).

If the "stem" bending is the only feasible tunneling motion $\mathbf{C}_{2v}(\text{M})$ has to be correlated to $\mathbf{C}_s(\text{M})$, and it results that the levels of A' and A'' symmetry split up in two doublets with the relative spin statistical weights of 31 : 33 for both doublets (see Figure 3.8 right). States with an even value for K_a have a relative spin statistical weight of 31 and those with an odd value a relative spin statistical weight of 33. An additional "top" C_6 torsion ($\mathbf{C}_{2v}(\text{M}) \leftarrow \mathbf{G}_{24}$ correlation) gives rise to a quartet splitting of each doublet level. The spin statistical weights of this quartet is basically 7 : 9 : 11 : 5 superposed by an 5 : 3 : 5 : 3 or 3 : 5 : 3 : 5 alternation for odd and even K_a , respectively. In this case the barrier for the "top" C_6 torsion is assumed to be higher than that of the "stem" bending and the experimentally observable splitting patterns would result from transitions between doublets with a quartet substructure (see Figure 3.8 right). The experimentally observable splitting pattern is therefore different from the one assuming that the barrier for "stem" bending is higher than for "top" C_6 torsion. This means that from the splittings observed in the experimental spectrum it can in principle be deduced whether the "top" C_6 torsion barrier or the "stem" bending barrier is higher in energy.

The splitting pattern of the rotational energy levels resulting from C_6 torsion tunneling in the "stem" and the "top" is obtained by $\mathbf{C}_{6v}(\text{M}) \leftarrow \mathbf{G}_{72}$ correlation and is shown in Figure 3.9. Each component of the 7 : 9 : 11 : 5 quartet resulting

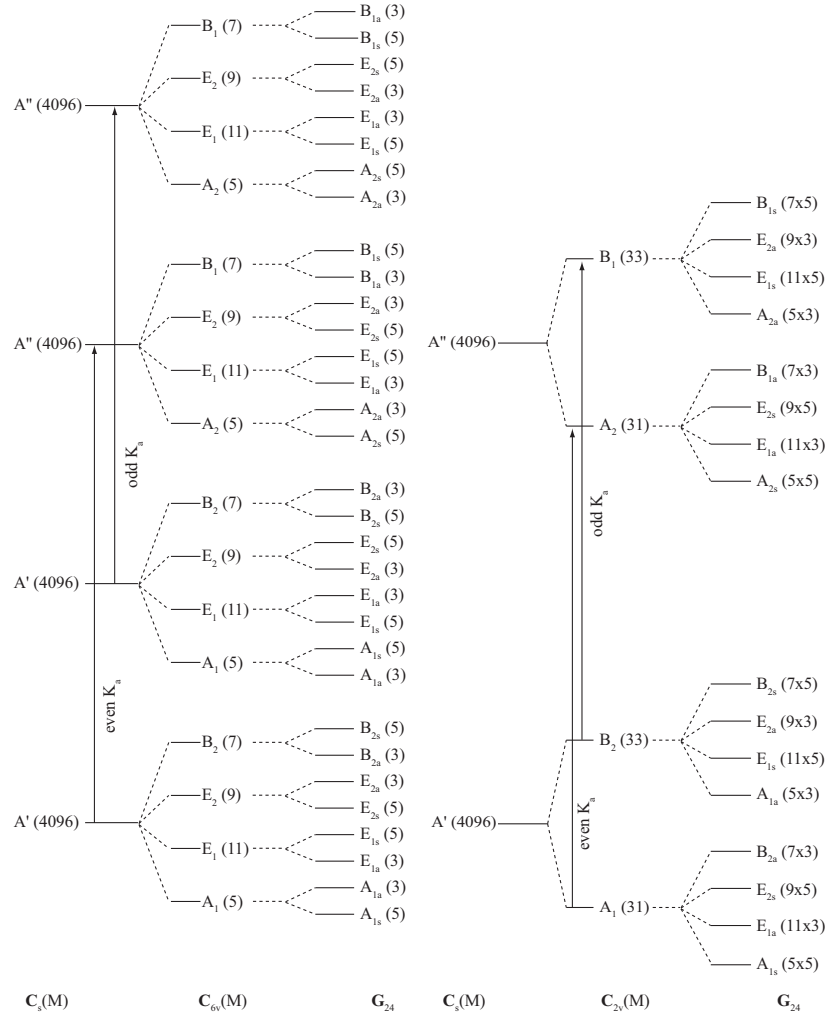


Figure 3.8: Pictorial representation of the tunneling splitting of the $C_s(M)$ rotational states of A' and A'' symmetry, allowing for "top" C_6 torsion ($C_{6v}(M)$) and "stem" bending in $(C_6H_6)_2(G_{24})$ (left) and of the tunneling splitting of the $C_{2v}(M)$ rotational states of A_1 , A_2 , B_1 and B_2 symmetry, allowing for "top" C_6 torsion in $(C_6H_6)_2(G_{24})$ (right). The relative nuclear spin statistical weights are given in parentheses.

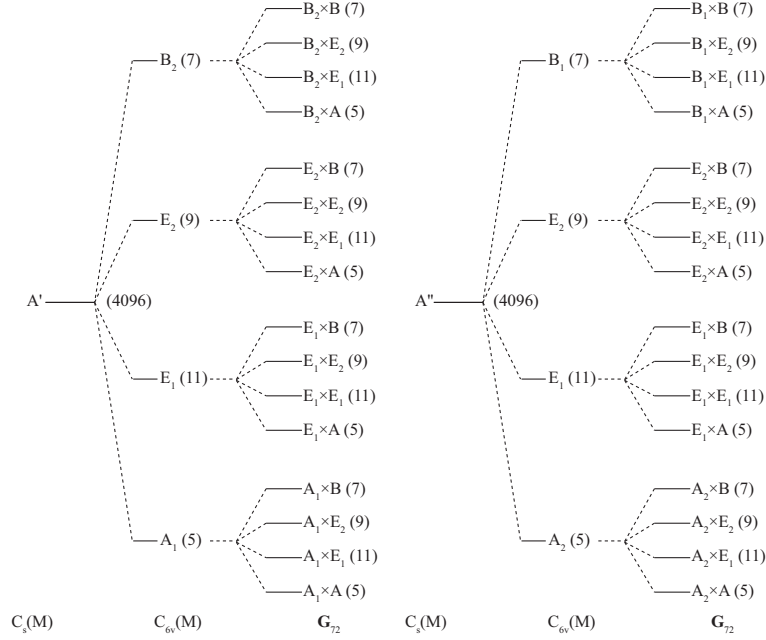


Figure 3.9: Pictorial representation of the tunneling splitting of the $\mathbf{C}_s(\mathbf{M})$ rotational states of A' and A'' symmetry, allowing for "top" and "stem" C_6 torsion in $(\mathbf{C}_6\mathbf{H}_6)_2$ ($\mathbf{C}_{6v}(\mathbf{M})_{top} \otimes \mathbf{C}_6(\mathbf{M})_{stem} = \mathbf{G}_{72}$). The relative nuclear spin statistical weights are given in parentheses.

from the "top" C_6 torsion ($\mathbf{C}_{6v}(\mathbf{M})$) is again split in a quartet with the same relative spin statistical weights. The spin statistical weights do not depend on the even- or oddness of K_a .

Allowing for all three tunneling motions already considered, i.e. for the C_6 torsion of the "stem" and of the "top" and for the "stem" bending, \mathbf{G}_{144} has to be correlated to \mathbf{G}_{24} , giving the rotational energy splitting as shown in Figure 3.10. Each level of the \mathbf{G}_{24} MS group is split in four components with relative spin statistical weights of either 13 : 9 : 11 : 7 or 1 : 9 : 11 : 3 depending on whether they arise from an s or a level, respectively. s and a denote levels that are symmetric or antisymmetric with respect to the permutation $(2'6')(3'5')$ in \mathbf{G}_{24} (see Figure 3.10 and Table A.5).

If the "top" turnover is an additional feasible tunneling pathway, the splitting patterns are determined by correlating the symmetries of \mathbf{G}_{288} with those of \mathbf{G}_{144} . Each energy level of the \mathbf{G}_{144} MS group is split in two levels (see Table 3.5). Irrespective of K_a the doublets have the relative spin statistical weights 7 : 3, 13 : 1 or 1 : 1.

If the C_6 torsion of the "top" and of the "stem", the "stem" bending and

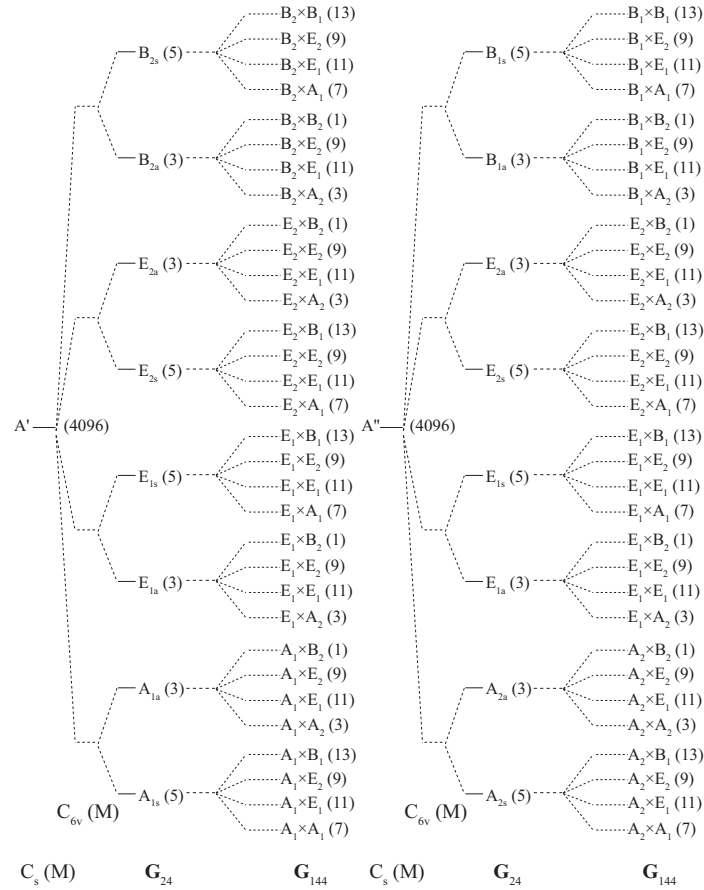


Figure 3.10: Pictorial representation of the tunneling splitting of the $C_s(M)$ rotational states of A' and A'' symmetry allowing for the "top" C_6 torsion and the "stem" bending (G_{24}) and additional "stem" C_6 torsion in $(C_6H_6)_2$ (G_{144}). The relative nuclear spin statistical weights are given in parentheses.

\mathbf{G}_{144}	$\text{sw}(\mathbf{G}_{144})^a$	\mathbf{G}_{288}	K_a	$\text{sw}(\mathbf{G}_{288})^a$
$A_1 \times A_1$	7	$A_{1g} \times A_1 + A_{2u} \times A_1$	even	7 : 3
$A_1 \times A_2$	3	$A_{1g} \times A_2 + A_{2u} \times A_2$	odd	7 : 3
$A_1 \times B_1$	13	$A_{1g} \times B_1 + A_{2u} \times B_1$	even	7 : 3
$A_1 \times B_2$	1	$A_{1g} \times B_2 + A_{2u} \times B_2$	odd	7 : 3
$A_1 \times E_1$	11	$A_{1g} \times E_1 + A_{2u} \times E_1$		7 : 3
$A_1 \times E_2$	9	$A_{1g} \times E_2 + A_{2u} \times E_2$		7 : 3
$A_2 \times A_1$	7	$A_{1u} \times A_1 + A_{2g} \times A_1$	even	7 : 3
$A_2 \times A_2$	3	$A_{1u} \times A_2 + A_{2g} \times A_2$	odd	7 : 3
$A_2 \times B_1$	13	$A_{1u} \times B_1 + A_{2g} \times B_1$	even	7 : 3
$A_2 \times B_2$	1	$A_{1u} \times B_2 + A_{2g} \times B_2$	odd	7 : 3
$A_2 \times E_1$	11	$A_{1u} \times E_1 + A_{2g} \times E_1$		7 : 3
$A_2 \times E_2$	9	$A_{1u} \times E_2 + A_{2g} \times E_2$		7 : 3
$B_1 \times A_1$	7	$B_{1u} \times A_1 + B_{2g} \times A_1$	even	13 : 1
$B_1 \times A_2$	3	$B_{1u} \times A_2 + B_{2g} \times A_2$	odd	13 : 1
$B_1 \times B_1$	13	$B_{1u} \times B_1 + B_{2g} \times B_1$	even	13 : 1
$B_1 \times B_2$	1	$B_{1u} \times B_2 + B_{2g} \times B_2$	odd	13 : 1
$B_1 \times E_1$	11	$B_{1u} \times E_1 + B_{2g} \times E_1$		13 : 1
$B_1 \times E_2$	9	$B_{1u} \times E_2 + B_{2g} \times E_2$		13 : 1
$B_2 \times A_1$	7	$B_{1g} \times A_1 + B_{2u} \times A_1$	even	13 : 1
$B_2 \times A_2$	3	$B_{1g} \times A_2 + B_{2u} \times A_2$	odd	13 : 1
$B_2 \times B_1$	13	$B_{1g} \times B_1 + B_{2u} \times B_1$	even	13 : 1
$B_2 \times B_2$	1	$B_{1g} \times B_2 + B_{2u} \times B_2$	odd	13 : 1
$B_2 \times E_1$	11	$B_{1g} \times E_1 + B_{2u} \times E_1$		13 : 1
$B_2 \times E_2$	9	$B_{1g} \times E_2 + B_{2u} \times E_2$		13 : 1
$E_1 \times A_1$	7	$E_{1g} \times A_1 + E_{1u} \times A_1$	even	1 : 1
$E_1 \times A_2$	3	$E_{1g} \times A_2 + E_{1u} \times A_2$	odd	1 : 1
$E_1 \times B_1$	13	$E_{1g} \times B_1 + E_{1u} \times B_1$	even	1 : 1
$E_1 \times B_2$	1	$E_{1g} \times B_2 + E_{1u} \times B_2$	odd	1 : 1
$E_1 \times E_1$	11	$E_{1g} \times E_1 + E_{1u} \times E_1$		1 : 1
$E_1 \times E_2$	9	$E_{1g} \times E_2 + E_{1u} \times E_2$		1 : 1
$E_2 \times A_1$	7	$E_{2g} \times A_1 + E_{2u} \times A_1$	even	1 : 1
$E_2 \times A_2$	3	$E_{2g} \times A_2 + E_{2u} \times A_2$	odd	1 : 1
$E_2 \times B_1$	13	$E_{2g} \times B_1 + E_{2u} \times B_1$	even	1 : 1
$E_2 \times B_2$	1	$E_{2g} \times B_2 + E_{2u} \times B_2$	odd	1 : 1
$E_2 \times E_1$	11	$E_{2g} \times E_1 + E_{2u} \times E_1$		1 : 1
$E_2 \times E_2$	9	$E_{2g} \times E_2 + E_{2u} \times E_2$		1 : 1

^arelative nuclear spin statistical weights

Table 3.5: Correlation table for the energy levels of the MS group \mathbf{G}_{288} to those of the MS group \mathbf{G}_{144} . The spin statistical weights of the energy levels given result when considering the "top" and "stem" C_6 torsion, the "stem" bending and the "top" turnover tunneling in $(\text{C}_6\text{H}_6)_2$.

MS group	$(\text{C}_6\text{H}_6)_2$	$(^{13}\text{C}_6\text{H}_6)^S(\text{C}_6\text{H}_6)^T$
$\mathbf{C}_s(\text{M})$	2^{12}	2^{18}
$\mathbf{C}_{2v}(\text{M})$	$31 : 31^{(e)}$ $33 : 33^{(o)}$	$127 : 127^{(e)}$ $129 : 129^{(o)}$
$\mathbf{C}_{6v}(\text{M})$	$7 : 9 : 11 : 5$	$7 : 9 : 11 : 5$
\mathbf{G}_{24}	$7 \times 5 : 9 \times 3 : 11 \times 5 : 5 \times 3^{(e)}$ $7 \times 3 : 9 \times 5 : 11 \times 3 : 5 \times 5^{(o)}$	
\mathbf{G}_{144}	$13 : 9 : 11 : 7^{(s)}$ $1 : 9 : 11 : 3^{(a)}$	$193 : 345 : 335 : 215^{(s)}$ $29 : 69 : 67 : 27^{(a)}$
\mathbf{G}_{288}	$7 : 3, 13 : 1, 1 : 1$	$7 : 3, 13 : 1, 1 : 1$

MS group	$(^{13}\text{C}_6\text{H}_6)_2$	$(\text{C}_6\text{H}_6)^S(^{13}\text{C}_6\text{H}_6)^T$
$\mathbf{C}_s(\text{M})$	2^{24}	2^{18}
$\mathbf{C}_{2v}(\text{M})$	$1025 : 1025^{(e)}$ $1023 : 1023^{(o)}$	$257 : 257^{(e)}$ $255 : 255^{(o)}$
$\mathbf{C}_{6v}(\text{M})$	$169 : 345 : 335 : 175$	$169 : 345 : 335 : 175$
\mathbf{G}_{24}	$359 : 733 : 712 : 372^{(e)}$ $317 : 647 : 628 : 328^{(o)}$	$169 \times 3 : 345 \times 5 : 335 \times 3 : 175 \times 5^{(e)}$ $169 \times 5 : 345 \times 3 : 335 \times 5 : 175 \times 3^{(o)}$
\mathbf{G}_{144}	$193 : 345 : 335 : 215^{(s)}$ $29 : 69 : 67 : 27^{(a)}$	$13 : 9 : 11 : 7^{(s)}$ $1 : 9 : 11 : 3^{(a)}$
\mathbf{G}_{288}	$8 : 5, 4 : 3, 1 : 1$	$8 : 5, 4 : 3, 1 : 1$

Table 3.6: Spin statistical weights for the torsional energy levels of the benzene dimer isotopologues $(\text{C}_6\text{H}_6)_2$, $(^{13}\text{C}_6\text{H}_6)_2$, $(^{13}\text{C}_6\text{H}_6)^S(\text{C}_6\text{H}_6)^T$ and $(\text{C}_6\text{H}_6)^S(^{13}\text{C}_6\text{H}_6)^T$ in several MS groups. The spin statistical weights are given as absolute values for $\mathbf{C}_s(\text{M})$ and as relative values for all other MS groups. The labels $^{(e)}$ and $^{(o)}$ designate spin statistical weights of levels with even and odd K_a values, respectively. The labels $^{(s)}$ and $^{(a)}$ designate spin statistical weights of levels originating from s or a levels in \mathbf{G}_{24} , respectively.

barrier [cm^{-1}]	splitting [cm^{-1}]		
	0-1	1-2	2-3
0	0.285	0.855	1.425
2	0.279	0.823	1.000
5	0.251	0.692	0.598
10	0.182	0.442	0.285
15	0.121	0.269	0.153
20	0.078	0.166	0.089
30	0.033	0.067	0.034
40	0.015	0.030	0.015
50	0.007	0.014	0.007

Table 3.7: Splittings between the torsional energy levels ($K_i = 0, 1, 2$ and 3) as a function of the C_6 torsional barrier height.

torsional level can be zero, and the number of observable transitions is smaller than the number of torsional levels.

In order to test whether the experimentally observed quartet intensity pattern may arise from the natural abundance (1.1%) of ^{13}C nuclei ($I=1/2$), the splittings of the rotational states and the respective nuclear spin statistical weights are also determined for the following isotopologues: $(^{13}\text{C}_6\text{H}_6)_2$, $(^{13}\text{C}_6\text{H}_6)^S(\text{C}_6\text{H}_6)^T$ and $(\text{C}_6\text{H}_6)^S(^{13}\text{C}_6\text{H}_6)^T$. The results are summarized in Table 3.6. It can be seen that the nuclear spin statistical weights of the split energy levels are unaffected by the isotopic composition of the non-tunneling counterpart. Especially for the small MS groups similarities to the spin statistical weights of $(\text{C}_6\text{H}_6)_2$ are found.

Additionally, the energies of the torsional levels of $(\text{C}_6\text{H}_6)_2$ with a C_6 torsion tunneling, located either in the "top" or in the "stem", are determined for $J = 0$ assuming different barrier heights for the C_6 torsion. The energies are calculated* with the program outlined in Reference [136] which uses an approximate effective torsion-rotation Hamiltonian

$$H_{RTRF} = A_F J_z^2 + B J_x^2 + C J_y^2 + F J_\rho^2 - 2A_C J_z J_\rho + \frac{V_6}{2} \cos(6\rho). \quad (3.21)$$

H_{RTRF} describes a rigid-top-rigid-frame system, neglecting contributions from centrifugal distortion and higher order kinetic coupling terms. J_x , J_y and J_z are the angular momentum operators for the rotations about the molecule fixed axes x , y and z , respectively. J_ρ is the angular momentum operator of the internal rotation with the angle ρ . A_F is the rotational constant A of the

*The calculations are run by P. R. Bunker.

$(\text{C}_6\text{H}_6)_2$	A	B	C
C_{2v} T-shaped	1902.3357	473.0754	436.8950
C_s over atom	1919.4642	476.3936	440.6282
C_s over bond	1920.1814	477.3120	441.4485

$(\text{C}_6\text{H}_6)^S(\text{C}_6\text{D}_6)^T$	A	B	C
C_{2v} T-shaped	1669.5224	451.2724	418.2362
C_s over atom	1685.6899	454.2163	421.7779
C_s over bond	1686.3824	455.0835	422.5678

Table 3.8: Rotational constants [MHz] of the near-prolate theoretical structures from Reference [71] calculated at the Austin Model 1 (AM 1) level of theory.

frame (the non-rotating benzene ring) and B and C are the molecular rotational constants. F includes the moments of inertia I of the rotor and the frame ($F \propto (1/I_\rho + 1/I_F)/2$) and A_C is the coefficient of the operator representing the Coriolis interaction between the K rotation and the internal rotation. V_6 represents the potential barrier height. The results are summarized in Table 3.7. It can be seen that V_6 barriers $\geq 20 \text{ cm}^{-1}$ are associated with a relative energy splitting of 1 : 2 : 1, which corresponds to the experimentally observed splitting, whereas lower barriers are responsible for an irregular spacing between the torsional levels.

3.4 Discussion

3.4.1 Benzene dimer - a symmetric top

From the rotational spectra of $(\text{C}_6\text{H}_6)_2$ and $(\text{C}_6\text{H}_6)^S(\text{C}_6\text{D}_6)^T$ the benzene dimer appears to be a symmetric top species. This is, considering the possible geometries with a permanent electric dipole moment (see structures I and II in Figure 1.11) and therefore being observable in a microwave spectrum, not evident at the first glance, as a symmetric top has at least a C_3 symmetry axis. In the following that and other aspects are discussed.

A rigid (distorted) T-shaped structure would give rise to a near-prolate asymmetric top spectrum. Only when assuming that the "top" moiety is freely rotating about its C_6 axis, the benzene dimer becomes a symmetric top with $I_A < I_B = I_C$ and the molecular symmetry changes to C_{6v} .

The rotational constants B estimated from the $(\text{C}_6\text{H}_6)_2$ and $(\text{C}_6\text{H}_6)^S(\text{C}_6\text{D}_6)^T$ rotational spectra are $427.7277 \pm 0.0002 \text{ MHz}$ (for the low transition frequency component of A symmetry) and $409.0090 \pm 0.0001 \text{ MHz}$ (for the central frequency), respectively. DiStasio *et al.* propose three theoretical minimum

structures which are all near-prolate symmetric tops: " \mathbf{C}_{2v} T-shaped", " \mathbf{C}_s over atom" and " \mathbf{C}_s over bond" with the rotational constants $A > B \approx C$ [71] (see Table 3.8). In a symmetric top benzene dimer B and C are equivalent. Therefore, the averaged rotational constants $(B + C)/2$ of each of these theoretical structures is compared to the experimental value of B . The comparison shows for $(\text{C}_6\text{H}_6)_2$ a difference of about 27 MHz for the \mathbf{C}_{2v} geometry and of about 31 MHz for both \mathbf{C}_s geometries. Nearly the same differences are found between the experimental B and the theoretical $(B + C)/2$ rotational constants of $(\text{C}_6\text{H}_6)^S(\text{C}_6\text{D}_6)^T$, strongly supporting that the observed symmetric top transitions originate from the benzene dimer.

The singlets and doublets, observed together with the regular quartets, that originate from $(\text{C}_6\text{H}_6)_2$, can have several possible origins. As proposed already by Gutowsky *et al.* [57] they can be due to another dynamic state of $(\text{C}_6\text{H}_6)_2$ than the one described by the rotational parameters given in Table 3.2, even due to an asymmetric top species. In another attempt the singlets and doublets can be considered as components of a large quartet splitting of $(\text{C}_6\text{H}_6)_2$ transitions. Furthermore, these transitions can simply be due to larger, polar C_6H_6 clusters [137–139] or to clusters of C_6H_6 with carrier gas atoms [140], with water molecules [141] or with both [140, 142], as water can be found in a very low concentration as an impurity in the carrier gas. Water clusters [143], even in very low concentrations, might be observed as well. The last possibility, that the transitions result from benzene clusters with other species or from the water dimer can be excluded as the rotational transition frequencies differ significantly from the experimentally determined values. However, theoretically a cyclic benzene trimer structure of \mathbf{C}_{3h} symmetry has been predicted to be the lowest energy configuration among three [137] and six [138] polar and non-polar low energy trimer structures. Also the reported minimum structures of the benzene tetramer [137, 138] and pentamer [138] have a permanent dipole moment and could thus be the origin of the singlet and doublet transitions.

3.4.2 Tunneling splitting pattern

All transitions summarized in Table 3.1 have a very regular 1 : 2 : 1 quartet splitting pattern with a small deviation of ± 3 %. The splitting can be due to one or several tunneling motions.

Since the two outer splittings ($\Delta\text{I-II}$, $\Delta\text{III-IV}$) are identical, the structure can result from tunneling with a small doublet splitting that splits one (large) doublet, induced by another tunneling process, in four components. As the splitting of a rotational transition is related to those of the rotational energy levels involved (see Figure 3.11), the consistency of this assumption can be checked using the tunneling matrix formalism [144]. This formalism can be applied to rotational energy levels assuming different plausible tunneling processes which are shown in Figure 3.7. "Top" turnover, "stem" bending and

"top"- "stem" interchange are tunneling motions between only two minimum structures and can therefore not alone, but in combination, lead to a quartet splitting of the energy levels. The only tunneling process that can split a rotational state into four energy levels by itself is the C_6 torsion of one benzene ring in the dimer. This $2\pi/6$ torsion connects six minimum energy structures and the coupling terms between these six minima can be described in a 6×6 matrix. The problem can be simplified assuming that only couplings between adjacent minima on the torsional tunneling pathway are allowed (high barrier formalism [145]). Diagonalization of the matrix produces the eigenvalues which represent the energy levels of the six states. Two of them are doubly degenerate so that four separate energy levels remain. These four levels are separated in energy in a ratio 1 : 2 : 1 which perfectly fits to the experimentally observed splitting. Energy differences between the four levels resulting from a C_6 torsion are calculated assuming different tunneling barrier heights. From the results shown in Table 3.7 it can be seen that barriers $\geq 20 \text{ cm}^{-1}$ have to be assumed to reproduce the 1 : 2 : 1 splitting justifying the simplification of the tunneling matrix formalism by the high barrier formalism.

According to this model each rotational state is split in four torsional components with a 1 : 2 : 1 spacing as a consequence of internal rotation of one of the two benzene rings around its C_6 axis. It is very likely that this pattern is reflected in the transitions which are observed in the experimental spectrum as well. The perfect coincidence between the experimental splitting and the one obtained from the tunneling matrix formalism strongly supports the C_6 benzene torsion to be the origin of the observed quartet structure. The assumption that two separate tunneling processes produce accidentally a 1 : 2 : 1 splitting pattern from two doublet splittings can rather be rejected.

The high barrier formalism assumes that only adjacent minima are coupled, whereas a rotation by $2\pi/3$ or π about the C_6 axis is considered to be less frequent, which is valid if high rotational barriers have to be crossed. The barrier for C_6 torsion of the "stem" is calculated to be by a factor of 30 higher than that of the "top", which is in contrast so low that the "top" can be considered as a free rotor [70]. Therefore, the C_6 torsion inducing the observed 1 : 2 : 1 splitting might rather be located in the "stem" of the benzene dimer.

But where is the spectral signature of the C_6 torsion in the "top" which should, due to its even lower barrier, occur as well? Generally, the width of the splitting is exponentially inversely proportional to the height of the tunneling barrier and to the mass of the tunneling atom group. Due to the very low barrier (about 30 times smaller than the "stem" barrier) the splitting that comes along with the C_6 torsion of the "top" is expected to be orders of magnitude larger than that associated with the "stem" C_6 torsion, and is most likely not observed. A similar behavior has been reported for the $\text{CH}_3\text{F} \cdot \text{CHF}_3$ complex, where the internal rotation of the CF_3 group is observed while that of the CH_3 group is not which is due to the 19 times smaller mass and the two times lower barrier height in the latter case [146].

In this context it is interesting to consider the observed singlet and doublet transitions. In a molecule with two internal rotors that are located such that they do not influence each other the two tunneling motions (with two different barriers) are independent. The tunneling splitting of the first internal rotor (e.g. a quartet) can be split by the tunneling of the second internal rotor (e.g. a doublet). In the local mode picture four identical doublets are therefore expected. However, if the sterical properties allow for an interaction between the two internal rotors the four doublets are not necessarily equal. In the benzene dimer the two internal rotors, i.e. benzene rings, do interact and the local mode picture is not valid. The C_6 tunneling with the lower barrier ("top") can cause a quartet splitting whose components are again split in four levels by the C_6 tunneling with the higher barrier ("stem") (see Figure 3.9). However, it is possible that the four expected quartets are unequal, depending on the symmetry of the energy level (A_1 , E_1 , E_2 or B_2) they result from. In the extreme case only one of the four quartets corresponds to those that we have assigned. The other three quartets can have much wider/narrower splittings, so that they might appear at first glance as singlets and/or doublets. This aspect might explain why only 22 of the more than 100 observed rotational transitions (2.5-6 GHz) found by Gutowsky *et al.* [57] have a distinctive quartet structure.

3.4.3 Stark effect and dipole moment

The Stark effect measurements performed on $(C_6H_6)_2$ show that transitions with $K = 0$ shift quadratically with respect to $\vec{\mu} \cdot \vec{E}$, and those with $K \neq 0$ linearly. This observation corresponds to the properties of a symmetric top species and thus supports the assignment made in Table 3.1, confirming that the species that is detected with the microwave is a symmetric top species.

The electric dipole moment of this symmetric top is estimated to be 0.580 ± 0.051 D based on the frequency shifts observed in the presence of an external electric field. This value is comparatively low and explains the weak spectral intensity. Theoretically the dipole moment of a T-shaped benzene dimer structure is estimated to be between 0.40 or 0.51 D depending on the basis set being used [58]. In spite of the deficient experimental precision, the experimental and the theoretical values agree fairly well. The experimentally determined value is similar to the one of the hexafluorobenzene-benzene dimer [75].

3.4.4 Comparison of experimental and theoretical intensity patterns

Permutation-inversion group theory is used to determine the energy level correlation patterns and the respective spin statistical weights for $(C_6H_6)_2$. The rotational transitions of the benzene dimer are split in four components with the relative intensities 3 : 2 : 2 : 1 when going from low to high transition

frequencies within a quartet pattern. This intensity pattern is irrespective of the even- and oddness of the quantum number K . In the following the various spin statistical weight ratios that result from the different tunneling motions are summarized.

The "stem" bending tunneling splits each rotational state of the rigid benzene dimer in two levels and transitions between states with an even or odd value of the quantum number K_a have an intensity ratio 31 : 33. Due to the expected intensity alternation for even and odd K states and due to the doublet (instead of quartet) splitting the "stem" bending tunneling cannot be the sole origin of the observed splitting pattern.

All combinations of tunneling processes involving the "stem" bending tunneling can be excluded to be the origin of the experimentally observed quartet tunneling splitting as well, as the alternation, depending on the even- and oddness of K_a remains.

Only the "top" C_6 torsion alone or in combination with the "stem" C_6 torsion gives rise to a quartet with an intensity pattern independent from K_a (see Figure 3.9). The relative intensities are $7 : 9 : 11 : 5 \equiv 1.4 : 1.8 : 2.2 : 1$ which is, however, not in agreement with the experimental intensity distribution $3 : 2 : 2 : 1$. The discrepancy between experiment and theory is due to one component.

From these MS group theoretical considerations and the experimental results, discussed before, it can be concluded that the observed spectral signatures can most probably be ascribed to the "top" and the "stem" C_6 torsion tunnelings. Permutation-inversion group theory and spin statistical weight calculations, to the extent as they have been performed here, seem to be insufficient to adequately describe the relative intensities of the tunneling splittings observed in the rotational spectrum of the benzene dimer. Possibly, additional effects are responsible for the mismatch between the calculated nuclear spin statistical weights of the torsional levels and the experimental transition intensities.

3.5 Conclusion and future prospects

Rotational spectroscopy of $(C_6H_6)_2$ and $(C_6H_6)^S(C_6D_6)^T$, Stark effect measurements of $(C_6H_6)_2$ and permutation-inversion group theory are performed in order to get insight in the internal dynamics of the benzene dimer.

The observed rotational transitions are split in quartets and can be assigned to $J+1, K \leftarrow J, K$ transitions. The quartets have a regular splitting pattern of $1 : 2 : 1$ and can be fitted to a symmetric top Hamiltonian, which is supported by Stark effect measurements on the assigned $(C_6H_6)_2$ transitions.

The very regular $1 : 2 : 1$ quartet splitting can be reproduced when assuming a C_6 torsion tunneling of one benzene subunit with a barrier $\geq 20 \text{ cm}^{-1}$ and the second benzene subunit being rigid in a (distorted) T-shaped structure. As the barrier for the "top" C_6 torsion is expected to be below 10 cm^{-1} , the observed

quartet splitting is probably due to the "stem" C_6 torsion. The C_6 torsion in the "top" should occur as well, however with a much larger separation of the four torsional levels, due to its lower barrier. In this picture both tunneling processes split the rotational states in four components which are each split again in quartets. From the four expected quartets for each rotational level J, K only one is found. The three other quartets might be shifted considerably, as the splitting of the "top" C_6 torsion is expected to be very large.

The intensity pattern of the quartets in the $(C_6H_6)_2$ spectrum is 3 : 2 : 2 : 1. Spin statistical weight calculations for the torsional levels assuming several tunneling pathways ("top" and "stem" C_6 torsion, "stem" bending, "top" turnover and "top"- "stem" interchange), however, cannot reproduce the experimental intensity pattern.

In order to get more insight in the internal dynamics of the benzene dimer, more experimental studies on isotopically labeled benzene dimers are necessary. The splitting patterns (absolute splitting width and relative intensities) of different isotopologues can yield valuable additional information as the absolute values of the splittings also depend on the isotopic composition of the tunneling benzene ring. The analysis of the absolute splittings of the dimers $(C_6H_6)_2$, $(C_6H_6)^S(C_6D_6)^T$ and $(C_6D_6)^S(C_6H_6)^T$, for example, can allow one to determine in which benzene moiety, if not in both, the tunneling is localized. The spectral broadening induced by quadrupole coupling of the deuterons, however, complicates the spectra. This difficulty can be avoided using a mixed dimer like $(^{12}C_6H_6)(^{13}C_6H_6)$. For this isotopologue, however, no preliminary work on the abundance of the different isomers exists yet. Furthermore, dimers of benzene isotopologues, such as CH_5D or CH_3D_3 , can also contribute to a deeper understanding of the benzene dimer, as they have a different molecular symmetry and the consequences should be spectroscopically observable.

Provided that both subunits internally rotate about their C_6 axes, three more quartets must exist for each rotational level. Proving their existence experimentally would support the current concept on the internal dynamics of the benzene dimer.

Chapter 4

Control and manipulation of conformational interconversion

4.1 Introduction

Since the pioneering work of Becker and Bier in 1954 [147] and due to the development of new experimental facilities, supersonically expanding molecular beams have become standard tools for gas phase experiments (see for example section 1.2). Techniques exist to generate pulsed or continuous molecular beams that can be used to investigate the entrained molecules, or as a probe to investigate various targets via molecular beam scattering techniques [3, 148, 149].

Often the molecules of interest are seeded in a carrier gas. Via collisions with the carrier gas in the beginning of the supersonic expansion the internal energy of the molecules drops. The cooling efficiency depends on the collision cross sections and also on the efficiency of energy transfer between the molecule and the rare gas atoms. While larger atoms or molecules are best suited to cool the rotational and vibrational degrees of freedom, small rare gas atoms better reduce the spread of the translational energy. At a certain distance from the nozzle of the valve the molecular beam provides a collision free environment which allows for experiments on isolated molecules. In this "zone of silence" only the lowest vibrational and rotational levels of the molecules are populated, giving rise to a less congested spectrum. The isolated species can then experience well defined perturbations (laser radiation, collisions with species of a second beam etc.) and their effects can be observed in a controlled way. Furthermore, due to the internal cooling in the expansion, very weakly bound complexes with small dissociation energies can be formed.

Molecular beam techniques provide perfect conditions to investigate the intrinsic properties of isolated molecules and clusters. Many molecules or molecular complexes can adopt various conformational structures that differ in potential energy. In molecular beam experiments these different conformations are often found to co-exist [150]. As an example of biological relevance, amino acids and nucleobase(pair)s, which are the building blocks of proteins and DNA strands, are often very flexible, and many low-energy conformers can exist [9, 151–156]. In particular, structures can be observed that have high potential energies, and the observed structural distributions are therefore frequently not in thermal equilibrium with the other degrees of freedom [150, 151, 157–163]. This can be rationalized by the height of the barriers that separate potential energy minima which might be hard to overcome under the conditions prevailing in the molecular beam experiments. The study of the potential energy landscape of gas phase molecules in the electronic ground state and the development of experimental methods to manipulate the conformational distribution of these species currently is an active field of research [164–166]. Exploration of their vibrational dynamics is of particular interest because it can help to get insight into the complex potential energy surface and to rationalize the observed conformational distribution.

There has been a variety of studies on the dependence of the conformational distribution in a molecular beam on the experimental parameters. The question how the composition of the carrier gas influences the relative population of different conformers in a supersonic expansion has been addressed by Ruoff *et al.* in 1990 [158]. In that work, microwave absorption measurements were performed ($T_{rot} \approx 3$ K) to deduce relative populations of the possible conformational structures of a variety of molecules in molecular beams. In such measurements, the effect of changing the rotational temperature and the effect of changing the relative abundance of a specific conformer can appear the same, and it is non-trivial to distinguish between these effects. Nevertheless, one of the important observations of that work is that conversion between conformers, separated by barriers of less than 350 cm^{-1} , appears to involve relatively long-range polarization effects and to take place relatively late in the expansion region. A molecular dynamics simulation addressing the problem of thermodynamic versus kinetic control of isomers of dihalogen - rare gas complexes in a supersonic expansion has been presented by Bastida *et al.* [167]. In a more recent theoretical study, the conformational changes of glycine by collisions with rare-gas atoms, with collision energies ranging from 100 to 1000 K, have been investigated [168]. In that work it is shown that attractive interactions between the colliding atoms and the glycine molecule can lower the barrier between conformers, i.e. that these interactions can catalyze conformer conversion. In 2006, Suhm and co-workers have investigated the isomerism of jet-cooled, isotopically mixed methanol dimers ($\text{CH}_3\text{OH}\cdot\text{CH}_3\text{OD}$) in a supersonic jet expansion [163]. They use Fourier Transform Infrared (FT-IR) absorption spectroscopy in the $3\text{--}4\text{ }\mu\text{m}$ (O-H and O-D stretch) region to study the degree of conformer conversion (or:

donor/acceptor isomerism) in their 10-20 K jet expansion. A complication in the latter studies is that it is difficult to spectroscopically distinguish the mixed dimers from their homodimer counterparts. For the mixed methanol dimer system spectra are only reported in a pure He expansion, and it is concluded that relaxation to the lowest energy conformer is incomplete in this case.

4.2 Conformational interconversion driven by rare gas atoms

4.2.1 Experimental method

Although several studies on the conformational distribution of molecules in molecular beams already exist, the microscopic mechanisms leading to the observed distributions are not fully understood yet.

We address this topic with an experiment that aims to investigate the dependence of the relative abundances of two conformers of a molecule on the nature of the carrier gas used in the supersonic expansion. The molecule of our choice is the isotopically mixed benzene dimer $(\text{C}_6\text{H}_6)(\text{C}_6\text{D}_6)$.

Although a variety of experimental [45, 46, 48, 49, 51, 55–57, 76] and theoretical [58, 62, 63, 70, 71, 84] studies exist, that discuss the benzene dimer not only as having two symmetrically inequivalent subunits, but also as a V-shaped, parallel displaced or "Sandwich" structure with two symmetrically equivalent sites, Raman [55], microwave [57] (see chapter 3) and recent infrared experiments [76] (see chapter 2) strongly support a (distorted) T-shaped structure for this loosely bound complex, with one site called the "top" and the other site called the "stem". In such a benzene dimer the two monomer units are inequivalent and do not interchange on the experimental timescale.

When one of the two rings is isotopically labeled ($(\text{C}_6\text{H}_6)(\text{C}_6\text{D}_6)$), two substitution isomers exist which can have a slightly different zero-point energy. The barrier between the two conformers is calculated to be 64 cm^{-1} [70]. Therefore, $(\text{C}_6\text{H}_6)(\text{C}_6\text{D}_6)$ is a very subtle system for the study of conformational conversion.

For this experiment the benzene dimer complexes are generated in a supersonic expansion of benzene (0.03%) and helium, neon or argon as a carrier gas at a stagnation pressure from two bars into vacuum. C_6H_6 and C_6D_6 are premixed in a 1:1 ratio and dimers of three different masses can be generated: the two homodimers $(\text{C}_6\text{H}_6)_2$ and $(\text{C}_6\text{D}_6)_2$ and the heterodimer $(\text{C}_6\text{H}_6)(\text{C}_6\text{D}_6)$. The relative abundances are probed in a two color- Resonance Enhanced Multi Photon Ionization (REMPI) experiment and detected mass selectively, under the experimental conditions described in section 1.2.1.

Section 4.2 adapted from:

U. Erlekam, M. Frankowski, G. von Helden, G. Meijer, Phys. Chem. Chem. Phys. **9**, 3786 (2007)

The method and the molecule chosen have several advantageous features. First, the REMPI technique is very sensitive and small changes in the population can be reliably detected. Second, by using mass-selective detection of $(\text{C}_6\text{H}_6)(\text{C}_6\text{D}_6)$ any interference by the signal of the homodimer is avoided. Third, via electronic spectroscopy one can unambiguously distinguish between the two substitution isomers $(\text{C}_6\text{H}_6)^S(\text{C}_6\text{D}_6)^T$ and $(\text{C}_6\text{D}_6)^S(\text{C}_6\text{H}_6)^T$, with either the "stem" or the "top" being protonated, respectively.

For more details on the substitution isomers of $(\text{C}_6\text{H}_6)(\text{C}_6\text{D}_6)$ the reader is referred to section 1.5.3 and chapter 2.

4.2.2 Results and Discussion

In Figure 4.1 the UV spectra for the different benzene dimer species are shown in the region of the origin of the $S_1 \leftarrow S_0$ transition using either helium (left) or neon (right) as a carrier gas. The spectra of the benzene dimer isotopologues with helium as a carrier gas are already discussed in detail in section 1.5.3. Therefore, the spectra themselves shall not be discussed here. The focus is rather put on the comparison/differences of the spectra depending on the carrier gas being used.

Using helium or neon as a carrier gas and monitoring $(\text{C}_6\text{H}_6)_2$, a peak around 38042 cm^{-1} is observed. With neon as a carrier gas an additional broad structure of low intensity appears to the blue side of the strong and sharp peak (see Figure 4.1 (c) and (f)). For $(\text{C}_6\text{D}_6)_2$ the same observation is made, except that the spectral features are shifted about 200 cm^{-1} to the blue (see Figure 4.1 (a) and (d)). However, for $(\text{C}_6\text{H}_6)(\text{C}_6\text{D}_6)$ two peaks, slightly shifted to the blue compared to the two homodimer transitions, are observed when using helium as a carrier gas, whereas only one peak is observed when using neon as a carrier gas (see Figure 4.1 (b) and (e)).

The 0_0^0 transition in a (distorted) T-shaped structure is only observed when the excitation occurs on the "stem" molecule (see section 1.5.3). The two substitution isomers of $(\text{C}_6\text{H}_6)(\text{C}_6\text{D}_6)$ differ in the isotopic composition of the "stem" and can therefore be selectively excited by choosing the appropriate UV frequency and can thus be detected separately. Ions generated using 38044 cm^{-1} light thus originate from dimers with a protonated "stem" $((\text{C}_6\text{H}_6)^S(\text{C}_6\text{D}_6)^T)$, whereas ions generated using light at 38246 cm^{-1} correspond to the isomer in which the "stem" is deuterated $((\text{C}_6\text{D}_6)^S(\text{C}_6\text{H}_6)^T)$. Consequently, in neon the sharp signature in the $(\text{C}_6\text{H}_6)(\text{C}_6\text{D}_6)$ spectrum corresponds to $(\text{C}_6\text{H}_6)^S(\text{C}_6\text{D}_6)^T$, and it appears that the other isomer with the "stem" deuterated and the "top" protonated is completely absent. In helium, however, both isomers occur with similar intensities in the spectrum.

Interestingly, the broad structure observed in the neon spectra to the blue side of the main peak is more pronounced in the homodimer spectra than in the one of the heterodimer. For $(\text{C}_6\text{H}_6)(\text{C}_6\text{D}_6)$ such a broad background is not only observed to the right of the sharp peak, but also near the position where

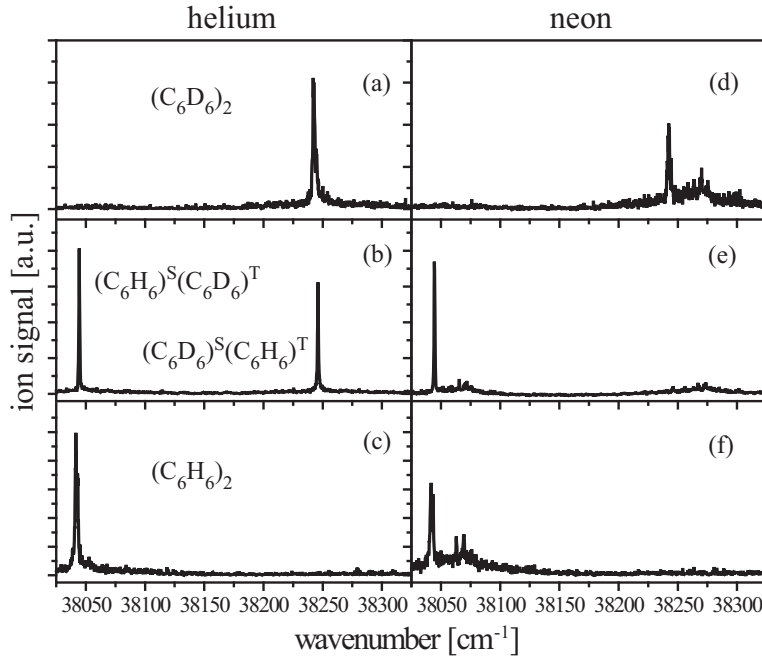


Figure 4.1: Two-color (1+1')-REMPI spectra of the benzene dimer around the origin of the $S_1 \leftarrow S_0$ transition. The measurements are performed in a molecular beam using helium (left) and neon (right) as a carrier gas. The upper spectra are recorded on the mass of the deuterated homodimer, the middle spectra on the mass of the mixed dimer and the lower spectra on the mass of the protonated homodimer. When neon is used as a carrier gas, the mixed dimer with the protonated monomer unit in the "stem" position is exclusively observed.

the second sharp peak is observed when using helium as carrier gas. Similar observations have been made before [55, 56]. The origin of the broad structure has so far not been fully understood and it is presently not clear why this structure is apparently absent when using helium as carrier gas.

In order to understand the differences in the dominant sharp spectral features observed for $(C_6H_6)(C_6D_6)$ in helium and neon, it is instructive to consider the benzene dimer in somewhat more detail. Theory suggests a binding energy of about 980 cm^{-1} [70]. The barrier for the exchange of the two monomeric units can be estimated as being the barrier separating the T-shaped structure from the parallel displaced structure which is calculated to be 64 cm^{-1} [70] (see Figure 4.2). When the two monomeric units are identical, their exchange will not cause a change in energy. The situation is different when the two units

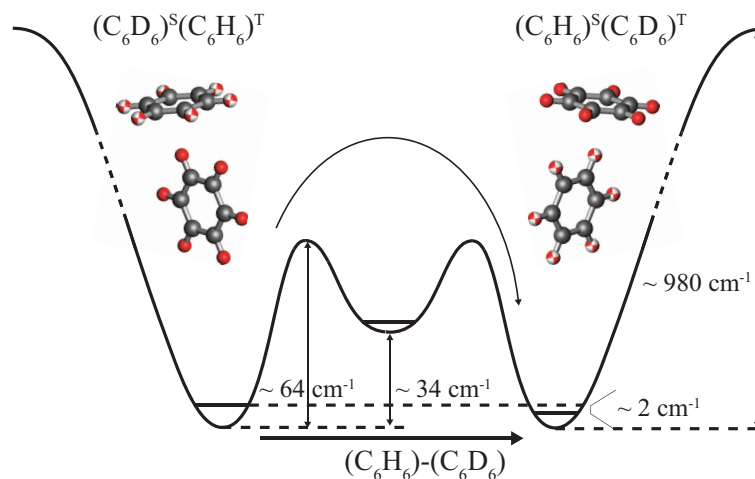


Figure 4.2: Scheme of the potential energy surface of the isotopically mixed benzene dimer $(\text{C}_6\text{H}_6)(\text{C}_6\text{D}_6)$. The two distorted T-shaped dimer isomers are separated by two transition states and a local minimum, corresponding to a parallel displaced configuration [70].

differ in isotopic composition. In that case, the electronic energy stays the same, however, the zero-point energy will depend on which of the monomers is in the "stem" or in the "top" position. In the "stem" molecule, hydrogen bonding causes the C-H (or C-D) vibrations to shift to the red, compared to either the "top" benzene ring or to the free benzene molecule [76]. Estimates based on experimental and calculated vibrational frequencies predict the zero-point energy of the $(\text{C}_6\text{H}_6)^S(\text{C}_6\text{D}_6)^T$ conformer to be about 2 cm^{-1} lower than that of the $(\text{C}_6\text{D}_6)^S(\text{C}_6\text{H}_6)^T$ isomer.

When the benzene molecules expand into vacuum, the adiabatic expansion causes a rapid cooling. Dimerization occurs, however, the incipient benzene dimer molecule is initially warm and cools via collisions with the buffer gas. As long as the internal energy of the dimer is above the isomerization barrier, the two subunits rapidly interchange. Once the energy drops to below this barrier, isomerization stops and the conformational distribution is frozen in. At the height of the barrier, the small difference in zero-point energy of about 2 cm^{-1} should have a negligible effect on the relative populations and one would expect a near equal abundance of the two conformations. This is indeed observed when helium is used as an expansion gas (see Figure 4.1 (b)).

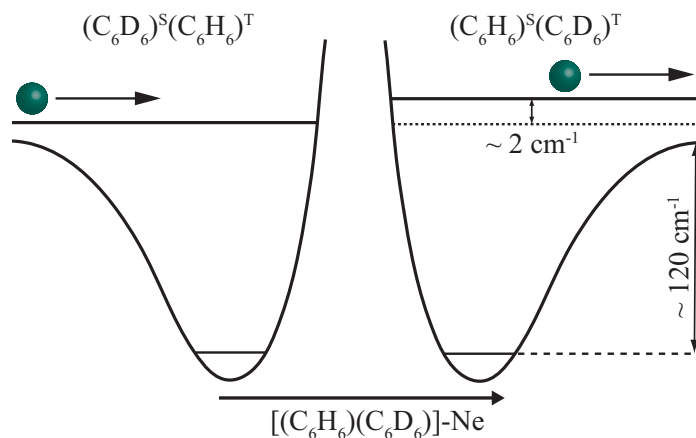


Figure 4.3: Schematic representation of the formation and dissociation of the neon-benzene dimer complex, converting the high energy isomer into the low energy isomer.

4.2.3 Catalysis model

Why is now the $(\text{C}_6\text{H}_6)(\text{C}_6\text{D}_6)$ conformer distribution completely different when neon is used as an expansion gas? When the benzene dimer molecules expand into vacuum, the collision rate drops very fast. A few nozzle diameters downstream, this rate gets so low that three-body collisions and clustering become unimportant. However, two-body collisions between the dimers and carrier gas atoms still occur frequently. As the translational temperature is then already low, those collisions occur with low energy. In such a cold collision between a benzene dimer molecule and a rare gas atom, a short lived complex is formed. The internal energy of this complex is the sum of the collision energy, the internal energy of the colliding partners before the collision and the binding energy of the complex. Late in the expansion or in the cold environment of the molecular beam, the last contribution is dominating by far. In the absence of a third collision partner, this complex will dissociate back to the reactants very fast (within a few pico- to nanoseconds, depending on the system) after the formation of the complex. Usually, such collisions and the formation of transient collision complexes are thus of little consequence. However, when the internal energy of the transient complex is higher than the barriers separating the conformers, isomerization can occur. This is exactly what can happen when a benzene dimer collides with a neon atom, as schematically shown in Figure 4.3. As an estimate for the internal energy of the benzene dimer-rare gas complex, the binding energy D_0 of a rare gas atom to the benzene monomer molecule can be taken, which is about 48 cm^{-1} [169] and 120 cm^{-1} [170] for helium and

neon, respectively. A transient complex of the benzene dimer with neon thus has enough energy for the exchange of the monomer units while a complex with helium has not (see Figure 4.2). If the complex is initially formed in the "high energy" conformer $(\text{C}_6\text{D}_6)^S(\text{C}_6\text{H}_6)^T$, complexation with neon can induce isomerization to the "low energy" conformer $(\text{C}_6\text{H}_6)^S(\text{C}_6\text{D}_6)^T$. The difference in zero-point energy of $\Delta E_{ZPE} \approx 2 \text{ cm}^{-1}$ is then available as kinetic energy for dissociating the complex, strongly enhancing the dissociation rate in that channel (see Figure 4.3 left \rightarrow right). Under the cold conditions of the molecular beam, the initial collision energy between the dimer and the rare gas atom is on the order of $E_{col} \approx 1\text{-}3 \text{ cm}^{-1}$. When the transient collision complex is formed from an initial "high energy" isomer its energy is $E_{col} + \Delta E_{ZPE}$ ($3\text{-}5 \text{ cm}^{-1}$) above the exit channel to form the "low energy" isomer, however only E_{col} ($1\text{-}3 \text{ cm}^{-1}$) above the exit channel to dissociate back to the reactant. When the transient collision complex is formed starting with the "low energy" isomer, its energy is with $E_{col} - \Delta E_{ZPE}$ either below or only slightly above the exit channel for the "high energy" isomer so that the reverse "low to high energy" isomerization is strongly disfavored. The above model is insensitive to the exact values of the energy difference ΔE_{ZPE} of the isomers involved and should thus be applicable as long as this energy difference is comparable to, or bigger than, the collision energy E_{col} .

The neon atoms thus effectively act as a catalyst for the isomerization in the benzene dimer, forming selectively the low energy isomer $(\text{C}_6\text{H}_6)^S(\text{C}_6\text{D}_6)^T$. The expression "catalyst" seems adequate since the neon atoms fulfill all conditions: (1) the neon atoms participate in the reaction they catalyze, but in the end they are available with the same properties as before the reaction (2) neon atoms lower the effective barrier/activation energy for the interconversion by following an alternative reaction channel, (3) neon atoms increase the reaction rate of the conformational interconversion and (4) neon atoms act selectively on the "high energy" isomer. The only difference to "normal" catalysts is that the interaction between the neon atom and the benzene dimer is dispersive and does not lead to the formation of a classical chemical bond.

This mechanism, in combination with calculated energies [70, 169], also predicts that the parallel displaced isomer should not survive in the molecular beam, as already helium would catalyze its destruction (see Figure 4.2). When using argon as a carrier gas, the same behavior as for neon is observed (not shown). This is again perfectly consistent with the model, since the binding energy between argon and benzene ($D_0 \approx 380 \text{ cm}^{-1}$ [171]) is even higher than in the case of neon.

4.2.4 Application

This mechanism is most likely of general importance. For example, it has been experimentally shown that the abundance of a particular conformer of the amino acid phenylalanine, namely of conformer E (nomenclature according to Reference

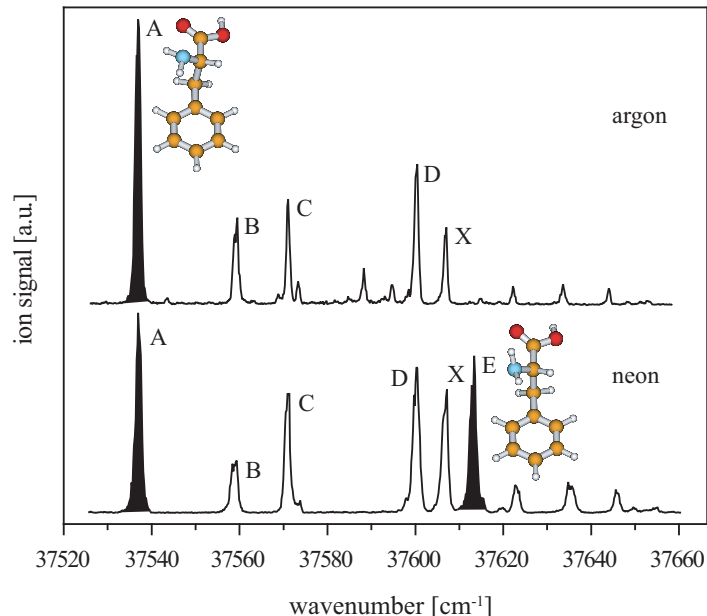


Figure 4.4: Electronic excitation spectrum in the region of the origin transition of the amino acid phenylalanine in the gas phase. While in argon the conformers A, B, C, D and X are identified, in neon an additional conformer, conformer E, is observed and the intensity of the signal representing conformer A is significantly reduced. Weak, additional peaks are observed in the spectrum to the low energy side of conformer D, when using argon as a carrier gas. These peaks probably originate from the excitation of complexes with argon atoms, which dissociate upon ionization, leaving an imprint of the spectrum of the phenylalanine-argon complex on the spectrum of plain phenylalanine.

[152]), in a supersonic expansion critically depends on the carrier gas that is being used. While a strong spectral feature around 37613 cm^{-1} is observed in the electronic excitation spectrum using neon as a carrier gas, no evidence of conformer E is found in the spectrum using argon as a carrier gas (see Figure 4.4). Additionally, the intensity of conformer A is increased in the spectrum when using argon. The same observation has been made independently by others [172]. The barrier for interconversion from conformer E to A is with 436 cm^{-1} very low [173]. It seems possible that the binding energy of phenylalanine to argon is as large as or even larger than this value. Furthermore, interconversion from conformer E to A comes along with an energetic stabilization of about 50 cm^{-1} . It seems likely that the above described model applies here as well.

Also, it is interesting to note that there presently is a large activity in the field of cold collisions [174]. This model is a potentially very important

application of cold collisions, namely the use of cold collisions in the preparation of selected conformations of gas phase molecules.

4.2.5 Conclusion

A mechanism describing the conformational interconversion catalyzed by rare gas atoms is proposed based on experimental results on the abundances of two conformers of $(\text{C}_6\text{H}_6)(\text{C}_6\text{D}_6)$ in a molecular beam with various carrier gases. Application to other systems than the benzene dimer demonstrate the relevance of this mechanism.

Briefly, in the cold environment of a molecular beam, the translational energy available in collisions is often not high enough to overcome barriers. The formation of a (short lived) complex with a collision partner, however, increases the internal energy by the complex binding energy which allows it to surmount barriers separating different isomers. Such a mechanism works best at low temperatures. In that case, even small energy differences can be large compared to the collision energy, strongly favoring a conversion from high to low energy isomers. The final conformational distribution can then resemble a thermal distribution at the prevailing translational temperature.

4.3 Conformational interconversion controlled by selective vibrational excitation

4.3.1 Introduction

Molecules in the size regime of amino acids can adopt various conformations that are often close in energy and separated by low barriers. Therefore, numerous isomerization pathways are feasible. The conformational distribution and dynamics can be investigated by a variety of optical [175–179] and non-optical [180] methods, using laser irradiation or external electric fields, respectively. For the first time optically induced isomerization has been observed in the nitrous acid HONO in a low temperature matrix (*cis-trans* isomerization by IR radiation) [181]. Laser induced excitation can raise the internal energy of a molecule in a controlled way. The additional energy excites a chosen vibrational mode of a specific conformer, and thus mode and conformer specific information can be obtained. Conformer specific IR-UV pump probe spectroscopy in combination with collisional cooling in a molecular beam allows one to study conformational interconversion.

The molecule chosen for the following experiment is the amino acid L-phenylalanine*. Intensive experimental and theoretical investigations reveal that the six spectroscopically identified structures (see Figure 4.4) correspond

*Phenylalanine is chiral and L designates the enantiomer.

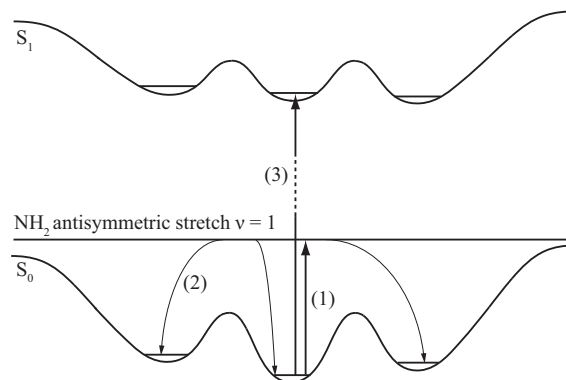


Figure 4.5: Schematic representation of the involved energy levels in the IR pump - UV probe experiment. (1) IR radiation excites the NH_2 antisymmetric stretch vibration of a chosen conformer. (2) Collisional cooling relaxes the excited molecules to the original or to a different conformational minimum. (3) The population changes are probed by a UV laser later in the collision free region of the expansion.

to the lowest energy conformers of phenylalanine [152, 157, 173, 182–185]. More details about phenylalanine are given in chapter 5.

4.3.2 Experimental method

Phenylalanine is laser desorbed from a graphite target (see section 1.2.1) and entrained in a gas pulse of neon atoms released from a Jordan valve. Early in the supersonic expansion the molecular beam is intersected by an IR laser beam. The IR laser energy is fixed to the NH_2 antisymmetric stretch frequency of a specific conformer. A fraction of the population of this conformer absorbs the IR radiation, depleting the ground state population. The NH_2 antisymmetric stretch vibration in phenylalanine is about at 3400 cm^{-1} and thus higher than the barriers separating each of the six conformers [173]. This additional amount of energy is available to overcome isomerization barriers and to drive conformational isomerization. After IR excitation still many collisions with rare gas atoms occur in the molecular beam, allowing the excited molecules to relax collisionally to the vibrational ground state level of the initial conformational minimum or to that of a different conformer. The collisional cooling can result in a modified conformer distribution which is then probed by Resonance Enhanced Multi Photon Ionization exciting the $S_1 \leftarrow S_0$ transition in the collision free region of the supersonic expansion. The UV laser is scanned in the range between 37530 and 37670 cm^{-1} and the difference in the REMPI signal with and without previous IR excitation reflects the change in conformational population. The

principle of this IR-UV pump probe experiment is schematically shown in Figure 4.5. In contrast to usual IR-UV pump probe experiments, the vibrational and electronic excitation are spatially and temporally separated and collisions need to occur between both events. The conformer distribution after conformer selective IR excitation and collisional cooling can be systematically studied, revealing isomerization barrier heights and feasible pathways for the interconversion between the different conformers [164].

4.3.3 Results and Discussion

In Figure 4.6 the UV spectrum in the region of the $S_1 \leftarrow S_0$ origin transitions of the six phenylalanine conformers A, B, C, D, X and E (nomenclature according to Reference [152]) with and without previous IR excitation are shown as solid black and gray lines, respectively. The IR laser is fixed to 3418 cm^{-1} to excite the NH_2 antisymmetric stretch vibration in conformer A. Conformer A has been chosen for vibrational excitation because it is among the low energy isomers the one with the second highest energy [173] and collisional relaxation to the ground state of another (energetically lower lying) conformer seems very likely since this process is accompanied by an energetic stabilization. Below each pump probe spectrum the difference spectrum ((IR+UV)-(UV)), representing the influence of prior IR excitation on the REMPI signal, is shown as a dashed line. A signal above the baseline corresponds to a population gain of the respective conformer, whereas a depleted population results in a signal below the baseline. The intensity of the signal of a conformer can be related directly to its population.

The spectra shown in Figure 4.6 are measured using neon and argon as a carrier gas. Both difference spectra (dashed lines) are qualitatively very similar. Other carrier gases like xenon or CO_2 have also been used, giving similar results but with an inferior signal to noise ratio and are therefore not shown. In the IR-UV pump probe spectra (black lines) the population of conformer A is depleted as a result of the excitation of its NH_2 antisymmetric stretch vibration. The weak spectral feature at the blue side of conformer C is due to a hot band of conformer A and therefore, also depleted. In argon the depletion of conformer A is more pronounced (33%) than in neon (13%). A small gain of population is found for the conformers B and C in argon. In neon, conformer C and a vibrationally excited state about 10 cm^{-1} to the blue of conformer E have a slightly increased population. However, only about one third of the depleted population contributes to the population gain of other conformers. In the difference spectra (dashed lines) weak positive and negative features for the conformers D and X are present. These features are most likely due to noise since they each seem to have equivalent contributions to the gain and to the depletion of the population of the respective conformer. However, the negative difference signal observed for conformer X can also partially be due to excitation of its NH_2 antisymmetric stretch vibration, simultaneously to the excitation of conformer A (see Figure 4.7). The same applies to conformer E.

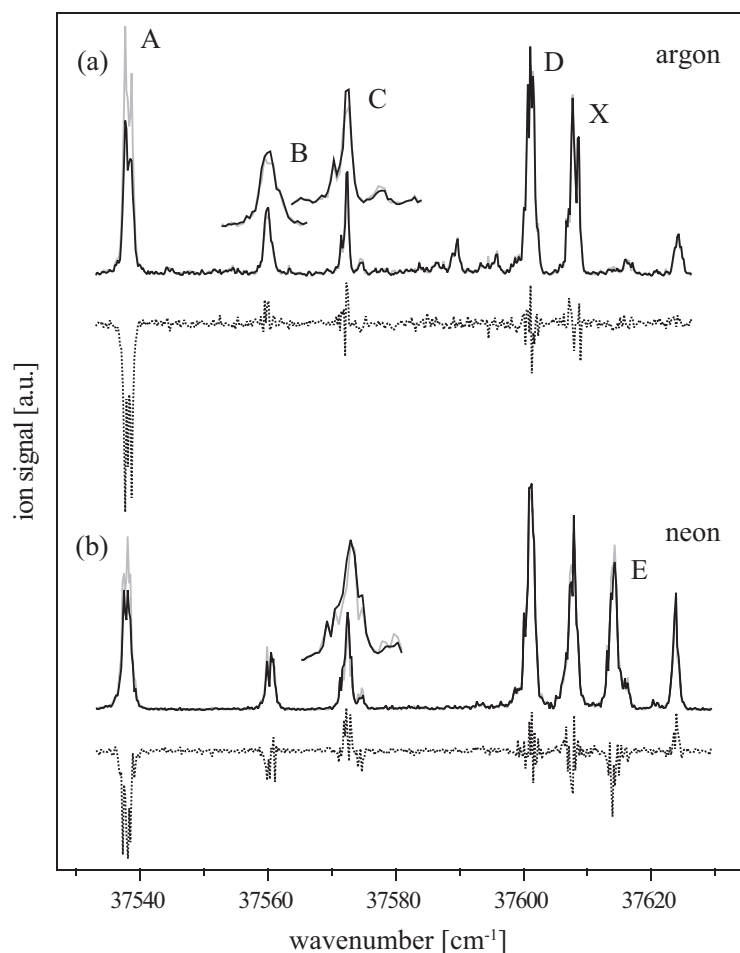


Figure 4.6: REMPI spectra of L-phenylalanine in the region of the vibrational origin of the $S_1 \leftarrow S_0$ transition recorded with (black line) and without (gray line) excitation of the NH_2 antisymmetric stretch vibration of conformer A. Spectrum (a) is measured using argon as a carrier gas and spectrum (b) with neon. The difference spectra (dashed lines below the respective absolute spectra) show directly the change of the conformational distribution induced by vibrational excitation.

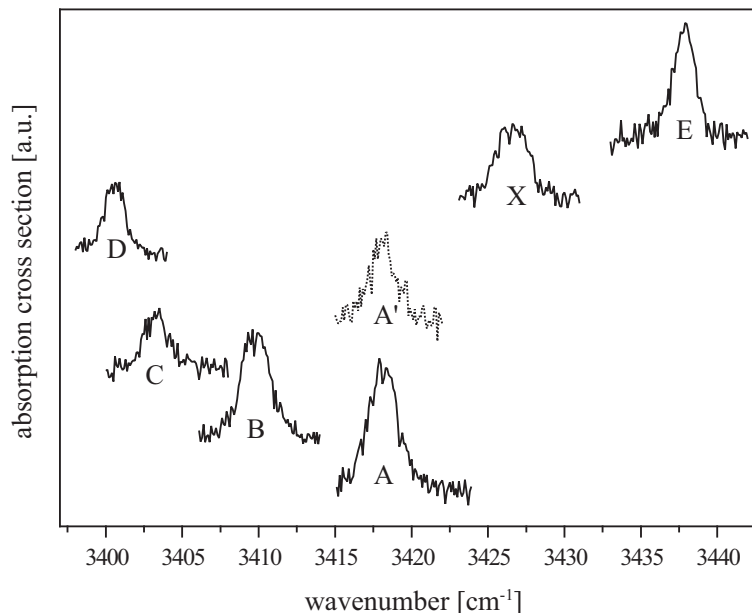


Figure 4.7: Absorption bands of the NH_2 antisymmetric stretch vibration in the six low energy conformers A, B, C, D, X, E. The spectra are vertically arranged according to their increasing $S_1 \leftarrow S_0$ excitation energy. The absorption spectrum A' (dashed line) results from a hot band of conformer A.

It is also worthwhile to note that no signatures of new/additional conformers appear in the UV spectrum.

From the experimental results shown in Figure 4.6 it is difficult to draw firm conclusions. The most striking observation made is that the depletion signal of conformer A is larger than the sum over the population gain signals of all other ground state conformers. This can most probably be ascribed to inadequate cooling after the vibrational excitation. Consequently a fraction of molecules remains in a vibrationally excited state and is thus invisible for the UV laser that probes the conformational distribution.

Cooling conditions are strongly dependent on the properties of the supersonic expansion, i.e. on the experimental setup. In this experiment phenylalanine is desorbed from a graphite target with a laser that is directed perpendicularly to the molecular beam axis (see Figure 1.2). The desorbed molecules thus have a momentum opposite to the propagation direction of the laser beam and perpendicular to the molecular beam axis. The first collisions with the rare gas atoms, released from the nozzle just behind the desorption spot, force the molecules in the direction of the molecular beam axis and are lost for cooling.

Only subsequent collisions can cool the internal degrees of freedom of the molecules. To ensure that the molecules are cold when they get vibrationally excited, the IR excitation occurs 3-4 mm downstream from the desorption spot. The collision rate drops rapidly with the distance from the valve, and in the region downstream the IR excitation it is much reduced. In this region, however, collisions are needed to relax the vibrationally excited molecules into the zero-point levels of the conformational minima accessible to them. This process can be incomplete, and a fraction of the excited molecules is lost for the UV probe. Changing the distance of the IR excitation from the nozzle is limited by two events: (1) If the IR laser intersects the molecular beam very close to the desorption spot the molecules are excited before they have been sufficiently cooled. Thus the absorption bands of different conformers are broadened and overlap, with the consequence that also other (warm) conformers absorb IR radiation. (2) If IR excitation occurs relatively late in the supersonic expansion, the collision rate afterwards is too low to cool the vibrationally excited molecules to one of the conformational ground states. The population of the chosen conformer is depleted, but the spectra do not contain any information about the dynamics of this fraction of molecules.

An additional complication is that the excitation to the $\nu=1$ level of the NH_2 antisymmetric stretch vibration is very close in energy for the different conformers (see Figure 4.7). In Figure 4.6 IR-UV pump probe spectra are shown with the IR laser exciting this vibration in conformer A. Alternatively, the same vibration has been excited in the conformers X and E. The expected depletion can be observed but the gain of other conformational population is not more pronounced than in the spectra shown. In the energy range covered by our IR laser system (see section 1.2.1) the NH_2 antisymmetric stretch vibration, however, is the only one which has relatively narrow and not overlapping spectral features. The other spectroscopically accessible vibrations, the NH_2 symmetric stretch and the OH stretch [152], do not represent a serious alternative.

To improve the cooling conditions, the initial experimental setup has been changed (see Figure 1.2 (b)). To facilitate the assimilation of the laser desorbed molecules into the molecular beam, tubes of different geometries (cylindrical and conical geometries with varying diameters, lengths and angles) have been installed directly after the orifice of the valve, elongating the nozzle by a few mm. A small hole allows the desorption laser to enter the tube from above and to ablate the molecules from the graphite target in the tube. Provided that the tube is firmly attached to the valve body, the elongation of the nozzle inhibits the desorbed species to propagate perpendicularly to the molecular beam axis and supports the co-expansion of the molecules and the rare gas atoms. The collisions are expected to cool more efficiently and the IR excitation can thus occur earlier in the expansion, providing a better cooling after the optical excitation. In principle a new conformational distribution can be created further downstream in the expansion this way. In a series of REMPI spectra

(not shown) measured with such tubes installed, no significant improvement has been observed relative to the spectra recorded without the tube.

4.3.4 Conclusion and perspectives

Phenylalanine, with six low energy conformations, has been used to probe laser induced isomerization in a molecular beam. The experimental results show that vibrational excitation and subsequent cooling result in an incomplete redistribution of the relative conformational population. IR induced depletion of the population of one conformer can clearly be observed, however, the vibrationally excited molecules do not seem to vibrationally relax and to contribute to the population of any other conformer. This is most probably due to the experimental arrangement. The results might be more convincing if the collisional cooling before and after IR excitation is more efficient than in our experimental setup.

More efficient cooling can be achieved for example if the molecules and the carrier gas are both released from a valve and co-expanded into vacuum, instead of an expansion of rare gas atoms that pick up laser desorbed molecules just after the nozzle of the valve. Species with a substantial vapor pressure can be premixed with the carrier gas, solids might be heated in a sublimation oven or in a chamber of the valve body, as for example in the setup presented by Zwier *et al.* [164]. A second possible attempt can be to use laser desorption in combination with a second supersonically expanding beam providing additional collision partners that cool the molecules efficiently after IR excitation. The first expansion can thus exclusively be used to cool the laser desorbed molecules, preparing them in the lowest rotational and vibrational states before IR excitation. After IR excitation collisions occur with atoms/molecules of the second beam. Both attempts would allow for a rapid cooling of the internal degrees of freedom after the release into vacuum, thus for a selective vibrational excitation of a single conformer, and they would provide, after the laser induced excitation, better collision conditions for a more efficient relaxation of the vibrationally excited states into one/several conformational ground state(s).

The potential energy surface can also be explored by quantum control [166]. Instead of collisions with the carrier gas, shaped laser pulses dump the vibrationally excited molecules in a specific ground state conformation. From the properties of the laser fields used to reach the different conformational minima barrier heights and interconversion pathways between the single conformers can be deduced.

Chapter 5

The amino acid phenylalanine

5.1 Introduction

With the development of electrospray [186] and matrix assisted laser desorption and ionization (MALDI) [187] it has become possible to bring large molecules intactly into the gas phase. This innovation, allowing one to study also larger molecules separately, free from perturbations, has paved the way to experiments on isolated biologically relevant systems, such as peptides. However, to understand their dynamics and structural properties on a fundamental level it is instructive to investigate their building blocks, amino acids and small sequences in a bottom up approach. The need for such gas phase experiments arises for example from the relevance of understanding the mechanism of protein folding, which crucially controls the functionality of the protein, on the molecular level.

Since the pioneering work of Levy *et al.* in 1986 [188], amino acids have been investigated intensively in molecular beams, especially the aromatic amino acids, tryptophan [9, 150, 188–200], phenylalanine [152, 172, 173, 182–185, 201–204] and tyrosine [153, 182, 192, 198, 205], which can, due to their aromatic chromophores, easily be probed by UV spectroscopy. Also small peptides are intensively studied [206–214]. Although being comparatively small, amino acids can have different relative orientations of the backbone and side-chain. The barriers between those conformers are often low and at room temperature conformational interconversion occurs frequently so that single conformers cannot be isolated. Under the cold conditions of a supersonic expansion, however, these barriers appear high compared to the internal energy of the amino acid

Adapted from:

G. von Helden, I. Compagnon, M. N. Blom, M. Frankowski, U. Erlekam, J. Oomens, B. Brauer, R. B. Gerber, G. Meijer, *Phys. Chem. Chem. Phys.* (2008) DOI: 10.1039/b713274c

and specific conformers can be discriminated. The resultant conformational distribution depends on the relative conformational energies, barrier heights and temperature. Therefore, amino acids, especially phenylalanine, serve as a benchmark system to investigate the conformational landscape in small molecular systems.

Studies on isolated amino acids (and small peptides) represent also a good preparation to investigate the amino acids embedded in a (partial) solvation shell. While in the gas phase amino acids are neutral [150, 188, 215–219], they adopt a zwitterionic structure in solution [216, 217, 219]. Several investigations of clusters with a gradually increasing number of solvent molecules (water, methanol) exist [172, 183, 195, 196, 220–225], discussing the observations in terms of isolated amino acids and solvated model systems [33, 34, 226, 227]. In a recent solvation experiment on tryptophan, it could be shown that at least five (eight) methanol molecules are necessary to observe spectral evidence of the CO_2^- stretch (NH_3^+ bend) vibration, indicating a zwitterionic structure of tryptophan [200]. Such experiments are important, since they reveal the structural properties and energetics at the limit between gas and solvated phase and allow one to determine the conformer specific energy, necessary to stabilize the zwitterionic structure. The potential energy surfaces of solvated amino acids are even more complex than those of the isolated ones and therefore a challenging playground for theoreticians, who aim to unravel the experimental results. For the investigation of complex, amino acid containing systems a detailed knowledge about the amino acid itself (structures and energies of conformers and energetic pathways connecting them) is important.

IR spectroscopy makes an important contribution to the exploration of intrinsic molecular properties. As the positions and shapes of spectral lines depend strongly on the geometric properties, the IR absorption spectrum is a unique identifier for the molecular structure.

The amino acid phenylalanine has been studied extensively in the gas phase, and five [182], later six [152] individual conformers have been discriminated in electronic excitation spectra. The first five conformers (see Figure 5.1) could be assigned by Snoek *et al.* [152] by comparing their IR spectra to those of calculated structures. These conformational structures can be divided in two subgroups according to the orientation of their internal hydrogen bonds. One subgroup constitutes the conformers B and X which both are stabilized by a daisy chain of hydrogen bonds from the carboxyl to the amino group, and from the amino group to the π -electrons of the phenyl ring. Conformers A, C and D are in a second group in which the backbone and side-chain do not interact via a $\text{NH}_2 \rightarrow \pi_{\text{phenyl}}$ hydrogen bond and in which the direction of the hydrogen bond between the carboxyl and the amino group is reversed, i.e. the NH_2 hydrogen atoms serve as proton donor and the carboxyl group as proton acceptor (see Figure 5.1). In the original work [152] IR spectra of conformer E have not been accessible due to its weak population under the experimental conditions. Initially, conformer E has been assigned to the theoretical low energy structure

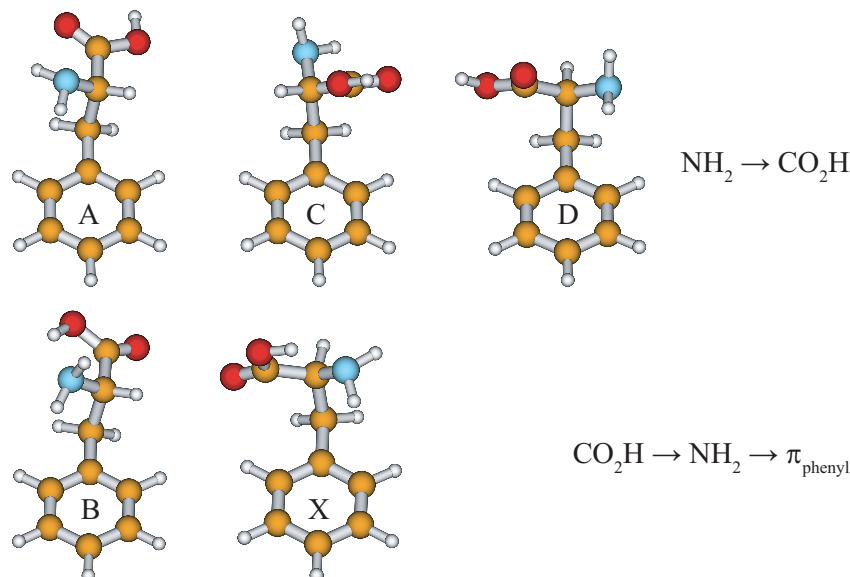


Figure 5.1: Structures of five low energy conformers of phenylalanine calculated at the MP2/6-311+(2df,2p) level of theory [173]. The labeling scheme is the same as the one introduced in Reference [152].

"IV" which belongs to the group with the cooperative sequence of hydrogen bonds $\text{COOH} \rightarrow \text{NH}_2 \rightarrow \pi_{\text{phenyl}}$ [152]. Later, conformer E has been assigned to structure "IX" from Reference [152] with a hydrogen bond of the $\text{NH}_2 \rightarrow \text{COOH}$ type [185]. This assignment is based on a comparison of UV rotational band contours of the experimentally observed conformers with those of a variety of calculated structures. However, such a comparison may not be unambiguous as the rotational band contours of the calculated structures resemble one another in some cases and the error bar of the underlying calculations is unknown.

In this chapter the experimental IR spectrum of the missing conformer E in the spectral range between 3150 and 3450 cm^{-1} is presented and compared to those of the conformers A and X, as representatives of the two structural subgroups. On this basis it is possible to unambiguously assign the structure of conformer E to one of both groups. Furthermore, the relative abundances of jet cooled phenylalanine conformers with respect to their relative zero point energies are investigated.

5.2 Experimental method

The experimental setup is described in more detail in section 1.2.1. Briefly, the non-volatile and thermally labile phenylalanine is laser desorbed from a graphite target and entrained in a pulse of neon atoms, expanding into vacuum. The molecular beam is skimmed and interrogated by pulsed UV and IR laser beams. The cold molecules are electronically excited and subsequently ionized by two UV-photons of the same energy (1-color REMPI). The ion signal is recorded as a function of the photon energy, giving the UV spectrum. IR spectra are obtained by ion-dip spectroscopy. In this technique the IR laser interacts ~ 50 ns prior to UV excitation with the internally cold molecules. If the IR laser is resonant with a vibration of the electronic ground state, population is transferred to a vibrationally excited state and a depletion in the ion signal is observed. By measuring the ion signal while tuning the IR photon energy, the ion-dip spectrum is recorded. Conformer selection is achieved by selecting the specific electronic excitation energy (see Figure 4.4). For these experiments the natural enantiomer L-phenylalanine is used.

5.3 Results and Discussion

5.3.1 Missing conformer E

In Figure 5.2 the IR spectrum of phenylalanine conformer E is shown in the range between 3150 and 3450 cm^{-1} , together with those of conformers A and X. Conformer A represents the group of conformers which have a $\text{NH}_2 \rightarrow \text{COOH}$ hydrogen bond, while X represents the other group with a $\text{COOH} \rightarrow \text{NH}_2 \rightarrow \pi_{\text{phenyl}}$ oriented chain of hydrogen bonds. In the spectrum of conformer E two narrow absorption bands at 3359 and 3438 cm^{-1} occur which result from the symmetric and antisymmetric NH_2 -stretch vibrations, respectively. The symmetric NH_2 -stretch modes of conformers A and X appear as weak spectral features redshifted from the appropriate transition in conformer E, both at 3340 cm^{-1} . The antisymmetric NH_2 -stretch modes (intense and narrow absorption signal) of conformers A and X appear redshifted by 19 and 11 cm^{-1} , respectively, from the transition of conformer E. The shape of these two modes are very similar for the three different isomers, although slightly broadened for conformer X. Solely based on the symmetric and antisymmetric NH_2 -stretch vibrations a classification of conformer E to one of both subgroups is not possible. In the spectrum of conformer X an additional broad and intense absorption band is observed at 3224 cm^{-1} , resulting from the OH-stretch vibration which is, however, involved in a hydrogen bond to the nitrogen atom of the amino group, and thus occurs at a lower frequency than an unperturbed OH-stretch vibration [152]. Such a feature is not present in the spectra of conformers A and E. This observation indicates that the structure of conformer E is rather similar to that

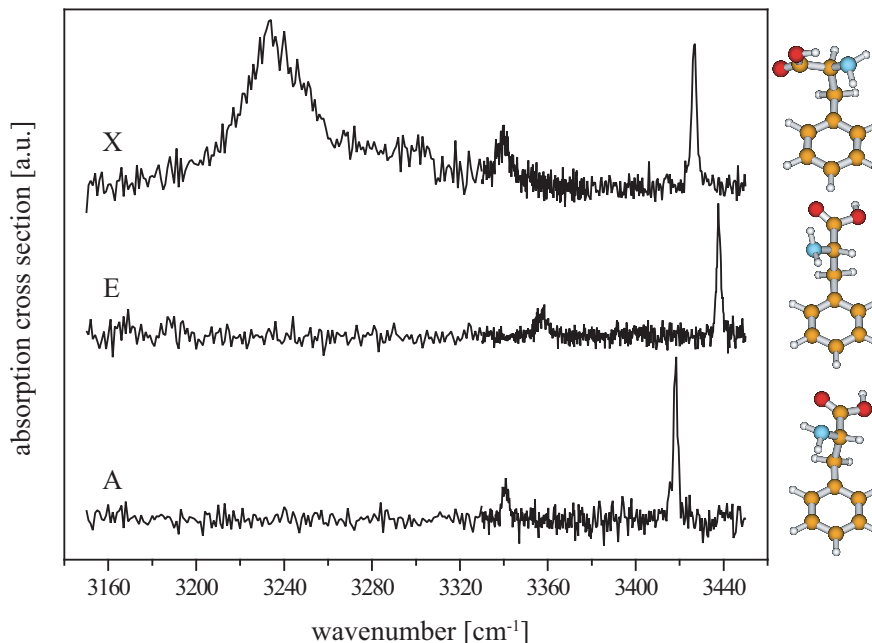


Figure 5.2: IR spectra of the phenylalanine conformers A, E and X in the range between 3150 and 3450 cm^{-1} . The calculated structures [173] support the assignment of conformer E to the structural subgroup represented by conformer A.

of conformer A and that it possesses a $\text{NH}_2 \rightarrow \text{COOH}$ hydrogen bond. In Figure 5.2, to the right of the appropriate spectra, the proposed structures [173] of the conformers A, E and X are shown.

The assignment is also supported by other observations: (1) In the REMPI spectrum of phenylalanine the intensities of the spectral features of the conformers A, C, D and E are substantially reduced when being solvated by one water molecule, whereas the monohydrated conformers B and X appear with similar intensities as their isolated counterparts [183]. Monohydrated structures with the water molecule binding to the carboxyl group are calculated to be lower in energy than those with the intermolecular hydrogen bond to the nitrogen atom of the amino group. This implies that stable phenylalanine-water complexes are formed of conformers whose carboxyl group is free and not involved in an intramolecular hydrogen bond (A, C, D, E). The depleted signals of the isolated molecules alone are not an unambiguous evidence for the formation of stable water complexes and thus for the common structural motif of the respective conformers, however this observation supports the results presented here very well. (2) Photoionization efficiency measurements [201] show a higher ionization

potential for conformers B and X than for A, C, D and E. Conformers with a backbone side-chain interaction, i.e. a $\text{NH}_2 \rightarrow \pi_{\text{phenyl}}$ hydrogen bond, are concluded to turn this in the S_0 state attractive interaction into a repulsive one upon ionization because of the newly emerged cationic charge on the phenyl ring, raising the ionization potential [184]. This observation indicates that conformer E has, like the conformers A, C and D, no backbone side-chain hydrogen bonding of the type $\text{NH}_2 \rightarrow \pi_{\text{phenyl}}$ and is thus different from the conformers B and X. However, it cannot determine differences between conformer E and A, C and D, such as the orientation of the hydrogen bond between the carboxyl and the amino group.

The results presented in this section "Missing conformer E" have been obtained in similar form independently in another laboratory at the same time [172, 202], supporting the correctness of our data.

5.3.2 On the observed conformer abundances of phenylalanine

Calculation

The structures (and IR spectra) of 14 conformers are calculated at the B3LYP/6-311++G(2d,p) as well as at the MP2/6-311+G(2df,2p) level*. In addition, single point energy calculations are performed at the CCSD(T)/6-311+G(2df,2p) level, using the MP2 optimized structures. The structures considered include the nine lowest energy structures from Reference [152] and [185], three additional low energy structures from Reference [204], as well as two low energy structures from Reference [203]. Transition states for the interconversion between the nine lowest energy conformers are considered as well, some of them being adapted from Reference [204].

Comparison of the theoretical IR spectra to experimental ones [173] in the range between 500 and 1900 cm^{-1} allows one to assign molecular geometries to the conformers A, B, C, D, X and E (not shown). As not relevant for the following discussion, the IR spectra are not discussed here. Briefly, the spectra resulting from B3LYP and MP2 calculations are very similar and it can be concluded that the large computational effort for the MP2 calculations is at least for this system not justified.

The vibrational state densities are calculated for the nine lowest energy structures as a function of energy with the Beyer-Swinehart algorithm [228], using the B3LYP vibrational frequencies. These state densities are used to estimate the relative conformer populations after cooling in the supersonic expansion.

*The calculations are run by G. von Helden.

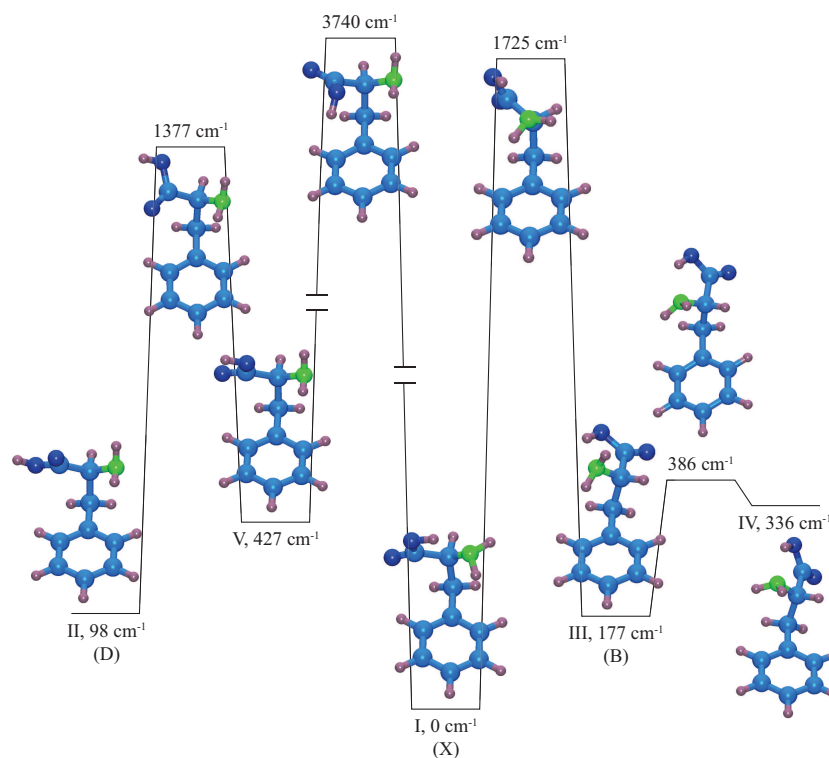


Figure 5.3: Structures and their relative energies are presented from different regions of the conformation space. The structures I, III and IV, having an internal $\text{CO}_2\text{H} \rightarrow \text{NH}_2$ hydrogen bond, are separated by the highest transition state at 3740 cm^{-1} from structure V, having a $\text{NH}_2 \rightarrow \text{CO}_2\text{H}$ hydrogen bond. A transition state at 1377 cm^{-1} leads from this structure to structure II, and therefore to the structures depicted in Figure 5.4. Some of the low energy structures can be assigned to the experimentally observed conformers A, B, C, D, E and X. The assignments are given in brackets.

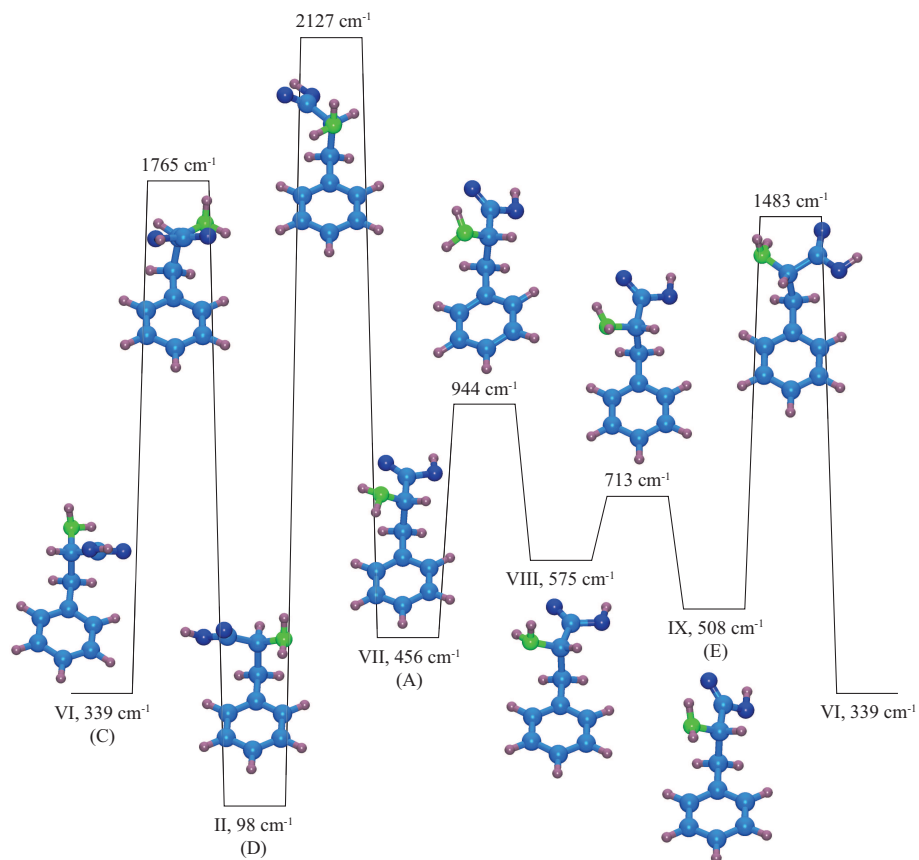


Figure 5.4: Relative energies and structures for five of the nine lowest energy conformers, as well as of the transition states separating them. Some of the low energy structures can be assigned to the experimentally observed conformers A, B, C, D, E and X. The assignments are given in brackets. The sequence corresponds from left to right to a clockwise rotation of the amino acid group about the C_α-CH₂C₆H₅ bond, accompanied by a reorientation of the amino group.

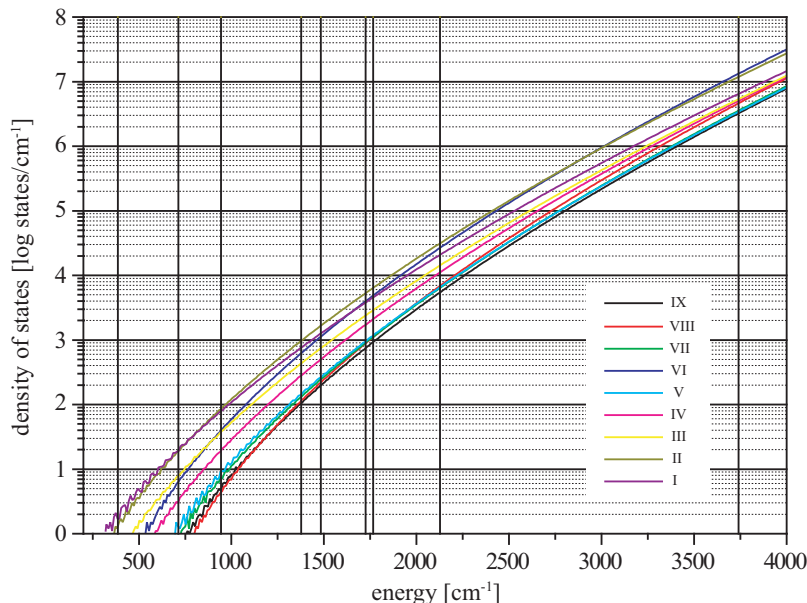


Figure 5.5: Vibrational state densities of the nine lowest energy conformers of phenylalanine. The relative origins are shifted according to their relative zero point energies.

The performance of the model - comparison between experimental and calculated conformer distributions

In Figures 5.3 and 5.4 the relative energies and structures of the nine lowest energy conformers of phenylalanine, as well as of several transition states separating them are shown. Experimentally it is observed that several conformers are simultaneously present in the molecular beam (see Figure 4.4). The vibrational and rotational temperature of the molecules can be estimated to be a few Kelvin. Thus, considering the energy differences between the experimentally observed conformers, it becomes clear that they cannot be in thermal equilibrium. The heights of the interconversion barriers, as well as the experimental conditions, crucially affect the dynamics of the different conformers. Just after laser desorption the vaporized molecules have high internal energies, much higher than the transition states shown in Figures 5.3 and 5.4, and under these conditions conformations are not defined. In the supersonic expansion the internal energy is gradually lowered via inelastic collisions with the carrier gas. Consecutively the molecules reach the energies of the different barriers. At the level of the highest barrier the population is separated in two groups which are separated in subgroups when the energy levels of the next lower barriers are reached. From

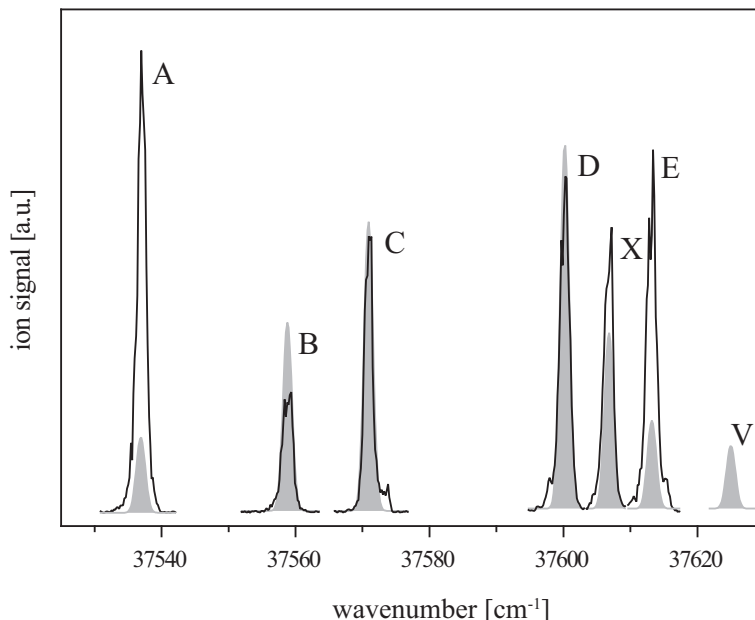


Figure 5.6: Comparison of the simulated intensity distributions (gray Gauss functions) with the experimental abundances (black contours) of conformers A, B, C, D, X and E, probed by 1-color REMPI and using neon as a carrier gas.

Figures 5.3 and 5.4 it can be seen that the highest considered barrier is between structure I and V and is 3740 cm^{-1} above the lowest energy structure. At this energy the population separates in two populations, one of which will be able to form the structures I, III and IV. The structures II, V, VI, VII, VIII and IX can originate from the population trapped "on the other side" of the barrier. The second highest barrier, 2127 cm^{-1} higher in energy than the lowest energy structure, corresponds to the transition state between structures II and VII, which represent two minima on the internal rotational path of the amino acid group about the $\text{C}_\alpha\text{-CH}_2\text{C}_6\text{H}_5$ bond. The highest barrier on a circular path has not to be crossed bringing about that the third highest barrier is the next relevant energy level to be considered, which is the transition state between structures II and VI at 1765 cm^{-1} , separating structure II from VI–IX. With further cooling the molecules reach consecutively the different barriers separating them in more and more conformational groups.

The relative population of the different minimum structures can be estimated assuming quasi equilibria at the height of the barriers separating them. Each barrier constitutes two new conformational subgroups. The ratio of the vibrational state densities of both subgroups is used to determine the relative

population at each conformational barrier. The model is independent on the rotational temperature as long as it is small compared to the conformational barriers. The nature of the carrier gas and its interactions with the molecules are not included in this model. Following all barriers from high to low energy gives the relative population of the single structures. The resulting populations are 14, 29, 11, 4, 5, 23, 6, 3 and 4% for the structures I–IX, respectively. The two lowest barriers at 713 and 386 cm^{-1} are so low, that it is likely that under the experimental conditions the structures being separated by the respective barriers cannot be distinguished. In Figure 5.6 the theoretical conformational distribution is compared to the experimental REMPI spectrum, using neon as a carrier gas. Structure V does not have an experimental counterpart and is shown for comparison to the right of the spectrum. The conformers A-E are assigned to the simulated structures according to Reference [173]. The calculated intensity of the structures III and IV as well as VIII and IX are added up, as the respective barriers are very small and can be overcome via collisions with the carrier gas.

Interestingly, the lowest energy conformer X (I) is predicted to be less populated than the conformers B (III+IV), C (VI) and D (II), and conformer D (II) to be the most intense one. The discrepancies between the expected relative population (when considering exclusively the relative zero point energies) and the simulated one can be rationalized by the relatively slow increase of the density of states as a function of energy. This in turn can be attributed to the strong intramolecular hydrogen bonds rendering the molecules more rigid and shifting the low frequency modes to higher frequencies.

Considering the crudeness of the model and the uncertainties in the computed parameters (relative energies, vibrational frequencies and state densities) the agreement between experimental and calculated intensities is surprising. Additionally, the experimental intensities do not necessarily reflect the neutral populations, as parameters such as Franck-Condon factors, absorption cross sections and excited (intermediate) state life times affect the observed distribution.

In the model only the nine lowest energy structures I–IX are considered. However, other structures with higher energies exist [173] and contribute to the relative population at energies as high as 3740 cm^{-1} , which is the highest barrier considered. All those "high energy" structures, although not populated at low energies, can act as funnels for other structures. Therefore, all structures that are in the energy range up to the highest relevant barrier (3740 cm^{-1}) would need to be considered for a more precise estimation of the conformational distributions.

5.4 Conclusion

The observation that conformer E is substantially populated in a molecular beam when using neon as a carrier gas allows one to spectroscopically investigate its properties, to compare it to the other (known) phenylalanine conformers and to make a structural assignment. It is shown that IR spectroscopy in the region of NH- and OH- stretch vibrations ($3150 - 3450 \text{ cm}^{-1}$) is perfectly suited to probe the structures of (non)hydrogen bonded amino acid backbones. The conformers of phenylalanine are separated in two subgroups according to their intramolecular hydrogen bonds. Its IR signature allows one to assign conformer E to one of these two subgroups.

The complex dynamics in a supersonic expansion and particularly the potential energy surface of a multi-conformational molecule strongly influence the observed conformer distribution. The pure effect of the potential energy surface has been studied with a simple model. At characteristic points (saddle points) on the potential energy surface, the relative conformer distribution is deduced from the relative vibrational state densities, assuming quasi-equilibria near the interconversion barriers. This model, although being rough, appears to describe the experimental conformer distribution reasonably well.

Summary and outlook

In order to understand the properties and functionality of biological matter on the macroscopic level, first the properties of the isolated molecular building blocks have to be investigated, aiming to understand their intrinsic properties. In further studies the parameters can be adapted to the near-natural environment.

Weak intra- and intermolecular interactions (of dispersive and electrostatic nature) can significantly influence the molecular structure and are thus of fundamental importance. In order to investigate these interactions at a fundamental level, simple model systems, primarily in the gas phase, can be studied. If they consist of a considerable amount of atoms, they can be flexible, and a variety of structures can exist whose relative population can yield valuable information on stabilizing and destabilizing interactions. Therefore, the experimental parameters influencing the relative abundances of the individual structures have to be well known and adequately considered in the interpretation of the experimental results.

In this thesis the structure and dynamics of the benzene dimer (C_6H_6)₂ have been spectroscopically investigated in the gas phase in the spectral range of rotations, vibrations and electronic transitions and discussed in terms of symmetry. The benzene dimer is a weakly bound van der Waals complex that can serve as a model system for dispersive intermolecular interactions. Due to the weak intermolecular interaction ($\sim 1000 \text{ cm}^{-1}$) a satisfactory theoretical description of the minimum energy structure and a precise determination of the binding energy of the benzene dimer is a challenging task. Therefore, detailed information from experimental studies needs to be available.

As the benzene dimer consists of relatively few atoms the spectra are expected to be rather clear. The benzene dimer is formed when benzene molecules, diluted in a carrier gas, are adiabatically expanded from a pressure of a few bar into vacuum. In the supersonic expansion the internal degrees of freedom of the monomeric benzene molecules are cooled via inelastic collisions with the carrier gas atoms to a rotational and vibrational temperature of a few K, and clustering can occur. Often the molecules in a supersonic expansion are not in thermal equilibrium, and in the case that a molecule can adopt various conformations

(as for example biomolecules) the dynamics of interconversion needs to be considered in order to rationalize the observed relative conformer abundances.

Depending on the balance between electrostatic and dispersive interactions, the two benzene molecules can be theoretically arranged as shown in Figure 1.9. The D_{6h} symmetry of the non-interacting benzene rings is lowered by dimerization. As the infrared (IR) activity of vibrational modes is linked to the symmetry of the molecule, symmetry reduction arising from dimerization can serve to determine fundamental modes of the benzene monomer that are IR inactive by symmetry. In chapter 2 it is shown how the C-H stretch spectra of the benzene dimer allow one to determine the so far unknown (IR and Raman inactive) fundamental mode ν_{13} of the benzene monomer.

The knowledge about the individual symmetries of the monomeric subunits is valuable information to determine the structure of the benzene dimer. For this purpose vibrational spectroscopy is a suitable tool. In the C-H stretch range two different vibrational signatures are found for the two benzene molecules, hinting to a structure with two symmetrically inequivalent benzene molecules, as for example in a dynamic, in its rigid form C_{2v} or C_s symmetric, (distorted) T-shaped geometry. This observation is in agreement with the latest theoretical results on the equilibrium structure of the benzene dimer.

Besides the experiments in the IR range, microwave (MW) spectroscopy can be used to determine the minimum energy structure (see chapter 3). The rotational spectrum of the benzene dimer has the characteristics of a symmetric top. The weak intermolecular interaction can allow for internal dynamics in the benzene dimer, that can be investigated by MW spectroscopy in combination with Molecular Symmetry (MS) group theory. From these studies it is currently assumed that both benzene subunits are arranged in a (distorted) T-shaped geometry and undertake internal rotations about their molecule fixed C_6 axes.

The experiments on the benzene dimer in this thesis are accompanied by studies on isotopically labeled species, as for example $(C_6H_6)(C_6D_6)$, in order to obtain supporting information. When assuming that the two subunits in the benzene dimer are symmetrically inequivalent, two substitution isomers of $(C_6H_6)(C_6D_6)$ are expected to exist and can be discriminated by electronic excitation. Although the electronic energy is the same and the difference in zero point vibrational energy in the electronic ground state of the two isomers is subtle, substantial differences have been observed concerning their abundances in a molecular beam. The relative abundances can be investigated as a function of the molecular beam properties, for example (as in this work) in dependence on the nature of the carrier gas, using Resonance Enhanced Multi Photon Ionization (REMPI) for detection. From the experimental observations a model has been developed, describing how collisions with rare gas atoms in a cold environment, as for example in a molecular beam, can catalyze the interconversion between structural isomers, leading selectively to the isomer with the lower internal energy (see chapter 4). The feasibility of the interconversion depends on the

height of the barrier separating the isomers involved and the binding energy between the collision partners. The mechanism works best at low temperatures where even small energy differences appear large in comparison to the collision energies.

This model applies most probably to the molecular beam experiments of the amino acid phenylalanine as well: it explains the absence of a theoretically predicted conformer in previous experimental studies and allows one to adapt the experimental conditions such that this "missing conformer" becomes experimentally accessible. The vibrational properties of the "missing conformer" have been investigated in the N-H stretch energy range allowing for a structural assignment (see chapter 5).

Six different low energy conformers of phenylalanine have been observed in a molecular beam. Considering the observed relative abundances of the various conformers together with their energy differences it can be seen that the distribution does not correspond to a distribution expected at thermal equilibrium. For a full description of the observed relative population the barriers separating the conformers have to be considered as well (see chapter 5) which requires adequate information about the potential energy surface. In order to explore the complex potential energy surfaces of multi-conformational molecules, as for example the phenylalanine, the interconversion energies and pathways have to be studied conformer selectively. This can be done, for example, in an excitation-relaxation experiment (see chapter 4). In the ideal case the excitation energy of a vibration in the electronic ground state is mode and conformer specific. If this energy is large enough to surmount (at least) one barrier separating the excited conformer from another one, a structural rearrangement can occur in the subsequent relaxation. Probing the changes of the relative conformer population as a function of the vibrational excitation energy can provide information about the potential energy surface of the system.

The experiments presented in this thesis contribute to a deeper understanding of the benzene dimer, an important model system for dispersive interactions that are often found in biologically relevant systems. Especially the experiments aiming for the internal rotations and the MS group theory are an encouraging starting point to finally solve with further studies the problems concerning the equilibrium structure and its internal dynamics. In future studies the focus should be put on isotopically labeled species.

Vibrations of highly symmetric molecules are often neither IR nor Raman active, might, however, be accessible using the here presented, elegant method which exploits IR activation by symmetry reduction upon complexation.

The model describing collision induced conformational interconversion will be helpful in molecular beam experiments of flexible molecules to understand the observed conformational distribution and especially to adapt the experimental conditions and thus to manipulate specifically the conformer abundances.

Conformer specific information is relevant to understand flexible molecules.

In order to obtain unambiguous information it is desirable to investigate not a mixture of conformers, but the conformers one by one. Therefore, it would be helpful to investigate them separated in space and/or time. A new experimental approach [229] exploiting the different m/μ ratios of the different conformers can separate polar neutrals spatially in a molecular beam by passing through an AC electric quadrupole. The switching frequency of the AC electric field is tuned and it is optimum for a certain m/μ ratio, in the ideal case for (selected quantum states of) one specific conformer, so that this conformer reaches the end of the quadrupole guide while the other conformers are defocused from the molecular beam axis by the interaction with the electric field. Once a conformer is isolated from the rest, precise spectroscopic studies can be performed conformer by conformer, contributing to a detailed overall picture.

Bibliography

- [1] J. Koolman and K.-H. Röhm. *Taschenatlas der Biochemie*. Georg Thieme Verlag Stuttgart, New York, 1998.
- [2] K. Autumn, M. Sitti, Y. A. Liang, A. M. Peattie, W. R. Hansen, S. Sponberg, T. W. Kenny, R. Fearing, J. N. Israelachvili, and R. J. Full. *Proc. Nat. Ac. Sci.*, **99**(19):12252, 2002.
- [3] G. Scoles, editor. *Atomic and Molecular Beam Methods*, volume 1 & 2. Oxford University Press, New York, 1988 & 1992.
- [4] R. D. Levine and R. B. Bernstein. *Molecular Reaction Dynamics and Chemical Reactivity*. Oxford University Press, New York, 1987.
- [5] H. Ashkenas and F. S. Sherman. *Rarefied Gas Dynamics*. In J. H. De Leeuw, editor, *Proc. IV Symp.*, volume II. Academic Press, New York, 1966.
- [6] H. C. W. Beijerinck and N. F. Verster. *Physica*, **111C**:327, 1981.
- [7] <http://www.rmjordan.com/Resources/C211-D103man.pdf>.
- [8] W. C. Wiley and I. H. McLaren. *Rev. Sci. Instrum.*, **26**(12):1150, 1955.
- [9] J. M. Bakker, L. Mac Aleese, G. Meijer, and G. von Helden. *Phys. Rev. Lett.*, **91**(20):203003–1, 2003.
- [10] J. M. Bakker. *Structural identification of gas-phase biomolecules using infrared spectroscopy*. PhD thesis, Radboud Universiteit Nijmegen, 2004. ISBN: 90-9018659-X.
- [11] G. Meijer, M. S. de Vries, H. E. Hunziker, and H. R. Wendt. *Appl. Phys. B*, **51**:395, 1990.
- [12] C. Unterberg, A. Jansen, and M. Gerhards. *J. Chem. Phys.*, **113**(18):7945, 2000.
- [13] J.-U. Grabow. private communication.

- [14] J.-U. Grabow and W. Stahl. *Z. Naturforsch. A: Phys. Sci.*, **45a**:1043, 1990.
- [15] J.-U. Grabow, W. Stahl, and H. Dreizler. *Rev. Sci. Instrum.*, **67**:4072, 1996.
- [16] T. J. Balle and W. H. Flygare. *Rev. Sci. Instrum.*, **52**:33, 1981.
- [17] C. Chuang, C. J. Hawley, T. Emilsson, and H. S. Gutowsky. *Rev. Sci. Instrum.*, **61**:1629, 1990.
- [18] U. Andresen, H. Dreizler, J.-U. Grabow, and W. Stahl. *Rev. Sci. Instrum.*, **61**:3694, 1990.
- [19] E.J. Campbell, W. G. Read, and J. A. Shea. *Chem. Phys. Lett.*, **94**:69, 1983.
- [20] M. Schnell, D. Banser, and J.-U. Grabow. *Rev. Sci. Instrum.*, **75**:2111, 2004.
- [21] P. W. Atkins and R. S. Friedman. *Molecular Quantum Mechanics*. Oxford University Press, Inc., New York, 1997.
- [22] H. Sponer, G. Nordheim, A. L. Sklar, and E. Teller. *J. Chem. Phys.*, **7**(4):207, 1939.
- [23] R. S. Mulliken. *J. Chem. Phys.*, **7**:353, 1939.
- [24] J. L. Kinsey. *Annu. Rev. Phys. Chem.*, **28**:349, 1977.
- [25] D. B. Johnston and S. Lipsky. *J. Phys. Chem.*, **95**:3486, 1991.
- [26] C. D. McGuinness, A. M. Macmillan, K. Sagoo, D. McLoskey, and D. J. S. Birch. *Appl. Phys. Lett.*, **89**:063901, 2006.
- [27] D. L. Feldman, R. K. Lengel, and R. N. Zare. *Chem. Phys. Lett.*, **52**(3):413, 1977.
- [28] T. G. Dietz, M. A. Duncan, M. G. Liverman, and R. E. Smalley. *J. Chem. Phys.*, **73**(10):4816, 1980.
- [29] J. Murakami, K. Kaya, and M. Ito. *J. Chem. Phys.*, **72**(5):3263, 1980.
- [30] U. Boesl, H. J. Neusser, and E. W. Schlag. *J. Chem. Phys.*, **72**(8):4327, 1980.
- [31] G. Herzberg. *Molecular Spectra and Molecular Structure*, volume 2. Van Nostrand Reinhold Company, Inc., 1945.
- [32] E. B. Wilson Jr., J. C. Decius, and P. C. Cross. *Molecular Vibrations*. Dover Publications, Inc., New York, 1980.

-
- [33] T. S. Zwier. *Annu. Rev. Phys. Chem.*, **47**:205, 1996.
- [34] T. S. Zwier. *J. Phys. Chem. A*, **105**:8827, 2001.
- [35] W. Gordy and R. L. Cook. *Microwave Molecular Spectra*. Wiley, New York, 3rd edition, 1984.
- [36] C. H. Townes and A. L. Shawlow. *Microwave Spectroscopy*. Dover Publications, Inc., New York, 1975.
- [37] D. M. Dennison. *Rev. Mod. Phys.*, **3**:280, 1931.
- [38] G. W. King, R. M. Hainer, and P. C. Cross. *J. Chem. Phys.*, **11**:27, 1943.
- [39] H. C. Longuet-Higgins. *Mol. Phys.*, **6**:445, 1963.
- [40] J. T. Hougen. *J. Chem. Phys.*, **37**:1433, 1962.
- [41] J. T. Hougen. *J. Chem. Phys.*, **37**:358, 1963.
- [42] P. R. Bunker and P. Jensen. *Molecular Symmetry and Spectroscopy*. NRC Research Press, Ottawa, 2nd edition, 2006.
- [43] D. M. Jonas. *J. Chem. Phys.*, **90**(10):5563, 1989.
- [44] P. Jensen and P. R. Bunker. *Mol. Phys.*, **97**(6):821, 1999.
- [45] K. C. Janda, J. C. Hemminger, J. S. Winn, S. E. Novick, S. J. Harris, and W. Klemperer. *J. Chem. Phys.*, **63**(4):1419, 1975.
- [46] J. B. Hopkins, D. E. Powers, and R. E. Smalley. *J. Phys. Chem.*, **85**:3739, 1981.
- [47] P. R. R. Langridge-Smith, D. V. Brumbaugh, C. A. Haynam, and D. H. Levy. *J. Phys. Chem.*, **85**:3742, 1981.
- [48] K. H. Fung, H. L. Selzle, and E. W. Schlag. *J. Phys. Chem.*, **87**(4):5113, 1983.
- [49] K. S. Law, M. Schauer, and E. R. Bernstein. *J. Chem. Phys.*, **81**(11):4871, 1984.
- [50] K. O. Börnsen, H. L. Selzle, and E. W. Schlag. *Z. Naturforsch.*, **39a**:1255, 1984.
- [51] K. O. Börnsen, H. L. Selzle, and E. W. Schlag. *J. Chem. Phys.*, **85**(4):1726, 1986.
- [52] J. R. Grover, E. A. Walters, and E. T. Hui. *J. Phys. Chem.*, **91**:3233, 1987.

- [53] R. H. Page, Y. R. Shen, and Y. T. Lee. *J. Chem. Phys.*, **88**(8):4621, 1988.
- [54] H. Krause, B. Ernstberger, and H. J. Neusser. *Chem. Phys. Lett.*, **184**(5,6):411, 1991.
- [55] B. F. Henson, G. V. Hartland, V. A. Venturo, and P. M. Felker. *J. Chem. Phys.*, **97**(4):2189, 1992.
- [56] W. Scherzer, O. Krätzschar, H. L. Selzle, and E. W. Schlag. *Z. Naturforsch.*, **47a**:1248, 1992.
- [57] E. Arunan and H. S. Gutowsky. *J. Chem. Phys.*, **98**(5):4294, 1993.
- [58] P. Hobza, H. L. Selzle, and E. W. Schlag. *J. Chem. Phys.*, **93**(8):5893, 1990.
- [59] P. Hobza, H. L. Selzle, and E. W. Schlag. *J. Phys. Chem.*, **97**:3937, 1993.
- [60] R. L. Jaffe and G. D. Smith. *J. Chem. Phys.*, **105**(7):2780, 1996.
- [61] P. Hobza, H. L. Selzle, and E. W. Schlag. *J. Phys. Chem.*, **100**:18790, 1996.
- [62] V. Špirko, O. Engkvist, P. Soldán, H. L. Selzle, E. W. Schlag, and P. Hobza. *J. Chem. Phys.*, **111**(2):572, 1999.
- [63] M. O. Sinnokrot, E. F. Valeev, and C. D. Sherrill. *J. Am. Chem. Soc.*, **124**:10887, 2002.
- [64] S. Tsuzuki, T. Uchimaru, K. Sugawara, and M. Mikami. *J. Chem. Phys.*, **117**(24):11216, 2002.
- [65] S. Tsuzuki, K. Honda, T. Uchimaru, M. Mikami, and K. Tanabe. *J. Am. Chem. Soc.*, **124**(1):104, 2002.
- [66] M. O. Sinnokrot and C. D. Sherrill. *J. Phys. Chem. A*, **108**:10200, 2004.
- [67] R. Schmied, P. Çarçabal, A. M. Dokter, V. P. A. Lonij, K. Lehmann, and G. Scoles. *J. Chem. Phys.*, **121**(6):2701, 2004.
- [68] T. Sato, T. Tsuneda, and K. Hirao. *J. Chem. Phys.*, **123**:104307, 2005.
- [69] T. Rocha-Rinza, L. De Vico, V. Veryazov, and B. O. Roos. *Chem. Phys. Lett.*, **426**:268, 2006.
- [70] R. Podeszwa, R. Bukowski, and K. Szalewicz. *J. Phys. Chem. A*, **110**:10345, 2006.
- [71] R. A. DiStasio Jr., G. von Helden, R. P. Steele, and M. Head-Gordon. *Chem. Phys. Lett.*, **437**(4-6):277, 2007.

-
- [72] A. H. Narten. *J. Chem. Phys.*, **48**(4):1630, 1968.
- [73] E. G. Cox, F. R. S., D. W. J. Cruickshank, and J. A. S. Smith. *Proc. R. Soc. A*, **247**:1, 1958.
- [74] G. E. Bacon, N. A. Curry, and S. A. Wilson. *Proc. R. Soc. A*, **279**:98, 1964.
- [75] J. M. Steed, T. A. Dixon, and W. Klemperer. *J. Chem. Phys.*, **70**(11):4940, 1979.
- [76] U. Erlekam, M. Frankowski, G. Meijer, and G. von Helden. *J. Chem. Phys.*, **124**:171101, 2006.
- [77] B. F. Henson, G. V. Hartland, V. A. Ventura, R. A. Hertz, and P. M. Felker. *Chem. Phys. Lett.*, **176**(1):91, 1991.
- [78] V. A. Ventura and P. M. Felker. *J. Chem. Phys.*, **99**(1):748, 1993.
- [79] J. G. Hill, J. A. Platts, and H.-J. Werner. *Phys. Chem. Chem. Phys.*, **8**:4072, 2006.
- [80] M. Schauer and E. R. Bernstein. *J. Chem. Phys.*, **82**(8):3722, 1985.
- [81] P. Hobza, H. L. Selzle, and E. W. Schlag. *J. Am. Chem. Soc.*, **116**:3500, 1994.
- [82] G. D. Smith and R. L. Jaffe. *J. Phys. Chem.*, **100**:9624, 1996.
- [83] C. Gonzalez and E. C. Lim. *J. Phys. Chem. A*, **104**:2953, 2000.
- [84] Y. C. Park and J. S. Lee. *J. Phys. Chem. A*, **110**:5091, 2006.
- [85] A. Puzder, M. Dion, and D. C. Langreth. *J. Chem. Phys.*, **124**:164105, 2006.
- [86] P. Čarský, H. L. Selzle, and E. W. Schlag. *Chem. Phys.*, **125**:165, 1988.
- [87] S. Tsuzuki, T. Uchimaru, K. Matsumura, M. Mikami, and K. Tanabe. *Chem. Phys. Lett.*, **319**:547, 2000.
- [88] L. V. Splichenko and M. S. Gordon. *J. Comp. Chem.*, **28**(1):276, 2006.
- [89] P. Hobza, H. L. Selzle, and E. W. Schlag. *Chem. Rev.*, **94**:1767, 1994.
- [90] E. C. Lee, D. Kim, P. Jurečka, P. Tarakeshwar, P. Hobza, and K. S. Kim. *J. Phys. Chem. A*, **111**:3446, 2007.
- [91] J. L. Atwood, F. Hamada, K. D. Robinson, G. W. Orr, and R. L. Vincent. *Nature*, **349**:683, 1991.

- [92] S. Suzuki, P. G. Green, R. E. Bumgarner, S. Dasgupta, W. A. Goddard III, and G. A. Blake. *Science*, **257**:942, 1992.
- [93] R. N. Pribble, A. W. Garret, K. Haber, and T. S. Zwier. *J. Chem. Phys.*, **103**(2):531, 1995.
- [94] P. Hobza, V. Špirko, H. L. Selzle, and E. W. Schlag. *J. Phys. Chem. A*, **102**(15):2501, 1998.
- [95] W. M. Latimer and W. H. Rodebusch. *J. Am. Chem. Soc.*, **42**:1419, 1920.
- [96] E. D. Isaacs, A. Shukla, P. M. Platzmann, D. R. Hamann, B. Barbiellini, and C. A. Tulk. *Phys. Rev. Lett.*, **82**(3):600, 1999.
- [97] P. Hobza and Z. Havlas. *Chem. Rev.*, **100**:4253, 2000.
- [98] B. Reimann, K. Buchhold, S. Vaupel, B. Brutschy, Z. Havlas, V. Špirko, and P. Hobza. *J. Phys. Chem. A*, **105**:5560, 2001.
- [99] B. J. van der Veken, W. A. Herrebout, R. Szostak, D. N. Shchepkin, Z. Havlas, and P. Hobza. *J. Am. Chem. Soc.*, **123**:12290, 2001.
- [100] I. V. Alabugin, M. Manoharan, S. Peabody, and F. Weinhold. *J. Am. Chem. Soc.*, **125**:5973, 2003.
- [101] P. Hobza and Z. Havlas. *Chem. Phys. Lett.*, **303**:447, 1999.
- [102] A. Masunov, J. J. Dannenberg, and R. H. Contreras. *J. Phys. Chem. A*, **105**:4737, 2001.
- [103] K. Hermansson. *J. Phys. Chem. A*, **106**:4695, 2002.
- [104] X. Li, L. Liu, and H. B. Schlegel. *J. Am. Chem. Soc.*, **124**:9639, 2002.
- [105] G. T. Trudeau, J. M. Dumas, P. Dupuis, M. Guerin, and C. Sandorfy. *Top. Curr. Chem.*, **93**:91, 1980.
- [106] M. Buděšínský, P. Fiedler, and Z. Arnold. *Synthesis*, page 858, 1989.
- [107] I. E. Boldeskul, I. F. Tsymbal, E. V. Ryltsev, Z. Latajka, and A. J. Barnes. *J. Mol. Struct.*, **436**:167, 1997.
- [108] P. Hobza, V. Špirko, Z. Havlas, K. Buchhold, B. Reimann, H. D. Barth, and B. Brutschy. *Chem. Phys. Lett.*, **299**:180, 1999.
- [109] U. Erlekam, M. Frankowski, G. von Helden, and G. Meijer. *Phys. Chem. Chem. Phys.*, **9**:3786, 2007.
- [110] S. D. Colson and T. L. Netzel. *Chem. Phys. Lett.*, **16**:555, 1972.
- [111] E. B. Wilson Jr. *Phys. Rev.*, **45**:706, 1934.

-
- [112] L. Goodman, A. G. Ozkabak, and S. N. Thakur. *J. Phys. Chem.*, **95**:9044, 1991.
- [113] S. Brodersen and A. Langseth. *Mat. Fys. Skr. Dan. Vid. Selsk.*, **1**(1):1, 1956.
- [114] J. Plíva and A. S. Pine. *J. Mol. Spect.*, **126**:82, 1987.
- [115] S. Rashev. *Int. J. Quant. Chem.*, **99**:894, 2004.
- [116] J. M. L. Martin, P. R. Taylor, and T. J. Lee. *Chem. Phys. Lett.*, **275**(3-4):414, 1997. and references therein.
- [117] A. Miani, E. Cané, P. Palmieri, A. Trombetti, and N. C. Handy. *J. Chem. Phys.*, **112**(1):248, 2000.
- [118] A. D. Boese and J. M. L. Martin. *J. Phys. Chem. A*, **108**(15):3085, 2004.
- [119] K. Yagi, K. Hirao, T. Taketsugu, M. W. Schmidt, and M. S. Gordon. *J. Chem. Phys.*, **121**(3):1383, 2004.
- [120] E. Cané, A. Miani, and A. Trombetti. *Chem. Phys. Lett.*, **340**(3-4):356, 2001.
- [121] S. Rashev. *J. Phys. Chem. A*, **107**(13):2160, 2003.
- [122] M.-L. Senent, P. Palmieri, S. Carter, and N. C. Handy. *Chem. Phys. Lett.*, **354**(1-2):1, 2002.
- [123] R. H. Page, Y. R. Shen, and Y. T. Lee. *J. Chem. Phys.*, **88**(9):5362, 1988.
- [124] A. B. Hollinger and H. L. Welsh. *Can. J. Phys.*, **56**:974, 1978.
- [125] A. B. Hollinger and H. L. Welsh. *Can. J. Phys.*, **56**:1513, 1978.
- [126] B. Reimann. PhD thesis, Johann Wolfgang Goethe-Universität Frankfurt/Main, 2002.
- [127] M. J. Frisch, G. W. Trucks, H. B. Schlegel, G. E. Scuseria, M. A. Robb, J. R. Cheeseman, Jr. J. A. Montgomery, T. Vreven, K. N. Kudin, J. C. Burant, J. M. Millam, S. S. Iyengar, J. Tomasi, V. Barone, B. Mennucci, M. Cossi, G. Scalmani, N. Rega, G. A. Petersson, H. Nakatsuji, M. Hada, M. Ehara, K. Toyota, R. Fukuda, J. Hasegawa, M. Ishida, T. Nakajima, Y. Honda, O. Kitao, H. Nakai, M. Klene, X. Li, J. E. Knox, H. P. Hratchian, J. B. Cross, C. Adamo, J. Jaramillo, R. Gomperts, R. E. Stratmann, O. Yazyev, A. J. Austin, R. Cammi, C. Pomelli, J. W. Ochterski, P. Y. Ayala, K. Morokuma, G. A. Voth, P. Salvador, J. J. Dannenberg, V. G. Zakrzewski, S. Dapprich, A. D. Daniels, M. C. Strain, O. Farkas, D. K. Malick, A. D. Rabuck, K. Raghavachari, J. B. Foresman, J. V. Ortiz,

- Q. Cui, A. G. Baboul, S. Clifford, J. Cioslowski, B. B. Stefanov, G. Liu, A. Liashenko, P. Piskorz, I. Komaromi, R. L. Martin, D. J. Fox, T. Keith, M. A. Al-Laham, C. Y. Peng, A. Nanayakkara, M. Challacombe, P. M. W. Gill, B. Johnson, W. Chen, M. W. Wong, C. Gonzalez, and J. A. Pople. Gaussian 03, revision c.02. Gaussian, Inc., Wallingford CT, 2004.
- [128] K. Szalewicz. private communication.
- [129] F. Filsinger, K. Wohlfahrt, M. Schnell, J.-U. Grabow, and J. Küpper. *Phys. Chem. Chem. Phys.*, page DOI: 10.1039/b711888k, 2008.
- [130] J. A. Odutola, D. L. Alvis, C. W. Curtis, and T. R. Dyke. *Mol. Phys.*, **42**(2):267, 1981.
- [131] A. van der Avoird. *J. Chem. Phys.*, **98**(7):5327, 1993.
- [132] T. D. Klots, T. Emilsson, and H. S. Gutowsky. *J. Chem. Phys.*, **97**(8): 5335, 1992.
- [133] T. Emilsson, H. S. Gutowsky, G. de Oliveira, and C. E. Dykstra. *J. Chem. Phys.*, **112**(3):1287, 2000.
- [134] J. K. G. Watson. *Can. J. Phys.*, **43**:1996, 1965.
- [135] R. Schmied and K. K. Lehmann. *J. Mol. Spect.*, **226**:201, 2004.
- [136] T. J. Sears, P. M. Johnson, P. Jin, and S. Oatis. *J. Chem. Phys.*, **104**(3): 781, 1996.
- [137] O. Engkvist, P. Hobza, H. L. Selzle, and E. W. Schlag. *J. Chem. Phys.*, **110**(12):5758, 1999.
- [138] C. Gonzalez and E. C. Lim. *J. Phys. Chem. A*, **105**:1904, 2001.
- [139] C. Gonzalez, T. C. Allison, and E. C. Lim. *J. Phys. Chem. A*, **105**:10583, 2001.
- [140] E. Arunan, T. Emilsson, and H. S. Gutowsky. *J. Chem. Phys.*, **101**(2): 861, 1994.
- [141] H. S. Gutowsky, T. Emilsson, and E. Arunan. *J. Chem. Phys.*, **99**(7): 4883, 1993.
- [142] E. Arunan, T. Emilsson, and H. S. Gutowsky. *J. Chem. Phys.*, **99**(8): 6208, 1993.
- [143] E. Zwart, J. J. ter Meulen, W. L. Meerts, and L. H. Coudert. *J. Mol. Spect.*, **147**:27, 1991.
- [144] J. T. Hougen. *J. Mol. Spect.*, **89**:296, 1981.

-
- [145] N. Ohashi and J. T. Hougen. *J. Mol. Spect.*, **121**:474, 1987.
- [146] W. Caminati, J. C. López, J. L. Alonso, and J.-U. Grabow. *Angew. Chem. Int. Ed.*, **44**:3840, 2005.
- [147] E. W. Becker and K. Bier. *Z. Naturforsch.*, **9a**:975, 1954.
- [148] J. Ross, editor. *Advances in Chemical Physics - Molecular Beams*, volume 10. Interscience Publishers, New York, 1966.
- [149] J. Koperski. *Van der Waals Complexes in Supersonic Beams*. WILEY-VCH Verlag GmbH & Co, Weinheim, 2003.
- [150] T. R. Rizzo, Y. D. Park, and D. H. Levy. *J. Chem. Phys.*, **85**:6945, 1986.
- [151] P. D. Godfrey, R. D. Brown, and F. M. Rodgers. *J. Mol. Struct.*, **376**:65, 1996.
- [152] L. C. Snoek, E. G. Robertson, R. T. Kroemer, and J. P. Simons. *Chem. Phys. Lett.*, **321**:49, 2000.
- [153] Y. Inokuchi, Y. Kobayashi, T. Ito, and T. Ebata. *J. Phys. Chem. A*, **111**(17):3209, 2007.
- [154] J. M. Bakker, I. Compagnon, G. Meijer, G. von Helden, M. Kabeláč, P. Hobza, and M. S. de Vries. *Phys. Chem. Chem. Phys.*, **6**:2810, 2004.
- [155] M. Y. Choi and R. E. Miller. *J. Am. Chem. Soc.*, **128**:7320, 2006.
- [156] M. S. de Vries and P. Hobza. *Annu. Rev. Phys. Chem.*, **58**:585, 2007.
- [157] E. G. Robertson and J. P. Simons. *Phys. Chem. Chem. Phys.*, **3**:1, 2001.
- [158] R. S. Ruoff, T. D. Klots, T. Emilsson, and H. S. Gutowsky. *J. Chem. Phys.*, **93**(5):3142, 1990.
- [159] P. D. Godfrey and R. D. Brown. *J. Am. Chem. Soc.*, **120**:10724, 1998.
- [160] G. M. Florio, R. A. Christie, K. D. Jordan, and T. S. Zwier. *J. Am. Chem. Soc.*, **124**:10236, 2002.
- [161] P. Butz, R. T. Kroemer, N. A. Macleod, and J. P. Simons. *Phys. Chem. Chem. Phys.*, **4**:3566, 2002.
- [162] L. C. Snoek, T. Mourik, and J. P. Simons. *Mol. Phys.*, **101**(9):1239, 2003.
- [163] C. Emmelmuth, V. Dyczmons, and M. A. Suhm. *J. Phys. Chem. A*, **110**:2906, 2006.
- [164] B. C. Dian, A. Longarte, and T. S. Zwier. *Science*, **296**(5577):2369, 2002.

- [165] B. C. Dian, J. R. Clarkson, and T. S. Zwier. *Science*, **303**(5661):1169, 2004.
- [166] T. Brixner and G. Gerber. *ChemPhysChem*, **4**:418, 2003.
- [167] A. Bastida, J. Zúñiga, A. Requena, B. Miguel, J. A. Beswick, J. Vigué, and N. Halberstadt. *J. Chem. Phys.*, **116**:1944, 2002.
- [168] T. F. Miller III, D. C. Clary, and A. J. H. M. Meijer. *J. Chem. Phys.*, **122**:244323, 2005.
- [169] S. Lee, J. S. Chung, P. M. Felker, J. López Cacheiro, B. Fernández, T. Bondo Pedersen, and H. Koch. *J. Chem. Phys.*, **119**(24):12956, 2003.
- [170] T. Brupbacher, J. Makarewicz, and A. Bauder. *J. Chem. Phys.*, **101**(11):9736, 1994; D_0 is estimated by subtracting 33 cm^{-1} zero point vibrational energy from the given value of D_e of 151 cm^{-1} .
- [171] P. Hobza, O. Bludský, H. L. Selzle, and E. W. Schlag. *J. Chem. Phys.*, **91**(1):335, 1996.
- [172] T. Ebata, T. Hashimoto, T. Ito, Y. Inokuchi, F. Altunsu, B. Brutschy, and P. Tarakeshwar. *Phys. Chem. Chem. Phys.*, **8**:4783, 2006.
- [173] G. von Helden, I. Compagnon, M. N. Blom, M. Frankowski, U. Erlekam, J. Oomens, B. Brauer, R. B. Gerber, and G. Meijer. *Phys. Chem. Chem. Phys.*, DOI: 10.1039/b713274c, 2008.
- [174] R. V. Krems. *Int. Rev. Phys. Chem.*, **24**(1):99, 2005; and references therein.
- [175] D. W. Pratt. *Science*, **296**:2347, 2002.
- [176] T. Ebata, K. Kouyama, and N. Mikami. *J. Chem. Phys.*, **119**(6):2947, 2003.
- [177] B. C. Dian, G. M. Florio, J. R. Clarkson, A. Longarte, and T. S. Zwier. *J. Chem. Phys.*, **120**(19):9033, 2004.
- [178] J. R. Clarkson, E. Baquero, V. A. Schubert, E. M. Myshakin, K. D. Jordan, and T. S. Zwier. *Science*, **307**:1443, 2005.
- [179] T. M. Selby, J. R. Clarkson, D. Mitchell, J. A. J. Fitzpatrick, H. D. Lee, D. W. Pratt, and T. S. Zwier. *J. Phys. Chem. A*, **109**:4484, 2005.
- [180] F. Dong and R. E. Miller. *Science*, **298**:1227, 2002.
- [181] J. D. Baldeschwieler and G. C. Pimentel. *J. Chem. Phys.*, **33**(4):1008, 1960.

-
- [182] S. J. Martinez III, J. C. Alfano, and D. H. Levy. *J. Mol. Spect.*, **156**:421, 1992.
- [183] K. T. Lee, J. Sung, K. J. Lee, S. K. Kim, and Y. D. Park. *J. Chem. Phys.*, **116**(19):8251, 2002.
- [184] K. T. Lee, J. Sung, K. J. Lee, S. K. Kim, and Y. D. Park. *Chem. Phys. Lett.*, **368**:262, 2003.
- [185] Y. Lee, J. Jung, B. Kim, P. Butz, L. C. Snoek, R. T. Kroemer, and J. P. Simons. *J. Phys. Chem. A*, **108**:69, 2004.
- [186] J. B. Fenn, M. Mann, C. K. Meng, S. F. Wong, and C. M. Whitehouse. *Science*, **246**:64, 1989.
- [187] F. Hillenkamp, M. Karas, R. C. Beavis, and B. T. Chait. *Anal. Chem.*, **63**:1193A, 1991.
- [188] T. R. Rizzo, Y. D. Park, L. A. Peteanu, and D. H. Levy. *J. Chem. Phys.*, **84**(5):2534, 1986.
- [189] T. R. Rizzo, Y. D. Park, L. Peteanu, and D. H. Levy. *J. Chem. Phys.*, **83**(9):4819, 1985.
- [190] L. A. Philips, S. P. Webb, S. J. Martinez III, G. R. Fleming, and D. H. Levy. *J. Am. Chem. Soc.*, **110**(5):1352, 1988.
- [191] C. K. Teh, J. Sipior, and M. Sulkes. *J. Phys. Chem.*, **93**:5393, 1989.
- [192] A. Lindinger, J. P. Toennies, and A. F. Vilesov. *J. Chem. Phys.*, **110**(3):1429, 1999.
- [193] F. Piuzzi, I. Dimicoli, M. Mons, B. Tardivel, and Q. Zhao. *Chem. Phys. Lett.*, **320**:282, 2000.
- [194] L. C. Snoek, R. T. Kroemer, M. R. Hockridge, and J. P. Simons. *Phys. Chem. Chem. Phys.*, **3**:1819, 2001.
- [195] L. C. Snoek, R. T. Kroemer, and J. P. Simons. *Phys. Chem. Chem. Phys.*, **4**:2130, 2002.
- [196] P. Çarçabal, R. T. Kroemer, L. C. Snoek, J. P. Simons, J. M. Bakker, I. Compagnon, G. Meijer, and G. von Helden. *Phys. Chem. Chem. Phys.*, **6**:4546, 2004.
- [197] F. O. Talbot, T. Tabarin, R. Antoine, M. Broyer, and P. Dugourd. *J. Chem. Phys.*, **122**:074310–1, 2005.
- [198] O. V. Boyarkin, S. R. Mercier, A. Kamariotis, and T. R. Rizzo. *J. Am. Chem. Soc.*, **128**(9):2816, 2006.

- [199] N. C. Polfer, J. Oomens, and R. C. Dunbar. *Phys. Chem. Chem. Phys.*, **8**(23):2744, 2006.
- [200] M. N. Blom, I. Compagnon, N. C. Polfer, G. von Helden, G. Meijer, S. Suhai, B. Paizs, and J. Oomens. *J. Phys. Chem. A*, **111**(31):7309, 2007.
- [201] K. T. Lee, J. Sung, K. J. Lee, Y. D. Park, and S. K. Kim. *Angew. Chem. Int. Ed.*, **41**(21):4114, 2002.
- [202] T. Hashimoto, Y. Takasu, Y. Yamada, and T. Ebata. *Chem. Phys. Lett.*, **421**:227, 2006.
- [203] Z. Huang, W. Yu, and Z. Lin. *J. Mol. Struct. (Theochem)*, **758**:195, 2006.
- [204] A. Kaczor, I. D. Reva, L. M. Proniewicz, and R. Fausto. *J. Phys. Chem. A*, **110**:2360, 2006.
- [205] L. I. Grace, R. Cohen, T. M. Dunn, D. M. Lubman, and M. S. de Vries. *J. Mol. Spect.*, **215**:204, 2002.
- [206] R. Cohen, B. Brauer, E. Nir, L. Grace, and M. S. de Vries. *J. Phys. Chem. A*, **104**(27):6351, 2000.
- [207] C. Unterberg, A. Gerlach, T. Schrader, and M. Gerhards. *J. Chem. Phys.*, **118**(18):8296, 2003.
- [208] S. Wiedemann, A. Metsala, D. Nolting, and R. Weinkauff. *Phys. Chem. Chem. Phys.*, **6**:2641, 2004.
- [209] J. M. Bakker, C. Plutzer, I. Hunig, T. Haber, I. Compagnon, G. von Helden, G. Meijer, and K. Kleinerhanns. *ChemPhysChem*, **6**(1):120, 2005.
- [210] W. Chin, I. Compagnon, J. P. Dognon, C. Canuel, F. Piuuzzi, I. Dimicoli, G. von Helden, G. Meijer, and M. Mons. *J. Am. Chem. Soc.*, **127**(5):1388, 2005.
- [211] Y. S. Kim, J. P. Wang, and R. M. Hochstrasser. *J. Phys. Chem. B*, **109**(15):7511, 2005.
- [212] W. Chin, M. Mons, J. P. Dognon, R. Mirasol, G. Chass, I. Dimicoli, F. Piuuzzi, P. Butz, B. Tardivel, I. Compagnon, G. von Helden, and G. Meijer. *J. Phys. Chem. A*, **109**(24):5281, 2005.
- [213] W. Chin, F. Piuuzzi, I. Dimicoli, and M. Mons. *Phys. Chem. Chem. Phys.*, **8**:1003, 2006.
- [214] I. Compagnon, J. Oomens, G. Meijer, and G. von Helden. *J. Am. Chem. Soc.*, **128**(11):3592, 2006.

-
- [215] P. D. Godfrey, S. Firth, L. D. Hatherley, R. D. Brown, and A. P. Pierlot. *J. Am. Chem. Soc.*, **115**:9687, 1993.
- [216] J. H. Jensen and M. S. Gordon. *J. Am. Chem. Soc.*, **117**:8159, 1995.
- [217] M. S. Gordon and J. H. Jensen. *Acc. Chem. Res.*, **29**:536, 1996.
- [218] L. J. Chapo, J. B. Paul, R. A. Provencal, K. Roth, and R. J. Saykally. *J. Am. Chem. Soc.*, **120**:12956, 1998.
- [219] M. Nagaoka, N. Okuyama-Yoshida, and T. Yamabe. *J. Phys. Chem. A*, **102**:8202, 1998.
- [220] L. A. Peteanu and D. H. Levy. *J. Phys. Chem.*, **92**:6554, 1988.
- [221] E. Tajkhorshid, K. J. Jalkanen, and S. Suhai. *J. Phys. Chem. B*, **102**:5899, 1998.
- [222] A. Fernández-Ramos, Z. Smedarchina, W. Siebrand, and M. Z. Zgierski. *J. Chem. Phys.*, **113**(21):9714, 2000.
- [223] E. Kassab, J. Langlet, E. Evleth, and Y. Akacem. *J. Mol. Struct. (Theochem)*, **531**:267, 2000.
- [224] S. Xu, M. Nilles, and Jr. K. H. Bowen. *J. Chem. Phys.*, **119**(20):10696, 2003.
- [225] E. G. Diken, J. M. Headrick, and M. A. Johnson. *J. Chem. Phys.*, **122**:224317–1, 2005.
- [226] T. Ebata, A. Fujii, and N. Mikami. *Int. Rev. Phys. Chem.*, **17**:331, 1998.
- [227] A. T. Paxton and J. B. Harper. *Mol. Phys.*, **102**(9-10):953, 2004.
- [228] T. Beyer and D. F. Swinehart. *Algorithm 448 Number of Multiply Restricted Partitions [A1]*, *Commun. ACM*, volume **16**. 1973.
- [229] F. Filsinger, U. Erlekam, G. von Helden, J. Küpper, and G. Meijer. submitted.

Appendix A

The character tables

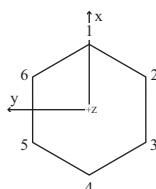


Figure A.1: The benzene monomer with the bonded carbon-hydrogen nuclei being numbered 1-6.

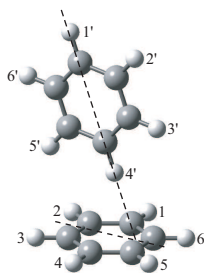


Figure A.2: The benzene dimer with the bonded carbon-hydrogen nuclei being numbered 1-6 for the "top" and 1'-6' for the "stem". The "stem" plane bisects the "top" between 612 and 543 with 4' pointing at the bond connecting 5 and 6.

Table A.1: The group $\mathbf{D}_{6h}(\mathbf{M})$

$\mathbf{D}_{6h}(\mathbf{M})$	E	(123456)	$(135)(246)$	$(14)(25)(36)$	$(26)(35)$	$(14)(23)(56)$	E^*	$(123456)^*$	$(135)(246)^*$	$(14)(25)(36)^*$	$(26)(35)^*$	$(14)(23)(56)^*$
	1	2	2	1	3	3	1	2	2	1	3	3
A_{1g}	1	1	1	1	1	1	1	1	1	1	1	1
A_{1u}	1	1	1	1	1	1	-1	-1	-1	-1	-1	-1
A_{2g}	1	1	1	1	-1	-1	1	1	1	1	-1	-1
A_{2u}	1	1	1	1	-1	-1	-1	-1	-1	-1	1	1
B_{1g}	1	-1	1	-1	1	-1	-1	1	-1	1	-1	1
B_{1u}	1	-1	1	-1	1	-1	1	-1	1	-1	1	-1
B_{2g}	1	-1	1	-1	-1	1	-1	1	-1	1	1	-1
B_{2u}	1	-1	1	-1	-1	1	1	-1	1	-1	-1	1
E_{1g}	2	1	-1	-2	0	0	-2	-1	1	2	0	0
E_{1u}	2	1	-1	-2	0	0	2	1	-1	-2	0	0
E_{2g}	2	-1	-1	2	0	0	2	-1	-1	2	0	0
E_{2u}	2	-1	-1	2	0	0	-2	1	1	-2	0	0

Table A.2: The group $\mathbf{C}_s(\mathbf{M})$

$\mathbf{C}_s(\mathbf{M})$	E	$(14)(23)(56)^*$
	1	1
A'	1	1
A''	1	-1

Table A.3: The group $\mathbf{C}_{2v}(\mathbf{M})$

$\mathbf{C}_{2v}(\mathbf{M})$	E	$(14)(25)(36)(2'6')(3'5')$	$(14)(23)(56)^*$	$(26)(35)(2'6')(3'5')^*$
	1	1	1	1
A_1	1	1	1	1
A_2	1	1	-1	-1
B_1	1	-1	-1	1
B_2	1	-1	1	-1

Table A.4: The group $\mathbf{C}_{6v}(\mathbf{M})$

$\mathbf{C}_{6v}(\mathbf{M})$	E	(123456)	$(135)(246)$	$(14)(25)(36)$	$(26)(35)^*$	$(14)(23)(56)^*$
	1	2	2	1	3	3
A_1	1	1	1	1	1	1
A_2	1	1	1	1	-1	-1
B_1	1	-1	1	-1	1	-1
B_2	1	-1	1	-1	-1	1
E_1	2	1	-1	-2	0	0
E_2	2	-1	-1	2	0	0

Table A.5: The group \mathbf{G}_{24}

\mathbf{G}_{24}	E	(123456)	$(135)(246)$	$(14)(25)(36)$	$(26)(35)^*$	$(14)(23)(56)^*$	$(2'6')(3'5')$	$(123456)(2'6')(3'5')$	$(135)(246)(2'6')(3'5')$	$(14)(25)(36)(2'6')(3'5')$	$(26)(35)(2'6')(3'5')^*$	$(14)(23)(56)(2'6')(3'5')^*$
	1	2	2	1	3	3	1	2	2	1	3	3
A_{1s}	1	1	1	1	1	1	1	1	1	1	1	1
A_{2s}	1	1	1	1	-1	-1	1	1	1	1	-1	-1
B_{1s}	1	-1	1	-1	1	-1	1	-1	1	-1	1	-1
B_{2s}	1	-1	1	-1	-1	1	1	-1	1	-1	-1	1
E_{1s}	2	1	-1	-2	0	0	2	1	-1	-2	0	0
E_{2s}	2	-1	-1	2	0	0	2	-1	-1	2	0	0
A_{1a}	1	1	1	1	1	1	-1	-1	-1	-1	-1	-1
A_{2a}	1	1	1	1	-1	-1	-1	-1	-1	-1	1	1
B_{1a}	1	-1	1	-1	1	-1	-1	1	-1	1	-1	1
B_{2a}	1	-1	1	-1	-1	1	-1	1	-1	1	1	-1
E_{1a}	2	1	-1	-2	0	0	-2	-1	1	2	0	0
E_{2a}	2	-1	-1	2	0	0	-2	1	1	-2	0	0

Appendix B

The IR laser system* - troubleshooting

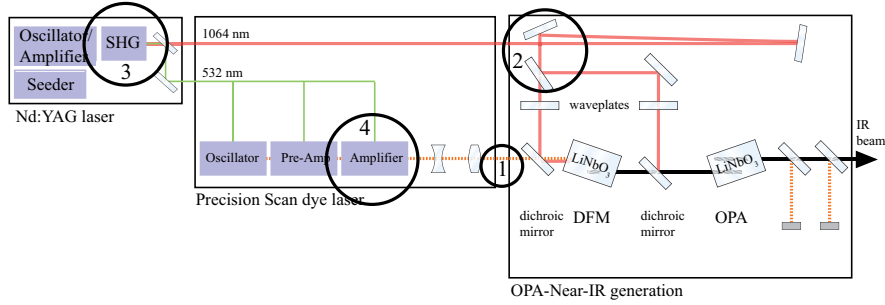


Figure B.1: Scheme of the laser system that has been used for the IR experiments described in this thesis. The circles indicate the technically weak points of the system.

The IR laser system used in this thesis is described in detail in section 1.2.1. The presentation given there implies a smoothly operating laser system. This and the supposed IR laser energy of about 10 mJ/pulse at 3000 cm^{-1} have, however, not been realized after the installation and adjustment by the service engineer of the respective laser company.

The first major problem was a by about 50 % periodically changing IR laser pulse energy on a time scale of a few minutes, not allowing one to work correctly.

After several tests the origin of these fluctuations could be located. In order to protect the IR generation unit from dust particles, it has originally been

*Used for the experiments described in chapter 2 and section 4.3.

covered entirely, creating a fairly closed system. However, the two LiNbO_3 crystals used for difference frequency mixing (DFM) and optical parametric amplification (OPA) need to be heated to about 100°C in order to avoid that water molecules adsorb on the crystal surfaces. In the closed system the heat dissipates only irregularly and provokes steadily changing phase matching parameters, especially for the OPA. In such a situation the phase matching can of course not be controlled and the power of the generated IR radiation is fluctuating, depending on the temperature. When not covering the IR generation stage the fluctuations of the laser power can be significantly reduced to the common deviations of less than 1 %.

The next problem came up when the laser dye had to be changed from Styryl 9 to Styryl 11. This was not expected to cause trouble as the fluorescence spectra of the two dyes overlap and the required readjustments of the dye laser are supposed to be small. The changes were indeed small, however, large enough to avoid that the dye laser beam passed correctly through the first LiNbO_3 crystal. (correctly in the sense that it perfectly overlaps with the 1064 nm beam along the full path of the crystal).

The dye laser system is designed such that resonator and preamplifier share the same dye cuvette. The resonator is pumped by the Nd:YAG laser beam (532 nm) in the lower half of the cuvette, its output is then guided by a 180° turning prism back into the upper half of the cuvette where it is preamplified in a second pumping stage. The preamplified beam passes then a telescope and a second (capillary cell) cuvette where the laser beam is efficiently amplified. In this arrangement, the only technical possibility to improve the overlap between the dye laser beam and the 1064 nm beam in the non-linear crystal would have been to adjust the 180° turning prism that guides the laser beam into the preamplification stage. This is, however, almost impossible as each displacement of the turning prism would require a readjustment of the preamplifier and the amplifier. The adjustment of these two stages can again change the position of the final dye laser beam with respect to the 1064 nm beam, resulting in a long-lasting, iterative alignment procedure. In order to avoid that, four high reflective mirrors have been installed just behind the dye laser unit (see Figure B.1, circle 1). Due to a lack of space, mirrors have been chosen that can be adjusted from above. In this modified setup it is now possible to align the dye laser beam and the 1064 nm beam separately and to perfectly overlap them along the whole path in the first and the second crystal. In order to assure a perfect overlap in the crystals, the overlap at a distance of 2 m from the crystals is checked as well.

The adjustment of the 1064 nm beam is, however, not very convenient, as the beam splitter (indicated as 2 in Figure B.1) cannot be adjusted from above, but only from the rear side of the mount, implying that one would have to put one's hand in the 1064 nm beam that is supposed to pump the first LiNbO_3 crystal. An adjustment is therefore only possible when blocking completely the

1064 nm beam and checking the relative intensity distribution of the separated beams after adjusting the beam splitter. Simply replacing the mount of the beam splitter by one that can be adjusted from above would allow for a faster and more convenient alignment procedure.

In spite of several changes, the advertised IR laser pulse energy of about 10 mJ could still not be reached. Therefore, the laser system has been investigated further. Interestingly, the two separated 1064 nm beams pass each through a $\lambda/2$ plate before entering the respective crystals. Additionally, in the manual the following phrase can be found "The polarization and the beam path of the Nd:YAG laser depends on the Nd:YAG laser energy."

The Nd:YAG laser generates linearly polarized light with a wavelength of 1064 nm. For the dye laser system the second harmonic radiation is required which is generated in a KD*P (KD_2PO_4) crystal. In order to optimize the second harmonic generation, the polarization of the 1064 nm beam can be rotated with a $\lambda/2$ plate that is placed in front of the KD*P crystal. Depending on the 532 nm laser beam power required, the $\lambda/2$ plate can be rotated. As the efficiency of the IR generation and amplification depends on the polarization of the incoming 1064 nm beam the $\lambda/2$ plates in front of the crystals can be used to balance the rotation of the linear polarization effectuated with the $\lambda/2$ plate in the Nd:YAG laser. However, it turned out that the polarization of the residual 1064 nm beam was undefined and not linear at all. This means that in both LiNbO_3 crystals only that portion of light with the right polarization contributed to the IR generation and amplification. The rest of the beam was just passing through the crystals, losing a lot of conversion efficiency, and the $\lambda/2$ plate in front of the LiNbO_3 crystals were simply useless. We found that the KD*P crystal installed in the Nd:YAG laser was not suited for this IR laser system. The so-called type II KD*P crystal is used if a highly efficient second harmonic generation is required and if the residual 1064 nm beam is not further used. This is, however, not the case for this IR laser system. The residual 1064 nm beam is used for difference frequency mixing, and a well defined polarization is essential for an efficient conversion. For this application the so-called type I KD*P crystal is required. Therefore, the crystals have been exchanged (see Figure B.1, circle 3). Additionally, a $\lambda/2$ plate has been placed in front of the IR generation unit into the path of the 1064 nm beam. This additional $\lambda/2$ plate is necessary as the beam splitter (indicated as 2 in Figure B.1) is polarization dependent. The relative distribution of the two 1064 nm beams can therefore conveniently be changed by adjusting the $\lambda/2$ plate, and touching the beam splitter is no longer necessary for this purpose. This also avoids (in contrast to the original setup) a complete realignment of all optical components located after the beam splitter. With the type I crystal the whole 1064 nm beam can be used to generate and to amplify the IR radiation. Although the dye laser is pumped by a 532 nm beam with less power than when using the type II crystal, the overall efficiency could be increased significantly. By measuring the laser

power at different stages in the laser system we found that the IR generation is less sensitive on the polarization than the IR amplification process.

Additionally to the new $\lambda/2$ plate we installed a polarizing beam splitter just behind. The combination of both allows one to attenuate the laser beam power. This is important for the alignment of the IR generation unit which is preferentially done with low laser power. However, "the laser beam path depends on the Nd:YAG laser energy". The advantage of the additional $\lambda/2$ plate - polarizing beam splitter combination is that although the effective 1064 nm beam power is attenuated, the Nd:YAG laser is operated at full power (like during an experiment) and the beam path is the same for the alignment and the normal operation mode (this was not the case in the original setup).

Finally, in order to improve further the performance of the system the divergence of the Nd:YAG laser beam has been minimized and the second dye cuvette (see Figure B.1, circle 4), which was initially a capillary cell, has been replaced by a rectangular cell. The difficulty of the capillary cell was, that the beam profile was only homogeneous at low dye concentrations, too low to generate an intense (about 30 mJ/pulse) dye laser beam. An elevated concentration caused an intense absorption of the pump beam directly behind the dye cell wall, and therefore a "half moon" shaped laser profile was obtained. The efficiency of the subsequent IR generation was thus strongly affected by the dye laser beam profile. With the rectangular amplifier cell a fairly homogeneous dye laser beam profile can be obtained with a satisfactory power of the dye (and IR) laser output.

The combination of all technical changes of the laser system described here helps to improve significantly the stability and to increase the pulse energy of the IR laser.

Zusammenfassung

Seit jeher ist es das Bestreben der Menschheit zu erkennen, was die Welt im Innersten zusammenhält. Ein interessantes und wichtiges Thema beispielsweise beschäftigt sich mit dem Ablauf biologisch relevanter Prozesse und den Eigenschaften der darin involvierten Materie. Um diese jedoch auf makroskopischer Ebene zu verstehen, müssen zunächst die molekularen Bausteine untersucht werden. Dies geschieht im ersten und grundlegenden Schritt möglichst an isolierten Systemen in der Gasphase, um die intrinsischen Eigenschaften genau bestimmen zu können. In folgenden Untersuchungen können die Parameter denen der natürlichen Umgebung angepasst werden.

Schwache intra- und intermolekulare Wechselwirkungen dispersiver und elektrostatischer Natur können die molekulare Struktur erheblich beeinflussen und sind daher von großer Bedeutung. Um diese Wechselwirkungen unabhängig von molekülspezifischen Eigenschaften zu untersuchen, werden vereinfachte Modellsysteme, vorzugsweise in der Gasphase, herangezogen. Oft bestehen diese bereits aus einer beträchtlichen Anzahl von Atomen, können daher sterisch flexibel sein, und die möglichen verschiedenen Konformationen müssen dementsprechend bei der Auswertung berücksichtigt werden.

In der vorliegenden Arbeit werden die strukturellen Eigenschaften und die (interne) Dynamik von Benzoldimer (C_6H_6)₂ in der Gasphase mit Hilfe spektroskopischer Methoden, die die Energiebereiche der Rotationen, Vibrationen und elektronischen Übergänge abdecken, untersucht und hinsichtlich der Symmetrieeigenschaften diskutiert. Benzoldimer ist ein schwach gebundener Van der Waals Komplex und kann als Modellsystem für dispersive intermolekulare Wechselwirkungen dienen. Aufgrund der schwachen Bindungsenergie ($\sim 1000 \text{ cm}^{-1}$) ist die theoretische Beschreibung derjenigen Struktur, die dem globalen Minimum auf der Potentialhyperfläche entspricht, bis heute eine Herausforderung. Deshalb sind detaillierte Informationen aus experimentellen Studien sehr wertvoll.

Da Benzoldimer aus relativ wenigen Atomen besteht, ist zu erwarten, dass die Spektren verhältnismäßig übersichtlich sind. Benzoldimerkomplexe entstehen, wenn Benzol, verdünnt in einem Trägergas, adiabatisch von einem Hintergrunddruck von mehreren bar in Vakuum expandiert wird. In der Überschallexpansion

werden die internen Freiheitsgrade der Monomere durch unelastische Stöße mit den Trägergasatomen auf Rotations- und Schwingungstemperaturen von wenigen Kelvin gekühlt, und Clusterbildung kann eintreten. Die Moleküle in einer Überschallexpansion sind oft nicht im thermischen Gleichgewicht und im Fall von Molekülen mit mehreren Konformeren (z.B. Biomolekülen) ist die Dynamik der gegenseitigen Umwandlung zu berücksichtigen, um die relative Population der einzelnen Konformere zu verstehen.

Je nach Ausmaß der elektrostatischen und dispersiven Wechselwirkungsbeiträge können zwei Benzolmoleküle theoretisch eine der Dimergeometrien, die in Abbildung 1.9 gezeigt sind, annehmen. Durch Dimerisierung wird die D_{6h} Symmetrie der nicht wechselwirkenden Benzoleinheiten erniedrigt. Da die Infrarot (IR) Aktivität von Schwingungsmoden unmittelbar mit der Molekülsymmetrie verknüpft ist, kann die Erniedrigung der Symmetrie, wie etwa durch Dimerisierung, genutzt werden, um prinzipiell symmetrieverbotene Schwingungsübergänge zu untersuchen. In Kapitel 2 wird gezeigt, wie mit Hilfe der C-H-Streckschwingungsspektren des Benzoldimers die bisher unbekannte, Raman und IR inaktive Fundamentalschwingung ν_{13} des Benzolmonomers beobachtet und deren Schwingungsenergie bestimmt werden konnte.

Von großem Interesse für die Strukturaufklärung sind die individuellen Symmetrieeigenschaften der beiden Benzolmoleküle im Benzoldimer, die beispielsweise mittels Schwingungsspektroskopie untersucht werden können. Die C-H-Streckschwingungsspektren unterscheiden sich deutlich für die beiden Dimerhälften, was ein Indiz für eine Dimerstruktur ist, in der die Anordnung der beiden Benzolmoleküle zu jeweils unterschiedlichen Symmetrienumgebungen führt. Diese Beobachtung kann möglicherweise durch eine dynamische, in ihrer starren Form C_{2v} oder C_s symmetrische, T-förmige Anordnung erklärt werden und unterstützt neueste theoretische Ergebnisse.

Neben den schwingungsspektroskopischen Untersuchungen kann die Mikrowellen (MW) Spektroskopie hilfreich für die Aufklärung der Gleichgewichtsgeometrie sein (siehe Kapitel 3). Das Rotationsspektrum des Benzoldimers hat charakteristische Eigenschaften, die typisch für einen symmetrischen Kreisel sind. Die sehr schwache intermolekulare Wechselwirkung wirft die Frage nach der internen Dynamik des Benzoldimers auf, die mittels MW Spektroskopie in Kombination mit der Permutations-Inversions-Gruppentheorie untersucht wurde. Diese Untersuchungen führen momentan zu der Vermutung, dass beide Benzolmoleküle in einer (nahe) T-förmigen Geometrie angeordnet sind und Torsionen um ihre molekülfesten C_6 Symmetrieachsen durchführen.

Die Experimente an Benzoldimer werden in der vorliegenden Arbeit ergänzend an isotopensubstituierten Spezies, wie beispielsweise $(C_6H_6)(C_6D_6)$, durchgeführt, um wertvolle Zusatzinformationen zu erhalten. Unter der Annahme, dass die beiden Benzolpositionen im Dimer unterschiedliche Symmetrien haben, sind zwei Substitutionsisomere des $(C_6H_6)(C_6D_6)$ zu erwarten, die auch im elektronischen Spektrum unterschieden werden können. Obwohl die beiden

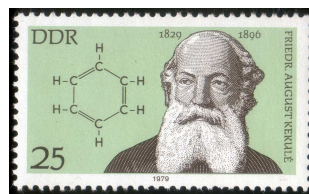
Isomere die gleiche elektronische Energie und nur eine geringfügig unterschiedliche Nullpunktsschwingungsenergie haben, können wesentliche Unterschiede bezüglich ihrer Abundanz im Molekularstrahl beobachtet werden. Mit Hilfe der Resonanzverstärkten Mehrphotonenionisation (REMPI), einer sehr sensitiven Nachweismethode, können die relativen Populationen als Funktion der Molekularstrahleigenschaften, wie beispielsweise in dieser Arbeit in Abhängigkeit von der Art des verwendeten Trägergases, untersucht werden. Auf Grundlage der experimentellen Beobachtungen wurde ein Model formuliert, das beschreibt, wie Kollisionen mit Edelgasatomen bei tiefen Temperaturen, wie sie beispielsweise in einem Molekularstrahl erreicht werden, die Umwandlung des Isomers mit höherer Energie in das Isomer mit niedriger Energie katalysieren (siehe Kapitel 4). Ob eine solche Isomerisierung stattfindet, hängt hauptsächlich von der Höhe der Barriere, die die betreffenden Isomere trennt, und von der Bindungsenergie der Kollisionspartner ab. Dieser Mechanismus funktioniert am besten bei niedrigen Temperaturen, bei denen (objektiv) sehr kleine Energieunterschiede groß im Vergleich zu den Kollisionsenergien erscheinen.

Dieses Model kann höchstwahrscheinlich auch zur Interpretation der Molekularstrahlexperimente an der Aminosäure Phenylalanin herangezogen werden: es erklärt, warum ein mittels theoretischer Studien hervorgesagtes Konformer in den bisherigen experimentellen Untersuchungen nicht beobachtet werden konnte, und ermöglicht, die experimentellen Bedingungen dahingehend zu verändern, dass das „fehlende“ Konformer experimentell zugänglich ist. Die N-H-Streckschwingungen des „fehlenden“ Konformers konnten untersucht werden und ermöglichten dessen strukturelle Zuordnung (siehe Kapitel 5).

Insgesamt werden sechs Phenylalanin Konformere im Molekularstrahl identifiziert. Betrachtet man jedoch deren relative Population im Zusammenhang mit ihren Energieunterschieden, stellt man fest, dass die beobachtete Populationsverteilung nicht derjenigen entspricht, die man im Fall eines thermischen Gleichgewichtes erwarten würde. Für eine angemessene Beschreibung der beobachteten Populationsverteilung müssen zusätzlich die Barrieren, d.h. die Energien der Übergangszustände, zwischen den Konformeren berücksichtigt werden (siehe Kapitel 5). Dazu muss die Potentialhyperfläche des Systems hinreichend bekannt sein. Um die Potentialhyperfläche eines Moleküls, das in verschiedenen Konformeren auftreten kann, zu untersuchen, können die Energien und Pfade möglicher gegenseitiger Umwandlungen konformerspezifisch untersucht werden. Das kann beispielsweise in Anregungs-Relaxations-Experimenten erfolgen (siehe Kapitel 4). Im Idealfall ist die Anregungsenergie einer Schwingung im elektronischen Grundzustand konformerselektiv. Wenn diese Energie ausreicht, um (mindestens) eine Barriere, die das schwingungsangeregte Konformer von einem anderen trennt, zu überwinden, kann in der anschließenden Schwingungsrelaxation eine Strukturänderung erfolgen. Die Änderungen der relativen Konformerpopulationen, gemessen in Abhängigkeit von der Anregungsenergie, können einen Beitrag zum Verständnis der Potentialhyperfläche leisten.

Die in dieser Arbeit vorgestellten Experimente tragen zu einem tieferen Verständnis des Benzoldimers bei, das ein wichtiges Modellsystem für dispersive Wechselwirkungen ist, die häufig in biologisch relevanten Systemen auftreten. Vor allem die experimentellen Untersuchungen hinsichtlich der internen Rotationen und die Permutations-Inversions-Gruppentheorie sind ein viel versprechender Ausgangspunkt, um durch weitere Untersuchungen die noch offenen Probleme bezüglich der Gleichgewichtsgeometrie zu lösen. In zukünftigen Experimenten sollte der Fokus auf isotopensubstituierten Benzoldimerspezies liegen. Schwingungen hochsymmetrischer Moleküle sind oft IR und Raman inaktiv, können jedoch mit der hier vorgestellten, eleganten Methode der Symmetriereduktion durch Komplexierung experimentell zugänglich gemacht werden. Das Modell, das stoßinduzierte Konformationsänderungen beschreibt, ist nützlich, um in Experimenten, die an sterisch flexiblen Molekülen in einem Molekularstrahl durchgeführt werden, die beobachtete Konformationsverteilung zu verstehen, und vor allem, um die experimentellen Parameter gezielt zu verändern, um definiert Konformerpopulationen zu manipulieren.

Konformerspezifische Informationen sind für das Verständnis eines sterisch flexiblen Moleküls von großer Bedeutung. Um auf direktem Weg möglichst eindeutige Ergebnisse zu erhalten, ist es von Vorteil, Experimente nicht an Mischungen von Konformeren durchzuführen, sondern individuell an jedem Konformer. Deshalb wäre es von großem Nutzen, diese räumlich und/oder zeitlich getrennt untersuchen zu können. Ein neuer experimenteller Ansatz [229], der die unterschiedlichen m/μ Verhältnisse der einzelnen Konformere ausnutzt, kann neutrale, polare Spezies räumlich in einem Molekularstrahl trennen, indem diese das Wechselfeld eines elektrischen Quadrupols passieren. Die Frequenz, mit der die Orientierung des Quadrupolfeldes geändert wird, kann durchgestimmt werden und ist für ein spezifisches m/μ Verhältnis, d.h. im Idealfall für ein bestimmtes Konformer, optimal, so dass dieses Konformer (genauer gesagt, dieses Konformer in einer beschränkten Anzahl von Quantenzuständen) das Ende des Quadrupolfilters erreicht, während die übrigen Konformere durch die Wechselwirkung mit dem elektrischen Feld von der Molekularstrahlachse abgelenkt werden. Wenn dann ein Konformer isoliert von den anderen vorliegt, können sehr präzise, spektroskopische Untersuchungen erfolgen, da nur wenige Quantenzustände hinreichend besetzt sind.



Das war's!

Résumé

De tous temps le désir de l'humanité a été de pouvoir connaître ce que le monde cache en lui-même [Goethe]. Un sujet passionnant et important, par exemple, est le déroulement des processus biologiques pertinents et les propriétés de la matière impliquée. Pourtant pour comprendre celles-ci au niveau macroscopique, les modules moléculaires doivent d'abord être investigués. Dans une étape initiale, des systèmes isolés sont investigués en phase gazeuse, ce qui permet de déterminer précisément leurs propriétés intrinsèques. Dans des études suivantes on les étudie dans un environnement qui se rapproche de l'environnement naturel des processus biologiques.

Des interactions faibles, de nature dispersive ou électrostatique, peuvent modifier considérablement la structure moléculaire et elles ont donc une importance majeure. Pour investiguer ces interactions indépendamment des propriétés spécifiques d'une molécule, des systèmes modèles sont utilisés, de préférence en phase gazeuse. Souvent ces modèles consistent déjà en un nombre d'atomes considérable, ils ont donc une structure flexible et les différents conformères possibles doivent être connus et considérés correctement pour interpréter les résultats expérimentaux.

Dans cette thèse les propriétés structurelles et la dynamique (interne) du dimère de benzène $(\text{C}_6\text{H}_6)_2$ ont été investiguées en phase gazeuse par spectroscopie dans les gammes énergétiques des rotations, des vibrations et des transitions électroniques, et elles sont discutées sous l'angle de la symétrie. Le dimère de benzène est un complexe van der Waals faiblement lié et peut servir de modèle pour des interactions intermoléculaires dispersives. Due à sa petite énergie de liaison ($\sim 1000 \text{ cm}^{-1}$), la description théorique de la structure qui correspond au minimum de la surface de potentiel moléculaire est toujours un défi. C'est pourquoi des informations détaillées résultant des études expérimentales sont très précieuses.

Comme le dimère de benzène est composé de relativement peu d'atomes on attend des spectres plutôt simples. Le dimère de benzène se forme si du benzène, dilué dans un gaz porteur, est en expansion adiabatique d'une pression de quelques bars dans le vide. Dans l'expansion supersonique les degrés de liberté internes sont refroidis par des collisions inélastiques avec les atomes du

gaz porteur. La température rotationnelle et vibrationnelle descend à quelques degrés Kelvin et la formation des agrégats devient possible. Les molécules dans une expansion supersonique sont souvent hors équilibre thermique et dans le cas où plusieurs conformères coexistent la dynamique de la conversion mutuelle doit être considérée pour interpréter la population relative des différents conformères.

Les deux sous-unités du dimère peuvent théoriquement adopter une des structures présentées dans la figure 1.9, en fonction de la contribution des interactions électrostatiques et dispersives. La symétrie D_{6h} du benzène libre est baissée par dimérisation. Comme l'activité infrarouge des modes vibrationnels est liée directement à la symétrie moléculaire, l'abaissement de la symétrie, comme par exemple par dimérisation, peut être exploité pour investiguer des transitions vibrationnelles qui sont interdites dans le monomère. Dans chapitre 2 il est montré que, basé sur des spectres de vibration C-H stretch du dimère de benzène, le mode fondamental ν_{13} du monomère de benzène, qui est infrarouge et Raman inactif, peut être observé et attribué à une énergie vibrationnelle.

Pour explorer la structure du dimère de benzène les symétries individuelles des deux composantes peuvent être investiguées, par exemple par la spectroscopie vibrationnelle. Les structures des spectres de vibration C-H stretch diffèrent considérablement pour les deux moitiés du dimère, ce qui indique que l'arrangement des deux molécules de benzène dans le dimère provoque deux symétries différentes pour les deux sous-unités. Cette observation peut être expliquée par une structure dynamique en forme de T et conforte les derniers résultats théoriques. Une telle structure a dans sa forme rigide la symétrie C_{2v} ou C_s .

A côté de la spectroscopie vibrationnelle la spectroscopie microondes peut servir à élucider la structure d'énergie minimale (chapitre 3). Le spectre rotationnel du dimère de benzène a les propriétés caractéristiques d'une toupie symétrique. La faible interaction intermoléculaire permet une dynamique interne qui a été investiguée par la spectroscopie microondes en combinaison avec la théorie des groupes de permutation-inversion. En ce moment ces recherches laissent supposer que les deux molécules de benzène sont arrangées en forme de T (strictement 90° ou légèrement vrillé) et qu'elles tournent sur leurs axes moléculaires C_6 .

Dans cette thèse les expériences sur le dimère de benzène sont accompagnées par des études sur des espèces isotopiquement substituées, comme par exemple $(C_6H_6)(C_6D_6)$, pour obtenir des informations supplémentaires. A supposer que les deux molécules de benzène du dimère ont des symétries différentes, $(C_6H_6)(C_6D_6)$ devrait exister en deux isomères. Effectivement, ces deux isomères peuvent être discriminés par leurs spectres électroniques. Bien que les deux isomères aient la même énergie électronique et diffèrent seulement très peu dans leurs énergies vibrationnelles de point zero, des différences énormes concernant leurs abondances dans le jet moléculaire pouvaient être observées. Resonance Enhanced Multi Photon Ionization (REMPI) est une méthode de détection très sensible et peut servir pour mesurer la population relative en fonction des

propriétés du jet moléculaire, comme par exemple l'influence de la nature du gaz porteur. Basé sur les résultats expérimentaux un modèle est proposé qui décrit comme des collisions avec des atoms du gaz porteur à température basse, comme atteinte par exemple dans un jet moléculaire, catalysent l'isomérisation de l'isomère plus énergétique à l'isomère moins énergétique (chapitre 4). La faisabilité d'une telle isomérisation dépend principalement de la hauteur de la barrière séparant les deux isomères et de l'énergie de liaison des partenaires de collision. Ce mécanisme marche le mieux à température basse, où des différences d'énergie très petites apparaissent grandes par rapport aux énergies de collision.

Ce modèle sert aussi à interpréter des résultats des expériences sur l'acide aminé phénylalanine dans un jet moléculaire : il explique pourquoi un des conformères théoriquement prédit ne pouvait pas être observé dans les études antérieures et permet d'adapter les conditions expérimentales de manière à observer ce conformère. Son spectre vibrationnel N-H stretch pouvait être mesuré et il permettait une attribution structurale (chapitre 5).

En total, six conformères de phénylalanine sont identifiés dans le jet moléculaire. En regardant leurs populations relatives en rapport avec leurs différences énergétiques on trouve que la distribution de la population ne correspond pas à celle attendue à l'équilibre thermique. Pour une description convenable de la distribution observée, les barrières entre conformères, c'est-à-dire les énergies des états de transition, doivent être considérées (chapitre 5). Pour cela la surface de potentiel moléculaire du système doit être suffisamment connue. Pour explorer la surface de potentiel moléculaire d'une molécule qui peut apparaître sous plusieurs conformères différents, les énergies et les trajets des inversions mutuelles peuvent être investigués sélectivement pour chaque conformère. Cela peut être réalisé avec une expérience d'excitation accompagnée de relaxation (chapitre 4). Dans le cas idéal l'énergie d'excitation d'une vibration dans l'état fondamental électronique sélectionne un conformère. Si cette énergie est suffisamment haute pour surmonter (au moins) une barrière qui sépare le conformère vibrationnellement excité d'un autre, la structure peut changer pendant la relaxation suivante. La redistribution des populations des conformères, mesurée en fonction de l'énergie d'excitation, peut contribuer à explorer la surface de potentiel moléculaire.

Les expériences présentées dans ce manuscrit contribuent à une compréhension plus profonde du dimère de benzène, qui est un modèle important pour des interactions dispersives, qui se trouvent souvent dans des systèmes d'importance biologique. Surtout, les expériences concernant les rotations internes et la théorie des groupes de permutation-inversion sont encourageantes et stimulent d'autres études qui probablement permettront de répondre aux questions restées ouvertes. Des études ultérieures devraient se focaliser sur des dimères de benzène isotopiquement substitués. Les vibrations des molécules avec une haute symétrie sont souvent inactives pour les transitions infrarouge et Raman, mais

peuvent, en fonction du système, être accessibles par la méthode élégante de réduction de symétrie par complexation présentée dans cette thèse. Le modèle, qui décrit la conversion des conformères induite par des collisions, est utile pour comprendre la distribution des conformères d'une molécule flexible dans un jet moléculaire et aussi pour changer sciemment les paramètres expérimentaux pour manipuler la distribution des populations des conformères. Des informations spécifiques au conformère ont une importance majeure pour la compréhension des molécules flexibles. Pour obtenir des résultats explicites il est désirable de ne pas investiguer une mixture de conformères mais chaque conformère individuellement. Pour cela la séparation des conformères en temps et/ou en espace serait très utile. Une nouvelle approche expérimentale [229] exploitant les différentes proportions m/μ des conformères différents peut séparer des molécules polaires et neutres dans un jet moléculaire en espace en les laissant traverser le champ alternant d'un quadrupole électrique. La fréquence avec laquelle l'orientation du champ quadripolaire est changée peut être variée et est optimale pour une valeur spécifique de la proportion m/μ , soit au cas idéal pour quelques états quantiques d'un seul conformère. Ce conformère arrivera au bout du filtre quadripolaire pendant que les autres conformères sont déviés de l'axe du jet moléculaire par l'interaction avec le champ électrique. Lorsque un conformère est isolé des autres il est à la disposition des études spectroscopiques extrêmement précises puisque seulement peu d'états quantiques sont peuplés.

Publikationsliste

- *Adsorption of methane and ethane on RuO₂(110) surfaces*
U. Erlekam, U. A. Paulus, Y. Wang, H. P. Bonzel, K. Jacobi, G. Ertl
Z. Phys. Chem. **219** (7), 891 (2005)
- *An experimental value for the B_{1u} C-H stretch mode in benzene*
U. Erlekam, M. Frankowski, G. Meijer, G. von Helden
J. Chem. Phys. **124** (17), 171101 (2006)
- *Cold collisions catalyse conformational conversion*
U. Erlekam, M. Frankowski, G. von Helden, G. Meijer
Phys. Chem. Chem. Phys. **9** (28), 3786 (2007)
- *Mid-IR spectra of different conformers of phenylalanine in the gas phase*
G. von Helden, I. Compagnon, M. N. Blom, M. Frankowski, U. Erlekam,
J. Oomens, B. Brauer, R. B. Gerber, G. Meijer
Phys. Chem. Chem. Phys. (2008) DOI: 10.1039/b713274c
- *A selector for structural isomers of neutral molecules*
F. Filsinger, U. Erlekam, G. von Helden, J. Küpper, G. Meijer
submitted
- *Different symmetries, different vibrational properties: the two subunits in the benzene dimer*
U. Erlekam, G. Meijer, G. von Helden
in preparation
- *Internal dynamics of the benzene dimer - an experimental and theoretical study*
U. Erlekam, P. R. Bunker, M. Schnell, J.-U. Grabow, G. von Helden, G. Meijer
in preparation

Selbstständigkeitserklärung

Hiermit erkläre ich, Undine Erlekm, die vorliegende Arbeit selbstständig und nur unter Verwendung der angegebenen Hilfsmittel und Literatur angefertigt zu haben.

Berlin, 18/12/2007
Undine Erlekm

Danksagung

Zu guter letzt möchte ich mich bei allen bedanken, die mir in den vergangenen Jahren mit Rat und Tat zur Seite standen.

Allen voran bei Gerard Meijer. Gerard ist ein bewundernswerter Manager, hervorragender Wissenschaftler (und leidenschaftlicher Fußballfan). Trotz vieler Termine und Verpflichtungen findet er für jeden in unserer Arbeitsgruppe immer einen Moment Zeit. Ich danke ihm für unsere lehrreichen und interessanten wissenschaftlichen Diskussionen, die diese Arbeit vorangetrieben haben.

Gert von Helden danke ich für die Betreuung dieser Arbeit. Gert ist ein experimentierfreudiger und begeisterungsfähiger Wissenschaftler, der immer zur Stelle war, wenn ich ihn um Hilfe rief. Sogar für das Putzen von Prismen war er sich nicht zu schade ;-). Gert hat mit vielen sehr guten Ideen und Vorschlägen einen großen Beitrag zu dieser Arbeit geleistet. Dankeschön dafür!

I want to thank Phil Bunker for introducing me into the field of the MS group theory, for our nice cooperation and many interesting and constructive discussions. And thank you for the discussions beyond the benzene dimer.

Bei Jens-Uwe Grabow und Melanie Schnell bedanke ich mich für die Unterstützung, Benzoldimer zum rotieren zu bringen (dieses brachte uns dann wiederum zur Verzweiflung - aber egal), für die vielen Tage und Nächte, die wir gemeinsam im Labor in Hannover verbracht haben, und den Spaß, den wir dabei hatten.

Mit Frank Filsinger und Jochen Küpper zerpfückte ich meine Vakuumkammer in zwei Teile, und wir setzten vier lange Elektroden dazwischen. Ich danke beiden für die gute und sehr interessante Zusammenarbeit, die dann folgte. Frank danke ich für die lustigen und auch anstrengenden Stunden im Labor.

Viele, viele Stunden, Tage und Wochen habe ich an einem IR Lasersystem gearbeitet. Zum Glück war ich nicht ganz allein dabei. In der ersten Zeit bekam ich Unterstützung von Uwe Lehmann und später von Sandy Gewinner. Bei beiden möchte ich mich bedanken für ihre scheinbar endlose Geduld und ihre Hilfsbereitschaft. Zusammen haben wir oft über immer wieder neue, seltsame Verhaltensweisen des Lasers gestaunt, geflucht....und derer abgeholfen. Trotz mancher hoffnungslos scheinender Tage war es mir ein großes Vergnügen, mit Euch beiden zu arbeiten, und mit und von Euch zu lernen.

I wish to thank Boris Sartakov for the stimulating discussions on the benzene dimer.

Bei Joost Bakker möchte ich mich ebenfalls bedanken. Joost, Du hattest immer ein offenes Ohr, wenn mir im Labor mal wieder die Decke auf den Kopf gefallen war. Auch wenn Du das eine oder andere Mal über das Ziel hinaus geschossen bist, war es gut, dass Du da warst.

I want to thank Marcin Frankowski for showing me how to regard (subjectively bad) situations from another point of view. When we (especially me) were freezing in our air conditioned lab and sweating in our office he explained me that dogs can lower their body temperature only by panting - no perspiratory glands, nothing. Thank you for this and other cheering stories. Dziękuję bardzo.

Wolfgang Erlebach danke ich für die Anfertigung vieler technischer Zeichnungen, und den Mitarbeitern der Feinwerktechnik für die Anfertigung der darauf abgebildeten Elemente. Besonders dankbar bin ich für die Bereitschaft „nur dieses kleine Teil - vielleicht heute noch?“ anzufertigen, so dass ich ganz schnell wieder am Experiment arbeiten konnte. Natürlich möchte ich auch all den motivierten Mitarbeitern des Elektroniklabors und jenen von PP&B danken. Den PP&Blern vor allem dafür, dass sie sich auch eines im Prinzip selbstadministrierten Rechners bereitwillig annahmen.

Ich möchte mich bei André Fielicke bedanken, den ich vor acht Jahren als Tutor für Physikalische Chemie kennenlernte und mit dem ich in den letzten Jahren ein Büro teilte. Er hatte immer einen großen Vorrat an Schokolade, die er gerne teilte - sofern man gut fangen konnte.

Mein Dank gilt auch unseren Technikern Jürgen Maier, Rolf Meilicke, Manfred Erdmann und unserer Sekretärin Beatrix Wieczorek.

Inga von Dölln-Grossmann ist die gute Seele unserer Abteilung und sorgt dafür, dass sich alle wohlfühlen. Für ihr Engagement (auch beim Berlin Marathon) bedanke ich mich recht herzlich.

Ich danke natürlich auch den noch nicht erwähnten Doktoranden, Post docs und Diplomanden, die insgesamt zu der tollen Atmosphäre in der Gruppe beigetragen haben: Sophie, Adela, Cyndi, Kirstin, Jacqueline, Amudha, Michael, Philipp, Bas, Joop, Ludwig, Steven, Andreas, Frauke, Peter, Werner, Marko, Thomas und Moritz.

Herrn Klaus Rademann danke ich für die freundliche Unterstützung und die Bereitschaft zur Begutachtung dieser Arbeit.

Meiner Familie und meinen Freunden danke ich für die moralische Unterstützung und das Verständnis, dass ich den einen oder anderen Besuch verschoben und zahlreiche Konzerte abgesagt habe.

J'aimerais remercier surtout mon très cher mari Nico pour alles ce que Du fais für moi, für ton amitié, Deine soutien moral, Dein intérêt für mon travail, unsere discussions und plein de moments unvergesslich.

... und Danke Berlin!